COMPUTATIONAL FLUID DYNAMICS MODELLING OF DISPLACEMENT NATURAL VENTILATION

Y. JI

PhD

2005

Computational Fluid Dynamics Modelling of Displacement Natural Ventilation

Yingchun Ji Beng

This thesis is submitted to De Montfort University, Leicester, in partial fulfilment of the requirements for the degree of Doctor of Philosophy

March 2005

Abstract

Natural ventilation is widely recognised as contributing towards low-energy building design. The requirement to reduce energy usage in new buildings has rejuvenated interest in natural ventilation.

This thesis deals with computer modelling of natural displacement ventilation driven either by buoyancy or buoyancy combined with wind forces. Two benchmarks have been developed using computational fluid dynamics (CFD) in order to evaluate the accuracy with which CFD is able to model natural displacement ventilation flow. The first benchmark considers the natural ventilation of a single ventilated space with high and low level openings connected to the exterior driven by combined forces of wind and buoyancy. The second benchmark considers natural ventilation flow in a single space connected to an atrium driven by pure buoyancy. Simulation results of key ventilation parameters (stratification depth, temperature gradient and ventilation flow rate) have been compared with analytical and experimental models and close agreements have been achieved.

The two benchmarks are defined using the RNG k-epsilon turbulence model. A pressure boundary is applied onto the ventilation openings directly and a porous medium boundary is used to assist the development of the thermal plume. This method has proved to be robust and the close agreement between the three modelling techniques indicates that CFD is able to model natural ventilation flows in simple geometries with acceptable accuracy and reliability.

Using the benchmarks the influences of key CFD modelling parameters and building design issues have been investigated. For example, representing openings, heat source representation, stack height, and air inlet strategies.

Natural displacement ventilation of a multi-storey building comprising an atrium is also addressed. Simple analytical models have been developed to describe the key air flow features within the ventilation system.

Acknowledgements

This research was supported with funding from an EPSRC project (GR/N37346). The support of the EPSRC is gratefully acknowledged.

I would like to thank my supervisor, Dr. Malcolm Cook (De Montfort University) whose support, sound guidance, and meticulous attention to detail throughout this research has been greatly appreciated. I would also like to thank my second supervisor Prof. Vic Hanby (De Montfort University) and my external advisor Dr. Gary Hunt (Imperial College London) whose complimentary backgrounds ensured a varied and balanced approach to my research. I am also thankful to Dr. Simon Rees for his enlightening discussions and to Dr. Paul Cropper for his help with IT matters.

I would like to thank all of the staff at the IESD for their moral support and encouragement.

The support of my family and friends in China is essential for me to complete this thesis. I am very grateful for their spiritual support.

Contents

List of Figures

List of Tables

Nomenclature

a_{in} , a_{out}	inlet and outlet opening area of the space (m^2)
a_i	opening area at location i (m^2)
ach^{-1}	air changes per hour
A^*	effective opening area of benchmark 1 cases (m^2)
A_a	effective opening area at atrium outlet opening (m^2)
A_b	effective opening area of an atrium inlet opening (m^2)
A_i^*	effective opening area at location i (m^2)
A_{js}	total effective opening area of the single storey for the j^{th} floor (m^2)
A_s	effective opening area of a single storey (m^2)
A_t	effective opening area of a storey and an atrium (m^2)
A_{tot-4}^*	effective opening area of a single storey
A_{tot-5}^*	effective opening area of a single storey & the atrium (m^2)
A_u	effective opening area of the atrium outlet opening (m^2)
A_{jt}	total effective opening area of the j^{th} floor (m^2)
B	buoyancy flux of the heat source (m^4s^{-3})
B_i	body force (i.e. due to buoyancy) (m^4s^{-3})
B_s , B_{solar}	buoyancy flux for solar energy (m^4s^{-3})
c_p	specific heat capacity at constant pressure ($m^2s^{-2}K^{-1}$)
C	plume entrainment constant ≈ 0.143 (-)
C_D , C_e	discharge and expansion coefficients (-)
C_μ , $C_{1\varepsilon}$, $C_{2\varepsilon}$, $C_{3\varepsilon}$	turbulence model constants (-)
$C_{1\varepsilon}^*$	model constant determined by RNG theory (-)
C_D'	an empirical constant (≈ 1.0)
C_d , C_{di}	loss coefficients at openings, location i (-)
C_{dji}	loss coefficients at location i of the j^{th} floor (-)
C_p	wind pressure coefficient (-)
C_{pw} , C_{pl}	windward and leeward wind pressure coefficients (-)
d_c	the distance from the middle of the upper opening to the ceiling (m)
d	diameter of top-down-chimney (m)
$\overline{d}$	hydraulic diameter of top-down chimney (m)
D	diameter of heat source (m)

E	heat source strength (W)
E'	a log-layer constant depending on wall roughness (-)
f (≈ 0.005)	frictional constant along the top-down chimney (-)
F	volume flow rate through the plume at the interface (m^3s^{-1})
Fr	Froude number (-)
g	acceleration due to gravity (ms^{-2})
g'	reduced gravity of the warm upper layer (ms^{-2})
g'_h	reduced gravity at the interface height (ms^{-2})
g'_0	initial reduced gravity for a brine source(ms^{-2})
g'_a	reduced gravity of the atrium air (ms^{-2})
g'_s	reduced gravity in the upper layer of the single storey (ms^{-2})
G'	reduced gravity in the thermal plume (ms^{-2})
G_k	production term due to buoyancy (varies)
G'_H	reduced gravity in the thermal plume at the ceiling (ms^{-2})
h	interface height in the ventilated space (m)
h_a	interface height in the atrium (m)
h_s	single storey interface height (m)
H	height of the ventilated space (m)
He	enthalpy ($J \cdot kg^{-1}$)
k	turbulent kinetic energy (m^2s^{-2})
K	mean kinetic energy (m^2s^{-2})
l	top-down-chimney length (m)
l_m	mixing length scale used in zero equation model (m)
l_s	a length scale to determine μ_t (m)
L	length of the ventilated space (m)
m	hydraulic mean depth (m)
M	atrium height (m)
M_{eff}	effective atrium height (m)
p_1, p_2	internal pressures at level of lower and upper openings (Pa)
P	absolute pressure (Pa)
P'	the modified pressure (Pa)
P_k	the production of turbulent kinetic energy (varies)
P_{ref}	reference pressure (Pa)
ΔP	pressure difference across a ventilation opening (Pa)
Q	ventilation flow rates through a ventilated space (m^3s^{-1})
Q_B, Q_W	ventilation flow rates due to buoyancy, wind effects (m^3s^{-1})
Q_h	volume flow rate at the interface height (m^3s^{-1})

Q_H	volume flow rate in the thermal plume at the ceiling (m^3s^{-1})
Q_s	volume flow rates through the space (m^3s^{-1})
Q_0	initial volume flux for a brine source (m^3s^{-1})
$\overline{Q}_{low}$, $\overline{Q}_s$, $\overline{Q}_{up}$	dimensionless form of the volume flow rates through the atrium inlet opening, the single storey and the atrium outlet opening (-)
$\Delta\overline{Q}_s$	dimensionless volume flow induced by an unventilated tall atrium (-)
R_e	Reynolds number (-)
s	perimeter of the TDC (m)
S_T	source term of the enthalpy equation (varies)
S_Φ	general source term (varies)
t	time (s)
T	absolute temperature (K)
ΔT	temperature difference between the ambient and warm upper layer (K)
T_o	reference temperature and the ambient temperature (K)
u_i , u_j (= u , v , w)	velocity vectors (ms^{-1})
u_i' , u_j'	fluctuation velocities (ms^{-1})
u^+ , u_τ	normalised near wall velocity and the friction velocity (-)
U	characteristic velocity (ms^{-1})
$U_j(U_i)$	velocity components in the conservation equations (ms^{-1})
$U_{ref}(U_w)$	reference mean wind velocity (ms^{-1})
W	width of the ventilated space (m)
x_i	position vector (m)
y	vertical distance from the heat source (m)
y_{avs}	virtual source origin (m)
y_v	dimensionless asymptotic virtual source origin (-)
y^+	normalised distance from wall (-)
y_o^+	wall function constant (-)
Δ	pressure drop across a building envelope (Pa)

Greek

α	'top-hat' entrainment coefficient (-)
α_G	'Gaussian' profile entrainment coefficient, $\alpha = \sqrt{2}\alpha_G$ (-)

β	coefficient of thermal expansion (K^{-1})
ε	dissipation rate of turbulent kinetic energy (m^2s^{-3})
ϕ	time averaged general variable (varies)
ϕ'	fluctuation term of time averaged general variable (varies)
γ	volume porosity of porous media (-)
η	variable used for Renormalisation Group theory (-)
η_0	RNG k-epsilon model constant (-)
Φ	a general variable of the conservation equations (varies)
λ	thermal conductivity ($Wm^{-1}K^{-1}$)
λ'	temperature coefficient ($0<\lambda'<1$) (-)
μ	dynamic viscosity ($kgm^{-1}s^{-1}$)
μ_t	turbulent viscosity ($kgm^{-1}s^{-1}$)
ν	kinematic viscosity of fluids (m^2s^{-1})
κ	the Von Karman constant (-)
υ_t	lateral turbulence velocity (ms^{-1})
ρ	air density (kgm^{-3})
$\Delta\rho$	density difference between the warm upper layer and the ambient (kgm^{-3})
ρ_o	reference density used in CFX (kgm^{-3})
σ , σ_t	Prandtl numbers for laminar viscosity and turbulence viscosity (-)
σ_ε , σ_k	turbulent Prandtl number for ε , k (-)
σ_H (= 0.9)	turbulent Prandtl number for enthalpy (-)
τ_w	wall shear stress (Pa)
ξ (= h/H)	dimensionless interface height (-)
ξ_s (= h/H)	single storey dimensionless interface height (-)
ξ_a (h_a/H)	dimensionless interface height of the atrium (-)
Γ	diffusivity of fluids ($kgm^{-1}s^{-1}$)
Γ_e , Γ_t	effective diffusion coefficient, turbulence diffusion coefficient ($kgm^{-1}s^{-1}$)

Suffices

m	model scale
f	full scale
τ_{ij} (e_{ij})	see Appendix A

Chapter 1

Introduction

1. Introduction

It is important to provide sufficient ventilation for human health and comfort. Ventilation can be categorised as natural, mechanical or hybrid. The purpose of ventilation is to supply fresh, clean air, remove stale, contaminated air and balance the cooling and heating loads of buildings for occupants.

In the UK, around half of the total energy consumption is used by buildings, and mechanical ventilation (e.g. air-conditioning) plays a significant role for this energy usage (CIBSE 1998). Also, with the worldwide awareness of greenhouse gas emissions and global warming, natural ventilation using wind and thermal buoyancy effects (e.g. lights, household electric appliances, people, solar gain etc.) has become an increasingly attractive method for providing ventilation and improving the indoor environment for occupants. However, there are barriers preventing the wide spread acceptance of natural ventilation. Firstly, there is a lack of knowledge regarding the airflow patterns generated by these natural forces, and secondly, a relatively low level of control compared with mechanical ventilation systems.

It is desirable to be able to predict the performance of ventilation strategies at the design stage in order to know whether the strategy is practical or not. Different types of techniques, such as simple mathematical models, small-scale laboratory experiments and numerical methods, have been developed to study natural displacement ventilation in buildings. Simple mathematical models can be used to predict the main parameters of natural ventilation flows (for example: the ventilation rate through the building and the height of the fresh air zone for occupants), while the data produced by small-scale laboratory experiments are useful for visualizing the flow and validation of analytical models. Numerical methods are far more complex than these two traditional methods. However, with the aid of high-speed modern computers, numerical simulations using CFD (Computational Fluid Dynamic) programs are becoming more viable. CFD programs are used to solve a fluid flow problem using mathematical equations based on the conservation laws of physics. The fluid domain of interest is divided into small cells and the conservation equations of mass, momentum and energy are solved to predict

velocity, pressure, temperature and turbulence parameters in each cell. To predict the turbulence parameters, additional conservation equations are used, for example, turbulent kinetic energy and its dissipation rate.

It is preferable to use simple analytical models before conducting experiments since experimental studies are costly, time consuming and difficult to modify. However, the analytical models are not able to provide detailed information, such as the detailed distributions of air temperatures and velocities, while numerical simulations using CFD are capable of predicting such features. CFD has now become a useful tool for modelling airflows in buildings although the sophisticated partial differential equations on which the technique is based need to be solved with care and validation of the technique is still needed.

1.1 Aim and objectives

The aim of this work is to increase confidence in the ability of CFD programs to predict displacement natural ventilation in buildings. This aim was achieved through the following objectives:

- To develop new benchmarks for evaluating the accuracy of CFD for modelling naturally ventilated spaces.

The benchmarks developed in this thesis are standardized test cases that serve as a basis for evaluation or comparison. The first benchmark is to investigate natural ventilation in an enclosure driven by combined forces of wind and buoyancy. The second benchmark is to investigate natural ventilation in a single space connected to an atrium driven by thermal buoyancy. For both cases the natural ventilation flow is restricted to a displacement ventilation mode.

- To investigate the influence of key CFD modelling issues using the new benchmarks.

For modelling natural ventilation airflows, these issues include: how to represent the heat source; the effect of solid obstructions; how to model the losses of ventilation flow at openings; how to maintain an vertical thermal

plume; which turbulence model is suitable for modelling these natural ventilation strategies with respect to both accuracy and computing time.

- To investigate the influence of key building design features using the new benchmarks.

This objective considers the effect of changing key aspects of the building design. Design features, such as ‘stack height’, ‘floor-to-ceiling height’, ‘floor plan depth’ and ‘air inlet strategies’, were investigated. The influence of these features on air change rate, stratification level and the air temperature gradient across such stratifications have been examined.

- To provide guidance on the use and reliability of CFD for modelling natural ventilation flows in buildings.

A set of guidelines will be provided on how best to model natural ventilation flows for the two benchmarks developed in this research.

1.2 Thesis contents

A literature review and background study is provided in chapter 2. Purely buoyancy-driven flows and buoyancy combined with wind-driven flows are the main interest in this research. The fundamental mathematical analysis of thermal effects within confined regions is discussed in this chapter followed by the analytical models used to develop the benchmarks of this study. The previous research of numerical modelling for natural ventilation is also addressed

Chapter 3 describes the salt bath modelling of natural ventilation in a single space and connected spaces. Salt bath experiments were used to validate the analytical predictions of chapter 2 and good agreement has been achieved. Another experimental method, the fine bubble technique, is also introduced. The results of the fine bubble technique support the salt bath modelling in predicting natural ventilation flows. The use of experimental data to evaluate the CFD modelling is also outlined in this chapter.

Details of the CFD model used are presented in chapter 4. The mathematical descriptions of fluid flows are given as governing equations which can be

solved using turbulence modelling. The mathematical forms of turbulence modelling used in CFD codes are discussed. The algorithms for solving turbulence models numerically are given in Appendix B. The final part of this chapter gives a method for evaluating the CFD codes used in this research.

In chapter 5, the first benchmark cases are investigated in detail using CFD. Both assisting and opposing wind effects on thermal buoyancy are considered. The CFD predictions of stratification levels, temperature changes across such levels, ventilation flow rates and the pressure gradients within the space are evaluated.

The second benchmark cases are presented in chapter 6. An atrium is connected to a single space to enhance the stack effect, and therefore increase the ventilation flow through the space. The influence of building design features is addressed in this chapter using benchmark 2 as a basis.

In chapter 7, new mathematical models are developed for a multi-storey building connected to an atrium. When the ventilation flow rate through each storey is the same, simple analytical models can be derived. More complex mathematical models (simultaneous equations) can be used when a multi-storey building requires different ventilation flow rate at each storey. A root-finding algorithm was used to solve the simultaneous equations.

The conclusions and suggestions of future work are presented in chapter 9.

Chapter 2

Fundamentals of Natural Ventilation

2. Fundamentals of Natural Ventilation

In order to replenish oxygen used by occupants and remove pollutants generated by breathing, cooking, and the emissions from building materials and furnishings, it is crucial for buildings to have an indoor/outdoor exchange of air. This is particularly true today since people spend 90% of their time indoors (Awbi, 1991).

Unhealthy buildings are sometimes related to poor ventilation. Miller (1992) highlights the relationship between increasing bacteriological concentration with decreasing ventilation rates. Through a historical view, Billington (1982) pointed out the importance of ventilation in improving health and reducing the spread of illness. Studies reported by Seppanen et al (1999) showed that ventilation rates below 10 Ls^{-1} per person in all building types were associated with statistically significant worsening in health and air quality; ventilation rates of up to approximately 20 Ls^{-1} per person further significantly decreased the prevalence of SBS (sick building syndrome) symptoms or further significantly improve the air quality. Therefore, a carefully designed ventilation system with an adequate ventilation rate can have a positive contribution on the health and comfort of occupants.

Air movement in buildings caused by ventilation has a profound effect on energy consumption and thermal comfort. Generally, there are three types of ventilation methods: mechanical (or forced) ventilation, natural ventilation and hybrid ventilation which is the combination of the first two methods. Ventilation by mechanical means requires the use of a system that employs electric fans to drive a flow through a building. In a well insulated building, such systems can provide full control of heating, cooling and humidity. This method can be both energy-intensive and have high maintenance costs, as well as yielding poor air quality for occupants in poorly designed and/or maintained systems.

Natural ventilation can be achieved using natural driving forces. Dynamic pressure variations due to the flow of wind around a building can drive a flow through the building; static pressure differences due to temperature differences inside and outside a building (known as stack effect) can also be

used to drive a flow. Due to the use of natural sources natural ventilation has the potential for saving energy despite the difficulty of controlling the natural driving forces.

This research work concentrates purely on natural ventilation. This chapter provides a background to natural ventilation in which its mechanisms, operating modes, and historical review and modern applications, are discussed. Analytical modelling of natural ventilation induced by buoyancy, buoyancy combined with wind, is also addressed and followed by the numerical modelling of natural ventilation flow driven by thermal buoyancy.

2.1 Background of natural ventilation

Natural ventilation considered in this research has three forms:

- Wind-driven cross ventilation
- Buoyancy-driven displacement ventilation, and
- Ventilation induced by buoyancy combined with wind.

2.1.1 Wind-driven cross ventilation

When wind flows around a building there will be a dynamic pressure drop between the windward and the leeward sides. If there are openings located in the building envelope the dynamic pressure drop will drive a flow through the openings (Figure 2.1).

A difference in wind pressure between the openings on the high and low pressure sides is essential to effectively remove heat and pollutants from the space. At the windward side the absolute pressure outside the box is larger than that of inside, which leads to an inflow of air into the space. At the leeward side the absolute pressure outside the box is smaller than that of inside, therefore an outflow of air will occur. Air in the space will then be forced out due to this flow driven by the pressure differences.

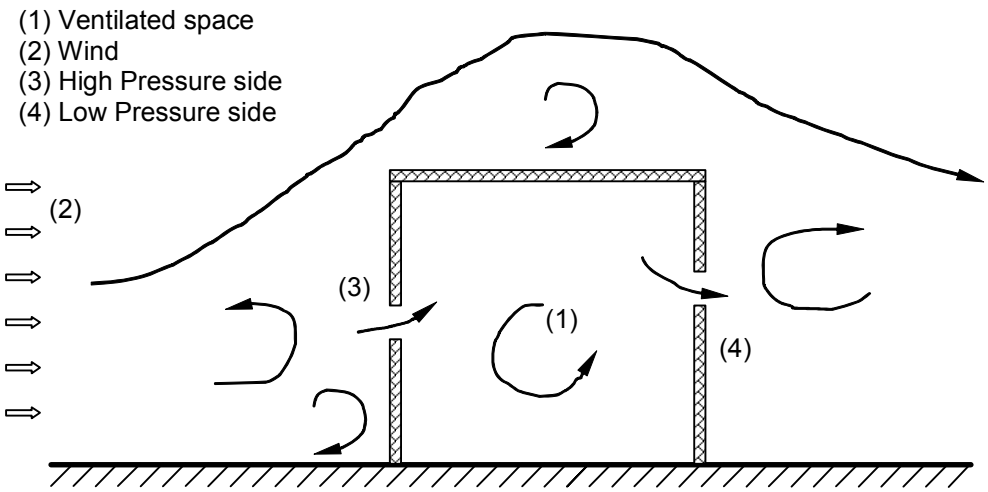

Figure 2.1 Schematic of wind-driven cross ventilation through a single space

2.1.2 Buoyancy-driven displacement ventilation

Density differences in air between the interior and exterior of a ventilated space will lead to different hydrostatic pressure drops over the same vertical distance. When the air inside the space is warmer than outside, which is a common situation, the change of pressure with height inside the space will be smaller than that outside. Therefore the absolute pressure inside the space is larger than the absolute pressure outside above some height. This pressure difference (known as the stack effect) will drive a flow out of the space at high level (Figure 2.2). The converse occurs at low level.

Generally, the pressure differences across the openings (e.g. P_a-P_b and P_c-P_d) will draw cool, exterior ambient air in at low level ventilation openings and exhaust warm, interior air at high level ventilation openings. Without the presence of wind effects, the flow is steady, and a natural displacement ventilation flow will be established. However, this buoyancy driving force induced by the hydrostatic pressure difference is very small (a few Pascals for both commercial and domestic buildings) and difficult to control (BSI 1991). An atrium or chimney is often used to enhance the stack effect and create sufficient ventilation. From Figure 2.2, if the vertical distance of lines da and cb is increased under the same gradient, the pressure magnitudeof (P_a-P_b) will be increased.

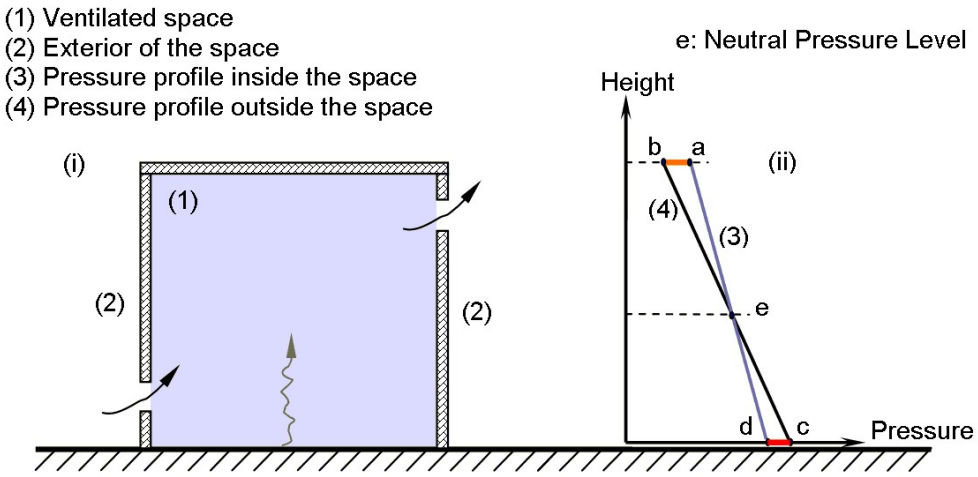

Figure 2.2 (i) Schematic of buoyancy-driven natural ventilation assisted by wind and (ii) the pressure profiles inside and outside the space.

2.1.3 Ventilation induced by buoyancy combined with wind

When both thermal buoyancy and wind are present the ventilation flow depends on the wind direction and the relative strength of the two natural forces. Buoyancy assisted by wind happens when the low level openings are facing windward and the high level openings are located in the lee. The dynamic pressure difference induced by wind will assist buoyancy to drive a flow. If the wind pressure difference is smaller than (or similar to) the static pressure difference, the flow will be similar to that with purely buoyancy-driven displacement ventilation. In contrast a strong wind will lead to a flow similar to purely wind-driven cross ventilation. When the dynamic pressure difference induced by the wind acts against thermal buoyancy the flow patterns can be either a displacement or a mixing form. Figure 2.3(ii) shows a case when wind is assisting buoyancy. The two pressure contributions are working together to provide a ventilation flow for the space, e.g. the pressure difference at high level openings $P_{a'}$-P_b is the combination of the wind induced pressure difference $P_{a'}$-P_a and the buoyancy induced pressure difference P_a-P_b.

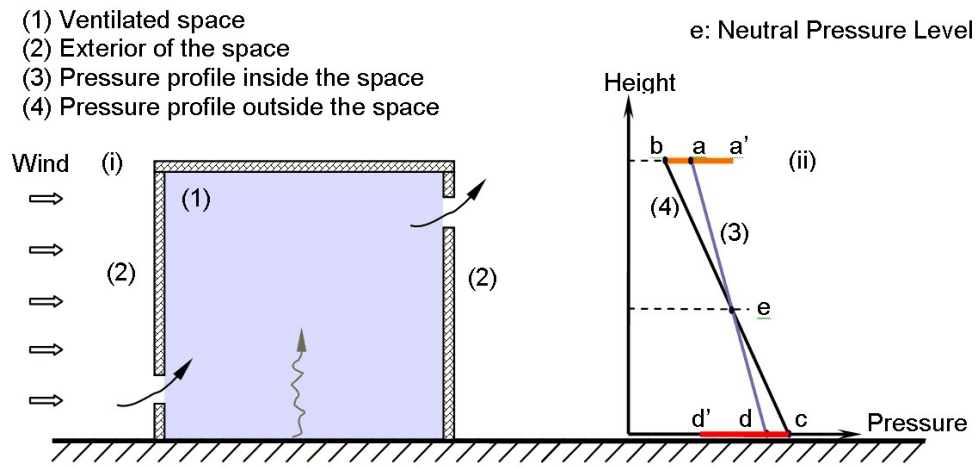

Figure 2.3 (i) Schematic of buoyancy-driven displacement ventilation through a single space and (ii) the pressure profiles inside and outside the space

2.1.4 Examples of naturally ventilated buildings

Examples of naturally ventilated buildings were introduced into the CIBSE Applications Manual (CIBSE AM10,1997). Among these examples, the Queens Building, the engineering school of De Montfort University, Leicester, was said to be “one of the most important projects of the 1990s” (CIBSE BSJ 1993).

The natural ventilation strategy used for the Queens Building is thermal stack-induced cross-ventilation. Figure 2.4 gives an illustration of this ventilation strategy.

Chimneys used in Figure 2.4 are to generate a pressure difference along vertical distance between inside and outside. Following the analysis of section 2.1.2, the air temperature inside chimneys is required to be warmer than ambient in order to provide a stack effect and drive an upward displacement flow. Chimneys might have large surface areas exposed to ambient air, so insulation is important to maintain the temperature difference between inside and outside.

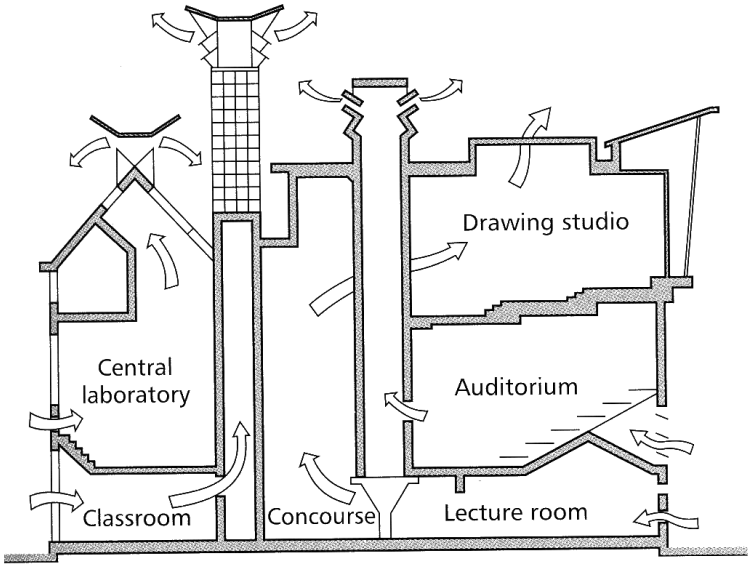

Figure 2.4 Chimney ventilation at De Montfort University (after CIBSE AM10 1997, arrows show the intended airflow directions)

Different strategies of natural ventilation are used in the Queens Building, e.g. shallow plan electrical laboratories are cross ventilated while the central section of the building is ventilated in a displacement mode by the stack effect provided by the chimneys. The two auditoria are (one shown on Figure2.4) also ventilated by the displacement mode. In the auditorium spaces, fresh ambient air enters via a plenum below raked seats (pre-warmed if necessary). The internal heat gains generated by occupants, electrical equipment, and lighting form a layer of warm air below the ceiling. This warm air fills up the chimneys and a temperature difference is built up between inside and outside of these chimneys. The warm air in these chimneys will then drive a flow through the building and natural ventilation then takes place.

Figure 2.5 shows the exterior view of the building structure and figure 2.6 shows some details of where air enters the building and how it is driven out.

Figure 2.5 The exterior view of the Queens Building, De Montfort University, Leicester (After CIBSE AM10, 1997)

(a)

(b)

Figure 2.6 (a) South elevation showing air inlets to an auditorium, (b) exhaust stacks from the central concourse (After CIBSE AM10, 1997)

Another example shown here is the Canning Crescent Centre (Figure 2.7). This is a stack and wind driven naturally ventilated building built in 1994, located on a busy high street in Wood Green, an urban area of London (BRE).

The natural ventilation system was developed using a series of separated vertical stacks which allow air to be drawn through the building (Figure 2.7a). Air change is driven by wind and/or buoyancy forces, according to prevailing weather conditions.

(a)

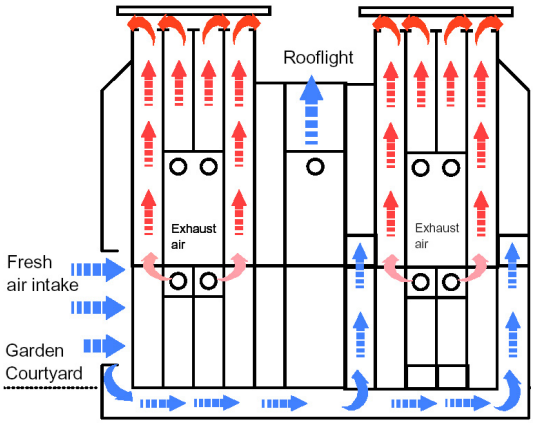

(b)

Figure 2.7 (a) Ventilation strategy for the Canning Crescent Centre and (b) View of the Canning Crescent Building from the High Street.

Each room is serviced, via a high level extract grille, by its own exhaust stack. Adjustable air flow dampers in the stacks control the air change rate in each room. In general, the dampers are set centrally to be fully open in the summer to aid cooling, and almost closed in the winter to provide reduced flow rates sufficient to maintain optimum indoor air quality.

2.2 Theoretical modelling of natural ventilation

The three modelling techniques discussed in this research are simple analytical modelling, small scale laboratory experiments and numerical modelling using CFD. In this section, analytical modelling is discussed. Detailed descriptions for small scale laboratory experiments and numerical methods will be presented in chapters 3 & 4.

2.2.1 Theories for turbulent buoyant plumes

As mentioned in section 2.1, natural ventilation can be induced by thermal stack effects. These thermal effects can be generated by buoyant plumes. Therefore, the structures and the properties of turbulent buoyant plumes have been the subject of much research in the field of natural ventilation. For example, the structure of circular buoyant turbulent plumes in still and un-stratified environments is a classical problem that has been widely studied in

order to gain a better understanding of buoyancy/turbulent interactions (Morton et al (1956), Morton (1959), Baines & Turner (1969) and Turner (1986)). Among these researches, Morton et al (1956) derived the basic governing equations for a maintained plume in a uniform ambient fluid based on the following three assumptions:

- that the profiles of vertical velocity and buoyancy are similar at all heights,
- that the rate of entrainment of fluid at any height of the plume is proportional to a characteristic velocity in the plume at that height, and
- that the fluids are incompressible and do not change volume on mixing and that local variations in density throughout the motion are small compared with some reference density.

An important outcome of Morton et al's work is the equation set relating the volume flux (Q) and the reduced gravity (G') along the vertical distance y in a plume, see below.

Figure 2.8 shows a turbulent buoyant plume within a large, stationary, unstratified fluid, generated by a point heat source without initial momentum and mass flow.

The rising thermal plume is surrounded by cooler ambient air and heat is transferred from the surface of the source to the adjacent air and a density difference is produced. This density difference is the origin of buoyancy of the heat source, interpreted as a reduced gravity G' acting upwards. Entrainment occurs at the shear layer between the warm air in the plume and the surrounding air (denoted by the horizontal arrows in figure 2.8), which causes

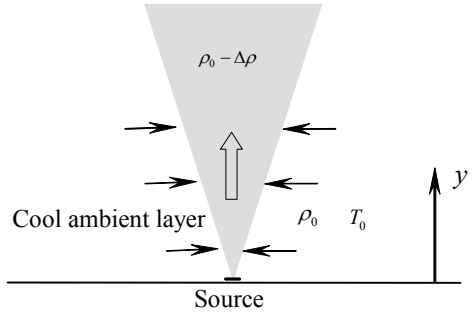

Figure 2.8 Schematic drawing of a free buoyant plume

a reduction in the temperature difference with the increasing height of the plume and an increasing plue width.

The buoyancy flux, B, indicating the strength of a buoyancy source, is defined as:

$$B = G'Q \text{ = constant} \qquad \text{Eq (2.1)}$$

where $$Q\ (y, B) = C(By^5)^{1/3} \qquad \text{Eq (2.2)}$$

and $$G'(y, B) = (B^2 y^{-5})^{1/3} / C \qquad \text{Eq (2.3)}$$

where: y denotes a vertical distance from the point source (m),

C is a constant dependent upon the 'top-hat' entrainment coefficient α.

The expression for C in terms of 'top-hat' entrainment coefficient α is given by

$$C = 1.2\alpha(0.9\alpha)^{1/3}\pi^{2/3} \qquad \text{Eq (2.4)}$$

The experimental measurements of Morton et al (1956) were based on the 'Gaussian profile entrainment coefficient α_G' multiplied by $\sqrt{2}$, namely:

$$\alpha = \sqrt{2}\ \alpha_G \qquad \text{Eq (2.5)}$$

Different values of α_G were measured by a number of researchers. For example, α_G = 0.083 was used by Turner (1986) while α_G = 0.093 and 0.074 were suggested by Morton et al (1956) and Baines (1983) respectively.

Baines and Turner (1969) studied the effect of continuous convection from small sources of buoyancy on the properties of the surrounding environment when the region of interest is confined. This was called a 'filling boxes model'. The basic assumption was that the entrainment into the plume was at a rate proportional to the local mean upward velocity, which is similar to one of the assumptions made by Morton et al (1956). In the study, heat sources were placed in a finite and closed region, which means the convection of the plume

was confined rather than free convection; the whole surface layer was considered instead of treating the atmosphere close to the ground under the assumption of nearly steady heat flux and constant with height; and a time-dependent solution which takes into account the interaction between the buoyant elements and the environment was used. Another feature of convection in confined regions is that the environment away from boundaries is stable (Figure 2.9).

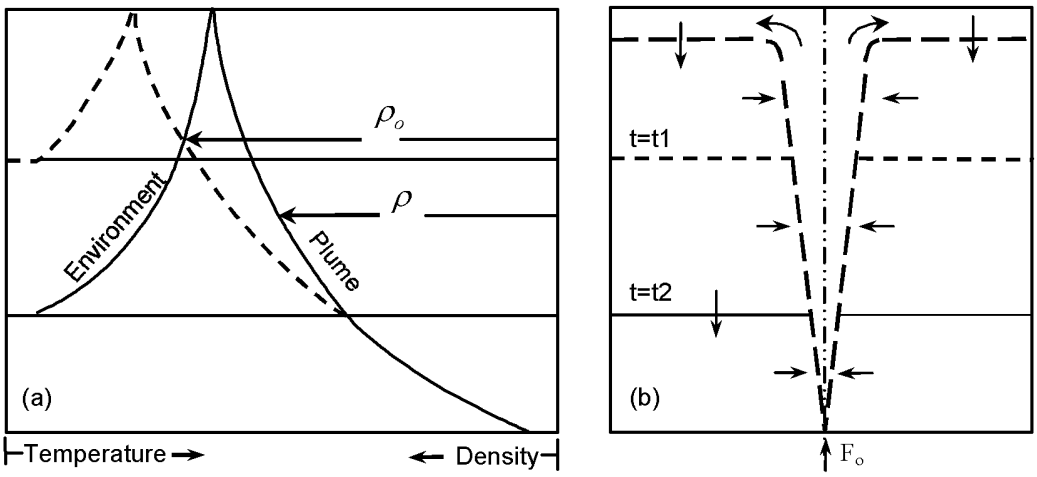

Figure 2.9 (a) Sketch of development of stratified environment due to a heat source, showing the motions in the plume and environment, and (b) the corresponding vertical temperature profiles in the plume at times t = t1 and t = t2. (After Baines & Turner (1969))

The dimensionless clean zone height, ξ, defined by Baines and Turner (1969), is an important parameter in building ventilation because this height indicates the effective ventilated level (Eq (2.6)).

$$\xi = h / H \qquad \text{Eq (2.6)}$$

where h and H are fresh fluid depth (m) and the height (m) of the confined region.

2.2.2 Wind engineering

It is important to have a deep understanding of the considered atmosphere region when conducting wind engineering. The region of interest is normally defined as the atmospheric boundary layer: the region of the earth's

atmosphere where the effects of the surface (friction, heating and cooling) are felt directly on a time scale of less than a day, and in which significant fluxes of momentum, heat or enthalpy are carried by turbulent motions on a scale of the order of the depth of the boundary layer or less (Garrat (1992)). Wind speeds and characteristics need to be quantified in terms of mean values and turbulent fluctuations within the atmospheric boundary layer.

In this study, the internal airflow is of interest rather than the wind structures outside the building. However, a basic knowledge about the pressure distribution around a building structure will assist in understanding the airflow inside. The pressure differences between the ventilation openings are induced by the pressure distribution around the building structure, and are controlled by the pattern of airflow around the structure. The pressure coefficients in terms of the pressure differences are given by:

$$C_p = \Delta P / (0.5 \rho U_{ref}^2) \qquad \text{Eq (2.7)}$$

where: ΔP the pressure difference on the building surface relative to the pressure at some reference point;

ρ the density of air; and

U_{ref} the reference mean wind velocity (normally taken at the building roof height).

'Bluff bodies' are often used for representing building structures. A body is defined as aerodynamically 'bluff' when the flow streamlines do not follow the surface of the body, but detach from it leaving regions of separated flow and a wide trailing wake (Figure 2.10 (a) and (b)).

As shown in Figure 2.10, the 'stagnation point (1)', where air is brought to rest, of the windward face is at about two-thirds of the total height of the cubic building. Above the stagnation point, air flows up and over the roof of the building while below the point, air is forced to move down the face until reaching the ground. Air moving towards the ground has greater kinetic energy than the on coming wind at the same height. This greater energy allows the flow to move against the wind after it reaches the ground, but will

finally be brought to rest at some distance away from the windward face. A vortex close to the ground in front of the windward face is then built up (See Figure 2.10a).

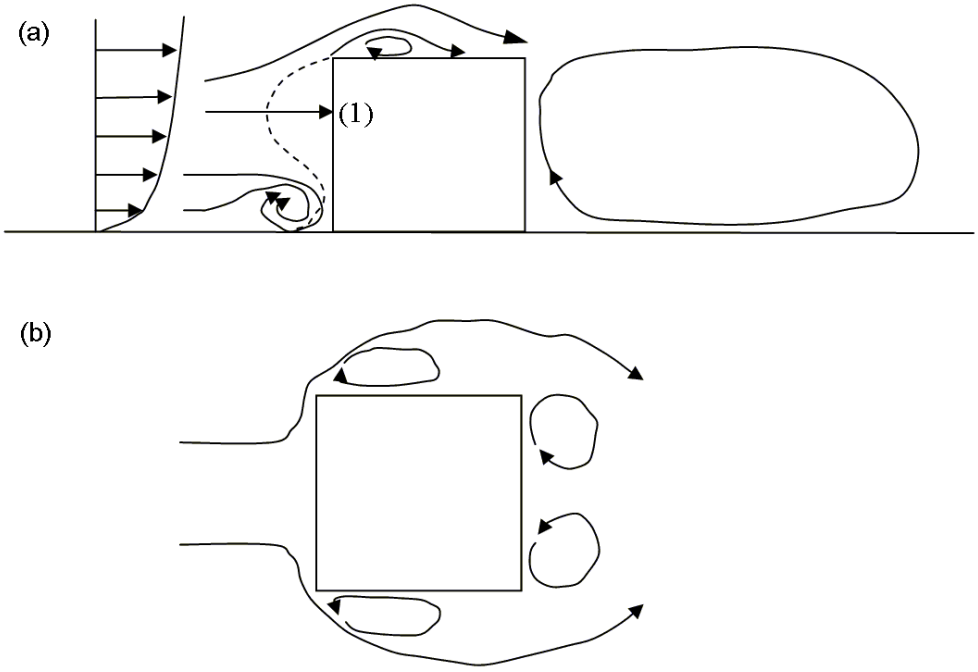

Figure 2.10 Airflow around a cubic structure in sheared flow. (a) Flow field at centre section, side elevation; (b) Plan elevation. (After Cook (1992)).

In this sheared boundary layer, the maximum dynamic pressure will be located at the stagnation point and the corresponding pressure coefficient there would be in the range of 0.7 to 0.9 (Cook (1992)) and the pressure distribution across the roof shows high negative values at the upwind edge which become less negative towards the downwind edge.

Deflected air across the windward face separates along the line of the corner with each of the side faces and creates two vortices. Flow in this region is significantly faster than the wind at some distance away from the block at the same height. Pressure at the upwind edge of the cube is highly negative due to the separation of the flow and becomes less negative at the leeward edge. In the lee of the cube, a large separation of flow occurs and re-circulating wakes form downstream (Figure 2.10b). A large re-circulation zone driven by the shear layer over the roof can be seen in Figure 2.10a, this vortex tends to draw the corner vortices vertically upwards. The wakes and the vortices in the

lee of bluff bodies make the downstream flow complex and unsteady and this effect can exist over a distance of nine times of the cube height before the original wind profile is completely re-constructed (Oke (1987)).

2.2.3 Buoyancy-driven flows in a single space

Simple mathematical methods for representing natural ventilation in buildings are useful for architects and engineers because the methods offer an easy means of understanding the characteristics of airflow in buildings (e.g. Linden at el (1990), Cooper and Linden (1996), Li (2000) and Chen and Li (2002)). Among these, Linden at el (1990) provided a typical analytical model for buoyancy-driven flow in a single space with high and low level openings.

Linden at el (1990) considered a turbulent, entraining plume rising from a source of buoyancy in a space with one opening in the floor and one in the ceiling. The layer of buoyant air near the ceiling (see Figure 2.11) drives a flow through the openings due to a pressure difference between internal and external air at the upper openings. Assuming ρ_o as the density of ambient air, $\Delta\rho$ as the density difference between ambient air and air in the upper layer of the space, then the reduced gravity of the upper layer, g', is given by $g' = g\Delta\rho / \rho_o$. The volume flow driven through the ventilation openings will depend on this reduced gravity g' within the space.

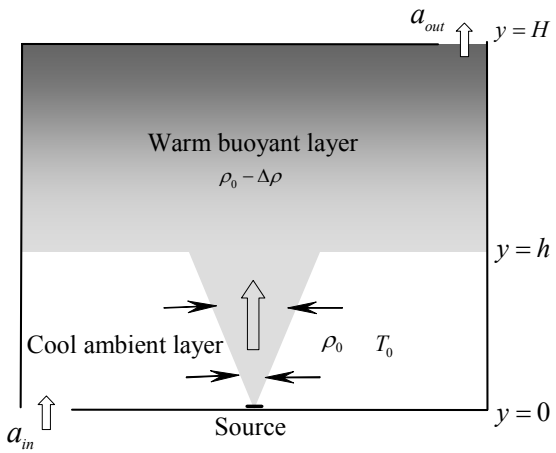

Figure 2.11 Natural ventilation in a single space driven by a point heat source.

In Figure 2.11, the temperature of interior air is higher than that of the exterior, two openings with areas of a_{out} in the ceiling and a_{in} in the floor. Linden et al (1990) assumed that the incoming air does not mix with the fluid in the space but forms a layer of increasing depth, h. The horizontal area of the space should be much larger than the areas of openings so that the velocity of the interface between the dense, ambient air and the warm, buoyant air is negligible. $\Delta\rho$, the difference between reference density ρ_o and the internal density, is small enough to apply Bernoulli's theorem, which states that the law of conservation of energy in the sum of the kinetic energy, energy due to pressure height and potential energy (i.e. the total energy) is constant. Based on these assumptions, the volume flow rate F through high and low level openings is given by:

$$F = A^*(g'(H-h))^{1/2} \qquad \text{Eq (2.8)}$$

where: H, h the total height, interface height of the space (m)

A^* the effective opening area which is the combination of the high and low level openings, defined by

$$A^* = \frac{C_D a_{in} a_{out}}{\left(0.5\left((C_D/C_e)a_{out}{}^2 + a_{in}{}^2\right)\right)^{1/2}} \qquad \text{Eq (2.9)}$$

where: C_D and C_e are the discharge and expansion coefficient respectively, representing the energy losses at corresponding openings.

By equating the volume flow rate from the plume theory (Eq (2.2)) at the interface height ($y = h$, outside the plume the net transportation of air across the interface is assumed to be zero) and the flow rate through the space (Eq (2.8)), the dimensionless interface height $\xi = h/H$ (was defined as a fresh air zone height by Baines and Turner (1969)) is given by

$$\frac{A^*}{H^2} = C^{3/2}\left(\frac{\xi^5}{1-\xi}\right)^{\frac{1}{2}}. \qquad \text{Eq (2.10)}$$

This shows that the interface height is dependent on the dimensionless effective opening area A^*/H^2 and the entrainment constant C (defined by Eq (2.4)) but is independent on the strength (buoyancy flux B) of the localised point source because it does not appear in equation (2.10). The interface height can be source dependent when multiple sources are used. Cooper and Linden (1996) examined steady-state displacement ventilation produced by two non-interacting plumes of unequal strengths B_1 and B_2. A three-layer stratification was produced and the heights of the interfaces were found to depend on A^*/H^2, the buoyancy flux ratio B_1/B_2 and entrainment into the plume.

The effect of heat diffusion by radiation in air was not taken into account by Linden at el (1990). Therefore the accuracy of equation 2.10 has been challenged by other researchers. Li (2000) used surface thermal radiation effects and deduced a more general mathematical model in which a temperature coefficient, λ', was introduced to represent the effects of both convective and radiative heat transfer coefficients at the ceiling and floor. The model equation then becomes:

$$\frac{A^*}{H^2} = C^{3/2}\left(\frac{\xi^5}{1-(1-\lambda')\xi}\right)^{1/2} \qquad \text{Eq (2.11)}$$

This model shows that without the use of the temperature coefficient λ' ($0<\lambda'<1$) the dimensionless interface height will be slightly under-predicted by model equation 2.10.

A study on a single space with three ventilation openings was carried out by Chen & Li (2002). Two openings were arranged in the same manner as that in the experiments of Linden et al (1990) while the third opening was located in the side of the space. This opening experiences different flow directions (either in or out of the space) depending on its vertical locations. If it is located

higher than the neutral pressure level, there will be an outflow through the opening and vice versa.

The interface height can also be altered due to the vertical location of the heat source above floor. Park & Holland (2001) pointed at that the temperature profile as well as the interface level would be significantly affected by the vertical position of the heat source.

All these studies considered the behaviour of one (or more) buoyant plume(s) within a confined space with openings connected to exterior. They were solely thermal induced natural ventilation in displacement mode. The interface height of this type of stratified flow is of key interest for natural ventilation strategies. One of the general design guidelines for naturally ventilated buildings is to keep this height above the occupants.

2.2.4 Buoyancy combined with wind-driven airflows

Most of the time the airflows in naturally ventilated buildings are driven by combined forces of wind and buoyancy. Hunt & Linden (1999) pointed out that the wind normally provides the dominant driving force for natural ventilation while the thermal effects still play a key role for the air movements and the flow patterns, especially for forming the stratification. Once the building structures are fixed (for example, the opening arrangements of a single space), the wind, as a driving force, can either assist buoyancy or oppose it depending on the wind directions. The details of the analytical models of Hunt & Linden (2001, 2005) for these two situations are summarised in the following sections.

2.2.4.1 Buoyancy assisted by wind

Hunt & Linden (2001) extended the study of Linden et al (1990) by considering the wind effect on buoyancy within a space with high (a_{out}) and low (a_{in}) level openings in the side of the space (Figure 2.12).

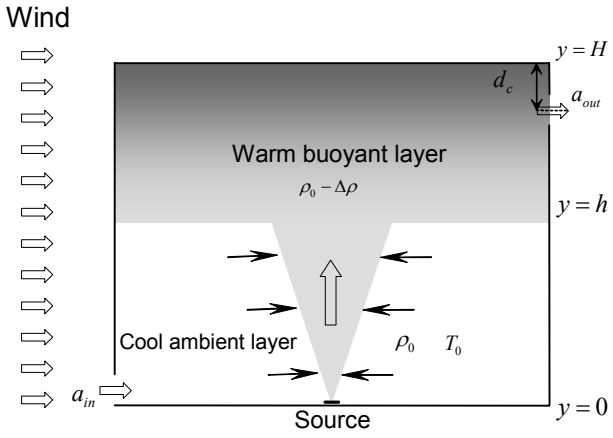

Figure 2.12 Sketch of natural ventilation in a single space driven by a point heat source assisted by wind

The wind considered in this study is uniform without any effect due to the roughness of ground. As mentioned in section 2.2.2, when wind flows around a cube (a single space building here) a dynamic pressure difference will be produced between the windward and leeward sides. This pressure drop Δ is contributing part of the ventilation flow (Q_W) through the space. Another contribution to the volume flow rate (Q_B) is the stack effect created by the buoyancy source. The total ventilation flow rate Q is given by (Hunt & Linden 2001):

$$Q = \left(Q_W^2 + Q_B^2\right)^{1/2} \qquad \text{Eq (2.12)}$$

where,

$$Q_W = A^*\left(\Delta/\rho\right)^{1/2} \qquad \text{Eq (2.13)}$$

$$Q_B = A^*\left(g'\left(H - h - d_c\right)\right)^{1/2}. \qquad \text{Eq (2.14)}$$

Bernoulli's theorem was used to deduce the expressions for Q_W and Q_B, in which $(H - h - d_c)$ is the useful depth of the buoyant layer, d_c denotes the vertical distance between the midpoint of the upper opening and the top of the space, and A^* is the effective area, rearranging Eq (2.9) to give:

$$A^* = a_{in}a_{out}\sqrt{(2C_e C_D^2)/(C_e a_{in}^2 + C_D^2 a_{out}^2)} \qquad \text{Eq (2.15)}$$

The analytical model representing buoyancy assisted by wind in the space is given by equating Eq (2.12) and Eq (2.2) at the height of the interface h:

$$\frac{A^*}{H^2} = \frac{C^{3/2}\xi^{5/3}}{\left((1-\xi-d_c/H)/\xi^{5/3}+CF_r^2\right)^{1/2}}. \qquad \text{Eq (2.16)}$$

The dimensionless Froude number Fr, compares the wind force with the buoyancy force and is defined by:

$$Fr = \sqrt{(\Delta/\rho)/(B/H)^{2/3}}. \qquad \text{Eq (2.17)}$$

The wind (with speed U_w m/s) pressures at windward and leeward openings are given by P_W and P_L:

$$P_W = \frac{1}{2}C_{pw}\rho U_w^2 \text{ and } P_L = \frac{1}{2}C_{pl}\rho U_w^2 \qquad \text{Eq (2.18)}$$

where C_{pw} and C_{pl} denote the pressure coefficients at the windward and leeward openings. The pressure drop Δ induced by wind is therefore defined by the difference of P_W and P_L

$$\Delta = \rho U_w^2 (C_{pw} - C_{pl})/2. \qquad \text{Eq (2.19)}$$

For a normally incident wind and an exposed, low-rise building, the pressure coefficients at the windward and leeward faces were suggested to take values of C_{pw} =0.7 and C_{pl} = -0.2 respectively (Orme et al (1994)).

In Eq (2.17), buoyancy flux B (m^4s^{-3}) is related to the heat source E by

$$B = g\beta E/\rho c_p \qquad \text{Eq (2.20)}$$

where β the thermal expansion coefficient, K^{-1},

c_p specific heat capacity at constant pressure, $m^2s^{-2}K^{-1}$.

In Hunt & Linden (2001), the expansion and discharge coefficients are treated as constants with C_e =0.5 and C_D =0.6; the entrainment constant C is

calculated based on the Gaussian profile entrainment coefficient α_G =0.083 using Eq (2.4) and Eq (2.5). Dimensionless quantities of

$$Q/(B^{1/3}H^{5/3}) = C\xi^{5/3} \quad \text{and} \quad g'/G'_H = \xi^{-5/3} \qquad \text{Eq (2.21)}$$

for variable dynamic pressure drops, and

$$Q/(H^2(\Delta/\rho)^{1/2}) = CFr^{-1}\xi^{5/3} \quad \text{and} \quad g'/(\Delta/\rho H) = C^{-1}Fr^{-2}\xi^{-5/3} \qquad \text{Eq (2.22)}$$

for variable source strengths were introduced in Hunt & Linden (2001), in which g' is the reduced gravity at the interface level in the plume (also representing the reduced gravity above the interface outside the plume) and G'_H is the reduced gravity in the plume at the ceiling level. They may be defined by Eq (2.23) and Eq (2.24) respectively using the plume theory (Eq (2.3)) of Morton et al (1956).

$$g' = (B^2h^{-5})^{1/3}/C \qquad \text{Eq (2.23)}$$

$$G'_H = (B^2H^{-5})^{1/3}/C \qquad \text{Eq (2.24)}$$

Equations (2.12) to (2.24) provide a full description of this analytical model for buoyancy-driven flows assisted by wind forces. Eq (2.16) shows that the dimensionless interface height $\xi(=h/H)$ is no longer independent of the buoyancy flux B as was the case in Linden et al (1990). It depends on the dimensionless effective opening area A^*/H^2, entrainment constant and the relative strength of wind forces (Δ) and buoyancy forces (B). Theoretical predictions of Eq (2.16) and scalings (Eq (21, 22) are shown as followings.

As shown in Figure 2.13a, the dependence of h on A^* at low Fr is relatively weak since a significant depth of warm upper layer is required to drive a flow. As wind increases (Froude number increases) there arises a strong dependence between h and A^* even when the ventilation openings are large. On windy days, natural ventilation rate is governed primarily by wind forces rather than buoyancy although the internal airflow patterns are still strongly affected by buoyancy.

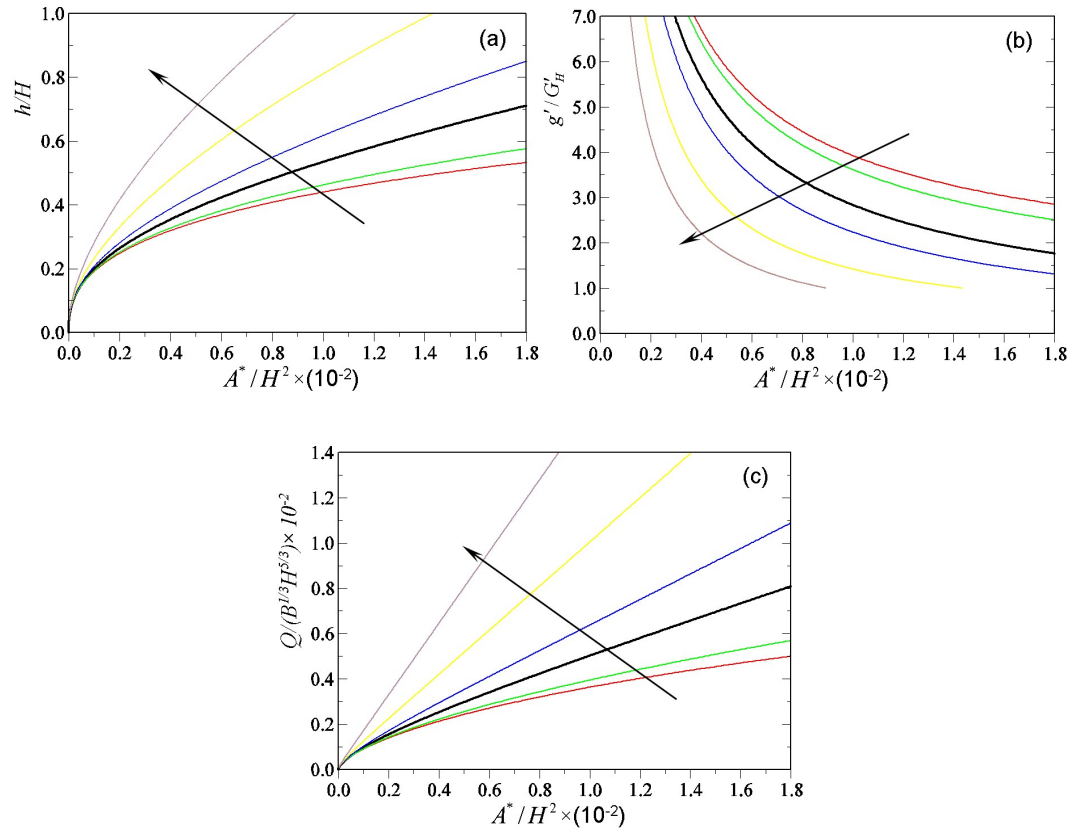

Figure 2.13 Theoretical predictions of buoyancy-driven flow assisted by wind. A^*/H^2 vs (a) h/H ,(b) g'/G'_H and (c) $Q/(B^{1/3}H^{5/3})$ for Fr =0, 2, 4.2, 6, 10, 16. The arrow indicates the direction of increasing Fr .

With a fixed Froude number, Figure 2.13 shows that increasing the ventilation openings will increase the interface height (a), decrease the reduced gravity (b) and increase the ventilation rate (c).

Similar trends are shown in the theoretical predictions of Figure 2.14. With a fixed ventilation opening size, increasing Froude number (equivalent to increasing the wind effects), figure 2.14a shows an increased interface height, figure 2.14b shows a reduced temperature change across the interface, and figure 2.14c shows a increased ventilation rate.

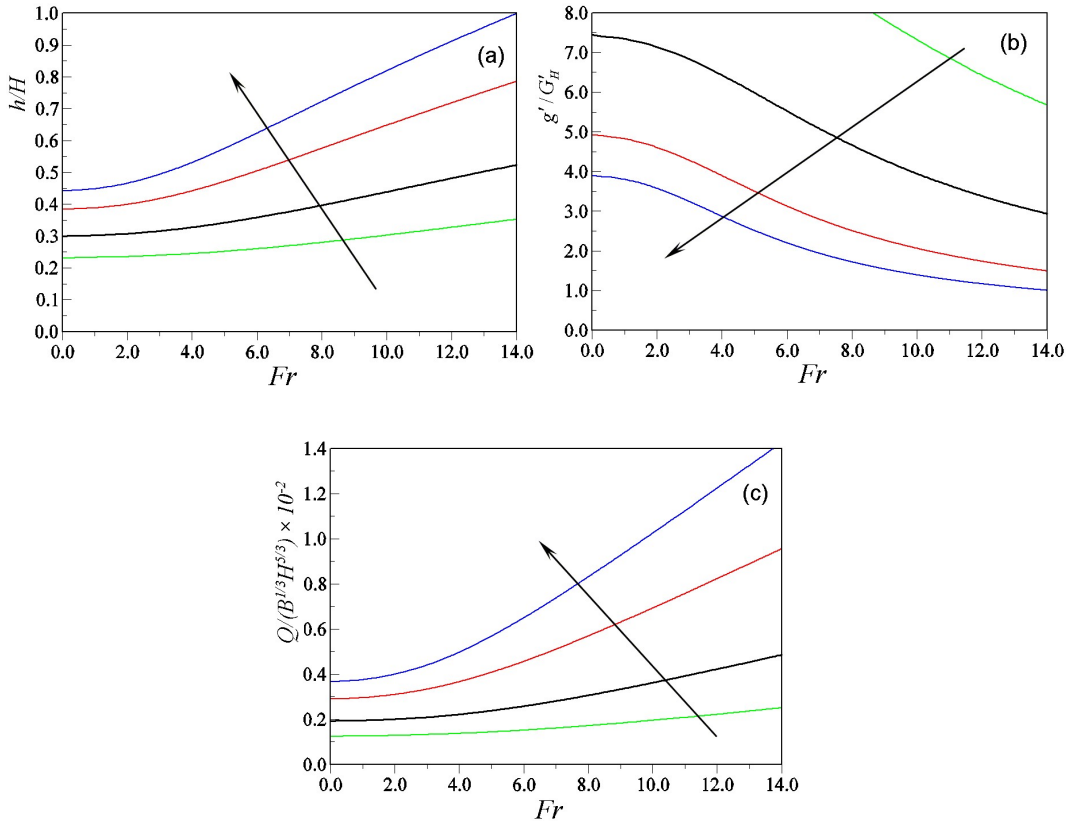

Figure 2.14 Theoretical predictions of buoyancy-driven flow assisted by wind. Fr vs (a) h/H ,(b) g'/G'_H and (c) $Q/(B^{1/3}H^{5/3})$ for A^*/H^2 = (1.7, 3.4, 6.8, 10.2) × 10^{-2}. The arrow indicates the direction of increasing A^*/H^2.

Figure 2.15 shows the effect of varying the buoyancy flux B on g' of the upper layer and volume flux Q. On increasing B, the ratio between the wind-driven and buoyancy-driven velocities decreases (Fr decreases) and the height of the interface decreases and approaches the value established in the absence of wind (Figure 2.14a). The reduced gravity G' in the plume at the level of the original interface increases and consequently, as the reduced gravity of the upper layer equals that in the plume at the level of the interface in the steady state, the reduced gravity of the upper layer increases (Figure 2.15a).

As the interface falls and the depth of the buoyant upper layer increases, the stack effect increases consequently, the total volume flow rate through the space increases (Figure 2.15b). However, this is only a relatively weak effect because the volume flow rate has weak dependence on buoyancy ($Q \sim B^{1/3}$; refer to Eq (2.2)).

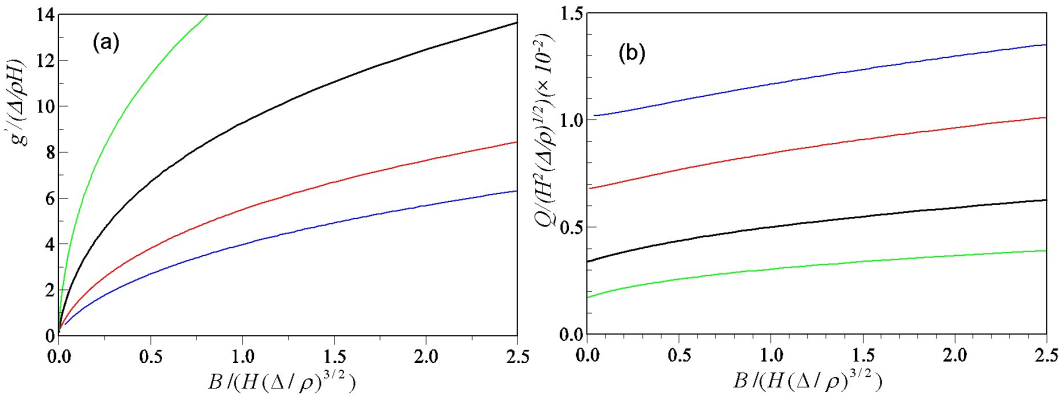

Figure 2.15 Theoretical predictions of buoyancy-driven flow assisted by wind. $B/(H(\Delta/\rho)^{3/2})$ vs (a) $g'/(\Delta/\rho H)$ and (b) $Q/(H^2(\Delta/\rho)^{1/2})$ for A^*/H^2=(1.7, 3.4, 6.8, 10.2) × 10^{-2}. The arrow indicates the direction of increasing A^*/H^2.

The black lines in Figures 2.13 and 2.14 are used in chapter 5 to make comparisons between different modelling techniques.

2.2.4.2 Buoyancy opposed by wind

Extended from Hunt & Linden (2001), the effect of an opposing wind on the steady stratification produced by a buoyancy heat source on the floor of a ventilated space is further considered by Hunt & Linden (2005). The different wind direction leads to different flow patterns within the space. With an opposing wind, the high level ventilation openings are located on the windward face and low level openings on the leeward. The two natural driving forces are therefore acting against each other (Figure 2.16). The flow through the space is no longer unidirectional like the assisting wind case, but can be either a displacement flow (fresh air enters the space from low level openings on the leeward and flows out through high level openings on the windward) when the opposing wind is small or a mixing flow (fresh air enters the space through high level openings and leaves the space through low level openings after being mixed with warm buoyant air) when the opposing wind force is sufficiently large.

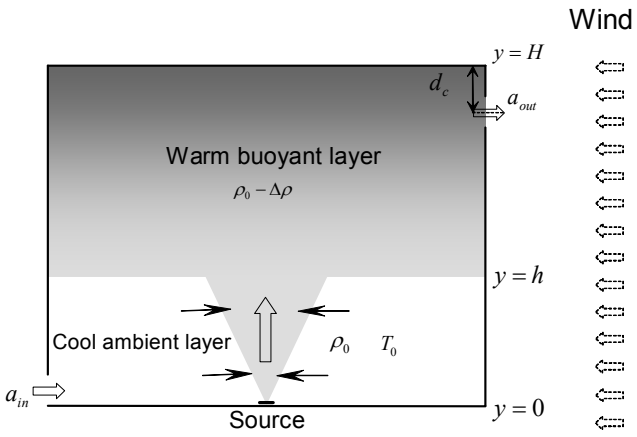

Figure 2.16 Natural ventilation in a single space driven by a point heat source with an opposing wind.

For small opposing wind cases, the displacement mode natural ventilation can still be maintained. The thermal stratification level and the volume flow rate through the space can be determined by a similar approach used in Hunt and Linden (2001). Bernoulli's theory is used to calculate the volume flow rate induced by both buoyancy and wind through the space. In steady state the volume flow rate in the plume at the stratification level (Eq (2.2)) will be the same as the flow rate through the space. By equating these two flow rates, the following expression is derived:

$$\frac{A^*}{H^2} = \frac{C^{3/2}\xi^{5/3}}{\left(\left(1-\xi-d_c/H\right)/\xi^{5/3} - CFr^2\right)^{1/2}} \qquad \text{Eq (2.25)}$$

where the relevant parameters are defined the same as Hunt & Linden (2001) except the expansion coefficient C_e in A^* (Eq (2.15)).

The distance of d_c was ignored from the analytical model in Hunt & Linden (2005). Here d_c was remained in order to match the geometry of the CFD model and the structure of the salt bath experiments. Theoretical predictions using Eq (2.25) are given in figures 2.17, 2.18, 2.19 and 2.20.

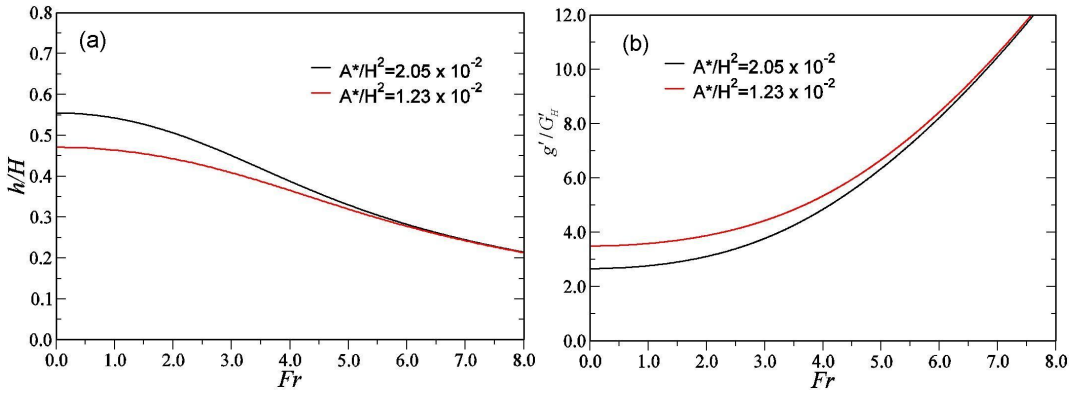

Figure 2.17 Theoretical predictions of buoyancy-driven flow opposed by wind. Fr vs dimensionless (a) interface height h/H and (b) reduced gravity g'/G'_H.

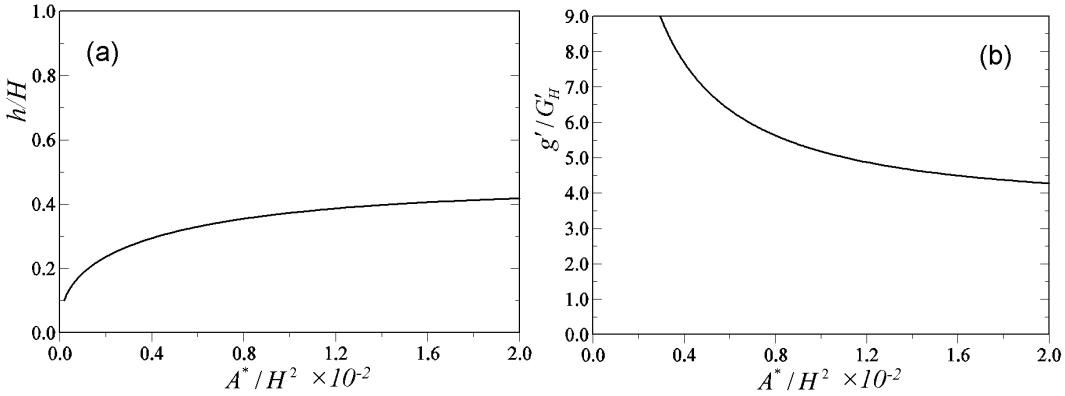

Figure 2.18 Theoretical predictions of buoyancy-driven flow opposed by wind. (a) A^*/H^2 vs h/H and (b) A^*/H^2 vs g'/G'_H at Fr =3.5

Figure 2.17 shows the effect of Fr on the interface height and reduced gravity at different effective opening area A^*/H^2. For a fixed value of A^*/H^2, h/H decreases (Figure 2.17a) and the reduced gravity g' increases (Figure 2.17b as the Froude number increases. The increase of the reduced gravity and the upper layer depth as Froude number increases implies an increase in buoyancy-driven flow but the ventilation flow rate through the space is reduced due to the wind effect. It is also shown in Figure 2.17 that the effect of an increase in Fr on h/H and g'/G'_H is more dramatic as A^*/H^2 increased, which implies that a ventilated space with large openings is more significantly affected by wind than one with smaller openings.

h/H increases (Figure 2.18a) and the reduced gravity g' decreases (Figure 2.18b) as the dimensionless effective opening area A^*/H^2 increases. This is the cause of an increase in the ventilation flow rate through the space. The

ventilation flow through the space can still be enhanced when the ventilation opening sizes are enlarged when the wind effect is stable (fixed Fr).

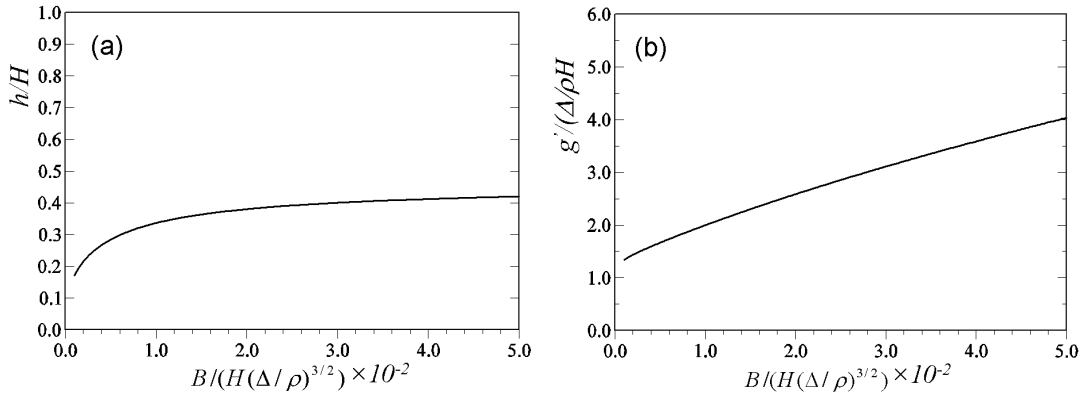

Figure 2.19 Theoretical predictions of buoyancy-driven flow opposed by wind. (a) $B/(H(\Delta/\rho)^{3/2})$ vs dimensionless interface height h/H and (b) $B/(H(\Delta/\rho)^{3/2})$ vs dimensionless reduced gravity $g'/(\Delta/\rho H)$ with a fixed pressure drop Δ.

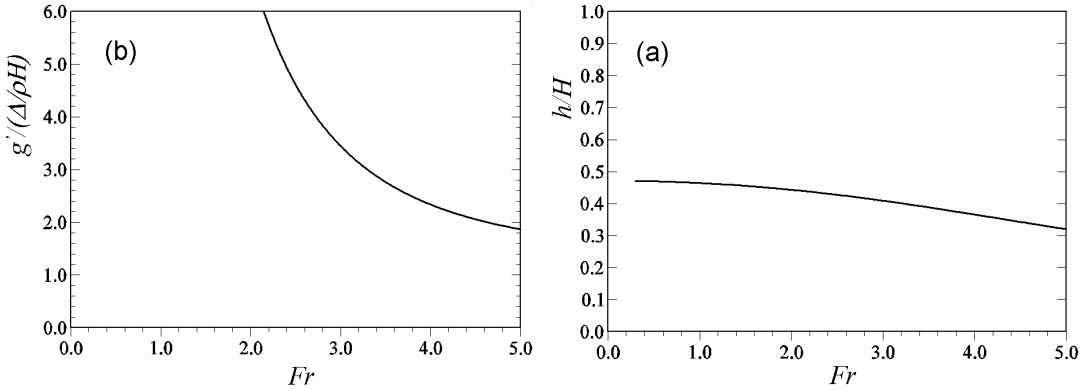

Figure 2.20 Theoretical predictions of buoyancy-driven flow opposed by wind. The effect of varying Fr due to the changes of buoyancy flux B on (a) h/H and (b) $g'/(\Delta/\rho H)$ with a fixed pressure drop Δ.

The heat into the space is increased by increasing the buoyancy flux B (for a fixed wind effect, this means the Froude number is decreased), then the interface height is increased and so is the volume flow rate through the space (Figure 2.19(a)). However, the dimensionless reduced gravity $g'/(\Delta/\rho H)$ is increased as a result of increasing buoyancy flux B (Figure 2.19(b)) rather than decreased like g'/G'_H (Figure 2.18(b)). When buoyancy flux B is increased a direct result will be an increase of the temperature difference across the interface, which leads to an increase of the reduced gravity g'. For

this case, the pressure drop Δ is fixed, therefore the combination of $(\Delta / \rho H)$ is fixed, therefore $g' /(\Delta / \rho H)$ will be increased. G'_H is the reduced gravity in the plume at the ceiling height H (Eq (2.3)). When increasing buoyancy flux B, the increase of G'_H is more significant than the increase of the temperature difference across the interface, hence g' / G'_H will be decreased as shown in Figure 2.18.

Figure 2.20 is another illustration for varying buoyancy flux B with a fixed pressure drop across the windward and leeward. As shown in Eq (2.17), increasing B will lead to a decrease of Fr, an increased dimensionless interface height h / H (Figure 2.20a) and a increased dimensionless reduced gravity $g' /(\Delta / \rho H)$ (Figure 2.20b).

2.2.5 Analytical models for atrium-assisted natural ventilation (single space)

By introducing an atrium, the stack pressure due to the temperature difference between interior and exterior can be enhanced by increasing the depth of the interior warm layer in the absence of wind forces. This can directly lead to an enhancement of ventilation. Some building designs use tall atria connected to ventilated spaces to gain a sufficient buoyancy driving force. Holford & Hunt (2003) extended the work of Linden et al (1990) by adding an atrium to a ventilated space where a point heat source was located on the floor. Theoretical models were developed for ventilated and unventilated atria (Figure 2.21a and b).

Figure 2.21a shows a single storey (the ventilated space space) connected to an unventilated atrium. This is a one-way system since air can only flow through the storey then to the atrium. For the ventilated atrium case (Figure 2.21b), air can also flow from the bottom inlet in the atrium to its top outlet. It is also geometrically possible for air to flow from the space and out from the bottom inlet of the atrium. However, this is dynamically impossible when the building is heated and surrounded by a stationary ambient environment. Here the heat exchange through the building fabric is assumed to be negligible compared with the heat fluxes generated by the ventilation flow.

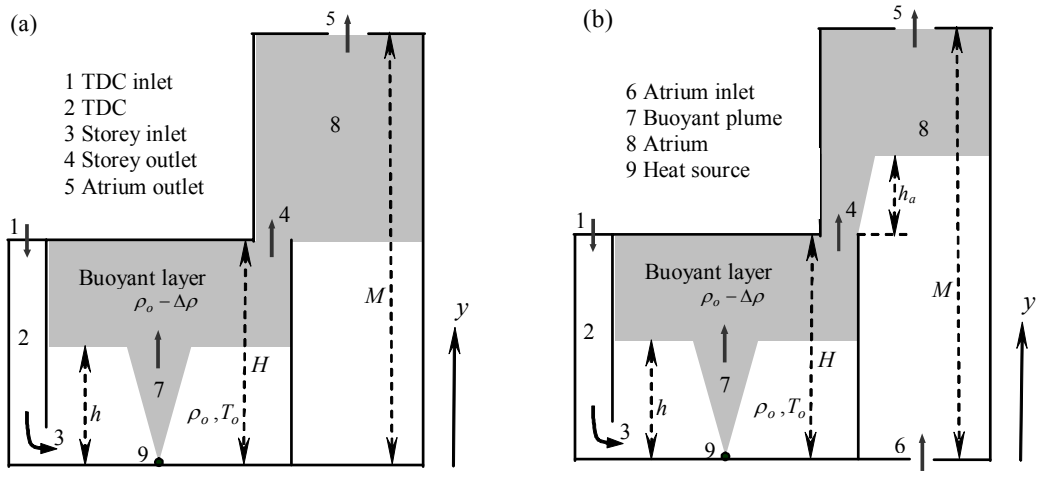

Figure 2.21 Ventilation of a single space connected to an atrium and a top-down chimney (TDC), (a) an unventilated atrium and (b) ventilated atrium.

The effective opening area in Holford & Hunt (2003) is defined by individual openings rather than the combination of two or more openings together as shown previously (Eq (2.15)). For example, with airflow through an opening with area a, the effective opening area for this individual opening a is given by:

$$A^* = \sqrt{2} C_d a \qquad \text{Eq (2.26)}$$

The volume flow rate Q_o can be defined by the combination of the pressure difference ΔP, reference density ρ_o and the loss coefficient C_d at the opening (Nakayama & Boucher (1999)):

$$Q_o = C_d a \sqrt{2\Delta P / \rho_o} \qquad \text{Eq (2.27)}$$

The total effective opening area can be deduced by adding the individual effective opening areas together:

$$1/A_{tot-n}^{*2} = \sum_{i=1}^{n} (1/A_i^{*2}) \qquad \text{Eq (2.28)}$$

i indicates an individual effective opening areas along an airflow path, which may include the top-down chimney (TDC) inlet A_1^*, the TDC A_2^*, the storey

inlet A_3^* (TDC outlet), the storey outlet A_4^*, the atrium top outlet A_5^* and the atrium bottom inlet A_6^*.

Assuming Q_s, Q_{up}, Q_{low} are the volume flow rates through the single storey, top outlet of the atrium and bottom inlet of the atrium, a relationship between the stratifications of the ventilated space and the atrium and the volume flow rates can be given along a specific flow path: (Hunt & Holford (1998)). For example, airflow from the storey outlet to atrium top outlet,

$$Q_s^2(1/A_{tot-4}^{*2}) + Q_{up}(1/A_5^{*2}) = g_s'(H - h_s) + g_a'(M - H - Max(h_a, 0)) \qquad \text{Eq (2.29)}$$

and airflow through atrium bottom inlet to its top outlet

$$Q_{low}^2(1/A_6^{*2}) + Q_{up}(1/A_5^{*2}) = g_a'(M - H - h_a) \qquad \text{Eq (2.30)}$$

where g_s' and g_a' are the reduced gravity in the upper layers of the storey and the atrium respectively (see Figure 2.21).

When the atrium is not ventilated (Figure 2.21(a)) and no other heat source (like solar energy) present, there is unidirectional airflow from the storey to the atrium and warm air accumulates in both the upper part of the storey and the atrium (see Figure 2.21(a)). After a steady state is reached, the two flow rates and both reduced gravities in Eq (2.29) will be identical, i.e. $Q_s = Q_{up}$ and $g_s' = g_a'$. Equating the volume flow rate and the reduced gravity of the plume theory by Morton et al (1956) at the interface height h_s (Eq (2.2 & 2.3)), the theoretical model for a single storey assisted by an unventilated atrium is given by:

$$\frac{A_{tot-5}^*}{H^2} = \left(\frac{C^3 \xi_s^{\,5}}{M/H - \xi_s}\right)^{1/2} \qquad \text{Eq (2.31)}$$

where ξ_s (= h_s / H) is the dimensionless interface height of the storey.

When the non-ventilated atrium contains a heat source, for example, solar radiation in the atrium, the reduced gravity in the atrium g_a' will be larger than

g_s' because the air in the atrium is heated by both the heat source in the storey (with a buoyancy flux B_s) and the solar input in the atrium (with a buoyancy flux B_{solar}). This will potentially increase the stack pressure to enhance the flow. The effect of a heated atrium is equivalent to an increased atrium height. Therefore the model of an unventilated atrium with a heat source in the atrium is equivalent to Eq (2.31) by replacing M with M_{eff}, where M_{eff} is the new height of the unheated atrium and defined by:

$$\frac{M_{eff}}{H} = \frac{M}{H} + \frac{B_{solar}}{B}\left(\frac{M}{H} - 1\right) \qquad \text{Eq (2.32)}$$

However, increasing the stack height using an atrium does not necessarily enhance the flow through the single space since one more opening (A_5^*) is added to the ventilation system and consequently the total effective area is reduced. Therefore, in order to enhance the flow for the storey, the atrium top outlet needs to be at least an intermediate size (Holford & Hunt (2000)).

When the atrium is ventilated (Figure 2.21(b)), two flow paths exist (Eq (2.29 & 2.30)). The system is far more complicated than the unventilated atrium case with seven independent variables. The precise forms of this model will not be addressed here. Detailed descriptions can be found at Holford & Hunt (2003) and more comments will be given at the stage of verification and validation of the theory in chapter 6.

The following figures show the ventilation properties of the single space connected to a tall atrium. Figure 2.22 shows the theoretical predictions in a space with an unheated, unventilated atrium. The ratio of M/H is equal to 1, 2, 2.35, 3, 6 (arrow indicates increasing the ratio of stack height M and space height H).

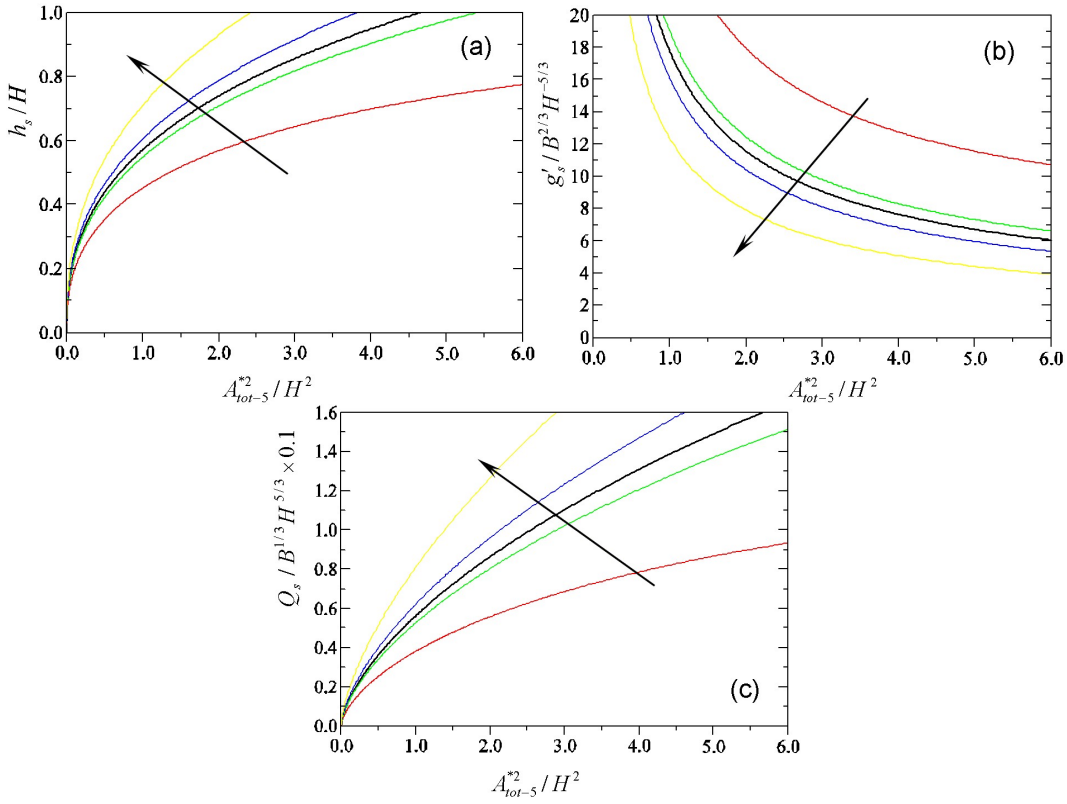

Figure 2.22 Dimensionless predictions of total effective opening area vs (a) interface height, (b) reduced gravity and (c) volume flow rate.

As shown in Figure 2.22, with a fixed total effective opening area, increasing the atrium height M with the same space height will increase the interface height of the single space (a), decrease the temperature change across the interface (b), and consequently increase the ventilation flow rate through the space (c). Increasing the total effective opening area with a fixed ratio of the atrium height and the space height will lead to an increase of the interface height and the volume flow rate, and a decrease of the reduced gravity. However, these predictions are all based on the assumption that only upward flow along the flow paths is dynamically possible.

The flow properties of a heated atrium connected to a single space can be treated by considering an increase of the atrium height (Eq (2.28 & 2.29)), which can be easily understood that with a fixed total effective opening area, increasing M / H will lead to an increase of interface height of the space, a decrease of reduced gravity and an increase of volume flow rate through the space. These properties will be further verified by numerical modelling in Chapter 6. Also, with a fixed opening area combination of the storey and the

atrium height, the flow features for varying the area of the atrium top outlet will be addressed in Chapter 6 together with the verification of the numerical simulations. The theoretical prediction of M/H =2.35 (black line in Figure 2.22 (a), (b) and (c)) will be validated by both salt bath experiments and CFD simulations.

When the atrium is ventilated (Figure 2.21(b)), the second flow path from the atrium bottom inlet to the atrium top outlet will alter both the volume flow rates of the storey (Q_s) and the reduced gravities of the storey and the atrium. As shown in Figure 2.23(a), with an increase in area of the atrium bottom inlet, the interface height in the storey is decreased and the interface height in the atrium ($\xi_a = h_a/H$) is increased. When this atrium bottom inlet is significantly large the interface height of the storey coincides with the level of the storey for the case with no atrium ventilation. This implies that the enhancement of the stack effect by using a tall atrium has been reduced to its minimum, e.g. the atrium is no longer beneficial for increasing the interface height of the single storey. The same trend is observed by the changes in the volume flow rate of the storey (Figure 2.23(b)). The volume flow rate of the storey decreases as the area of the atrium bottom inlet increases, and then reaches the level for a single storey for the case of no atrium ventilation. In figure 2.23(b), $\Delta\overline{Q}_s$ is the volume flow induced by an unventilated tall atrium. However, this enhancement is reduced when the atrium is ventilated (shown as the decrease of $\overline{Q}_s$).

Theoretical predictions of Figure 2.23 are given under the conditions of M/H =2.0, unheated atrium, A^*_{tot-4}/H^2 =0.05 and A^*_5/H^2 =0.05. The dimensionless forms of the volume flow rates $\overline{Q}_s$, $\overline{Q}_{up}$ and $\overline{Q}_{low}$ are obtained using their original forms in Holford & Hunt (2003) divided by $B_s^{1/3}H^{5/3}$.

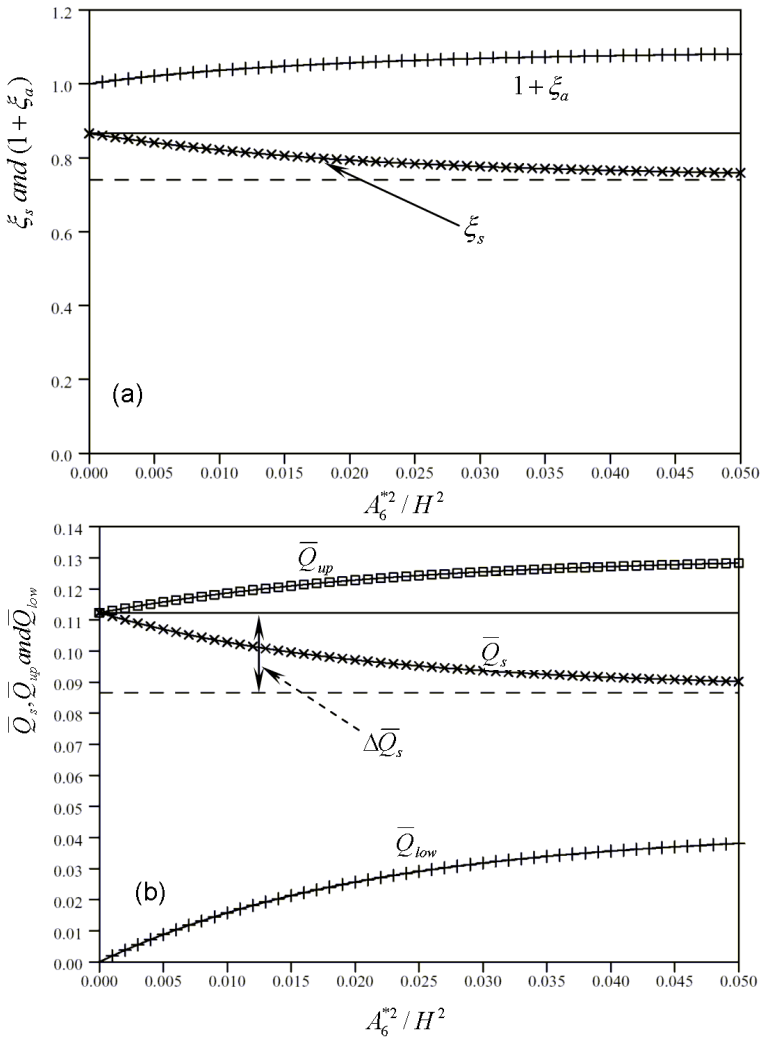

Figure 2.23 Variations in interface positions (a) and flow rates (b) with variation in A_6^{*2}/H^2. Values for an unventilated atrium are shown as the solid lines and for a single storey without an atrium by dashed lines (after Holford &Hunt (2003)).

2.3 Numerical modelling of natural ventilation

With the recent advances in computing power, the process of creating a CFD model and analysing the results has become much less labour-intensive, reducing the time and therefore the cost. CFD technique has the potential of offering detailed special data of computing domains and has been widely used to model natural ventilation flow in buildings.

Cook et al (1998) conducted numerical simulations of pure buoyancy-driven displacement flows in an enclosure using CFD. Two eddy viscosity turbulence models (standard k-epsilon model and RNG k-epsilon model) were evaluated.

Three benchmarks were developed in the study for: two-dimensional point heat source, two-dimensional line heat source and three-dimensional point heat source. Predictions from the simulations were compared with the analytical and experimental results of Linden et al (1990). Good agreement between the three modelling techniques was achieved although discrepancies existed. In the study, special care was taken to control the iteration process to ensure that a converged solution could be obtained, for example, false time steps of 0.1 were used for all the three momentum equations. The flow domain was extended beyond the ventilated space to avoid imposing boundary conditions at ventilation openings directly. For the two models used, the RNG k-epsilon model gave results closer to the work of Linden et al (1990) than the standard k-epsilon model when predicting the volume flow rate and interface height within the enclosure.

A great number of researchers have carried out work on natural displacement ventilation in buildings using CFD. Various turbulent models, solution techniques and differencing schemes have been investigated to study different airflows in buildings (e.g. natural convection, forced convection, mixed convection, jets etc.) in which the researchers attempted to provide guidelines on how best to use the technique in engineering purposes (Chen 1995, Chen & Chao 1997, Chen & Xu 1998 and Xu & Chen 2001,). However, little attention has been paid to the combined forces of buoyancy and wind for a single ventilated space and pure buoyancy force for connected spaces.

This research is to extend the work of Cook (1998) to provide guidelines on how best to model combined forces of buoyancy and wind for a single space and buoyancy-driven flow in connected spaces. These will be addressed in details in the following chapters. The selection of the literatures (Linden et al 1990, Hunt & Linden 2001, 2005 and Holford & Hunt 2003) as a basis for evaluating the capability of CFD in the modelling of natural ventilation is based on the substantial research that has been done for these simple geometries. Analytical models and small scale experiments are reported in the literature and the well presented data are available to use. These data offer the opportunity for using CFD to model similar cases and sensible comparisons between them can be made.

2.4 Summary

In this chapter a background of natural ventilation is addressed in which its mechanisms, operating modes, historical review and modern applications, are discussed.

For analytical modelling of natural ventilation, the turbulent buoyant plume theories of Morton et al (1956) were first introduced and these theories were used to study airflow features in confined single space and connected spaces. A purely buoyancy driven flow in a single box with openings connected to exterior was studied by Linden et al (1990) and the work was extended by Hunt & Linden (2001, 2005) in which buoyancy combined with wind forces were used to drive ventilation flows. Buoyancy driven flows in a single space connected to a tall atrium (Holford & Hunt 2003) was also addressed in this section. These mathematical models would be used for the benchmark development in the chapter 5 and 6.

Some of the previous research of natural ventilation using CFD was also presented in this chapter. The CFD modelling guidance offered by Cook & Lomas (1998) will be used as a reference for the development of the benchmark cases in this thesis.

Chapter 3

Experimental studies on natural ventilation

3. Experimental studies of natural ventilation

Generally speaking, experiments are preferred before applying any theory into practice. In this thesis, the theoretical models are all based on the plume theory in which a number of assumptions are used. These assumptions (section 2.2.1) simplified the situations considered. However, they could be far from reality. Experimental studies on natural displacement ventilation in buildings are used to provide information for validating the analytical models and assisting the building design.

There are a number of ways to model natural ventilation using small scale laboratory experimental techniques. Salt bath modelling (Linden et al (1990), Hunt & Linden (1996, 1997)) is the one which has been widely used for the last decades. Theoretical predictions (section 2.2) and the numerical studies of natural ventilation in this thesis (chapters 5, 6, and 7) will be validated by salt bath experiments. The fine bubble technique developed by Chen et al (2001a) has been used to model building natural ventilation in recent years and the authors assert that the technique has advantages compared with salt bath modelling due to the cost and the speed of data acquisition.

In this chapter, salt bath modelling is discussed in detail and the fine bubble technique is outlined.

3.1 Salt bath modelling technique

Salt bath modelling uses a perspex model to represent a building, brine to represent the effects of buoyancy, and water is used to represent ambient air. The model is then inverted to give a picture of what happens in a building. Density differences are used to simulate the buoyancy effects using fresh water outside the box and salt water in the box. The box is put into a large flume tank with fresh water. When conducting the experiments, buoyancy effects alone occur if the fresh water in flume tank is motionless; buoyancy combined with wind effects can be produced if the fresh water in the flume generates a flow past the Perspex box (Figure 3.1). This technique uses water movements in a small-scale box to simulate air movement in a full-scale room

or building, therefore dynamic similarity for the two flows has to be matched before conducting experiment.

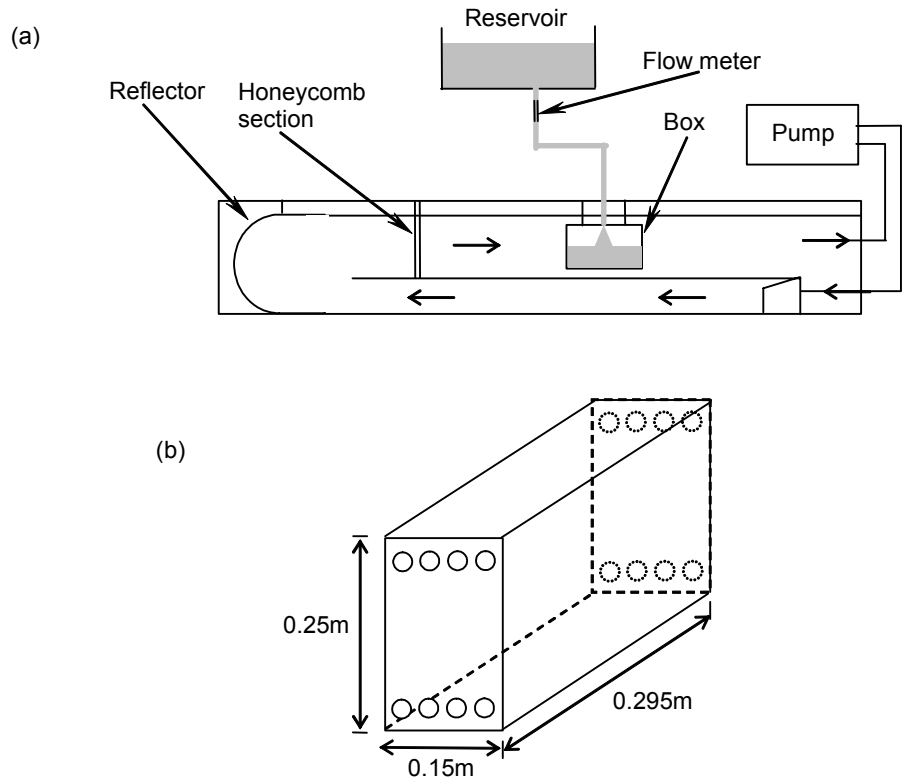

Figure 3.1 A schematic diagram showing the set-up of salt bath experiments. (a) The flume tank system and (b) and ventilation box. (After Hunt and Linden (1999)).

Dynamic similarity between the flows at small-scale and those at full-scale air is achieved when the ratio of the Reynolds number and Peclet number at full scale and model scale are equal to 1:

$$\mathrm{Re}_m / \mathrm{Re}_f = (g'_m / g'_f)^{1/2} (H_m / H_f)^{3/2} (\nu_f / \nu_m) = 1 \qquad \text{Eq (3.1)}$$

$$Pe_m / Pe_f = (g'_m / g'_f)^{1/2} (H_m / H_f)^{3/2} (\Gamma_f / \Gamma_m) = 1 \qquad \text{Eq (3.2)}$$

where, suffix m and f denote the model scale and full scale respectively; ν is the kinematic viscosity of the fluid, Γ is the diffusivity and H is a characteristic length scale. If air is used as the working fluid and density differences are created using heat, then the Reynolds and Peclet numbers at small-scale would be reduced by a factor of $(H_m / H_f)^{3/2}$. Laboratory models are typically 1:20 – 1:100 scale and hence the Reynolds and Peclet numbers would be

reduced by two or three orders of magnitude. However, by using water as the working fluid, and brine to create density differences in the system, the reduction in the magnitude of the dimensionless groups due to the change in scale is counteracted as $v_{air} >> v_{water}$ and $\Gamma_{heat} >> \Gamma_{salt}$. In addition, significantly larger density differences can be achieved in the laboratory using fresh water and brine than occur in air due to temperature differences, hence $g'_m >> g'_f$.

Dynamic similarity between a small scale experiment and a full scale real geometry when both buoyancy and wind work on the fluids can be achieved if

$$Fr_m / Fr_f = (g'_f / g'_m)^{1/2}(U_m / U_f)(H_f / H_m)^{1/2} = 1 \qquad \text{Eq (3.3)}$$

where U_m and U_f denote the speeds of the fluid driven by the flume and wind respectively. When considering the small-scale laboratory model and the full-scale building, $g'_m >> g'_f$ and $U_m << U_f$ which assist the similarity.

As shown in Figure 3.1a, the box is arranged upside down to conduct the experiments due to the properties of the working fluids (brine is heavier than fresh water). In order to make sensible comparisons between the experiments and the airflow in a single space the visualization pictures of the experiments are rotated by 180 degrees (Figure 3.2 and 3.3).

Figure 3.2(a) shows a solely buoyancy-driven flow and (b) shows a buoyancy-driven flow assisted by wind. The stratification and the shape of the buoyant plume can be observed clearly. With the effect of wind, the stratification level is increased comparing with buoyancy alone case; the shadow of the upper layer in figure 3.2(b) is less dark than that in figure 3.2(b), which indicates a reduction of temperature changes across the interface.

In the salt bath experiments of Hunt & Linden (2001, 2005) the interface height was measured using a digital image processing system: DigImage (Dalziel 1993). The position of the interface was recorded corresponding to a particular intensity on the digitized images during the experiments and the density difference across the interface was measured by an Anton Paar densitometer. The flows within the ventilated box were visualized by adding dye to the brine and using a shadowgraph. Images were collected by a video

camera. The shadowgraph images were enhanced by making a correction for the non-uniform background lighting and then stretching the range of digitized intensities in an image in order to enhance the contrast between regions of mixing in the plume and the surrounding fluid. Using this method the parallax errors were estimated at less than 0.1cm (0.4% of the total height)

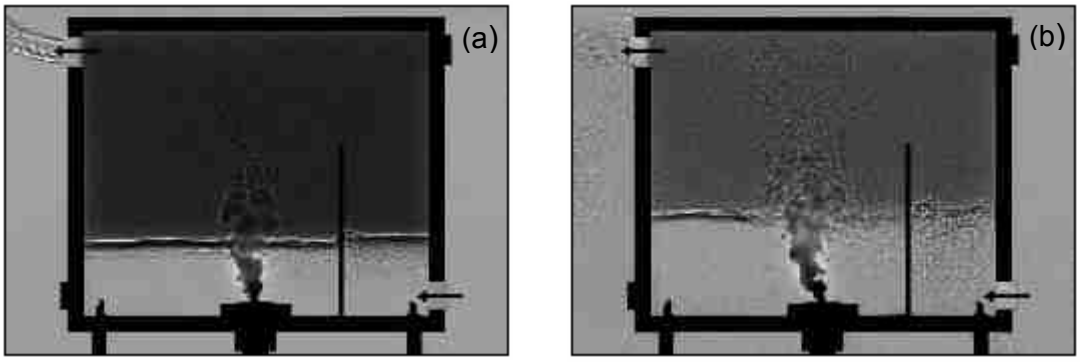

Figure 3.2 Enhanced shadowgraph images showing steady-state displacement flows in a single space: (a) buoyancy-driven alone and (b) buoyancy-driven flow assisted by wind (after Hunt & Linden (2001)).

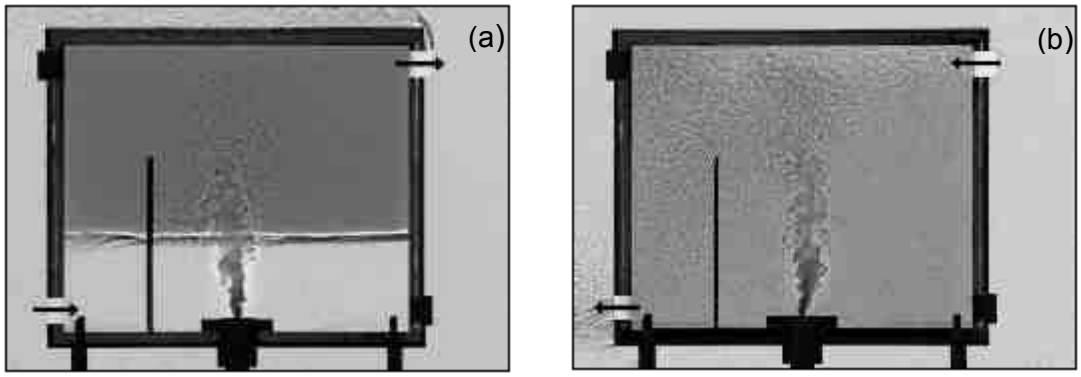

Figure 3.3 Enhanced shadowgraph images showing steady-state displacement flow (a) and mixing flow (b) in a single space driven by buoyancy and opposing wind (after Hunt & Linden (2005)).

Figure 3.3 shows the situation when wind is opposing the buoyancy force. When the opposing wind force is small (as in Figure 3.3a) the flow in the box can still be stratified to build-up a displacement flow. When the wind speed is large enough the wind starts dominating the flow, increasing the wind speed continually the flow direction will be changed, eventually a mixing flow mode established (Figure 3.3b).

Salt bath models have been applied to validate analytical models for natural displacement ventilation in single spaces by many researchers. Linden et al (1990), Cooper & Linden (1996) and Holford & Hunt (2003) used it to study buoyancy-driven steady state displacement ventilation. Hunt & Linden (1996, 1997, 1999 and 2001) applied it to investigate displacement ventilation driven by buoyancy combined with wind effects (Figure 3.2 & 3.3). The technique was further used to validate CFD predictions (Cook (1998)). An important point to note here is that Linden et al (1990) presented the box with two openings located in the top and the bottom of the box, while the two openings of Hunt & Linden (2001) were set in the sides of the box. A perforated plate (the dark line between inlets and the plume in Figure 3.2 & 3.3) was used to minimize the effects of horizontal momentum on the plume. Without the plate, the plume is forced over towards the high level opening even when the driving force is buoyancy alone.

The work of Hunt & Kaye (2001) presented a method to measure ventilation flow rates through a single ventilated space driven by buoyancy effect using salt bath experiments. The experimental box was the same as Hunt & Linden (2001) except the control of the supplied fresh water. In Hunt & Kaye (2001), fresh water was supplied to the tank at a known constant flow rate. During the experiments the steady flow was thought to be established when the interface reached a fixed elevation. At this stage there was no flow across the interface other than in the plume. Consequently, at the level of the interface the volume flow rate in the plume was identical to the volume flow rate at which the fresh water was supplied to the system. Hence, by measuring the steady height of the interface below the actual source, the volume flow rate in the plume at that height was deduced. By varying the supply and drainage flow rates, the volume flow rate in the plume was measured at various distances from the actual source. The interface height was tracked and visualised using the same method used in Hunt & Linden (2001, 2005).

Salt bath modelling has also been used to investigate airflow properties in single and multi-storey buildings connected to a tall atrium. Hunt & Holford (1998) conducted the salt bath experiments for a simplified two-storey building with an atrium. A top down chimney was also used to bring fresh ‘air’ from

high level into the storey spaces linked to the atrium (Figure 3.4). The model building was immersed upside-down in a large tank of fresh water, and heat gains were modelled as a continuous release of dense salt solution through a small opening in the floor of each storey.

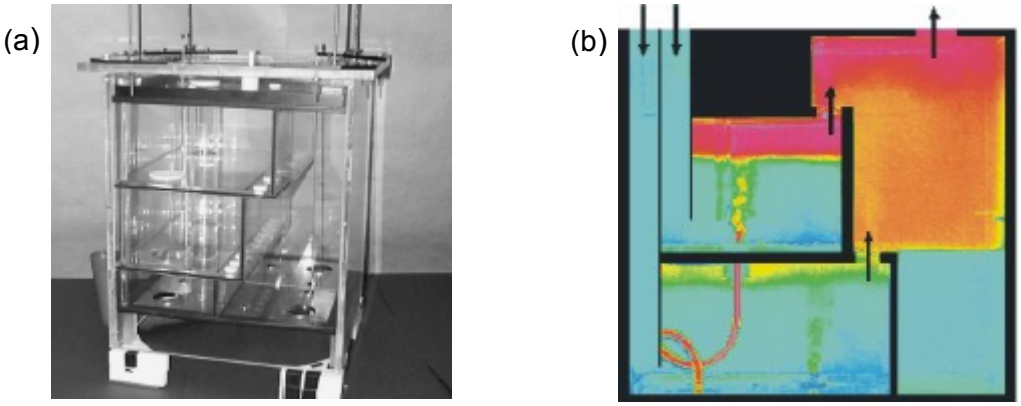

Figure 3.4 The model used in the salt bath experiments, (a) photograph of the testing box (after Holford & Hunt (2003)), and (b) inverted dye concentration image showing displacement flow in a two-storey building enclosure (after Hunt & Holford (1998)).

Stagnant layers were observed at the outlet opening levels in the atrium (Figure 3.4(b)). Although some experiments were performed by Hunt & Holford (1998), the experimental data were not available for use in the research presented here. Some experimental data were however recently published by Holford & Hunt (2003). These used a single storey building connected to an atrium. The same testing model was used to conduct the experiments by blocking the ventilation openings of the upper storey (Figure 3.4).

The experiments mentioned above were all used to predict qualitative properties (e.g. airflow patterns: displacement flow or mixing flow) and quantitative properties (such as the interface height and temperature changes across the interface). However, air volume flow rate, which is an important ventilation parameter, was not measured at the same time with these experiments. Separate experiments were done by Hunt & Kaye (2001) in which salt bath modelling was used to predict volume flow rates in a naturally ventilated space driven by buoyancy force.

Here are some selected examples of salt bath modelling for validating theoretical models of building natural ventilation (Figure 3.5 and 3.6). Pressure

fluctuations were recorded during the experiments within the range of 5% and 10% of the mean pressure drop. When plotting the results these fluctuations were represented by error bars (i.e. Figure 3.5a).

Besides the validation work for theoretical studies of natural ventilation, salt bath experiments have also proved valuable at the design stage of several naturally ventilated buildings, such as the School of Engineering at De Montfort University, Leicester (Lane-Serff et al (1991)), the Cable and Wireless building in Coventry (Edwards et al (1994)), and the New Energy Efficient Office at the Building Research Establishment, Garston (BRE 1997).

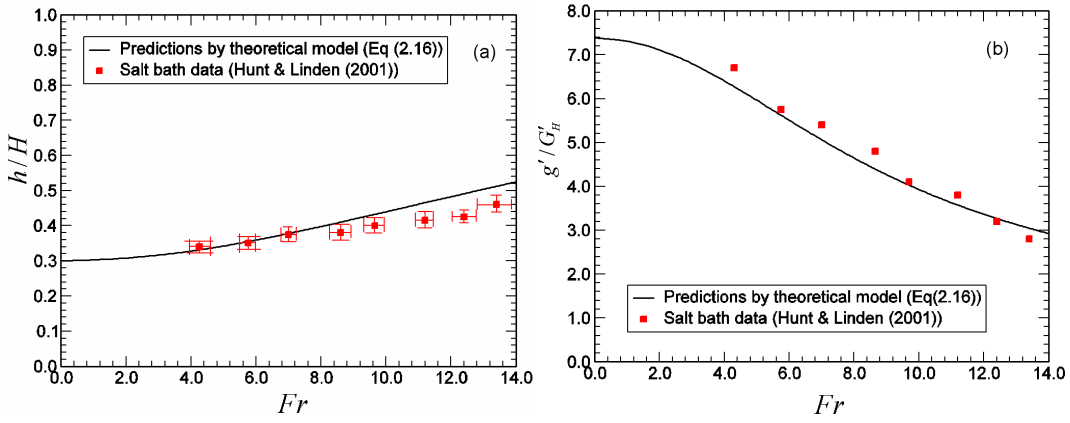

Figure 3.5 Influence of Froude number on (a) dimensionless interface height and (b) reduced gravity for buoyancy-driven natural ventilation in a single space assisted by wind (after Hunt & Linden (2001)).

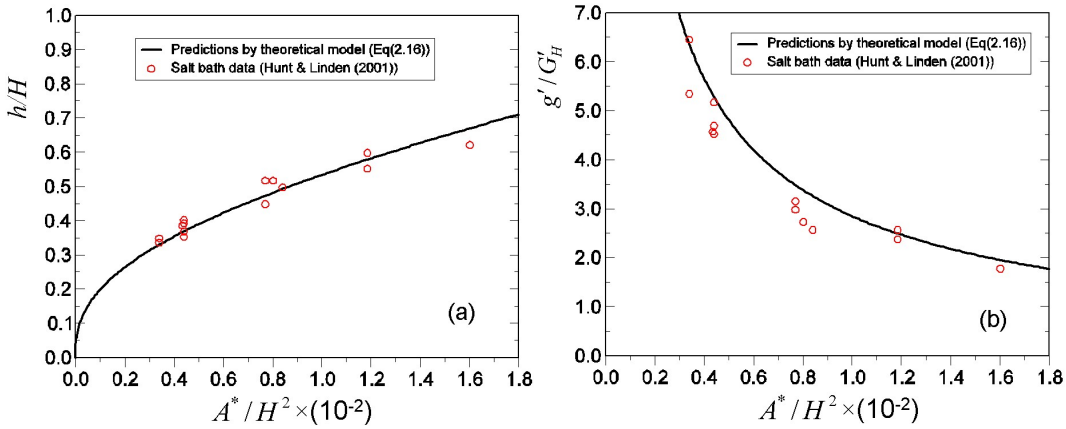

Figure 3.6 Influence of effective opening area on (a) dimensionless interface height and (b) reduced gravity for buoyancy-driven natural ventilation in a single space assisted by wind (after Hunt & Linden (2001)).

3.2 Fine bubble technique

This technique uses buoyancy plumes generated by fine bubbles in water to simulate the thermal stack effect in buildings (Chen et al (2001a, b)). Components of the system are shown in Figure 3. 7.

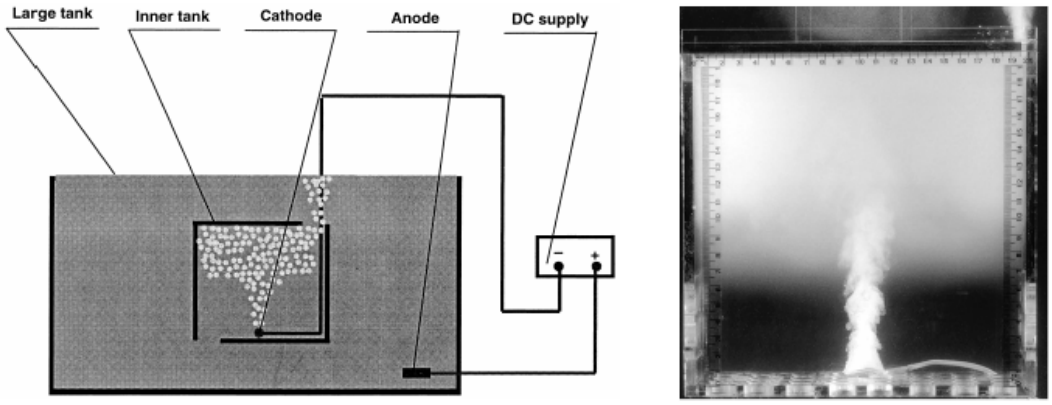

Figure 3.7 Components of the experimental system (left) and visualization of fine hydrogen bubble plume in a single space with top and bottom openings (right) (After Chen et al (2001a))

Here, the large tank represents the environment, the inner tank represents the ventilation single space and the combination of cathode, anode and DC supply is used to generate fine hydrogen bubble plumes.

This technique was applied to validate the theoretical models of Linden et al (1990) and Cooper et al (1998). Favourable agreement was achieved (Chen et al (2001b)) between the models and the fine bubble technique as well as salt bath modelling. In a sense, this supports the salt bath modelling technique (Linden et al (1990)) for modelling natural ventilation in buildings.

Although the two methods provide similar predictions for natural ventilation flow in a single space driven by buoyancy (Chen et al (2001a, b), it is necessary to note the special features of the fine bubble technique.

There are no heating elements involved in fine bubble technique; hence the set-up and operation for this system are simple. Also, fine bubble plumes generate positive buoyancy which leads to an upward buoyant flow, the same as a thermal buoyant flow. During the experiments the bubbles leave the free water surface and the properties of the water in the large tank will not change

throughout the experiments. Consequently, the fine bubble system does not require a big water tank and a simple, economical and compact modelling system can be easily constructed.

Limitations of this fine bubble method can be summarised as: (i) constant heat flux boundary conditions are difficult to simulate. Alternatively, constant temperature boundary has to be used for this method; (ii) unrealistic flow fields can be observed when the high level opening of the ventilation space is lower than the ceiling where bubbles accumulate; (iii) when the high level openings are large the slip velocity between the bubbles and water may influence the ventilation process at high level. Despite these limitations, the fine bubble technique can be used as an alternative for modelling natural ventilation in buildings.

3.3 The use of experimental data in this thesis

Quantitative and qualitative comparisons between analytical models, experiments and CFD predictions (chapters 5 & 6) are made to evaluate the accuracy of CFD for modelling natural and forced convection in simple geometry enclosures. The following literature is used for this purpose.

- Hunt & Linden (2001) and Hunt & Linden (2005) are used to study the natural displacement ventilation in an enclosure with combined wind and buoyancy forces. Both assisting and opposing wind cases are addressed.

- Holford & Hunt (2003) is used to study natural displacement ventilation in a single storey building connected to a tall atrium. In order to make comparisons with natural ventilation in a single space Linden et al (1990) is also used.

The above publications and corresponding experiments have been reviewed in chapters 2 and 3. In these publications, the predictions of interface heights, reduced gravities for the variations of ventilation openings, wind speeds, buoyancy source strength, stack height, or individual ventilation openings, were well presented and validated by salt bath experiments. However, the volume flow rate through the ventilated space/spaces was not validated. Hunt & Kaye (2001) presented a method for validating the volume flow rate through

a naturally ventilated space using salt both experiment techniques. All of these publications (Hunt & Linden (2001, 2005), Hunt & Kaye (2001) and Holford & Hunt (2003)) employed the same plume theory by Morton et al (1956) and use the principle of equating the volume flux through the space with the volume flux through the buoyant plume at the interface height. Therefore, Hunt & Kaye (2001) is used for validating volume fluxes predicted by the CFD modelling of buoyancy combined with wind driven flows (section 2.2.4) and the atrium assisted natural ventilation flows (section 2.2.5). Further detail of Hunt & Kaye (2001) is given in section 5.5.

In this thesis only the data from salt bath experiments are used to evaluate the accuracy of CFD. For fine bubble modelling technique, there are no experimental data for the cases considered in this thesis, therefore this modelling technique is not further discussed in this thesis.

3.4 Summary

Salt bath modelling for natural ventilation has been described in detail in this chapter. The model was used to validate the analytical models developed for natural ventilation flow in simple geometries. The comparisons between the analytical models (for example, Hunt & Linden 2001, 2005, Holford & Hunt 2003) and salt bath modelling have been made and close agreement between them were achieved. Further details will be addressed when comparisons are made between the analytical models (section 2.2), experimental measurements and CFD simulations (chapters 5 and 6).

Another technique for modelling natural ventilation, fine bubble method, is outlined to support the outcomes of the salt bath modelling for buoyancy driven flows. The experimental data by salt bath modelling will be used in this thesis.

The end of this section several key literatures are listed. The analytical and experimental data from these literatures are used to evaluate the accuracy of CFD for modelling natural ventilation flows discussed in this thesis.

Chapter 4

CFD techniques for modelling natural ventilation

4. CFD techniques for modelling natural ventilation

4.1 Introduction

The physical properties of fluid flows are governed by three fundamental conservation laws: the conservation of mass, momentum (Newton's second law) and energy. These laws can be interpreted in terms of partial differential equations. Computational Fluid Dynamics (CFD) is a numerical method of determining a solution to the governing equations of a fluid flow by advancing the solution through space and/or time to obtain a numerical description of the whole flow field of interest.

Newtonian fluid dynamics and the Navier-Stokes (N-S) equations (conservation equations of momentum for fluid flow) have been well known for a century. However, the analytical investigation of simplified forms of these equations is still an active area of research in which the problem of turbulent closure for the Reynolds averaged forms of the N-S equations (see section 4.4) needs to be advanced.

The improvement in computer power since the 1970s has led to the fast development of Computational Fluid Dynamics. In particular, over the last 20 years, more sophisticated commercial CFD codes have become available for a wide range of engineering applications. CFD complements experimental and theoretical studies of fluid dynamics by providing an alternative, economical means of simulating real fluid flows. Now, due to the recent advances in computing power, the process of creating a CFD model and analysing the results is much less labour-intensive, reducing the time and therefore the cost. As a result, CFD is now an established industrial design tool, which can be used in helping to reduce design timescales and improving processes throughout the engineering world.

In this chapter, the basis of CFD modelling technique will be presented. This will include its modern applications, governing equations of fluid flows, turbulence modelling, boundary conditions, natural ventilation modelling and solving the governing equations. This is followed by a brief introduction to the

commercial CFD codes (CFX4 and CFX5) and the procedures for evaluating the codes. These are two fundamentally different codes.

4.2 CFD applications

CFD is a numerical method in which fluid flow, heat transfer and associated phenomena such as particle transport etc are modelled. A wide range of industrial and non-industrial application areas of CFD was listed by Versteeg and Malalasekera (1995):

- Aerodynamics of aircraft and vehicles: lift and drag
- Hydrodynamics of ships
- Power plant: combustion in IC engines and gas turbines
- Turbo machinery: flows inside rotating passages, diffusers etc.
- Electrical and electronic engineering: cooling of equipment including micro-circuits
- Chemical process engineering: mixing and separation, polymer moulding
- External and internal environment of buildings: wind loading and heating/ventilation
- Marine engineering: loads on off-shore structures
- Environmental engineering: distribution of pollutants and effluents
- Hydrology and oceanography: flows in rivers, estuaries, oceans
- Meteorology: weather prediction
- Biomedical engineering: blood flows through arteries and veins

One of these application areas is the numerical modelling of building environments, which is the area of work represented in this thesis. This thesis focuses on the natural displacement ventilation airflows in buildings driven by either buoyancy or buoyancy combined with wind effect.

4.3 Governing equations of fluid flow

The conservation laws of fluid flow can be summarized as follows assuming a Newtonian fluid with Cartesian coordinates and three dimensions.

Considering a finite control volume of a fluid, the increase of mass within it should be equal to the difference between the mass inflow and mass outflow. The mathematical form of this law may be expressed by:

$$\frac{\partial \rho}{\partial t} + div(\rho U_i) = 0 \qquad \text{Eq (4.1)}$$

Newton's second law indicates that the rate of change of momentum equals the sum of the forces acting on the fluid control volume considered:

$$\frac{\partial \rho U_i}{\partial t} + div(\rho U_i U_j) = -\frac{\partial P}{\partial x_i} + div(\mu grad U_i) + B_i \qquad \text{Eq (4.2)}$$

(i) (ii) (iii) (iv) (v)

The rate of change of energy within a control volume is equal to the sum of the heat exchange rate and the rate of work done on the volume. This is the first law of thermodynamics and can be stated as:

$$\frac{\partial \rho He}{\partial t} + div(\rho U_i He) = -\frac{\partial P}{\partial t} + div(\lambda grad T) + S_T \qquad \text{Eq (4.3)}$$

Above are the most compact forms of the general governing equations for fluid flow. U_i (U_j), P, x_i, μ, t, B_i, He, λ, S_T and T are velocity components, pressure, corresponding directions of velocity components, fluid viscosity, time, body force, enthalpy, thermal conductivity, source term and temperature respectively. The suffixes i, j and the function symbols 'div', '$grad$' are explained in Appendix A.

Eq (4.2) is also known as the Navier-Stokes equation, in which the components (i), (ii), (iii), (iv) and (v) are respectively the time dependent term, the inertia term, the pressure term, the viscous term and the body force term. Details of the derivation of these equations can be found in Versteeg and Malalasekera (1995).

Introducing a general variable Φ, the following general form of transport equation for both vector and scalar quantities is normally used to represent the various transport processes:

$$\partial(\rho\Phi)/\partial t + div(\rho\Phi U_i) = div(\Gamma grad\,\Phi) + S_\Phi \qquad \text{Eq (4.4)}$$

where Γ is diffusion coefficient; the four terms of the equations are the rate of change, the convective, the diffusive and the source term respectively.

There are six independent unknown variables, U, V, W, P, ρ, T within five equations. For airflows, the system can be closed by the equation of state (Eq (4.5)) and the thermodynamic relation between state variables (Eq (4.6)):

$$P = P(\rho, T) \qquad \text{Eq (4.5)}$$

$$He = He(\rho, T) \qquad \text{Eq (4.6)}$$

The above governing equations are a system of coupled non-linear partial differential equations and are very difficult to solve directly using analytical methods, especially for complicated applications, e.g. turbulent flows, because the velocity components are varying rapidly in time and space, as well as the difficulties for solving the heat transfer if involved.

Fluid flows can be characterised as two main categories, either laminar or turbulent in terms of a Reynolds number, defined by:

$$R_e = UL/\nu \qquad \text{Eq (4.7)}$$

where U and L are the characteristic velocity and the length scale and ν is the fluid kinematic viscosity. Reynolds number is a relative measure of the inertia and viscous forces of the fluid. When the inertia force is much larger than viscous force (high velocity) the fluid tends to be turbulent. For a simple laminar flow without heat transfer, above equations (Eqs (4.1 - 4.6)) can possibly be solved analytically to give an exact solution of the fluid flow (Schlichting 1979). However, for complicated turbulent flows, these equations need to be solved numerically, using techniques, such as CFD. This is explained further in section 4.7

4.4 Turbulence modelling

The most accurate means of modelling fluid flow numerically is the direct numerical simulation (DNS) in which the mesh size of the domain needs to be small enough to model all the range of turbulent eddies within the domain (Murakami 1997). This is not practical due to the wide range of length scales of turbulent eddies. A typical flow domain of 0.1m by 0.1m with a high Reynolds number turbulent flow might contain eddies of 10 μm to 100 μm. In

this case, cells of 10^9 up to 10^{12} would need to be used to resolve the smallest eddies of the flow, which is far beyond the capability of modern computers, both desktop computers and supercomputers (Versteeg and Malalasekera (1995)). In order to reduce the computing cost, the real fluid properties are modelled by time-averaged mean quantities and the effects of their fluctuations. Considering the general variable Φ, its time-averaged form is given by:

$$\Phi(t) = \phi + \phi'(t) \qquad \text{Eq (4.8)}$$

The general time-averaged governing equation set therefore becomes:

$$\partial\rho/\partial t + \partial\rho u_i/\partial x_i = 0 \qquad \text{Eq (4.9)}$$

$$\frac{\partial(\rho u_i)}{\partial t} + \frac{\partial(\rho u_j u_i)}{\partial x_i} = -\frac{\partial p}{\partial x_i} + \frac{\partial}{\partial x_j}\left(\mu\left(\frac{\partial u_i}{\partial x_j} + \frac{\partial u_j}{\partial x_i}\right) - \rho\overline{u_i' u_j'}\right) + B_i \qquad \text{Eq (4.10)}$$

$$\frac{\partial(\rho\phi)}{\partial t} + \frac{\partial(\rho\phi u_i)}{\partial x_i} = \frac{\partial}{\partial x_i}\left(\Gamma\left(\frac{\partial\phi}{\partial x_i}\right) - \rho\overline{u_i'\phi'}\right) + S_\phi \qquad \text{Eq (4.11)}$$

Eq (4.10) is also called the Reynolds Averaged Navier-Stokes (RANS) equation. It has a similar form as Eq (4.2) except for the presence of the Reynolds stress: $-\rho\overline{u_i' u_j'}$, similarly, Eq (4.11) and Eq (4.3) differ by the presence of the Reynolds flux: $-\rho\overline{u_i'\phi'}$. In Eq(4.11), ϕ is treated as an arbitrary scalar variable. After this time-averaging procedure the individual details of the instantaneous fluctuations of the fluid flow are lost and as a result, there are nine additional unknowns generated by the Reynolds stress/flux components (three normal stresses, three shear stresses and three Reynolds fluxes). In total there are fourteen unknowns but with only five equations, hence the set of the time-averaged governing equations are not closed. These Reynolds stresses/fluxes need to be represented by some way to solve this closure problem, which leads to the development of turbulence modelling.

4.4.1 Eddy viscosity assumption.

Traditional turbulence models (e.g. mixing length and two equation models) are based on the eddy viscosity assumption in which the turbulent or eddy viscosity is assumed to be isotropic. Reynolds stresses can be treated to be proportional to the rate of deformation of fluid mean quantities, analogous to the viscous stresses in the momentum equation. For an incompressible fluid the viscous stresses are expressed by

$$\tau_{ij} = \mu e_{ij} = \mu\left(\frac{\partial u_i}{\partial x_j} + \frac{\partial u_j}{\partial x_i}\right) \qquad \text{Eq (4.12)}$$

where τ_{ij} and e_{ij} are the suffix notation to simplify the equation form, detailed expansion form of Eq (4.12) can be found in Appendix A. The form of the Reynolds stresses proposed by Boussinesq in 1877 is defined by Eq (4.13):

$$\tau_{ij} = -\rho\overline{u_i' u_j'} = \mu_t\left(\frac{\partial u_i}{\partial x_j} + \frac{\partial u_j}{\partial x_i}\right) \qquad \text{Eq (4.13)}$$

The only difference between Eq (4.12) and Eq (4.13) is the presence of turbulent or eddy viscosity μ_t. Similarly, turbulent transport of a scalar is taken to be proportional to the gradient of the mean value of the transported quantity, defined by:

$$-\rho\overline{u_i'\phi'} = \Gamma\frac{\partial \phi}{\partial x_i} \qquad \text{Eq (4.13)}$$

The aim of turbulence models is to determine the eddy viscosity μ_t on which a number of classical turbulence models are based.

4.4.2 Zero-equation model

In order to represent the eddy viscosity μ_t, an empirical formula was introduced by Prandtl (1925) in which a 'mixing length scale l_m' was introduced:

$$\mu_t = \rho\, l_m\, \upsilon_t \qquad \text{Eq (4.14)}$$

where υ_t is a lateral turbulence velocity, assumed to be proportional to the mixing length and the time-mean velocity gradient, expressed by $\upsilon_t = l_m \left|\partial u / \partial y\right|$, then

$$\mu_t = \rho l_m^2 \left|\partial u / \partial y\right| \qquad \text{Eq (4.15)}$$

The only unknown remaining here is the mixing length scale l_m. In general it is assumed to be proportional to the distance from the nearest wall or the width of a shear layer, a wake, a jet, etc. There are no extra transport equations introduced, this model is therefore called zero-equation model or mixing length model.

In the zero equation model, the way of representing the turbulence velocity $\upsilon_t = l_m \left|\partial u / \partial y\right|$ lacks generality. For example, a turbulent flow at the centre of a pipe where the velocity gradient $\partial u / \partial y$ is zero, which would lead to a zero μ_t (Eq (4.14)), whereas in fact μ_t is very large. Another drawback of the zero equation models is the difficulty of assigning a value for l_m in complex turbulence problems, e.g. when the flow involves separation and recirculation.

4.4.3 One-equation model

Before introducing the one equation model, it is first necessary to define the turbulent kinetic energy k. Similar to other transport variables (Eq (4.8)), the instantaneous kinetic energy $K(t)$ is defined as the sum of the mean kinetic energy and the turbulent kinetic energy:

$$K(t) = K + k \qquad \text{Eq (4.16)}$$

$$\text{where } K = \frac{1}{2}(u^2 + v^2 + w^2) \qquad \text{Eq (4.17)}$$

$$\text{and } k = \frac{1}{2}(u'^2 + v'^2 + w'^2) \qquad \text{Eq (4.18)}$$

The one-equation model suggested by Kolmogorov (1942) uses the turbulent kinetic energy k to represent the turbulence velocity υ_t ($\upsilon_t = \sqrt{k}$). The turbulent viscosity is then given by

$$\mu_t = C'_D \rho l_s \sqrt{k} \qquad \text{Eq (4.19)}$$

where C'_D is an empirical constant (≈ 1.0) and l_s is a length scale. k is treated as a new dependent variable and can be transported by the governing equation (Eq (4.2)). Its form is the same as the two-equation models for k and will be be addressed in section 4.4.4. This model is a one step improvement over the zero-equation model in terms of representing the turbulence velocity, υ_t, however, it still presents the same difficulty as the zero-equation model for determining the length scale l_s.

4.4.4 Two-equation models

In the one-equation model, the turbulence velocity υ_t is represented by turbulent kinetic energy k which can be transported by the governing equation (Eq (4.2)), while for two-equation models, efforts have been made to represent the length scale by some quantity which could be similarly transported in the same way as k. The dissipation rate of the turbulent kinetic energy ε, was introduced by Launder & Spalding (1974) and the length scale l is expressed by a combination of k and ε:

$$l = C_\mu k^{3/2} / \varepsilon \qquad \text{Eq (4.20)}$$

where C_μ is a constant. The turbulent viscosity μ_t is therefore defined by

$$\mu_t = C_\mu \rho k^2 / \varepsilon \,. \qquad \text{Eq (4.21)}$$

The transport equations for turbulent kinetic energy k and its dissipation rate ε are given as follows (Launder & Spalding 1974):

$$\frac{\partial(\rho k)}{\partial t} + \frac{\partial(\rho u_j k)}{\partial x_j} = \frac{\partial}{\partial x_j}\left[(\mu + \mu_t / \sigma_k)\frac{\partial k}{\partial x_j}\right] + P_k - \rho\varepsilon \qquad \text{Eq (4.22)}$$

$$\frac{\partial(\rho\varepsilon)}{\partial t}+\frac{\partial(\rho u_j\varepsilon)}{\partial x_j}=\frac{\partial}{\partial x_j}\left[(\mu+\mu_t/\sigma_\varepsilon)\frac{\partial\varepsilon}{\partial x_j}\right]+C_{1\varepsilon}P_k\frac{\varepsilon}{k}-\rho C_{2\varepsilon}\frac{\varepsilon^2}{k} \qquad \text{Eq (4.23)}$$

where the P_k is the production of turbulent kinetic energy due to shear stresses, expressed by:

$$P_k=(\mu+\mu_t)\frac{\partial u_i}{\partial x_j}\left[\frac{\partial u_i}{\partial x_j}+\frac{\partial u_j}{\partial x_i}\right] \qquad \text{Eq (4.24)}$$

The model introduced above is the standard $k-\varepsilon$ model, the most widely used and validated turbulence model for engineering applications (e.g. Kato et al (1992), Shankar et al (1995)). There are five adjustable constants used in this model (Table 4.1).

Table 4.1 Model constants for Standard $k-\varepsilon$ model

C_μ	σ_k	σ_ε	$C_{1\varepsilon}$	$C_{2\varepsilon}$
0.09	1.0	1.3	1.44	1.92

The values in Table 4.1 were determined by substantial investigation of experimental data and have been found to be applicable over a wide range of turbulent flows. However if these constants are sensitive to a numerical solution for a specific turbulent flow, the values can be adjusted. For example, the constant C_μ was changed from 0.09 to 0.11 by Kulmala (1997) in order to accurately predict the mean velocity in a thermal plume.

One improvement to the standard k-ε model was made by Yakhot et al (1992) in which a complex mathematical procedure termed the Renormalisation Group (RNG) Theory was applied. The following model equations are taken from Yakhot et al (1992):

$$\frac{\partial(\rho k)}{\partial t}+\frac{\partial(\rho u_j k)}{\partial x_j}=\frac{\partial}{\partial x_j}\left[(\mu+\mu_t/\sigma_k)\frac{\partial k}{\partial x_j}\right]+P_k-\rho\varepsilon \qquad \text{Eq (4.25)}$$

$$\frac{\partial(\rho\varepsilon)}{\partial t}+\frac{\partial(\rho u_j\varepsilon)}{\partial x_j}=\frac{\partial}{\partial x_j}\left[(\mu+\frac{\mu_t}{\sigma_\varepsilon})\frac{\partial\varepsilon}{\partial x_j}\right]+(C_{1\varepsilon}-C_{1\varepsilon}^*)P_k\frac{\varepsilon}{k}-\rho C_{2\varepsilon}\frac{\varepsilon^2}{k} \qquad \text{Eq (4.26)}$$

where, P_k is the same as in the standard $k-\varepsilon$ model, $C_{1\varepsilon}^*$ is defined as

$$C_{1\varepsilon}^* = \frac{\eta(1-\eta/\eta_0)}{1+\beta\eta^3}, \text{ with } \eta = \left(\frac{P_k}{\mu}\right)^{1/2}\frac{k}{\varepsilon}. \quad \text{Eq (4.27)}$$

The constants used in this RNG $k-\varepsilon$ model are given in Table 4.2.

Table 4.2 Model constants for RNG $k-\varepsilon$ model

C_μ	$C_{1\varepsilon}$	$C_{2\varepsilon}$	β	η_0
0.0845	1.42	1.68	0.012	4.377

Of the constants in Table 4.2, only β is adjustable, all the other constants are computed as part of the RNG process. The process uses the statistical mechanics approach for representing the effects of small scale turbulence by means of a random forcing function in the Navier-Stokes equation, and systematically removing the small scales of turbulence from the governing equations by expressing their effects in terms of larger scale motions and a modified viscosity. The RNG process makes the model better suited to the modelling of flows that experience separation and curvature compared with the standard $k-\varepsilon$ model. Comparisons between these two models on the prediction of room airflows have been made by a number of researchers, e.g. Chen (1995), Chen & Chao (1997), Cook & Lomas (1998) and Gan (1998). These studies concluded that the RNG $k-\varepsilon$ model performed slightly better than the standard $k-\varepsilon$ model for the prediction of room airflows.

The other two-equation models used in CFD are generally modifications of the standard $k-\varepsilon$ model. For example, the low Reynolds number $k-\varepsilon$ model is used for low Reynolds number (typically in the range of 5,000 to 30,000) turbulent flows. This model uses natural boundary conditions at walls rather than wall functions, therefore the equations are integrated through the laminar sub-layer (see section 4.6.1) where the eddy viscosity is damped and ε goes to zero. If the grid is fine enough in the sub-layer this model can be used for turbulent flows with any Reynolds numbers. The low Reynolds number $k-\omega$ model and the Menter modified low Reynolds number $k-\omega$ model of

CFX4 are not investigated in this research, the details of these models will not be introduced but can be found in the manual of CFX4.4 (2001).

All the models mentioned above (sections 4.4.2 – 4.4.4) are based on the eddy viscosity assumption in which the turbulent stresses are assumed to relate directly to the mean velocity gradient. However, this is not always the case. In flows involving separation and/or reattachment at boundaries, the shear stress may vanish where the mean velocity gradient is not zero. More complicated numerical ways to represent these Reynolds stresses/fluxes have been developed to improve the universality of CFD. These are briefly discussed in the following sections.

4.4.5 Reynolds Stress Model

In the Reynolds Stress Model (RSM) (Launder et al (1975)), the individual Reynolds stresses/fluxes (six Reynolds stresses in Eq (4.10) and three Reynolds fluxes in Eq (4.11)) are represented by exact transport equations rather than using the eddy viscosity assumption. The derivation of these Reynolds stresses/fluxes equations can be found in relevant literatures such as Launder & Spalding (1972), or Leschziner (1990).

Compared with two-equation turbulence models, RSM is a more accurate way to model fluid flows due to its rigorous and detailed mathematical formulation. However, a great deal of computational cost is added for solving the nine extra transport equations for Reynolds stresses/fluxes. For complicated turbulent flows it is still very difficult to handle even using modern computers. In order to reduce the computational cost, Rodi (1985) tried to simplify the transport equations by approximating the convection and diffusion terms into algebraic expressions, to give what is known as the Algebraic Stress Model (ASM). Although ASM is not as well validated as the $k-\varepsilon$ models it can be used in flows where the isotropic assumption of eddy viscosity is not appropriate.

4.4.6 Large Eddy Simulation

In the large-eddy simulations (LES) model (Deardorff (1970)) small eddies are filtered from the instantaneous motions and are modelled using some simple

models. The LES model can be used to resolve the unsteady, three-dimensional evolution of the large scale turbulent flow field and monitor the flow at any moment in time and if mean flow quantities are required the calculations must be done over a sufficient large time scale. Although its computational cost is less than the direct numerical simulations (Murakani (1997) of turbulence, it still requires impractical amounts of computing to be a model that can be recommended for engineering applications. This model has been used to investigate cases such as isothermal flows in channels (e.g. Deardorff (1970)) or over a cube (e.g. Murakami et al (1987)).

4.5 Modelling natural and forced convection

Natural convection flows in buildings are normally generated by thermal buoyancy. When a natural convection flow is influenced by other forces, e.g. pressure difference induced by wind effect, the convection flow becomes the combination of natural and forced convection. For engineering applications of these types of flows, where the temperature differences and compressibility effects are small, the flow is treated as incompressible and can be modelled using the Boussinesq approximation (Boussinesq (1903)). The fluid properties ρ , μ and Prandtl number (a relative measure of momentum diffusivity and thermal diffusivity) are treated as constants by the approximation except for the density in the momentum equations which is written as

$$\rho = \rho_o[1 - \beta(T - T_o)] \qquad \text{Eq (4.28)}$$

where ρ_o and β are the density and the thermal expansion coefficient at a reference temperature T_o. Normally, T_o is taken as the ambient temperature in a natural convection boundary layer or the average temperature in an enclosure, and $\beta \approx 1/T_o$.

Based on this approximation, the modelling equations for steady state, incompressible turbulent natural and forced convection flows are given by the following form.

$$\partial u_i / \partial x_i = 0 \qquad \text{Eq (4.29)}$$

$$\frac{\partial(\rho_o u_j u_i)}{\partial x_i} = g_i \rho_o \beta (T - T_0) - \frac{\partial P'}{\partial x_i} + \frac{\partial}{\partial x_j}\left(\mu_e\left(\frac{\partial u_i}{\partial x_j} + \frac{\partial u_j}{\partial x_i}\right)\right) + S_i \qquad \text{Eq (4.30)}$$

$$\frac{\partial(u_i T)}{\partial x_i} = \frac{\partial}{\partial x_i}\left(\Gamma_e\left(\frac{\partial T}{\partial x_i}\right)\right) + S_T \qquad \text{Eq (4.31)}$$

$$\frac{\partial(\rho_o u_j k)}{\partial x_j} = \frac{\partial}{\partial x_j}\left[(\mu + \mu_t / \sigma_k)\frac{\partial k}{\partial x_j}\right] + P_k + G_k - \rho_o \varepsilon \qquad \text{Eq (4.32)}$$

$$\frac{\partial(\rho_o u_j \varepsilon)}{\partial x_j} = \frac{\partial}{\partial x_j}\left[(\mu + \mu_t / \sigma_\varepsilon)\frac{\partial \varepsilon}{\partial x_j}\right] + C_{1\varepsilon} P_k \frac{\varepsilon}{k} - \rho_o C_{2\varepsilon} \frac{\varepsilon^2}{k} + C_{1\varepsilon} C_{3\varepsilon} G_k \frac{\varepsilon}{k} \qquad \text{Eq (4.33)}$$

where P_k and G_k are the production terms due to strain and buoyancy forces, given by

$$P_k = \mu_e\left(\frac{\partial u_i}{\partial x_j} + \frac{\partial u_j}{x_i}\right)\frac{\partial u_i}{\partial x_j} \qquad \text{Eq (4.34)}$$

$$G_k = -g_i \beta \Gamma_t \frac{\partial T}{\partial x_i} \qquad \text{Eq (4.35)}$$

where, $\mu_e = \mu + \mu_t$ is the effective viscosity, $\Gamma_e = \mu/\sigma + \mu_t/\sigma_t$ and $\Gamma_t = \mu_t/\sigma_t$ are effective diffusion coefficients, $\mu_t = \rho_o C_\mu k^2/\varepsilon$ is the turbulent viscosity, $P' = P + 2\rho_o k/3 - \rho_o g_i x_i$ is the modified pressure, S_i and S_T are source terms. The model constants are given in Table 4.3.

Table 4.3 Constants for modelling natural convection using standard $k-\varepsilon$ model

C_μ	$C_{1\varepsilon}$	$C_{2\varepsilon}$	$C_{3\varepsilon}$	σ_k	σ_ε	σ_t
0.09	1.44	1.92	1.0	1.0	1.3	0.9

These equations and model constants are used in this research for modelling buoyancy-driven flows. By default, the buoyancy production term G_k is switched off by setting $C_{3\varepsilon}$ = 0. It should be used when thermal buoyancy

effects are present, otherwise the resulting fluid flow predicted by CFD might be physically non-realistic.

When applying the Boussinesq approximation for modelling buoyancy-driven flows the temperature variation ΔT of the fluid domain should not be larger than 30 ºC (Etheridge & Sandberg (1996)). Assuming density is constant may be inappropriate for large temperature variations. In building simulations, the temperature differences in air are usually small and the density variation can be ignored. Therefore the Boussinesq approximation is assumed to be sufficient.

4.6 Boundary conditions

The equations discussed above require boundary conditions in order to start the calculation. Boundary conditions are those conditions by which the nature of the physical problems is defined. After the initial conditions are assigned to these variables, CFD starts to calculate based on an iteration process to find numerical solutions. There are five types of boundary conditions used in this research: wall boundary, pressure boundary, porous medium boundary and symmetry boundary. These are explained in this section.

4.6.1 Wall boundary conditions

A solid wall boundary condition is one of the most common boundaries used in CFD especially for applications with enclosed fluid flow (e.g. building ventilation). Fluid is not allowed to flow across the wall boundary surface therefore a no-slip condition is specified on the boundary for the velocity components. By default in CFX, zero heat flux is specified on the wall boundary. However this can be overridden by setting a temperature or a heat flux for the energy conservation equation. When the grid system near a wall boundary is not fine enough to resolve the viscous layer of the wall, a wall-function is used to calculate the wall shear stress and the wall heat flux (or the wall temperature) when the wall temperature (or the wall heat flux) is specified.

Three layers can be developed when a fluid flows along a wall (Figure 4.1): a turbulent outer layer, a log-law layer and a viscous sub-layer.

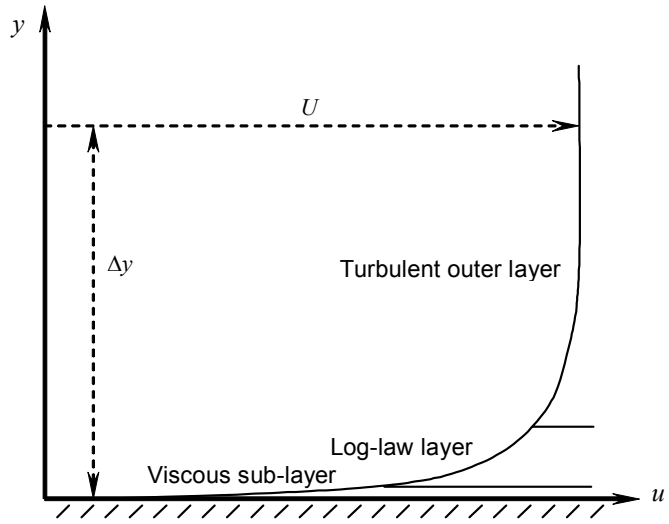

Figure 4.1 Fluid flow layers along a solid wall

In the turbulent outer layer (Figure 4.1), the flow is fully turbulent and the turbulence plays a major role in determining the flow properties. While in the 'viscous sub-layer', the flow is dominated by the molecular viscosity, and is almost laminar. Between these two layers, the effects of molecular viscosity and turbulence are of the same order. In CFD, the log-law layer and the viscous sub-layer are normally termed as the near wall region.

In the wall-function approach, empirical formulae are used to provide near-wall conditions for the mean flow and turbulence transport equations. The major advantage of this approach is that it saves considerable computing cost by avoiding the need to account for viscous effects in the turbulence models by using fine meshes. The logarithmic relation for the near wall tangential velocity U and the wall-shear-stress τ_w is given by (Patankar & Spalding (1967)):

$$u^+ = \frac{U}{u_\tau} = \frac{1}{\kappa}\log(E'y^+) \qquad \text{Eq (4.36)}$$

with, $y^+ = \rho \Delta y u_\tau / \mu$ and $u_\tau = (\tau_w / \rho)^{1/2}$ Eq (4.37a, b)

where u^+, U, u_τ, κ, y^+, E' and τ_w are the near wall velocity, the known tangential velocity at a distance of Δy (Figure 4.1), the friction velocity, the Von Karman constant, a log-layer constant depending on wall roughness and the wall shear stress, respectively.

For turbulent flows, τ_w is related to turbulent kinetic energy k by

$$\tau_w = \rho k C_\mu^{1/2} \qquad \text{Eq (4.38)}$$

Assuming y_o^+ is the cross-over point between the viscous sub-layer and the log-law layer, for $y^+ < y_o^+$, the viscous effects become significant and the velocity profile becomes linear, therefore $u^+ = y^+$; above the cross-over point ($y^+ > y_o^+$), the log-law of Eq (4.36) is used; when $y^+ = y_o^+$ Eq (4.36) gives $y_o^+ = \frac{1}{\kappa}\log(E' y_o^+)$. A value of y_o^+ =11.23 is calculated when E' and κ take values of 9.793 and 0.4187 for wall functions.

By employing wall functions, the first cell size above the wall boundary is very sensitive for the solution of the fluid flow. If the first cell is within the viscous sub-layer (say $y^+ \leq$ 5 to 10), the mesh is over refined for the wall functions; if the y^+ is over 300 (CFX4.4 Solver manual), the mesh is too coarse to resolve the near wall region. Approximately, when using the wall functions for turbulence modelling, y^+ values should normally be confined within the region of 11.23 $\leq y^+ \leq$ 150 to resolve the boundary (CFX4.4 Solver manual).

There are a number of limitations for wall functions and these have been reviewed by several researchers (e.g. Chen (1988), Yuan et al (1992)). Relevant corrections were made to improve the performance of the the wall functions. Chen (1998) introduced a logarithmic curve segment to represent the log-law layer and an extra curve segment is used in the range of 8 < y^+ <40. Yuan et al (1992) used a four layer model which incorporates the variation of turbulent Prandtl number with y^+.

4.6.2 Pressure boundary

Pressure boundaries are used in CFD for calculating the mass flow across a boundary where the detailed velocity distribution is unknown. It is possible to specify any part of the fluid domain boundary as a surface of known pressure.

- **Outflow through a pressure boundary**

When a pressure boundary experiences an outflow, a user-specified value is assigned to pressure; zero normal gradients are imposed on velocity; and zero normal gradients are also imposed on all other transported variables, such as k, ε, temperature and user scalars.

- **Inflow through a pressure boundary**

When a pressure boundary experiences an inflow, user-specified values are imposed on pressure and also on some transported variables, e.g. temperature for a non-isothemal flow, mass fractions for multi-component flow, user scalars, etc.; and zero normal gradients are imposed on velocity, turbulence quantities and Reynolds stresses, which is the same as the treatment for outflow.

When using pressure boundaries, some reference pressure has to be defined either by the user or the code. The pressures specified at the boundaries are pressures relative to the reference pressure. At the pressure boundaries (both inflow and outflow situations) the zero gradient condition of velocity leads to a fully developed flow, which may be inaccurate in presenting the real fluid flows where friction loses are involved across the boundaries, e.g. due to expansion or discharge. Care is needed to cope with these potential problems, which will be addressed in the following chapters (chapters 5 and 6).

4.6.3 Porous media boundary

A porous boundary is used to model fluid flows where the geometry is too complex to resolve with a grid, e.g. flows in rod or tube bundles. When using a porous media boundary both a generalisation of the N-S equations and of Darcy's law are used for flows in the porous region.

A porous media boundary is also used to achieve a pressure drop after a fluid flows through it. This depends on the velocities of the fluid flow and the porous media properties such as the volume porosity and the resistance constant. In CFD, the velocities are those calculated by the N-S equations, however, the volume porosity and the resistance need to be set by the user using the porosity tensor and the resistance tensor.

Discontinuities in porosity and resistance at porous boundary cause discontinuities in pressure and pressure gradient and this may lead to errors in CFD calculations. To allow efficient calculation of porous media flows in CFD, pressure gradients and all additional body forces are treated in a consistent fashion in the Rhie-Chow interpolation procedure (Rhie-Chow (1983)) and volume porosities are smoothed internally to ensure a monotonic change in velocity across a one-dimensional discontinuity in porosity.

4.6.4 Symmetry plane boundary

Symmetry plane boundaries are used when the fluid domain and all other boundaries are, in nature, symmetrical about some plane. Their use means that the computational cost is potentially reduced.

At a symmetry plane boundary, the velocity vectors normal to the symmetry plane are set to zero as well as the gradient of the tangential velocity component. The gradients normal to the symmetry boundary plane of all other scalar variables, such as p, T, k, ε, are specified to zero.

4.7 Solving the governing equations

The time-averaged governing equation set (Eqs (4.9 – 4.11)) together with turbulence modelling and boundary conditions are solved numerically by the CFD technique, in which a continuously-varying quantity is treated as an approximation of values at a finite number of points. The fluid domain of interest is divided into a large number of small cells and the transport equations are conserved within each cell. The differential equations (continuous) are converted into algebraic equations (discrete) and solved by an iteration process. After certain numerical criteria are achieved the iteration process is stopped. Details of the solution procedure are discussed in Appendix B.

4.8 CFD codes used in this research

The CFD codes, CFX4.4 and CFX5.6, were used in this research. All the steady state simulations were conducted using CFX4.4. The predictions of CFX4.4 are compared with both analytical and experimental data from the

literature (see chapter 2). For studying the flow development, time dependent simulations were carried out using CFX5.6.

CFX4.4 is a multiblock code in which geometries are defined using one or more topologically rectangular blocks. Each block is covered with a mesh and the governing equations are solved using the finite volume method (Versteeg and Malalasekera (1995)).

The coupled set of differential equations in CFX4.4 is solved in a segregated manner: starting with the existing solution or an initial guess to the flow field, each equation is solved sequentially. First, the U equation is solved, then V, then W and finally the pressure-correction mass flow equation. After solving the U equation, the value of U in the V equation is updated, and so on. When a full sweep of the equation set is completed, the code returns to the first equation since it knows nothing about the solution of other equations. These equations (momentum equations and mass conservation equation) are coupled equatioin set because the dependent variable in each equation appears as an independent variable in all of the others. The relative influence of one variable on the others will be dependent on the flow itself.

Instead of solving each equation sequentially, CFX5.6 assembles one large matrix for the entire set of the coupled equations and solves them simultaneously. All the equations are advanced together in time and there are no restrictions on the size of the time step due to its fully implicit solver technique. CFX5.6 also uses a multigridding system in which the solver does additional sweeps on coarser grids within each time step.

CFX4.4 and CFX5.6 are not the same CFD code with different versions. The terminologies and the solver techniques are different. It has been found that CFX5.6 experienced serious convergence difficulties of modelling buoyancy driven flow for the cases studied in this research, particularly when using the same mesh structure used in CFX4.4. Further discussions of CFX5.6 modelling will be addressed in Chapter 5.

4.9 Summary

This chapter has outlined the fundamental knowledge of numerical modelling in CFD, in which the fluid governing equations, turbulence modelling, natural ventilation modelling, Boussinesq approximation and boundary conditions are described in details. The turbulence modelling technique of CFD used to model natural and forced convection in building ventilation is also presented.

There is also a brief introduction of the different commercial CFD codes (CFX4.4 and CFX5.6). These two codes are fundamentally different in light of terminology, mesh structure and solver technique.

The RNG $k-\varepsilon$ model will be used for the development of the benchmark cases in the following chapters 5 & 6.

Chapter 5

CFD modelling of natural ventilation in an enclosure driven by wind & buoyancy

5. CFD modelling of natural ventilation in an enclosure driven by wind and buoyancy

This chapter focuses on the development of the first benchmark: the evaluation of CFD for predicting natural ventilation flows in an enclosure driven by combined wind and buoyancy forces. Two types of wind effects are considered in this chapter: assisting wind and opposing wind. In both situations the fluid dynamics has been restricted to steady-state displacement natural ventilation. In assisting wind cases, when the wind speed is sufficiently large, the vertical thermal plume breaks down and the plume theory is no longer applicable (Hunt & Linden (2001)); while in opposing wind cases, large wind speeds lead to a steady-state mixing flow (Hunt & Linden (2005)). These two situations are not included in this thesis for the development of the benchmark cases.

Section 5.1 gives the initial investigation using CFD. Two major difficulties are encountered using the guidance of Cook (1998) to investigate the first benchmark cases. Methods for solving these difficulties are addressed in this section. Details of simulation techniques are described in section 5.2. The analysis of the simulation results are presented in sections 5.3 and 5.4 in which CFD predictions (e.g. interface height, temperature gradient, mass flow rate) for both assisting wind and opposing wind cases are compared with the corresponding literatures of Hunt & Linden (2001, 2005). Section 5.5 depicts the validation of volume flow rate for assisting wind cases using the measurements from salt bath experiments. The internal stack pressure within the ventilated space is further examined in section 5.6. In section 6.7, CFX5.6 is used to investigate benchmark 1 cases and simulations are run in transient in order to study the development of the fluid flow in real time information. A summary is provided at the end of this chapter.

5.1 Initial investigation using CFD

Based on the analytical models and experimental studies by Hunt & Linden (2001, 2005) a simple geometry of the fluid flow of interest was defined for CFD simulations (Figure 5.1). The defined computing geometry is ten times greater than the perspex box used in the experiments. The flow inside the

enclosure in practice is influenced by conduction, convection, radiation. In this research, conductive and radiation effects were neglected in order to match the assumptions made in the analytical and experimental work.

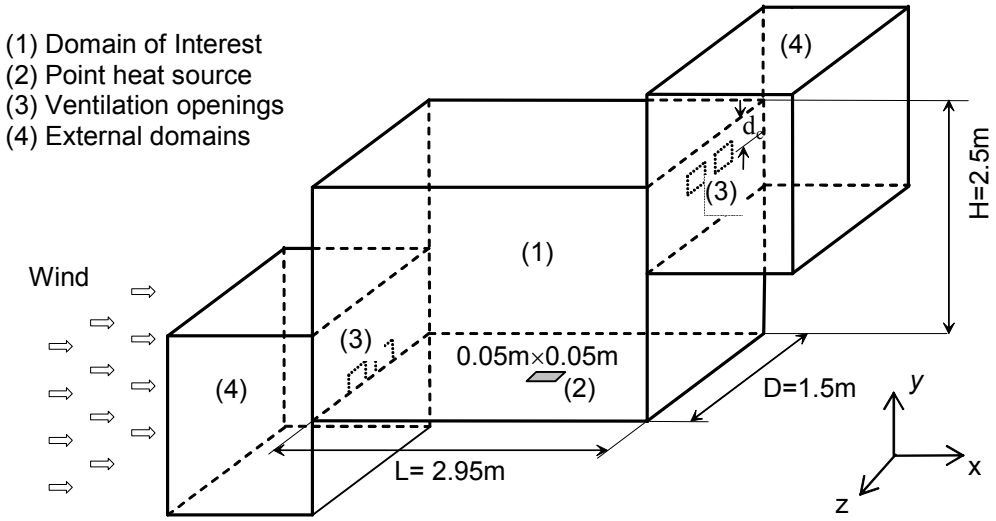

Figure 5.1 Initial CFD geometry of Benchmark 1

5.1.1 Consideration of boundary conditions

In CFX4.4, the heat source can be modelled as a wall type boundary condition with a constant heat flux. The geometry is symmetrical along a plane through the middle of the box; therefore, a symmetry boundary can be applied there. For cases in which one inlet and one outlet is used each will be located in the middle of the z direction, hence the symmetry plane boundary is still applicable (section 5.2.8). Setting boundary conditions on the ventilation openings is one of the most difficult tasks for modelling natural ventilation flows using CFD (Cook & Lomas 1998). In practice, when air flows through a ventilation opening, complex flow features (e.g. contraction and expansion) are observed. In order to avoid setting boundary conditions on the ventilation openings explicitly, some external fluid domain can be modelled (e.g. Cook & Lomas (1997). Using this approach the CFD predictions agreed favourably with the analytical and experimental work of Linden et al (1990). However, as shown in Chapter 3, the ventilation openings in this research are located in the side walls of the fluid domain, whilst for the work of Cook & Lomas they were located in the base and top of the domain. Consequently, the direction of the

incoming momentum into the domain is different. In this work, the incoming momentum is perpendicular to the vertical thermal plume, whilst the incoming momentum of Cook & Lomas (1997, 1998) was parallel to the thermal plume. It has been found in this research that the direction of the incoming momentum has a great influence on the behaviour the thermal plume.

For the initial simulations, external domains were used on both sides of the domain of interest following the guidelines of Cook & Lomas (1997). Pressure boundaries were set on the windward and leeward of the external domains. This pressure is relative to some reference pressure, normally 1.0 atm. When the airflow of the domain is driven purely by buoyancy, the relative pressure on the pressure boundary is set to zero. When wind effects are present, the relative pressure difference between the windward and leeward is assumed to be the same as the pressure drop induced by the incoming wind (Hunt & Linden (2001, 2005)).

5.1.2 Difficulties encountered

The air speed distribution and the temperature field predicted by the CFD model for buoyancy alone are shown in Figure 5.2. It can be seen that the CFD results produced using these boundary condition settings do not agree with the results of the analytical and experimental studies (chapters 2 and 3). Firstly, the vertical thermal plume has not been predicted but has been deflected by the incoming air. Secondly, the stratification was not established as assumed in the analytical model. When assisting wind effects were introduced (not shown here), there was an additional pressure drop between the windward and leeward openings, which led to an even stronger horizontal momentum force and the plume was eventually deflected to the floor.

From these initial simulation results (Figure 5.2), the first challenge encountered was: how to maintain a vertical thermal plume to meet the assumption. In the corresponding salt bath experiments (Figure 3.2), a perforated plate was used midway between the inlet opening and the plume in order to reduce the influence of the horizontal momentum. A similar measure was therefore considered in the CFD model.

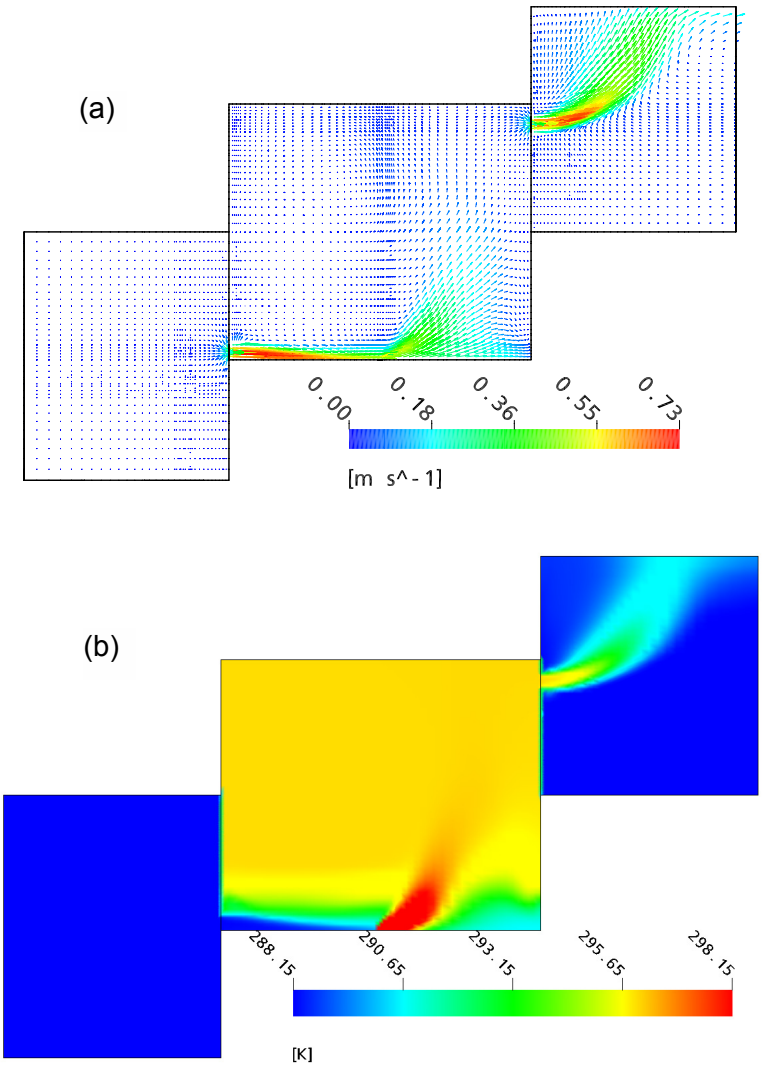

Figure 5.2 (a) Speed vectors and (b) temperatures on the symmetry plane of the flow field for buoyancy alone.

The second challenge was how to account for the pressure losses at the ventilation inlets and outlets economically. The aim of using external fluid domain by Cook & Lomas (1997, 1998) was to avoid setting pressure boundary conditions at the ventilation openings directly. Instead the pressure boundaries were set on the external domains to simulate a steady infinite environment for the flow field. The physical behaviours of the flow through openings (contraction and expansion) were taken into account by CFD automatically. Although this approach was successful in the cases studied by Cook & Lomas (1997, 1998) there are a number of uncertainties when applying this approach in a generic way.

Firstly, substantial effort is necessary to model external domains. For example, how big the exterior space should be modelled to meet the 'infinite environment' criteria and what will be the expected accuracy. Secondly, recent experimental studies have shown that the discharge coefficients can not be treated as constant when a density change is present across the ventilation openings (Hunt & Holford (2000), Holford & Hunt (2001)). Thirdly, all the ventilation openings are located on walls of the domain. The numerical calculation across the ventilation openings needs to reflect the physical processes of contraction and expansion therefore 'wall functions' applied on walls surrounding the openings play an important role for modelling these effects accurately. However, wall functions are mesh sensitive and dependent on first cell heights along the wall as discussed in chapter 4. Potentially, more investigations are needed beforehand to make sure CFD does account the loss coefficients accurately at the ventilation openings when using external domains.

5.1.3 Solving the major difficulties

5.1.3.1 Methods for maintaining a vertical thermal plume

As mentioned in section 5.1.2, in order to maintain a vertically descending brine plume in water a perforated plate was used. For the CFD simulations a similar method was used in which a piece of perforated wall was used to simulation the perforated plate (Figure 5.3).

The simulation result in Figure 5.3b showed that this method was able to reduce the horizontal momentum generated by the incoming air and maintained a vertical buoyant thermal plume. However, there are a few limitations of this method. It is very labour-intensive to define and is not universal for the different cases studied in this work. When boundary conditions were changed, e.g. wind speeds, source strengths, ventilation opening sizes, the density of the small wall patches and holes in the surface plate had to be rearranged in order to block the horizontal momentum sufficiently.

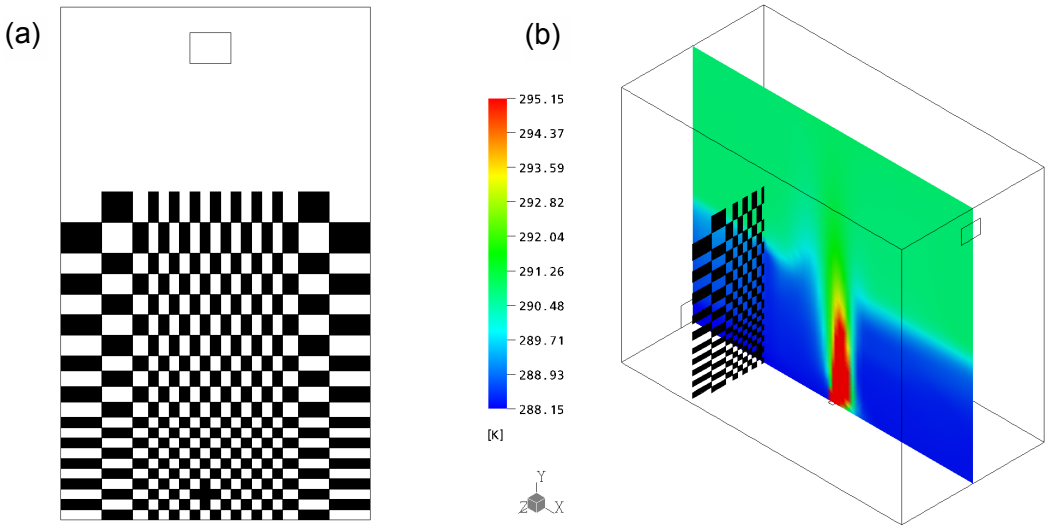

Figure 5.3 (a) The front view of the perforated wall and (b) the temperature contour of the domain.

An alternative was to use a porous medium boundary in the same way as the perforated plate used (see section 5.2.1, Figure 5.4). Such a boundary (described in section 4.6.3) can be used to achieve a pressure drop, absorb the horizontal momentum and maintain the vertical thermal plume. It has been found (e.g. Cook et al (2003), Ji (2004)) that using a porous medium boundary to simulate the perforated plate used in the salt bath experiments is robust. Therefore, the porous medium boundary was used for the development of the benchmark cases in this research.

5.1.3.2 Modelling flow losses at ventilation openings

In practice, when air flows through a ventilation orifice it experiences the physical processes of contraction and expansion. The effect of these processes was treated using loss coefficients (constants) at ventilation openings in section 2.2.4.1. Recall equation 2.15, assuming inlet and outlet openings have the same area, determined by:

$$a_{in} = a_{out} = A^* \sqrt{(C_e + C_D^2)/2C_e C_D^2} \qquad \text{Eq (5.1)}$$

where A^* is the effective opening area; and C_e and C_D are the loss coefficients due to expansion and discharge.

This is the equation for calculating the opening sizes used in the analytical model and salt bath experiments. Hunt & Linden (2001) used C_e =0.5 and C_D =0.6 as the loss coefficients at inlet and outlet openings respectively. Using Eq (5.1) the ventilation opening sizes a_{in} and a_{out} can be calculated. The presence of these loss coefficients contributes to a reduction of volume flow rate through the ventilation space (Nakayama & Boucher (1999), page 67).

External fluid domains could be used in order to account the loss coefficients at ventilation openings. However, whether the CFD can account these coefficients accurately or not is still an uncertainty (section 5.1.2).

The pressure boundary conditions in CFD impose zero normal gradients (Neumann boundary conditions) on velocity as well as other transported variables on the boundary (section 4.6.2). If pressure boundary conditions are applied directly onto the ventilation openings, the contraction and expansion processes do not take place and the reduction of volume flow rates does not occur. Therefore the loss coefficients at the ventilation openings in CFD simulations where pressure boundaries are used can be considered as unity and the ventilation opening sizes in the CFD simulations are given by Eq (5.1) with C_e = C_D = 1.0, i.e.

$$a_{in} = a_{out} = A^* \qquad \text{Eq (5.2)}$$

For the same effective opening area A^*, equations 5.1 and 5.2 provide different physical opening sizes for a_{in} and a_{out}: Eq (5.1) gives an 'exact' opening size for analytical and experimental work, while Eq (5.2) gives a 'reduced' opening size for CFD simulations when the pressure boundary conditions are applied directly onto the ventilation openings. For the calculation of both 'exact' and 'reduced' opening sizes, the effective opening area A^* is remained identical while using different values for the loss coefficients.

A number of simulations were carried out to verify mass flow rates through the ventilated space in order to select an applicable method (table 5.1).

Table 5.1 CFD calculated mass flow rates using different modelling methods

Fr.	opening size	location of pressure boundary	CFD: Mass flow rate (kg/s)	Analytical: Mass flow rate (kg/s)
0	Exact	External domain	1.43×10^{-2}	1.51×10^{-2}
0	Exact	openings	1.90×10^{-2}	
0	Reduced	openings	1.56×10^{-2}	
9	Exact	External domain	2.75×10^{-2}	2.65×10^{-2}
9	Exact	openings	3.72×10^{-2}	
9	Reduced	openings	2.66×10^{-2}	

From the comparisons in table 5.1, it was concluded that using the 'reduced' opening size method for CFD simulations compares more favourably with the analytical model than the other methods. The mass flow rate was considerably over-predicted when applying pressure boundary on the ventilation opening with 'exact' size. The method of using 'exact' opening size and an external domain also agreed reasonably well with the analytical calculations. However, this technique increases CPU computing time and can be case dependent due to the variation of density (Hunt & Holford (2000)).

5.2 Simulation techniques for Benchmark 1

5.2.1 Definition of Benchmark 1

The proposed method for modelling natural ventilation flow in a single space driven by combined wind and buoyancy is shown in figure 5.4.

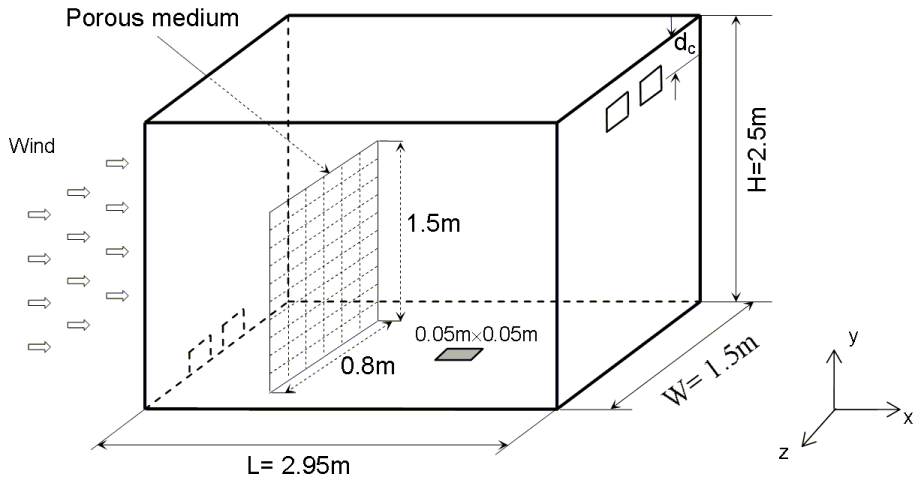

Figure 5.4 Geometry of CFD model

The geometry is representative of a small office space. The aspect ratios of the space are identical to the perspex box used in the salt bath experiments of Hunt & Linden (2001) although the scale is a factor of 10 greater. Openings of equal area were symmetrically located in the windward and leeward faces midway between the front and back faces of the space. The heat source is located in the centre of the floor. The porous medium is located midway between the windward openings and the heat source. As discussed in section 5.1, the porous medium (thickness 0.05m) is used here to reduce the horizontal momentum of the inflowing jet of air through the windward openings and ensure that the buoyant plume remains upright. This reflects the method used in the salt bath experiments of Hunt & Linden (2001) in which a perforated plate was applied in the same way. In real buildings, similar devices may be used in order to reduce draughts.

5.2.2 Mesh structure

The structured mesh shown in Figure 5.5 was generated by Meshbuild of CFX4.4. The cells of the mesh are non-uniform. Denser grids were arranged near the solid walls and the position of the anticipated vertical thermal plume in order to account for the large gradients of variables.

A mesh dependency test is necessary before presenting results produced by CFD. Whether the numerical modelling using CFD represents the real physics of the fluid flow or not depends on the numerical consistency. Details of the mesh dependence test are addressed in section 5.2.7.

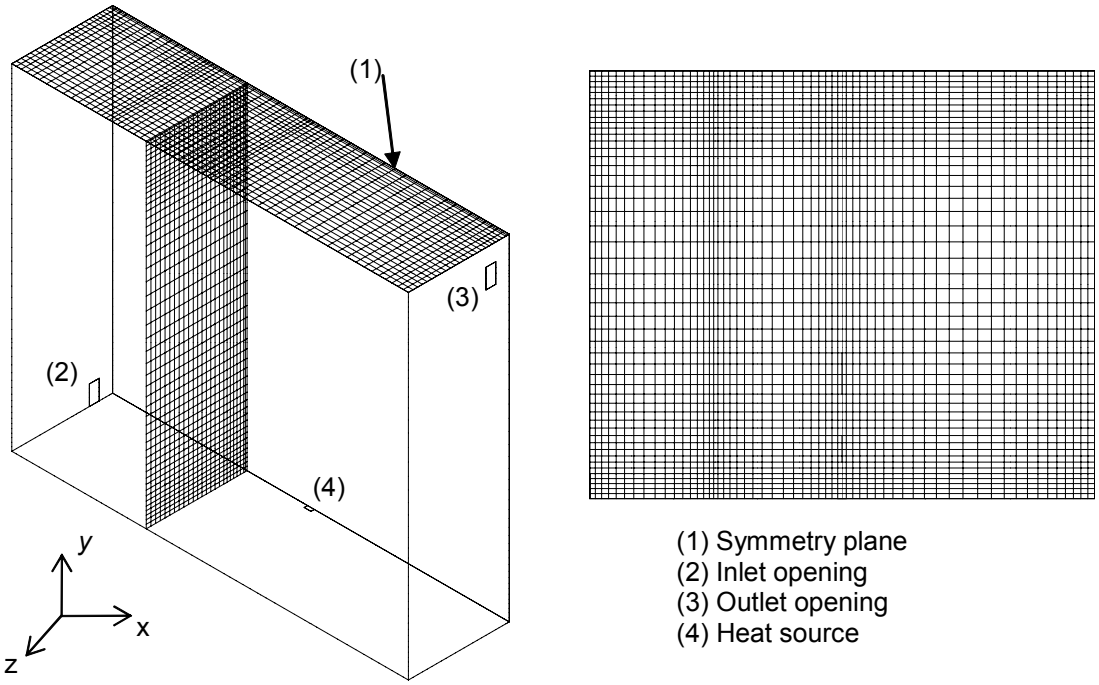

Figure 5.5 Typical mesh structure used for simulations of Benchmark 1. Left, half of the full domain, 3-D view; right, mesh on the symmetry plane, front view.

5.2.3 Details of boundary conditions

An initial investigation of boundary conditions was discussed in section 5.1, the following are the details of these boundary conditions based on the geometry discussed in section 5.2.1 (Figure 5.4).

- WALL boundary conditions

The ceiling, the floor (except the heat source) and the side walls of the enclosure were modelled as WALL type boundaries with a “no slip” condition and zero heat flux. The heat source was also modelled as a WALL type boundary but with a constant heat flux. Unreasonably high temperatures (over a thousand degree C) were predicted close to the heat source. In theory it is the nature of modelling a ‘point’ heat source for a given heat output, say 100W. A high temperature on the heat source is expected in order to achieve the required amount of heat being released into the ventilated space. Specifying a constant temperature on the heat source patch instead of a heat flux can be an alternative. However, it is difficult to define how high the temperature is in order to give the same heat output based on the given buoyancy flux of the

analytical models. The advantage for setting heat fluxes on the heat patch is that the heat flux values can be converted into buoyancy flux directly using Eq (2.20).

- Pressure boundary conditions

Section 5.1.3.2 gives a method to set pressure boundary conditions directly onto the ventilation openings. This pressure (P, a variable of the expression for the modified pressure P', Eq (4.30)) in CFX is a relative pressure to some reference pressure P_{ref}. For buoyant flows using Boussinesq approximation P_{ref} is set to be 0.0 Pa. This is used to avoid round off errors due to the weak driving forces produced by natural sources (e.g. the pressure difference produced by thermal buoyancy is only in the order of 1.0 Pa). For compressible flows, P_{ref} is set to be 1.013 x 10^5 Pa and it is used to avoid numerical errors caused by subtracting two large numbers, when computing pressure gradient (CFX4.4 (2001), Solver manual).

For buoyancy alone cases, the relative pressure P at pressure boundaries is set to be 0 Pa. The hydrostatic pressure difference along the vertical distance between windward and leeward openings is automatically taken into account by the governing equations (Eq (4.30)). When the driving forces are buoyancy combined with wind, a pressure drop (ΔP (Pa)) is induced by wind between the ventilation openings. This pressure drop is divided in terms of the pressure coefficients at the windward and leeward sides. For example, the pressure coefficients used in Hunt & Linden (2001) were 0.7 (for windward side) and -0.2 (for leeward side). The relative pressures on the pressure boundaries would be $(7/9)\times \Delta P$ (for windward) and -$(2/9)\times \Delta P$ (for leeward).

- Porous medium boundary conditions

Two main parameters for porous medium boundaries are needed: the volume porosity and the resistance constants. The volume porosity γ at a point is the ratio of the volume V' available to flow in an infinitesimal control cell surrounding the point and the physical volume V of the cell ($\gamma = V'/V$, CFX4.4 (2001), Solver manual). The resistance constant (kg/m^{3}s) represents

a resistance to flow in the porous medium based on the physical properties of the porous medium. It is part of the body force in equation 4.2.

Three zones of porous medium were used in the CFD simulations in this work (Figure 5.4). The first zone was from the floor to the height of the inlet ventilation openings. The second zone was from the top of the inlet ventilation openings to 0.7m and the third lay between 0.7m and 1.5m. The same volume porosity of 0.5 was set for all three regions while the resistances were set differently. High resistance was used for the lower region in order to combat the strong horizontal momentum, and lower resistances were used for the second and third zones.

- Symmetry plane boundary

At a symmetry plane, all variables are mathematically symmetrical. In this work, a symmetry plane was used in the $x-y$ plane bisecting the heat source (Figure 5.4). The symmetry plane boundary was not used when investigating the opening strategies due to the asymmetric nature of the openings (see section 5.3.6).

5.2.4 Initial conditions and fluid properties

The initial condition for temperature of the domain was set to be the ambient temperature (288.15K). This ensures that there were no temperature differences inside and outside of the domain. The ambient temperature ensures the incoming air temperature from the windward openings was always at 288.15K. The domain temperature was varied due to the heat input of the point heat source and the ventilation flow through the fluid domain.

The air properties (such as density ρ, viscosity μ, specific heat c_p, conductivity λ, thermal expansion coefficient β) were calculated by CFX based on a standard fluid reference temperature. The standard fluid reference temperature should reflect the average of the domain temperature which was related to the strength of the heat source and the ventilation flow rate. For example, when the standard air temperature is set 2K higher than the ambient temperature, the corresponding air properties are: ρ =1.221 Kg/m^3;

μ =1.798$\times$10^{-5} Kg/ms; c_p =1004 J/KgK; λ =2.54$\times$10^{-2} W/mK; β =3.414$\times$10^{-3} K^{-1}.

For buoyant flows, T_o in Eq (4.28) is the buoyancy reference temperature and T is the temperature of fluid domain. The difference between these two temperatures reflects the strength of the buoyancy force in the domain. With the same stack height, an increase of the temperature difference will cause an increase in the buoyancy driving force. In practice, the temperature difference of the domain temperature and the ambient temperature reflects the magnitude of the stack effects. Therefore the buoyancy reference temperature in this work needs to be set the same as ambient temperature so that no artificial buoyancy forces are generated.

The enthalpy reference temperature in CFX4.4 is used to specify a temperature at which the static enthalpy is zero. A value of 288.15K (the same as the ambient temperature) was used throughout the work in this thesis.

Zero velocity fields for the three momentum equations are set by the CFX automatically as the initial condition for its iteration processes.

5.2.5 Convergence criteria

A non-dimensional ratio of the mass residual and the total rate of mass flow through all inlet boundaries can normally be used to judge convergence. However this is not applicable for buoyancy-driven flows here because inlet boundaries were not used. In buoyancy-driven flows, accurate solution of the enthalpy equation is often found to be important (CFX4 2001). For benchmark 1 cases the airflow is driven by combined forces of wind and buoyancy. However, the displacement mode ventilation is considered by which thermal buoyancy within the ventilated space is dominating the airflow pattern. Considering the importance of the enthalpy changes within the domain due to the temperature changes, the following two convergence criteria were used: (i) the enthalpy residual is less than 1% of the total heat entering the domain; and (ii) the absolute values of all variables at the monitoring point should not change by more than 0.1% for the last 100 iterations. The enthalpy residual is not dimensionless. It is the sum of the absolute values of the net energy fluxes

into or out of every cell in the flow, thus it has the dimensions of Watt. The first criterion gives a reasonable non-dimensionalisation by comparing the enthalpy residual with the total energy into the computing domain. The second criterion reflects the stability of the system and the absolute values of all the variables are sensitive to the location of the monitoring point. Normally the monitoring is set downstream of the flow system. The criteria used in this work are the same as used by Chen & Srebric (2002), Cook et al (2003) and Ji (2004).

5.2.6 Solution techniques

Whether the solution of a CFD simulation represents a real physical flow phenomenon depend on many factors. The most important of which is probably the boundary conditions (section 5.2.3). Meeting the convergence criteria is also important when using CFD. If the solution does not converge, the results would most likely be non-realistic. However, even converged solutions can be non-realistic if inappropriate boundary conditions are used. Another concern of numerical methods is the numerical consistency (section 5.2.7). For example, the stability of the solution needs to be tested for mesh dependency, tighter convergence criteria, etc. This is particularly true when modelling buoyancy-driven airflows because of the difficulties of convergence due to small driving forces in the system (Symons & Peck (1984), Cook & Lomas (1997, 1998) and Cook et al (2003)).

If a solution exists and appropriate boundary conditions have been applied, the convergence of the system will be governed purely by numerical methods, such as solver techniques (segregated solver or coupled solver, explicit or implicit, see section 4.8 for details), differencing schemes, velocity-pressure coupling algorithms, under-relaxation factors, false time steps, etc. Differencing schemes are methods used to discretise the governing equations and convert the partial differential equations into algebraic equations which can be solved by either a segregated solver or a coupled solver. In this work, the central differencing scheme for mass conservation equation and the hybrid differencing scheme for all other transport equations were applied initially. The details of differencing schemes are addressed in Appendix B. Velocity-

pressure coupling algorithms are used to update pressure and correct velocity components for continuity. The algorithm of SIMPLEC was used in this research (Appendix B).

Under-relaxation factors (URF) in the rage of 0<URF<1 are used to scale the coefficient for the variables of the transport equations. This reduces the amount by which a variable changes and therefore helps to stabilise the solution. The smaller this factor is chosen to be, the more under-relaxation is employed. In this work, many combinations of URF have been investigated in order to get the solutions converged. However, the convergence could not be achieved for buoyancy-driven or buoyancy combined with wind-driven flows studied in this research by merely using under-relaxation factors. False time steps were needed to assist the convergence.

False time steps (FTS) are an alternative method of under-relaxing the transport equations. Using FTS the equations are modified in the same ways as URF if each outer-iteration is a time step, with two differences: the 'old' time values used are the most recently calculated values of each of the variables; and the time increment may be chosen arbitrarily to achieve the best convergence rate. This procedure may also be applied at each (true) time step of a transient calculation, in which case the equations are modified twice. Different false time steps can be used to accelerate each equation independently. These time steps should reflect the time scale over which each variable changes. Then every variable develops at its own optimum rate. The main drawback of false time stepping is that a knowledge of time scales is required. Cook (1998) investigated the false time scale of purely buoyancy-drive flows in a rectangular box with openings connected to the exterior. Results obtained using default under-relaxation factors and no false time-stepping were used to calculate a suitable time-scale. This approach was adopted in this research. It has been found that false time stepping is useful to assist convergence, particularly when several separate influences are driving the flow, e.g. flows driven by wind combined with buoyancy. Throughout this research, false time stepping was used to under-relax the three momentum equations, and the false time scale used was of the order of 0.01s. A typical converged history is show in Figure 5.6.

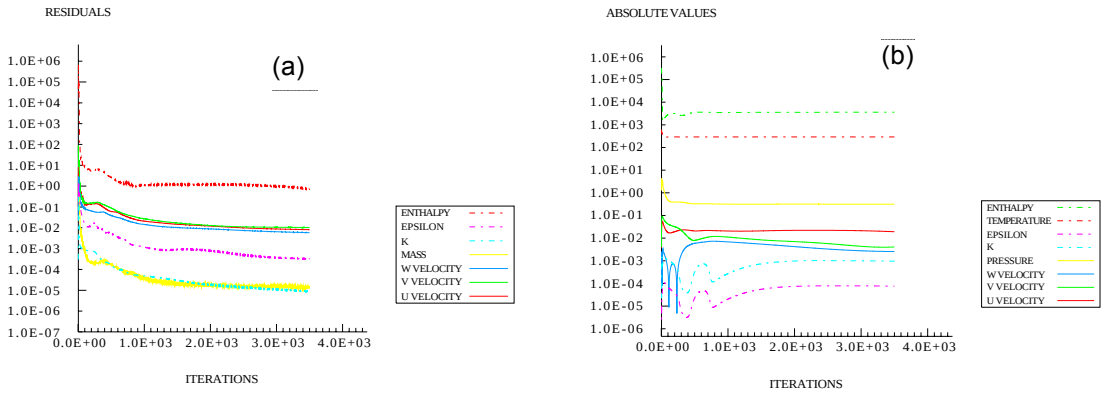

Figure 5.6 Typical convergence history of benchmark 1 (a) Residuals of variables and (b) Absolute values of variables

5.2.7 Mesh dependency test

A mesh dependency test was conducted in order to test the numerical consistency of the proposed numerical methods. Three mesh densities were used, Mesh1 (40k cells), Mesh2 (75K) and Mesh3 (145K). A typical mesh structure of Mesh2 for benchmark 1 is shown in Figure 5.5.

Grid refinement was carried out by increasing mesh density from Mesh1. Simulation conditions for the case selected here were: 100 watts heat input, total dimensionless effective opening area A^*/H^2 =3.4×10^{-3}, Fr =4.2.

The three computed mean velocities at x/L =0.5, y/H =0.5 and temperature profiles at x =2.5m (see Figure 5.4) are compared in Figure 5.7. The comparison showed that increasing the resolution did not lead to a significant difference and improvement for the mean velocities at different locations (Figure 5.7a), while the temperature profiles showed a relatively large difference between Mesh1 and Mesh3. Further examination of the mass flow rates through the space showed 5.0% difference between Mesh1 and Mesh3, 1.0% difference between Mesh2 and Mesh3. Considering both accuracy and CPU computing time, Mesh 2 was used for the development of Benchmark 1*.

* For a given CFD code the CPU computing time depends on the hardware and the cell numbers of the computing domain.

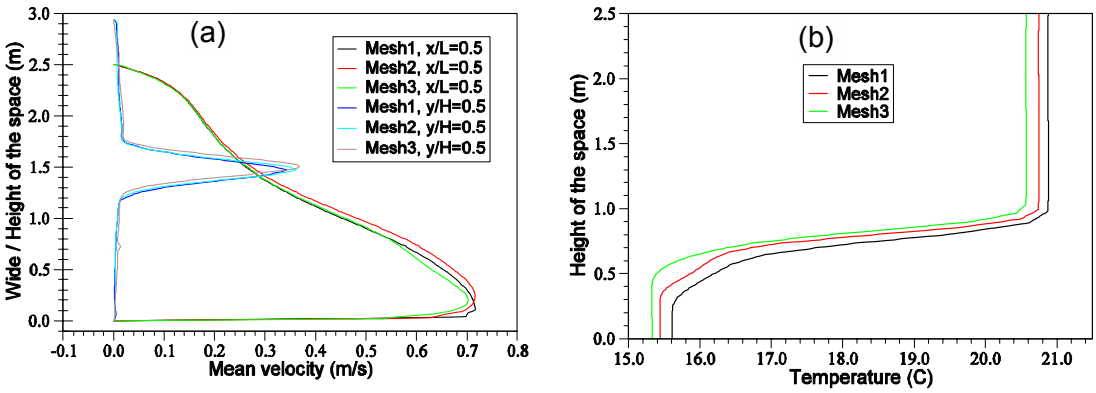

Figure 5.7 (a) Mean velocities at different locations (x/L=0.5 and y/H=0.5) and (b) temperature profile at x=2.5m

5.2.8 Simulation conditions

In order to demonstrate the capability of CFD for modelling the natural ventilation flows studied by Hunt & Linden (2001, 2005) simulations for varying wind speeds, dimensionless effective opening areas and heat source strengths were conducted for both assisting and opposing wind cases. The details of the simulation cases are shown in tables 5.2 ~ 5.4 (assisting wind), and tables 5.5 ~ 5.7 (opposing wind). The running conditions and together with these simulation cases are summarised in Appendix D.

The pressure drop Δ in the following tables are induced by wind, the relationship between the two is $\Delta = \rho U_w^2 (C_{pw} - C_{pl})/2$.

Table 5.2: Simulation conditions for varying Froude number (Fr) - assisting wind

Operating conditions for all cases	U_w (m/s)	Δ (Pa)	Fr
E =100 W	0.0	0.0	0.0
	0.47	0.12	3.0
(B = 2.75×10^{-3} m^{4}s^{-3} by equation 2.18)	0.93	0.47	6.0
	1.39	1.06	9.0
A^*/H^2 =3.4×10^{-3}	1.55	1.31	10.0
	1.85	1.88	12.0

Table 5.3: Simulation conditions for varying A^*/H^2 - assisting wind

Operating conditions for all cases	A^* (m^2)	A^*/H^2 ($\times10^{-2}$)
E =100 W, U_w =0.65m/s	0.025	0.4
	0.0375	0.6
(B = 2.75$\times10^{-3}$ m^{4}s^{-3} by equation 2.18)	0.050	0.8
	0.0625	1.0
Δ =0.23 Pa, Fr =4.2 (by equation 2.17)	0.075	1.2
	0.0875	1.4

Table 5.4: Simulation conditions for varying source strength E - assisting wind

Operating conditions for all cases	E (W)	B ($\times10^{-3}$ m^{4}s^{-3})	Fr
	5	0.1375	11.4
	20	0.55	7.18
Δ =0.23 Pa, U_w =0.65m/s	50	1.375	5.29
	75	2.0625	4.62
A^*/H^2 =3.4$\times10^{-3}$	100	2.75	4.20
	150	4.125	3.67
	500	13.50	2.45
	2000	55.0	1.55

Table 5.5: Simulation conditions for varying Froude number (Fr) - opposing wind

Operating conditions for all cases	U_w (m/s)	Δ (Pa)	Fr
E =100 W	0.0	0.00	0.0
	0.31	0.053	2.0
B = 2.75$\times10^{-3}$ m^{4}s^{-3}	0.47	0.120	3.0
	0.62	0.213	4.0
A^*/H^2 =2.05$\times10^{-2}$ and 1.23$\times10^{-2}$	0.78	0.334	5.0

Table 5.6: Simulation conditions for varying A^*/H^2 - opposing wind

Operating conditions for all cases	A^* (m^2)	A^*/H^2 ($\times10^{-2}$)
E =100 W, U_w =0.545m/s	0.020	0.32
	0.045	0.72
(B = 2.75$\times10^{-3}$ m^{4}s^{-3} by equation 2.18)	0.080	1.28
	0.097	1.55
Δ =0.1634 Pa, Fr = 3.5 (by equation 2.17)	0.125	2.00

Table 5.7: Simulation conditions for varying source strength E - opposing wind

Operating conditions for all cases	E (W)	B ($\times 10^{-3}$ m^4s^{-3})	Fr
Δ=0.1634 Pa, U_w=0.545m/s A^*/H^2=1.23$\times 10^{-2}$	50	1.375	4.45
	75	2.06	3.89
	100	2.75	3.50
	150	4.125	3.01
	200	5.50	2.80

5.3 Analysis of results for assisting wind

Table 5.8 shows a summary of the analytical analysis of section 2.2.4.1. Salt bath experiments have been used to validate these analytical predictions.

Table 5.8: Qualitative summary of analytical analysis of Hunt & Linden (2001)

Conditions	results		
	h/H (Eq 2.16)	g'/G'_H (Eq 2.21)	Q (Eq 2.12)
Increase Fr	increase	decrease	increase
Increase A^*/H^2	increase	decrease	increase
Δ=constant, increase E	decrease	increase	increase

Note: Details of these parameters can be found in section 2.2.4.1.

The quantitative comparisons between CFD predictions and the analytical models are made in the following sections (5.3.4, 5.3.5, 5.3.6).

5.3.1 Flow field discussion

The resulting speed vector field (Figure 5.8a) shows the rising plume from the heat source as assumed by the analytical model and observed by salt bath experiments (Hunt & Linden (2001)). The plume entrains the surrounding air as it rises and increases in width. This process forms a layer of warm, buoyant air in the upper region of the space and stratifies the flow field causing an interface which separates the warm, buoyant air above and the cool, ambient air below (Figure 5.9).

From Figure 5.8a, the position of the interface can be identified by the height at which there is least vertical motion outside the plume, and is accompanied by a sharp change in temperature. This bears out the analytical assumption

which assumes that the net transport of warm and cool air across the interface outside of the plume is zero. The cool, ambient air in the fluid domain is warmed up and transported to the upper region by the plume only. A steady state of this flow was achieved when the volume flow in the plume at the interface height is equal to the volume flow through the space.

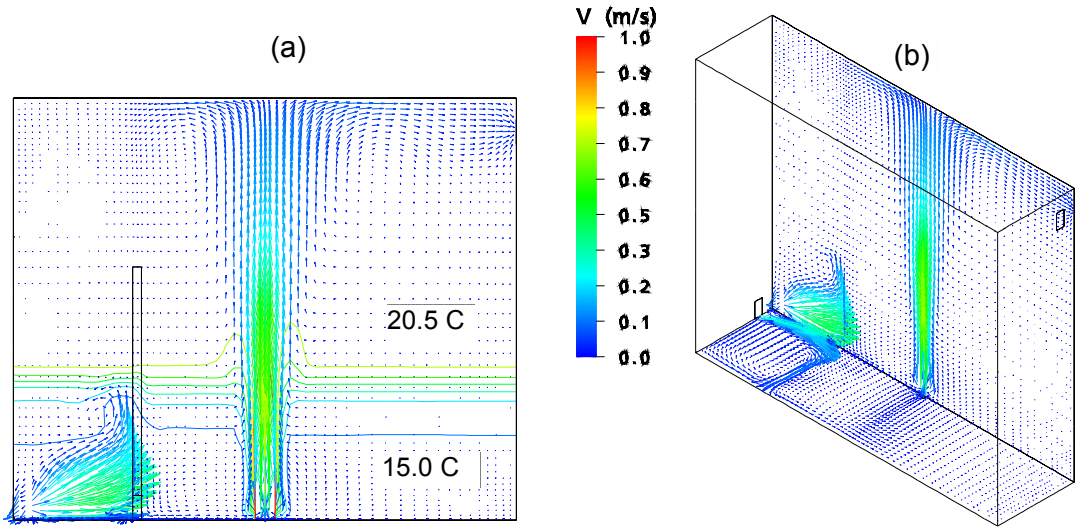

Figure 5.8 Typical speed vectors of the domain, (a) section view, (b) 3-D view.

Figure 5.8 also shows that the incoming air from the low level opening generates a strong horizontal momentum flow. This momentum is partially blocked by the porous medium midway between the inlet opening and the heat source, which can be seen by a sudden change (in both speed and direction) of the speed vectors at this point. After the porous medium the air speed is reduced. Although the air surrounding the heat source is still anisotropic, it has little effect on the plume after the porous medium because the heat source generates a relatively stronger vertical momentum flow. This vertical momentum flow entrains its surrounding air and dominates the flow field and forms the stratification (Figure 5.9).

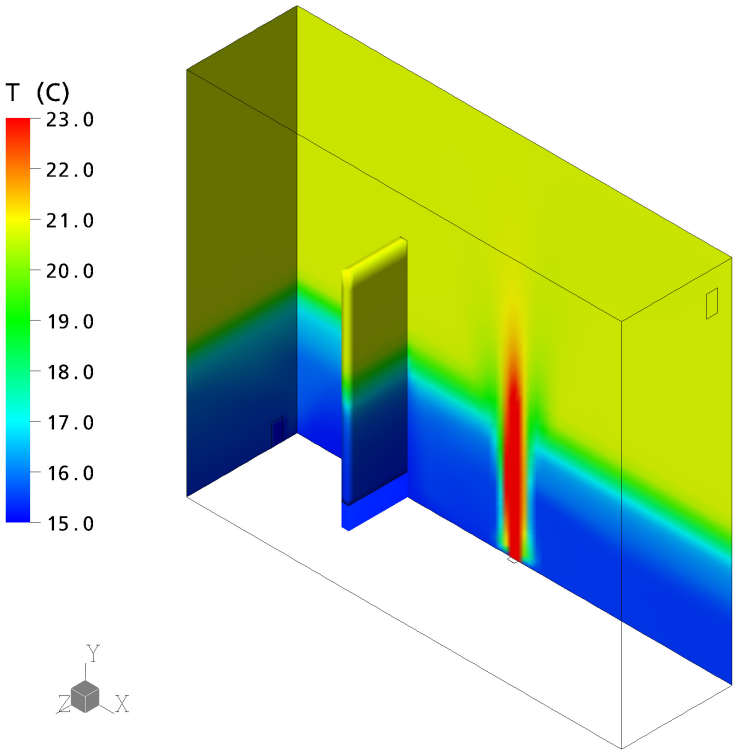

Figure 5.9 Typical temperature field, half of the domain is shown here

The temperature plots (Figure 5.10a and b) of purely buoyancy-driven flow and buoyancy-combined with wind-driven flow compare favourably with the density profiles of the salt bath experiments (Figure 3.2). The stratifications are clearly shown in these figures indicating that sharp interfaces were established. A lower interface and a higher temperature change (density contrast for salt bath experiments) across the interface was observed for purely buoyancy-driven flow (Figure 5.10a) compared with buoyancy combined with assisting wind (Figure 5.10b). The qualitative comparison of the two cases showed that the ventilation flow was enhanced and the temperature change across interface was reduced due to the presence of wind effects. Here the porous medium sufficiently avoided the impingement effect from the incoming horizontal momentum and the uprising thermal plumes were maintained. The images from the salt bath experiments showed some deflection of the brine plume due to the motion of fresh water used to simulate wind effects (Figure 3.2) which may indicate that the shielding effect of the perforated plate used in the experiments was insufficient.

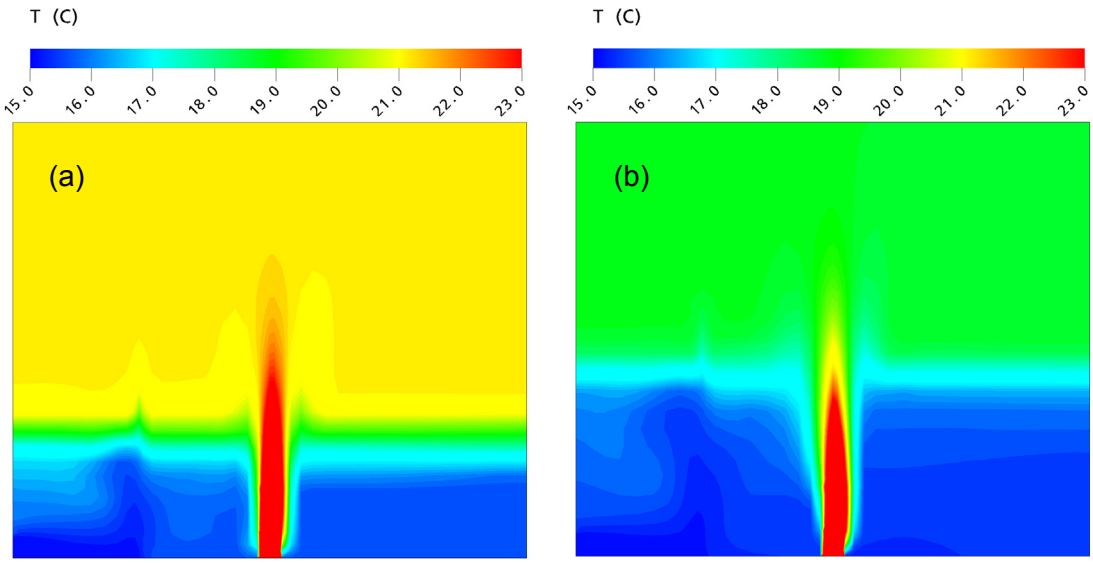

Figure 5.10 Temperature plots for (a) purely buoyancy-driven flow (Fr=0) and (b) buoyancy-combined with wind-driven flow (Fr=9)

5.3.2 Temperature gradient in the domain

In order to examine the details of the temperature gradient within the domain the values of temperature at different locations were plotted. Figure 5.11 shows the temperatures along different vertical (a) and horizontal (b) lines on the symmetry plane.

An almost constant temperature was predicted by the CFD model above the interface which bears out the assumption of the analytical model. However, this is not the case for the layer below the interface. The temperature field below the interface was slightly above the ambient temperature (Figure 5.11a), which contradicts one of the fundamental assumptions of the analytical model which assumes a uniform temperature below the interface (equal to ambient temperature). This discrepancy may be caused by the diffusion of heat in air in CFD calculations. For solving the governing equations of fluid flows, the diffusion term is always included (Eq (4.4)). While in the analytical model only natural convection was considered. Below the interface the thermal plume in CFD simulations may be warming its surrounding air due to the diffusion of heat. Furthermore, the existence of the porous medium also had some effects on the temperature distribution below the interface. For example, a small temperature change can be seen across the porous medium (Figure 5.11b).

The temperature on the horizontal lines below the inlet opening height (0.073m) on the left hand side of the porous medium was closed to the ambient temperature (15ºC). Above the inlet opening height the temperatures on the horizontal lines were all higher than the ambient. The temperature on the right hand side of the plume below the interface was constant but still about 0.45 ºC higher than that of the ambient air (Figure 5.11b).

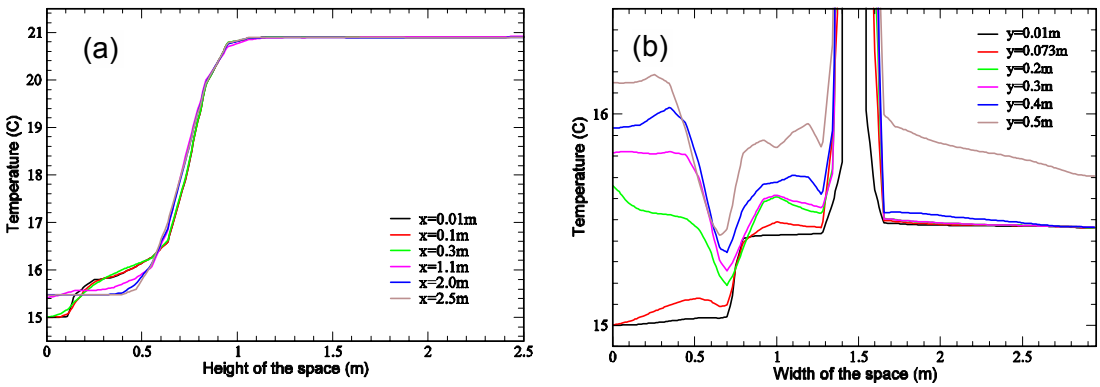

Figure 5.11 Temperature profiles, (a) along the vertical lines and (b) along the horizontal lines in the symmetry plane or z =0.75m when full domain is used (Fr =3).

Further investigation using different Froude numbers showed similar discrepancies (Table 5.9). When the Froude number was increased the low level temperatures of those profiles on the right hand side of the plume below the interface were decreased, but still higher than the ambient temperature. This phenomenon was investigated by Li (2000) in which the temperature of the layer below the interface was assumed warmer than ambient temperature. Only when the ventilation rate was sufficiently high, the air temperature below the interface was close to ambient temperature. Table 5.9 shows this trend when the ventilation flow rate is increased with the increase of Froude number.

Table 5.9 Temperature differences with different Froude number

Line location	x=2.7m, z=0.75m for each case (T_o = 288.15K)					
Fr	0	3	6	9	10	12
Below interface T (K)	288.73	288.62	288.57	288.48	288.42	288.37
T - T_o (K)	0.58	0.47	0.42	0.33	0.27	0.22

5.3.3 Definition of interface position

It is difficult to accurately define the location of the interface between the warm upper layer and the cooler lower layer because of the transitional zone between the two layers. The temperature does experience a sharp change between the two layers (Figure 5.10) but it is not as sharp as assumed in the analytical model (no thickness). There is an interface thickness in the CFD predictions. In this research, the interface height was defined at the location where the temperature is the average of those in the upper and lower layers. Figure 5.12 shows the method to define the interface. The case selected is from figure 5.11a at $x = 2.0$m. Efforts were made to reduce the thickness of the interface by increasing the mesh density at the expected stratification area. However, the simulation results showed that increasing the resolution does not help reduce the interface thickness much. This smearing zone is thought to be caused by the diffusion of heat due to the temperature difference between the upper and lower layers. The diffusion of heat in air tends to mix the air in the space while the thermal plume entrains the surrounding air and transports air into the upper region. The thickness of interface is physical fixed by these two driving strengths rather than sensitive to the mesh densities.

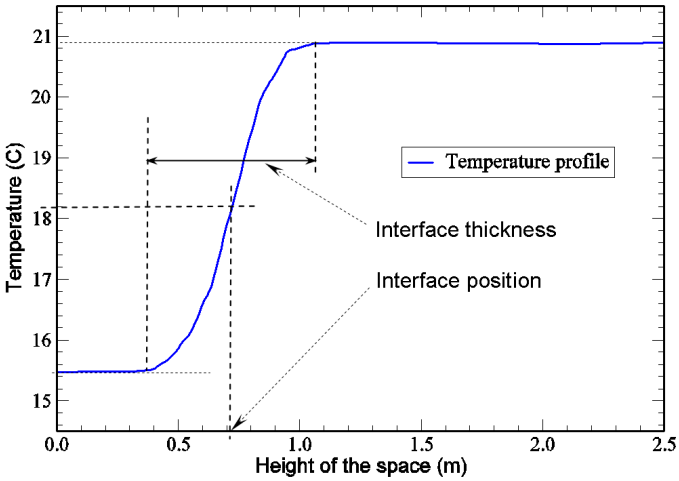

Figure 5.12 The vertical temperature profile at $x = 2.0$m and $z = 0.75$m (Fr =3)

5.3.4 Reduced gravity field

Reduced gravity, g', was defined as $g' = g\Delta\rho / \rho_o$ in section 2.2.3. In this work the air was assumed to be a perfect gas. Therefore density and temperature are related by the equation of state $P = \rho RT$ and hence

$$g' = g\Delta\rho / \rho_o = g\Delta T / T_o = g(T - T_o)/T_o \qquad \text{Eq (5.3)}$$

where T_o is the ambient temperature and T is temperature field of the fluid domain.

Another expression for calculating reduced gravities g' is using the enthalpy field of the domain, i.e. $\Delta T = \Delta He / c_p$, therefore

$$g' = g\beta\Delta He / c_p \qquad \text{Eq (5.4)}$$

where β is the coefficient of expansion ($1/T_o$). Because the value of enthalpy at the reference temperature T_o was defined as zero in the CFD calculations so ΔHe here can be obtained from the enthalpy field of the domain directly.

The reduced gravity fields using the two expressions (Eqs (5.3) and (5.4)) are given in Figure 5.13 ($x = 2.5$m, 1.475 m on the symmetry plane).

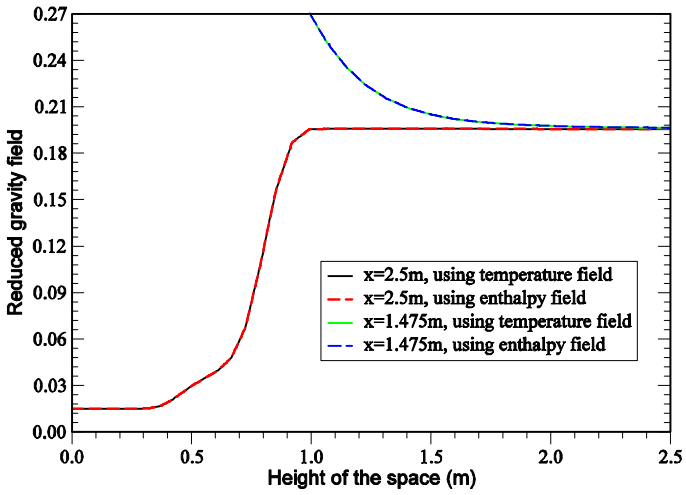

Figure 5.13 Reduced gravity fields at different locations

The black and red lines show the typical reduced gravity field outside the thermal plume while the blue and green lines show the reduced gravity field in the centre of the plume. The temperature and enthalpy in the centre of the plume are much higher than that of the fluid outside the plume. When the plume rises its temperature and enthalpy reduce and approach the temperature and enthalpy of the upper layer at the ceiling. Clearly, the two methods for calculating the reduced gravity field are identical. Eq (5.3) was used from here onwards.

5.3.5 Effects of wind speed

CFD predictions of interfaces and reduced gravities (Figure 5.14) for varying Froude numbers show good qualitative and quantitative agreement with both analytical models and salt bath experiments. Figure 5.14a shows that at small Froude numbers (when buoyancy dominates the flow) the interfaces were slightly under-predicted while at high Froude number (when wind force begins to dominate) this parameter was slightly over-predicted. This discrepancy is thought to be due to the inaccuracy in predicting the plume entrainment. The plume theory discussed in sections 2.2.1 and 2.2.4 assumes a vertical rising plume with constant entrainment. When the plume is not vertical the plume entrainment is no longer uniform over the height of the plume. These differences will effect the prediction of the interface position. When the entrainment is under-predicted the interface will be over-predicted (e.g. high Fr region) and vice versa.

A favourable agreement on the prediction of reduced gravity of the upper layer between CFD, analytical and salt bath experiments is shown in Figure 5.14b. This indicates that the CFD could calculate a reasonable temperature field with the accuracy that can be expected.

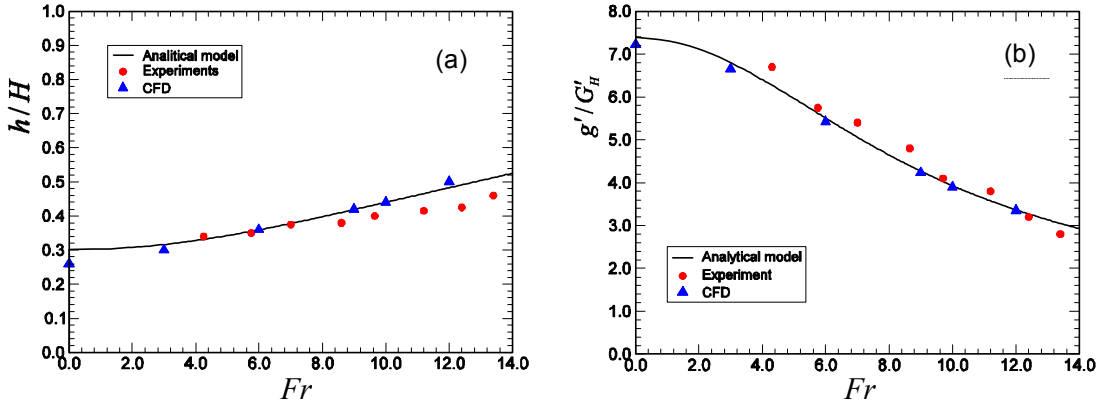

Figure 5.14 CFD predictions of (a) dimensionless interface height and (b) reduced gravities for varying Fr

CFD also predicts a reliable mass flow rate compared with the theory (Figure 5.15). The theoretical equation (Eq (2.2)) can be used to predict volume flow

rates at interface heights where the volume flow rates were assumed to be equal to the ventilation flow rates through the space. These flow rates were multiplied by the density of the air in order to obtain mass flow rates. In theory, this parameter is strongly correlated to the interface height ($Q \propto h^{5/3}$). Although the interfaces were under-predicted at small Fr and over-predicted at large Fr using CFD, the mass flow rates agreed with the theoretical line favourably. A test simulation ($Fr = 0$) was conducted without using porous medium in the domain and kept all other boundary conditions the same. The plume did not remaine vertical and there was no clear stratification formed. However, the mass flow rate through the domain was similar (less than 10 percent different) on that with a vertical plume. This indicates that the mass flow rate through the space was sensitive to neither the interface heights nor the plume entrainment for CFD simulations. It mainly depends on the physical geometrical factors and the strength of the driving forces.

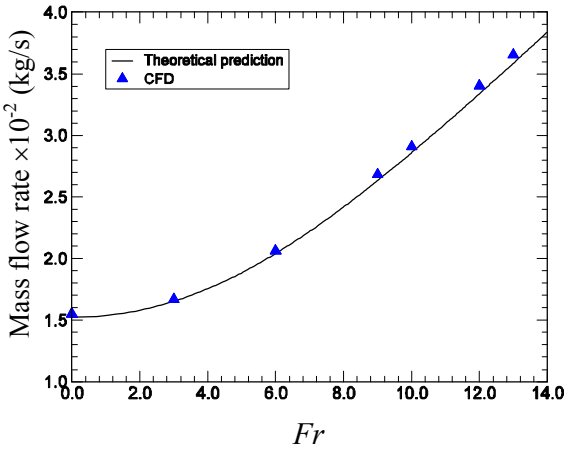

Figure 5.15 Variation of mass flow rate through the space with Froude number

5.3.6 Effects of opening sizes and locations

To investigate the dependence of the interfaces, the reduced gravities and the mass flow rates on opening sizes, simulations were carried out for various effective opening areas (table 5.3).

As in section 5.3.5, the results of CFD simulations for varying effective opening sizes showed good agreement with both analytical model and salt bath experiments (Figure 5.16).

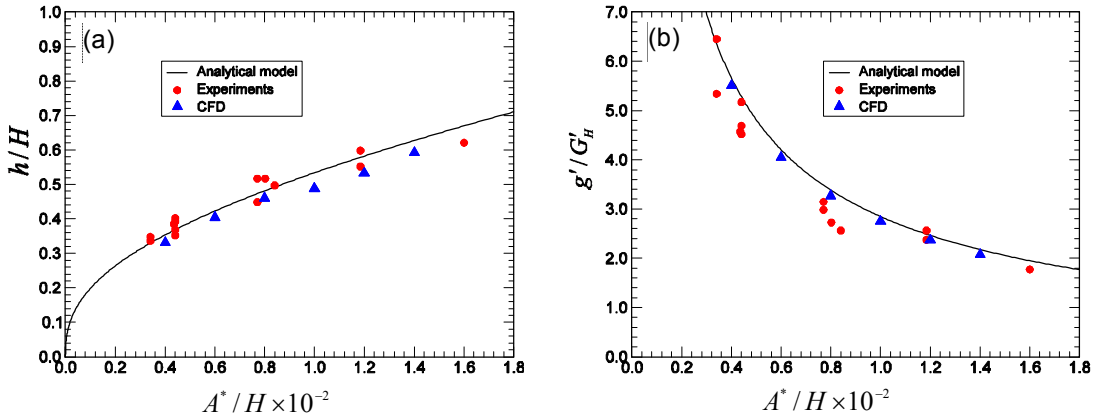

Figure 5.16 Variation of (a) dimensionless interface height and (b) reduced gravity with dimensionless effective opening areas (Fr = 4.2)

Figure 5.16a shows that an increase of ventilation opening size under constant wind effect (Fr =4.2) will lead to an increase of the interface and consequently, the reduced gravities were reduced (Figure 5.16b). The small under-prediction of interface heights in some cases may be caused by over-prediction of plume entrainment, causing the volume flux in the plume to increase more rapidly and therefore the interface to form lower down. However, this enhanced entrainment would lead to a warming of the upper layer which is not borne out in the CFD predictions (Figure 5.16b). This is thought to be due to the effects of wind and the horizontal momentum generated by the incoming air through inlet openings resulting in a non-uniform entrainment into the plume. Also, the ventilation flow rate predicted by CFD was reliable (Figure 5.17). This indicated that although the interface was under-predicted in some cases, the ventilation flow rates were still well predicted, by which the correct amount of heat input was driven out of the space by the ventilation flow. The reduced gravities were therefore well predicted by CFD calculations.

One of the conclusions made in Hunt & Linden (2001) was that the number and location of the ventilation openings below the interface have no effect on the interface height, reduced gravity and ventilation flow rate providing the total effective opening area A^* is the same. For the high level openings above the interface, this is also true if the distance from the middle of the upper openings to the top of the enclosure is kept the same. This argument was

investigated using the different opening strategies shown below (Figure 5.18a, b, c, d, and e).

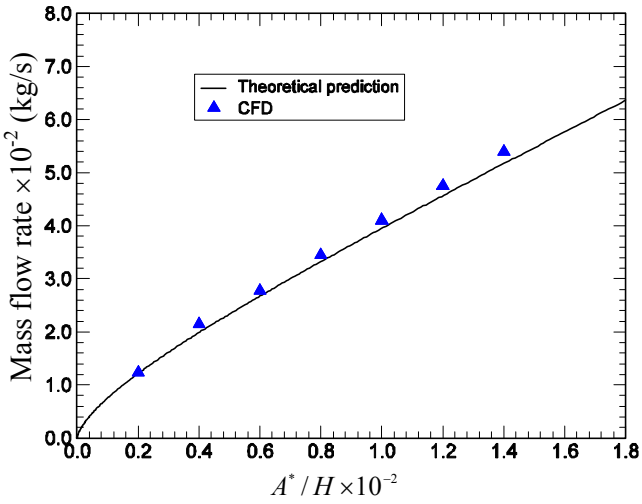

Figure 5.17 Variation of mass flow rates through the space with dimensionless effective opening areas

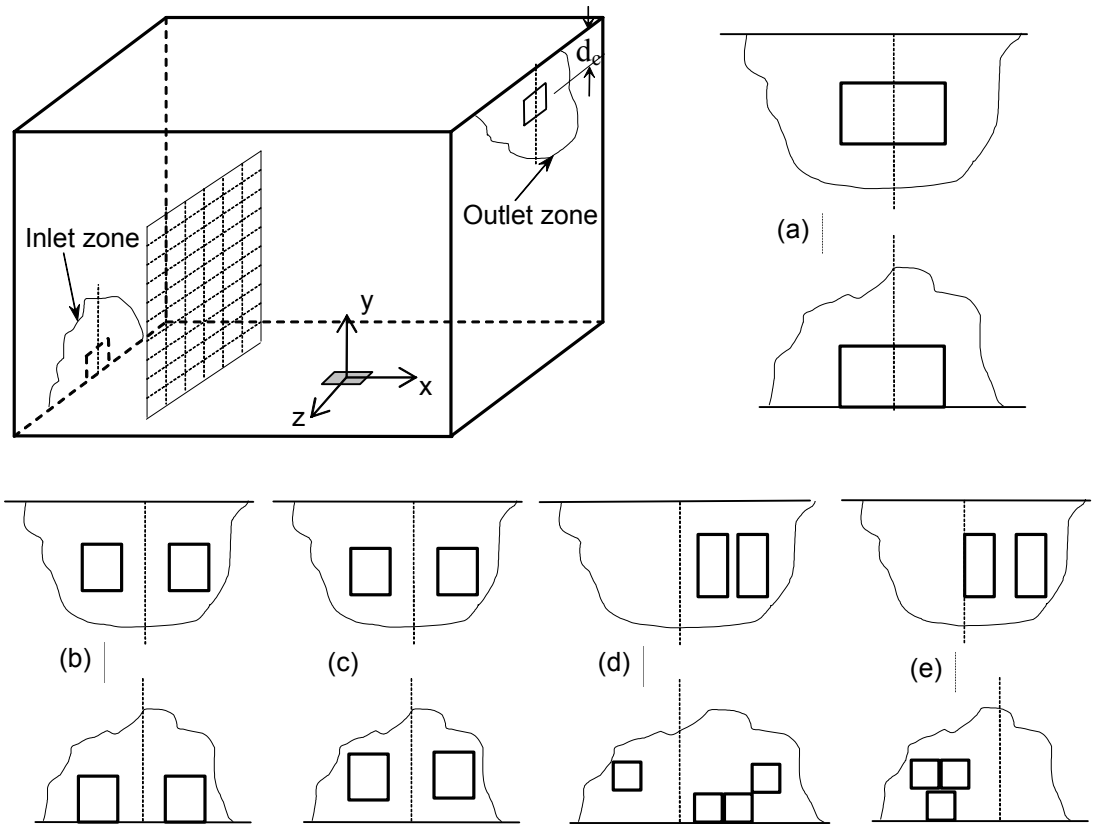

Figure 5.18 Opening strategies (a) single opening for both inlet and outlet, (b) two symmetrical openings for both inlet and outlet, (c) two symmetrical openings for both inlet and outlet but inlet openings are above floor level, (d and e) multi-openings.

The cases were selected from Table 5.2 (Fr = 0.0, 3.0 and 9.0). The simulation results for these opening strategies in predicting dimensionless interface height and reduced gravity are shown in Figure 5.19.

There were negligible variations between the different opening strategies. Figure 5.19 shows that the interface positions and reduced gravities are independent of these opening strategies when the dimensionless total effective opening area (A^*/H^2) is the same, which bears out the analysis of Hunt & Linden (2001) mentioned early in this section.

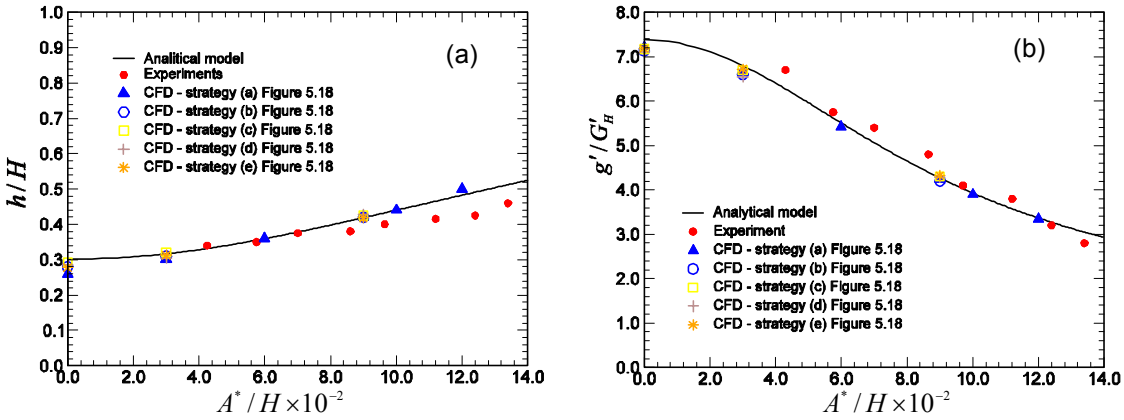

Figure 5.19 Variation of (a) interface heights and (b) reduced gravities with different opening strategies ($A^*/H^2 = 3.4\times10^{-3}$)

For benchmark 1 cases, the opening arrangement of figure 5.18b was most often used. The strategy shown in figure 5.18a was also used in some cases. The opening arrangements for them are both easy to apply symmetry planes which are used for reducing computing time. Figure 5.20 shows a typical vector plots.

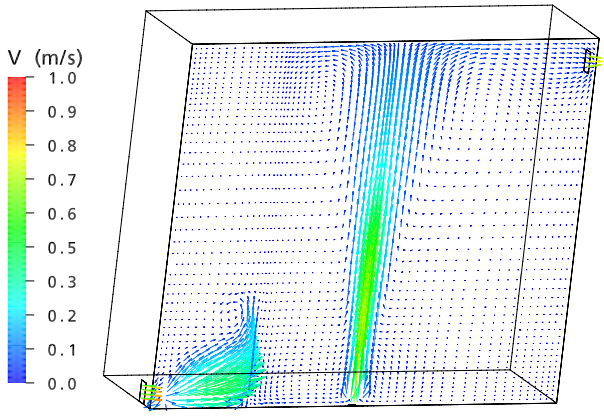

Figure 5.20 Speed vector plots of half fluid domain, windward and leeward opening strategies (two openings, as shown in Figure 18b).

5.3.7 Effects of source strengths

The analysis of Linden et al (1990) showed that the source strength had no effect on the location of the interface for purely buoyancy-driven flow in an enclosure (Eq (2.10)) and this conclusion was validated by salt bath experiments, as well as the CFD studies by Cook (1998). However, varying source strengths for buoyancy combined with wind-driven flow leads to variation of the Froude numbers (Eq (2.17)) for a steady wind speed. As discussed in section 5.3.4, the interface will be changed due to the variation of Froude number.

CFD simulations for various source strengths were conducted using the same effective opening area and constant pressure drop induced by wind (table 5.4). Figure 5.21 shows temperature fields when varying source strength (100W and 150W). An increase of source strength with constant pressure drop across the ventilation openings leads to a decrease in Froude number, consequently the interface position was formed lower down and the temperature of the upper layer was increased due to the higher heat input.

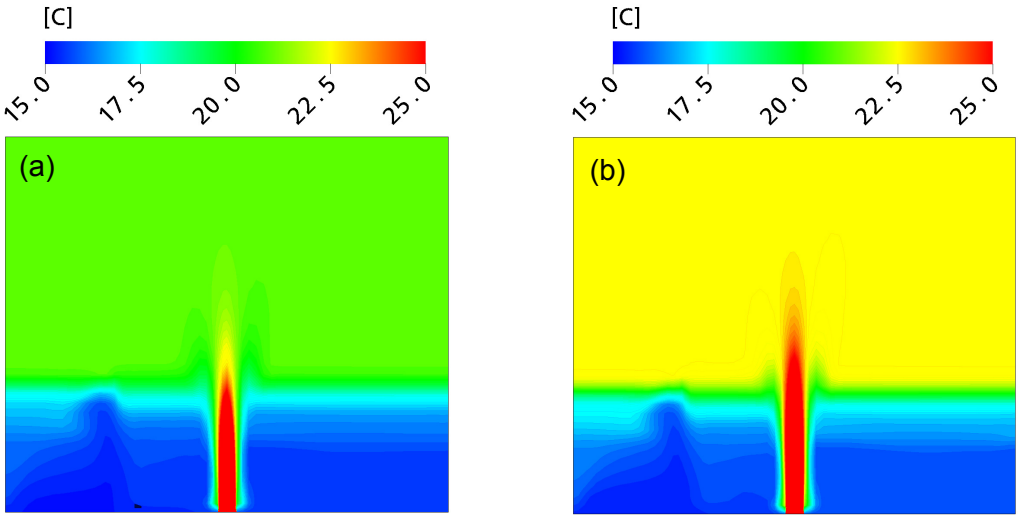

Figure 5.21 Temperature profiles for $A^*/H^2 = 3.4\times10^{-3}$ and $\Delta = 0.23$Pa, (a) E =100w and (b) E =150W

The quantitative comparisons of interfaces and reduced gravities between CFD, the analytical model and salt bath experiments showed good agreement for varying heat source strengths (Figure 5.22). The increase of source strengths can be converted into the increase of buoyancy flux B using Eq

(2.20). An increase of buoyancy flux B leads to a decrease of Fr therefore the interface is reduced (Eq (2.17)). As can be seen from figure 5.22a, there were only slight changes of the interface position when the heat input was varied dramatically. This is thought to be caused by the weak dependency between Froude numbers and the strength of buoyancy ($Fr \propto B^{-1/3}$). A large variation of buoyancy flux B can only lead to a small change of Fr. However, the change of non-dimensional reduced gravity strongly depends on the buoyancy flux B, as shown in figure 5.22b. This is caused by the large temperature variation across the interface when the heat input was increased, while the variation of the reduced gravity g' depends on the temperature difference between the lower and the upper layer ($g' = g\Delta T / T_0$).

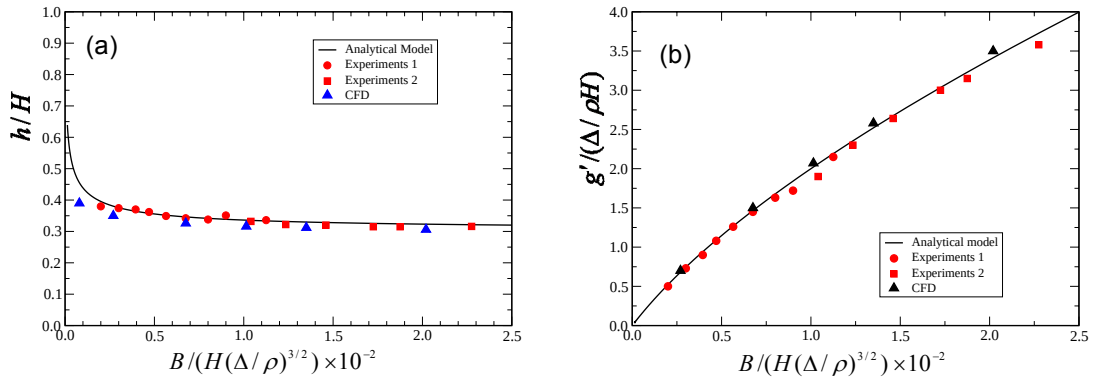

Figure 5.22 Variation of (a) interface heights and (b) reduced gravities with the change of buoyancy fluxes

Figure 5.23 shows the variation of the interface with Froude number due to the changes of the source strength. This is another way to investigate the dependence of the interface on the variation of source strength. The expected direction of change for the interface height (qualitatively)

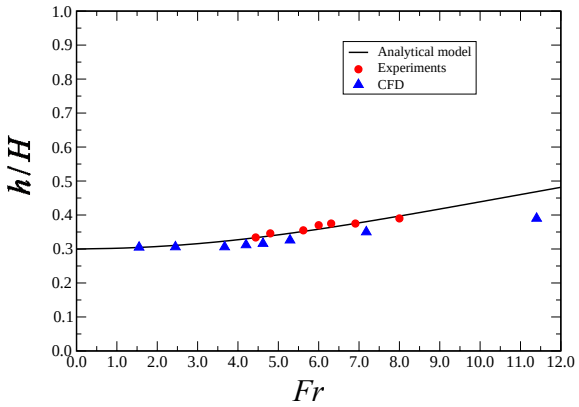

Figure 5.23 Variation of interface heights and with the change of Froude numbers due to the change of buoyancy fluxes

in table 5.8 is demonstrated and the quantitative comparisons also showed good agreement.

It is interesting to note that the more accurate positions of the interface were predicted by CFD at relatively high heat source strengths (left hand side of Figure 5.23). At relatively low heat source strengths (right hand side) the interface positions were under-predicted. A stronger heat source generates a stronger thermal plume. The plume is therefore more stable with a high buoyancy and can dominate the air flow pattern after the porous medium (Figure 5.10). As discussed in section 5.3.1, the intention of using a porous medium was to block the horizontal momentum in order to avoid it impinging on the thermal plume. If the air surrounding the plume was isotropic with uniform speed the numerical entrainments induced by the vertical momentum would be the same from all directions, then the numerical plume could be perfectly developed and maintained as assumed in the theory. However, this was not possible with the application of the porous medium boundary condition. The porous boundary can only minimise the effects of horizontal momentum to a level at which buoyancy induced vertical momentum begins to dominate the flow. Therefore, the stronger the heat sources, the more stable the uprising plume and the closer the prediction between theories and CFD.

The prediction of volume flow rates for different source strengths will be discussed and validated by the salt bath experiments (Hunt & Kaye (2001)) in section 5.5.

5.3.8 Effects of turbulence models

The eddy-viscosity two equation models are generally applicable for modelling indoor airflows, particularly when the indoor area is not well occupied (empty box for this study) and the first order fluid parameters are of the main interests (e.g. mean temperature, velocity etc.) rather than turbulent fluctuation details (Chen (1995)). Previous studies suggested that the Renormalisation Group (RNG) k-epsilon model (Yokhot et al (1992)) performed better than other eddy-viscosity models in the prediction of indoor airflow features (Chen (1995), Cook & Lomas (1998) and Gan (1998)). In this research, the RNG k-epsilon

model with Boussinesq approximation was applied to conduct most of the numerical simulations.

In order to compare the performances of different turbulence models for the cases studied in this research, a number of simulations using the standard k-epsilon model and the low Reynolds number k-epsilon model were carried out and were compared with the RNG model. Figure 5.24 shows the qualitative comparisons between the three models in the prediction of the temperature field of the domain.

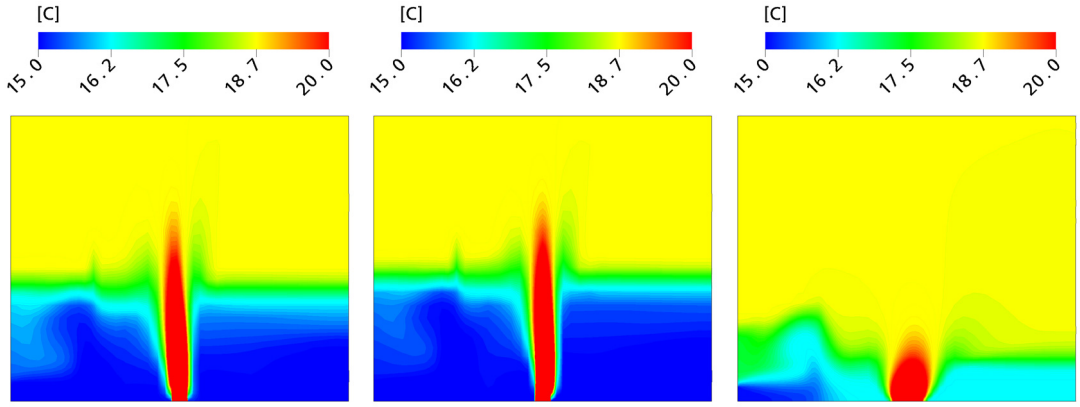

Figure 5.24 Temperature field of fluid domain for Fr =9 (from left to right, the standard $k-\varepsilon$ model, the RNG model and the low Reynolds number $k-\varepsilon$ model

As shown in figure 5.24, the standard $k-\varepsilon$ model and the RNG model produced similar predictions of the temperature field. However, a small difference of the position of stratification can be observed. A slightly lower interface was predicted by the standard $k-\varepsilon$ model compared with the RNG model. This was thought to be due to the plume properties predicted by these two models. Cook (1998b) examined the entrainment constant α of a thermal plume using these two models and it was reported that the entrainment of the plume was over-predicted by the standard $k-\varepsilon$ model compared with the RNG model. This is why the interface predicted by the standard $k-\varepsilon$ model is lower than that predicted by the RNG model. In this research, the details of the plume properties were not examined because the plumes studied here could not be well developed as assumed by analytical model. The surrounding air of the thermal plume was not stationary (isotropic) for the development of an uprising thermal plume due to the effect of the horizontal momentum

produced by the incoming airflow. The porous medium boundary used in CFD could effectively reduce this effect. However, the effects were still remained. The porous medium boundary guaranteed the overall performance of the thermal plume was similar to the analytical model and the salt bath experiments (Hunt & Linden (2001).

There are large differences in the prediction of temperature field of the domain between the low Reynolds number $k-\varepsilon$ and the RNG model (Figure 5.24). The plume shape predicted by the low Reynolds number $k-\varepsilon$ model was 'fat' and the interface was much lower compared with both the standard and the RNG $k-\varepsilon$ models. This may be due to the need for a very fine mesh near the wall when using this method. The mesh refinement required for the low Reynolds number model is equivalent to what is required for the direct numerical simulations (Laurence (1993)). The mesh used in figure 5.24 for the low Reynolds number model was already much finer than the standard and RNG models but the performance of this model was still poor. Considering the CPU computing time this model was therefore not further applied in this research.

The quantitative comparisons between the standard and RNG $k-\varepsilon$ models are given in figure 5.25.

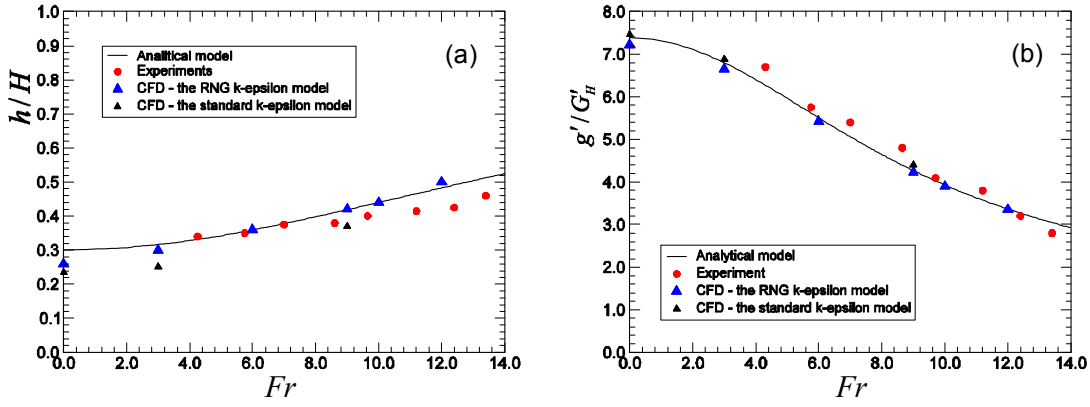

Figure 5.25 Variation of (a) interface heights and (b) reduced gravities with different turbulence models (Fr =0.0, 3.0, and 9.0)

The predicted interface heights by the standard $k-\varepsilon$ model are lower than expected from the analytical solution which is shown in Figure 5.25a. A low interface leads to a low ventilation flow rate, hence a high temperature in the

upper layer (Linden et al (1990) and Hunt & Linden (2001)). The reduced gravities of the upper layer would therefore be increased. However, the expected over-predictions of the reduced gravities in the upper layer were not observed (Figure 5.25b). In the CFD simulations, a similar ventilation flow rate was predicted by the standard $k-\varepsilon$ model and the RNG model (Figure 5.26), which means that the removal of heat from the ventilated box under steady state was similar between the two models. Therefore the temperature fields of the upper layers should not be significantly different.

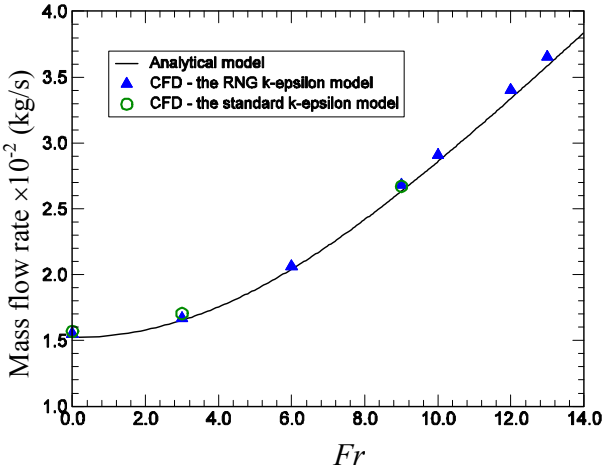

Figure 5.26 Mass flow rate predicted by different turbulent models

5.4 Analysis of results for opposing wind

Table 5.10 shows a summary of the mathematical analysis of section 2.2.4.2. And in the following sections, CFD simulations were carried out to compare these analytical predictions.

Table 5.10: Summary of analytical analysis of Hunt & Linden (2005).

Conditions	results		
	h/H (Eq 2.23)	g'/G'_H (Eq 2.19)	Q (Eq 2.12)
Increase Fr	decrease	increase	decrease
Increase A^*/H^2	increase	decrease	increase
Δ=constant, increase E	decrease	increase	increase

5.4.1 Flow pattern with different Froude number

When the opposing wind was small, the flow direction was the same as purely buoyancy driven flow in which fresh air flows into the ventilated box through

low level openings and out through high level openings. Therefore the resulting flow fields for small opposing wind cases are similar to assisting wind cases presented in section 5.3.1 and this led to a two-layer stratification flow (Figure 5.28a,b,c,d). If the opposing wind was strong enough to overcome the buoyancy force, the flow direction was reversed – fresh air enters the ventilated space from high level openings and flows out from low level (Figure 5.27). When this occurs the two-layer flow breaks down and becomes a mixing mode (Figure 5.28f). As shown in Figure 5.27, the porous medium boundary was still used. This was essential for maintaining a vertical thermal plume for the small opposing wind cases (Eq (2.25)).

The resulting temperature fields for different Froude numbers are shown in Figure 5.28. As Fr increases (due to the increase in wind speeds) the interface fell, and eventually the displacement flow broke down to give a mixing flow.

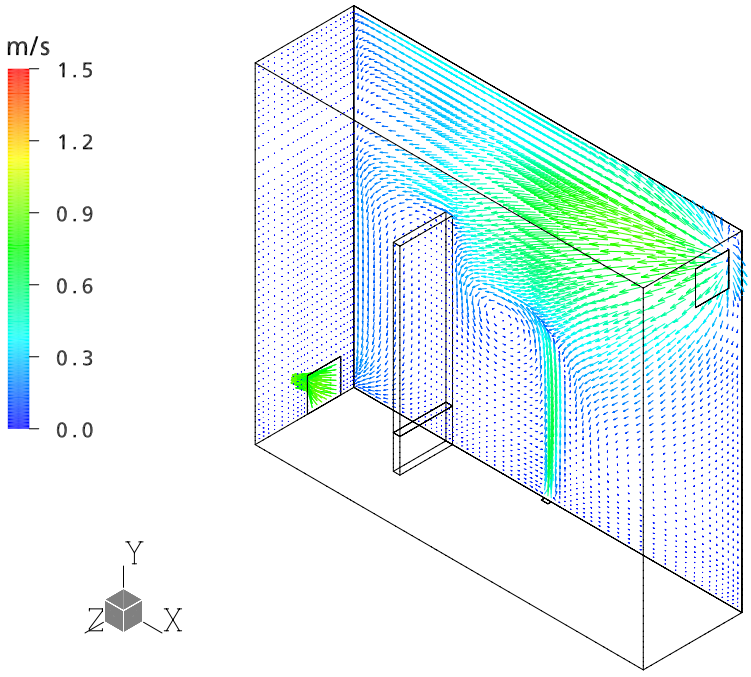

Figure 5.27 Resulting velocity field for strong opposing wind cases, Fr =7.0

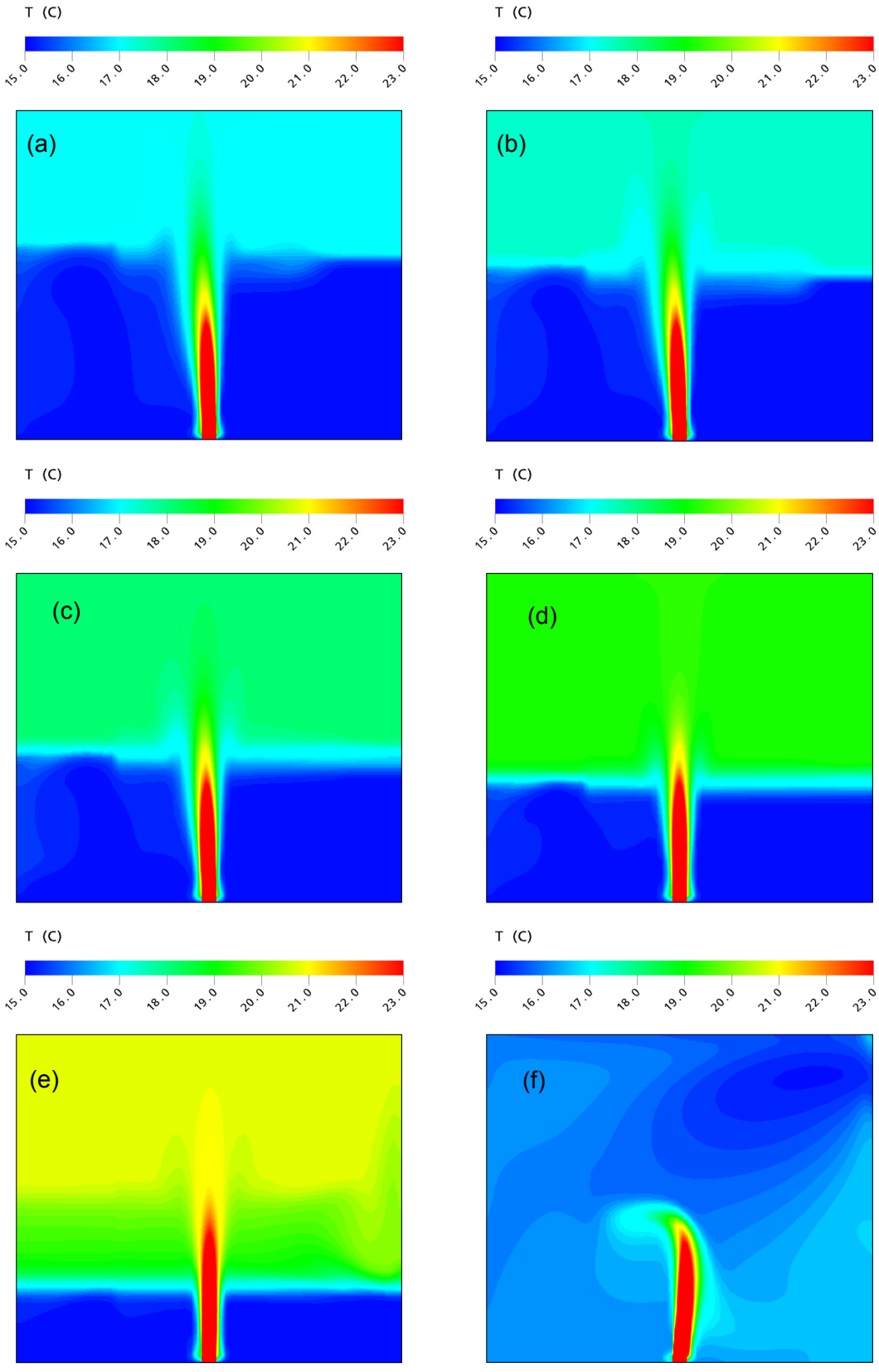

Figure 5.28 Resulting temperature fields for different Fr , (a) Fr = 0; (b) Fr = 2.0; (c) Fr = 3.0; (d) Fr =4.0; (e) Fr = 5.0; (f): Fr =7.0

5.4.2 Effects of wind speed

The same methods as the assisting wind cases (section 2.2.4.1) were used for the calculations of wind induced pressures (Eq (5.19)). CFD simulations were conducted in order to test the dependency of dimensionless interface heights and reduced gravities on different wind speeds (Table 5.5). Two different non-dimensional effective opening areas were used. The simulation results are shown in Figure 5.29.

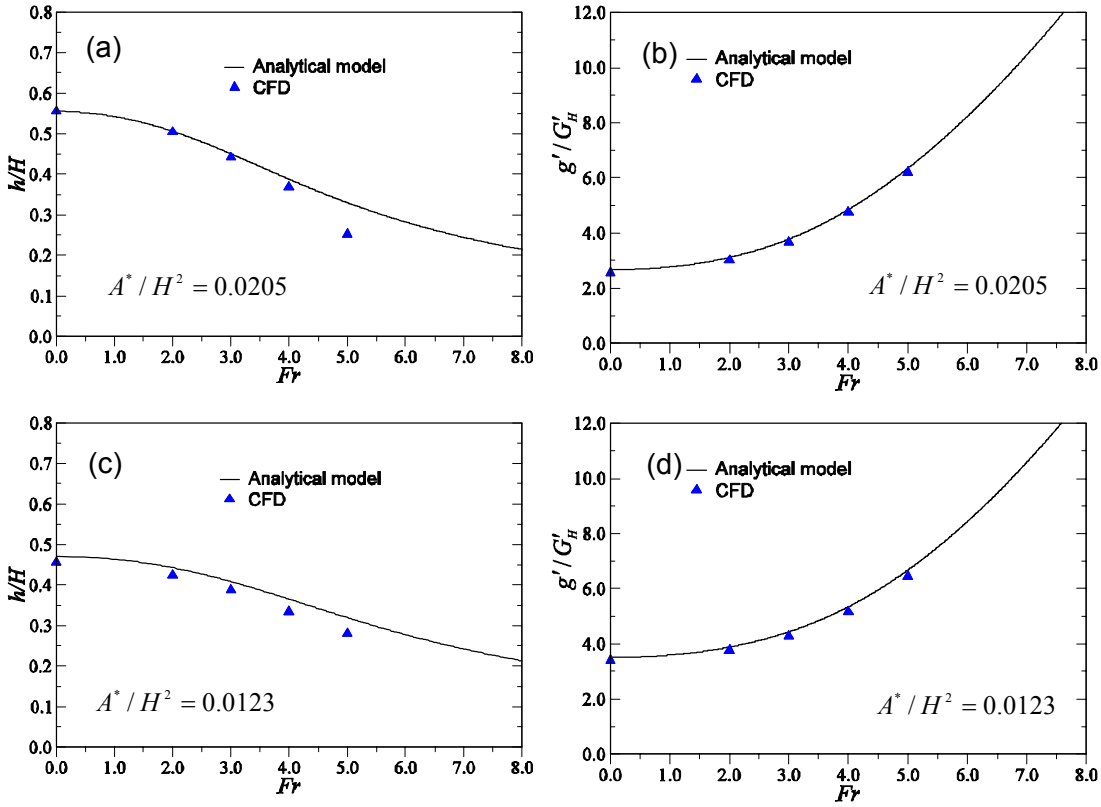

Figure 5.29 Comparisons between analytical model and CFD in the predictions of (a & c) interface heights (b & d) reduced gravities for varying Fr with different effective opening areas $A^*/H^2 = 0.0205$ & $A^*/H^2 = 0.0123$.

At small wind speeds (small Fr) more favourable agreement between CFD and analytical model was observed. When the wind speeds were large (large Fr in the figure) large discrepancies existed in the prediction of interface height. This may be caused by some inflow from the high level openings. For example, in the case of $Fr = 5.0$ (Figure 5.28e), the high level openings experienced both inflow and outflow. The inflow from the high level opening caused a thicker smearing zone close to the stratification level, which may

create a lower interface than the analytical predictions. It can also be seen from Figures 5.29a & c that the larger the effective opening area the larger the discrepancy resulting from the same wind effect (e.g. when Fr = 5).

The reduced gravities predicted by CFD agreed with analytical model favourably, which indicates the less sensitive nature between the reduced gravities and the wind effects.

5.4.3 Effects of opening sizes

The dependency of interfaces and reduced gravities on effective opening areas was investigated by CFD simulations using the conditions shown in Table 5.6. The quantitative comparisons between the analytical model and CFD are shown in Figure 5.30.

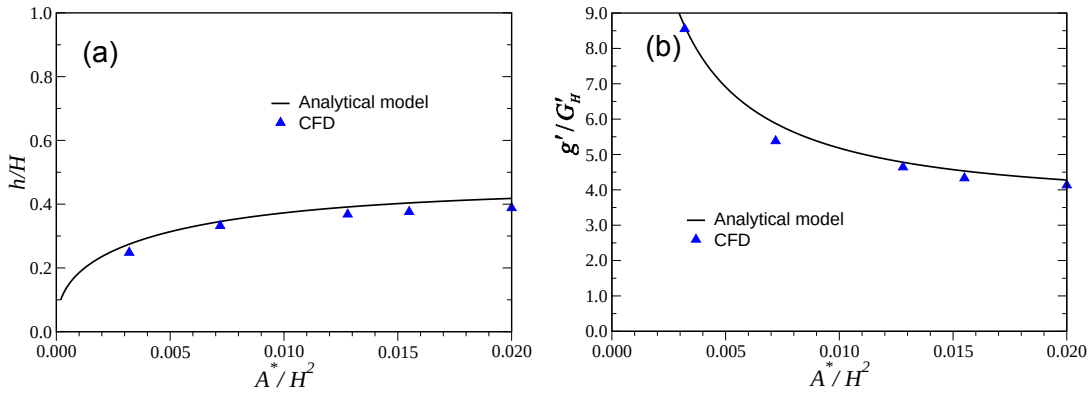

Figure 5.30 Comparisons between analytical model and CFD in the predictions of (a) interface heights (b) reduced gravities for varying A^*/H^2.

Good agreement for the predictions of interface heights and reduced gravities between CFD and analytical models was achieved using the solution technique discussed in section 5.2.6. For all different effective opening areas, the wind force remained the same ($Fr = 3.5$). This wind effect was not large enough to generate a mixing flow for the effective opening areas used, therefore relatively stable two-layer flows were maintained and strong and sharp stratifications were formed. This contributes to the close predictions of CFD compared with the analytical model. The close agreement in the predictions of reduced gravities between CFD and analytical model indicated that the ventilation flow through the space was well predicted by CFD

simulations and a relatively accurate amount of heat was driven out by this ventilation flow.

5.4.4 Effects of source strengths

A series of CFD simulations were carried out to test the dependency of interfaces and reduced gravities on heat source strengths with opposing wind. Under the opposing wind effect very large heat sources may lead to big temperature difference between the cool lower layer and warm upper layer. As a result, the Boussinesq approximation may not be applicable for CFD simulations (section 4.5). If heat sources are too small, the flow field might experience inflow from high level openings and mixing mode ventilation might occur following the collapse of the two-layer stratification.

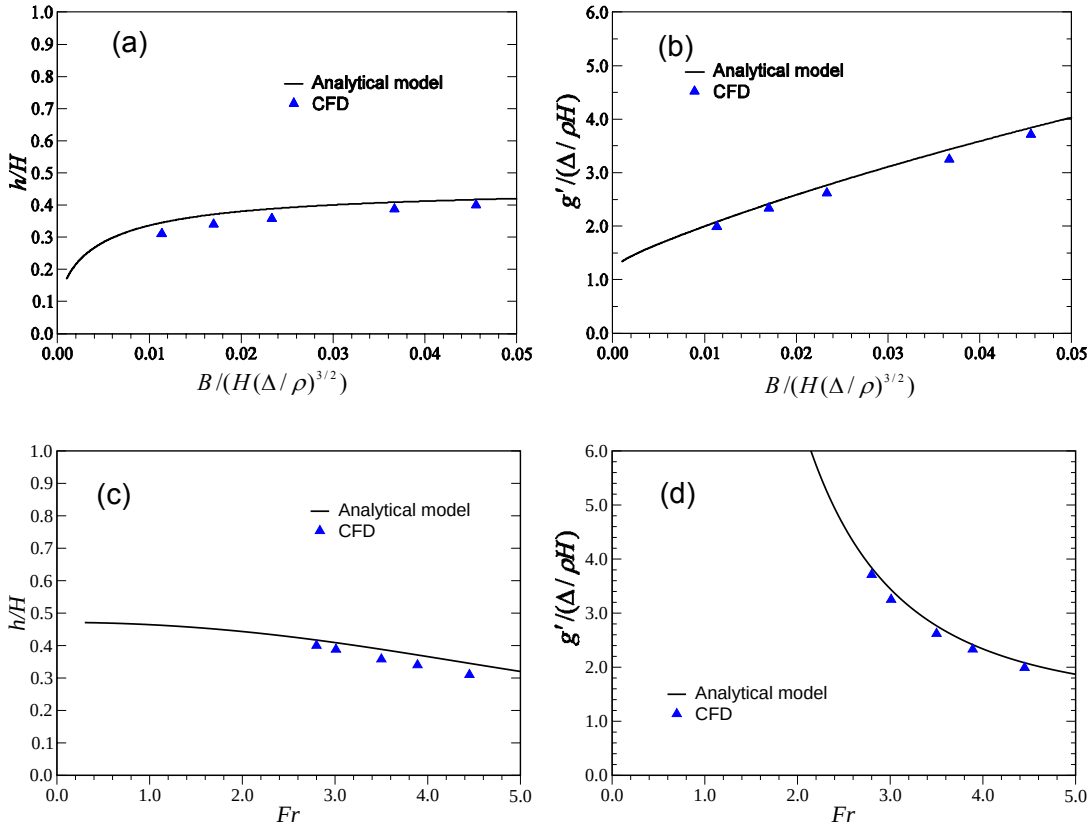

Figure 5.31 Comparisons between analytical model and CFD in the predictions of dimensionless (a & c) interface heights and (b & d) non-dimensional reduced gravities and non-dimensional source strength $B/(H(\Delta/\rho)^{3/2})$ & Froude number.

Figure 5.31 shows the CFD predictions of interface heights and reduced gravities for varying heat source strengths and Fr . Close quantitative

agreement has been achieved between CFD and the analytical model. The scalings used in Figure 5.31 are $B/(H(\Delta/\rho)^{3/2})$ and $g'/(\Delta/\rho H)$. They are non-dimensional forms of Froude number and dimensionless interface height, e.g. $B/(H(\Delta/\rho)^{3/2}) = Fr^{-3}$ and $g'/(\Delta/\rho H) = C^{-1}Fr^{-2}(h/H)^{-5/3}$. Under the constant wind effect (Δ is fixed) an increase of heat source leads to an increase of buoyancy flux B consequently an increase of the interface height (Figure 5.31a). Alternatively, an increase of heat source strength leads to a decrease of Fr, therefore an increase of the interface height (Figure 5.31c). Similarly, Figures 5.31b & d show variation of reduced gravity with source strength and Fr. An increase of heat source strengths leads to an decrease of Fr and consequently an increase of reduced gravities g'. CFD predictions of these parameters agreed favourably with the analytical predictions, which indicates that the proposed methods used in this chapter (section 5.2) are robust for opposing wind cases.

5.5 Validation of ventilation flow rate

The analytical equation for calculating volume flow through the thermal plume (Eq (2.2)) derived by Morton et al (1956) was used by many researchers to determine the volume flow through a ventilated space driven by buoyancy (e.g. Linden et al (1990), Hunt & Linden (2001, 2005), Holford & Hunt (2003)). The assumption used by these researchers was that the volume flow rate through the ventilated space was equal to the volume flow rate through the plume at the interface height. As discussed in section 4.9, this assumption was not validated by the experimental work conducted by these researchers. Hunt & Kaye (2001) used the assumption for buoyancy alone cases and tested the assumption using salt bath experiments. This is the reason why the measurements of the ventilation flow rates for buoyancy alone cases can be used to validate the ventilation flow rates predicted for buoyancy combined with wind cases. This section discusses the mathematical analysis and salt bath experiments for predicting the volume flow rate through a ventilated space driven by purely buoyancy. The CFD predictions of ventilation flow rates for buoyancy combined with wind effects (assisting wind cases) are validated by the work of Hunt & Kaye (2001).

5.5.1 Analysis for virtual origin correction

The analytical equation (Eq (2.2)) was derived for a pure thermal plume from a 'point' heat source without initial volume and momentum flux. However, it is very difficulty to apply a real 'point' source physically. Instead, an 'area' source is used for salt bath experiments. Furthermore, there are always initial volume fluxes present for real physical saline plumes generated by an 'area' source when conducting experiments. In order to account for these effects a source parameter (Γ) was defined by Hunt & Kaye (2001).

$$\Gamma \sim A^{5/2} g_0' / Q_0^2 \qquad \text{Eq (5.5)}$$

where A is the source area ($=\pi D^2/4$), Q_0 is the initial volume flux and g_0' is the initial reduced gravity, given by

$$g_0' = g\Delta\rho_0/\rho_0 \qquad \text{Eq (5.6)}$$

where ρ_0 and $\Delta\rho_0$ are the initial density and the initial density contrast.

From Hunt & Kaye (2001), a plume with non-ideal source was proved to be equivalent to a pure point source plume, located at an asymptotic virtual source at a distance $y=-y_{avs}$ below the actual source at $y=0$ (Figure 5.32).

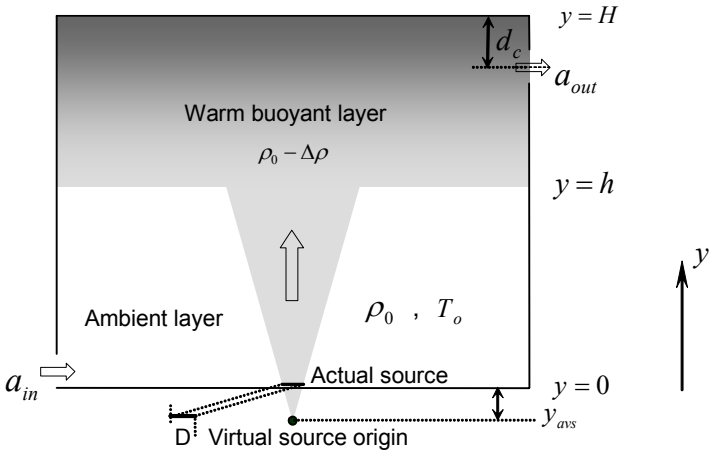

Figure 5.32 Schematic figure showing the location of the actual area source with diameter D ($y=0$) and the virtual source origin ($y=-y_{avs}$)

The dimensionless asymptotic virtual source origin was given by

$$y_v = \Gamma^{-1/5}(1-\delta) \qquad \text{Eq (5.7)}$$

where δ denotes an expression for Γ (see Hunt & Kaye (2001) for details).

From Eq (2.2), the interface position ($y = h$) with a given volume flow rate (Q) can be defined using the following expression

$$y + y_{avs} = C^{-3/5} Q^{3/5} B^{-1/5} \qquad \text{Eq (5.8)}$$

where C is defined the same form as Eq (2.4) with the Gaussian entrainment coefficient α_G=0.090 in Eq (2.5).

5.5.2 Salt bath experiments and results

Dimensionless results of salt bath experiments without the correction of virtual source origin are shown in Figure 5.33a together with the analytical prediction at different interface heights (with volume flow rate $Q(y = h)$). The measurements of the volume fluxes were linearly over-predicted by the experiments due to the initial conditions of the saline plumes (Figure 5.33a). Good agreement was achieved for the predictions of the analytical model and the salt bath experiments after the correction of the virtual source origin (Figure 5.33b).

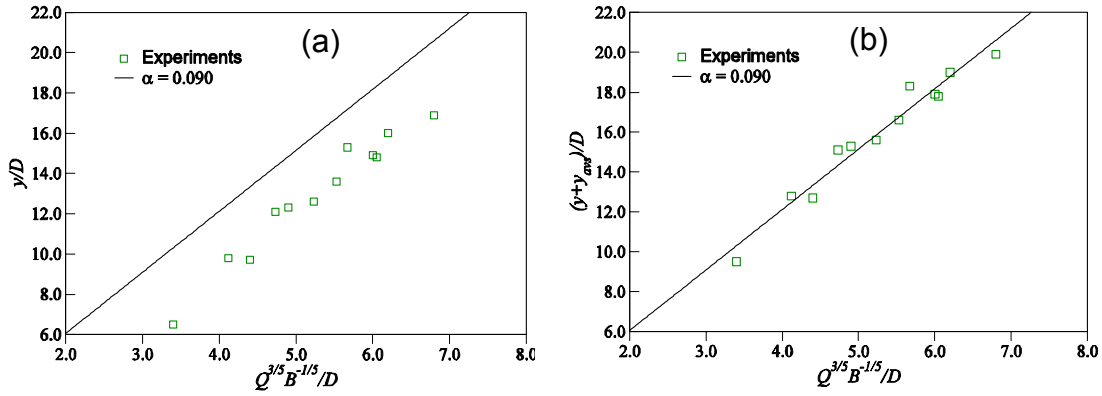

Figure 5.33 Experimental measurements for a turbulent plume with (a) uncorrected and (b) corrected virtual origin of the area source. Analytical prediction is plotted for α =0.090 (Eq (5.8) and Eq (2.4), after Hunt & Kaye (2001)).

Although the experimental conditions considered in Hunt & Kaye (2001) are buoyancy-driven alone cases the data plotted here can be used to validate natural ventilation flow rates induced by buoyancy combined with wind effects

due to the same assumption: the volume flow rates through the space are assumed to be equal to the volume flow rate through the plume at the interface height (Ji (2004)).

5.5.3 CFD predictions of volume flow rates

In CFD simulations, the heat source was modelled by setting a constant heat flux on a WALL type boundary with a finite area, which is the same method used in the salt bath experiments. The difference between the area heat source in CFD and the area heat source of salt bath experiments is that the heat source in the CFD model does not have initial volume fluxes (Q_0 = 0), while the initial reduced gravity could be very large due to a small area with a relatively large heat flux (a large density contrast present around the source area). The source parameter Γ is therefore large ($\Gamma \to \infty$, Eq (5.5)) and the virtual origin of the source is close to zero ($y_{avs} \to 0$, Eq (5.7)). It is therefore not necessary to correct the CFD predictions using the virtual source origin. However, there is still a geometrical difference between the CFD modelling and the mathematical analysis (area source and point source), which has led to an uncertainty in the CFD simulations.

In order to investigate the dependency of the key parameters (e.g. interface heights, reduced gravities and ventilation flow rates) of the fluid domain on the heat source area, a series of CFD simulations were conducted for varying heat source areas. It has been found that the area ratio (source area divided by floor area of the ventilated space) used in this research (5.65×10^{-4}) was small enough to accurately predict the key parameters of the fluid domain. Continually reducing the heat source area did not cause any change to the predictions of these parameters. However, the thermal plume shape does look different for different source areas. This is discussed further in Appendix C.

Cases for varying source strength with assisting wind effect (Table 5.4 or Table D1) were selected to make comparisons between CFD, analytical model and salt bath experiments. It is important to note that the entrainment constant α used in the work of Hunt & Linden (2001) was α = 0.083 while the work of Hunt & Kaye (2001) used α = 0.090. The difference of the analytical

predictions due to using different entrainment constants are shown in Figure 5.34.

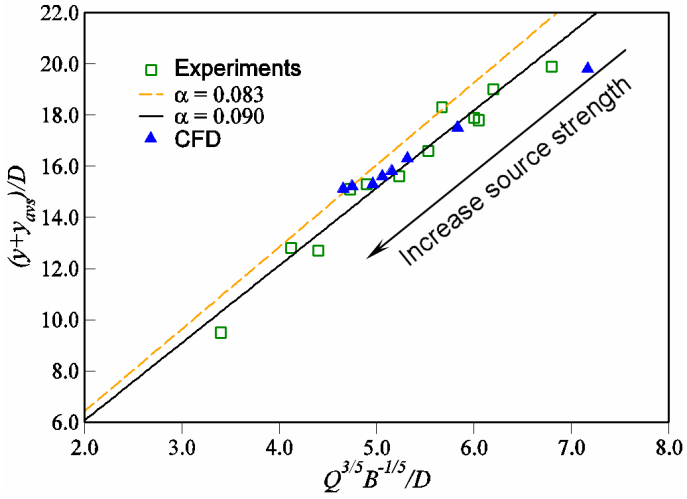

Figure 5.34 Dimensionless flow rates predicted by analytical model, salt bath experiments and CFD for the cases of table 5.4.

The gradient of the two analytical lines in figure 5.34 was different due to the different entrainment constants used (Eqs (2.4) and (5.8)). The experimental measurements showed the similar trend as the two analytical lines. The CFD cases selected here were for varying source strengths (Table 5.4). The interface positions of these cases did not vary significantly (Figures 5.22(a) and 5.23). The dimensionless quantities of the flow rates of these cases therefore look very localised in Figure 5.34, which dose not mean that the ventilation flow rates were similar. As discussed in section 5.3.7, the stronger the heat source, the more accurate predictions of CFD could be expected under the same situations (e.g. same wind effects, same parameters for porous medium boundary). This analysis is supported by Figure 5.34.

The mass flow rates predicted by CFD for the cases of varying Froude number and effective opening areas (Tables 5.2 and 5.3) agreed favourably well with the analytical model (Eq (5.8)). These predictions of Figures 5.17 & 5.19 can be converted into volume flow rates and comparisons between analytical model, salt bath experiments and CFD can be made (Figures 5.35a & b). The CFD predictions were closer to the analytical line of α =0.083 and were not as localised as Figure 5.34 due to the variation of interface heights.

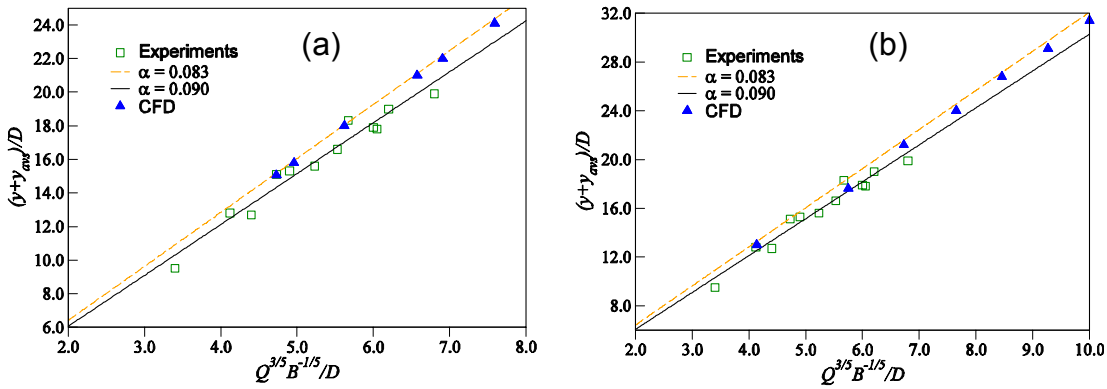

Figure 5.35 Dimensionless flow rates predicted by analytical model, salt bath experiments and CFD for the cases of (a) Tables 5.2 and (b) Table 5.3.

The values of $y + y_{avs}$ used in Figures 5.35a and b were from the analytical model. However, when the interface heights predicted by CFD were used, the predictions look different (Figures 5.36a & b). This is due to the poor predictions of interface height in some cases (Figures 5.16a & 5.18a) which lead to these differences. The differences shown between Figures 5.35 and 5.36 indicate that the volume flow rates predicted by CFD were not dependent on the interface heights. An accurate volume flow rate can be predicted even when there is a poor prediction of interface height.

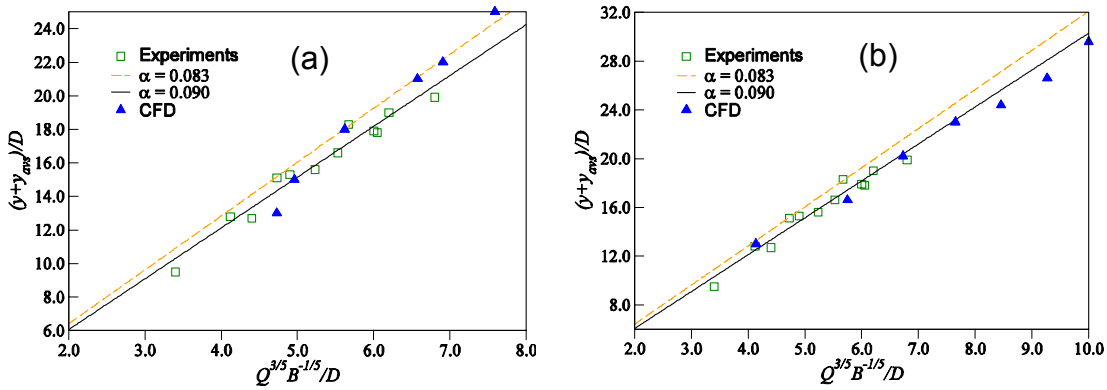

Figure 5.36 Dimensionless flow rates predicted by analytical model, salt bath experiments and CFD for the cases of (a) Table 5.2 and (b) Table 5.3. (CFD predicted interface heights were used)

5.6 Examination of stack pressure within the flow field

This section gives a brief discussion of the internal pressure profiles predicted by the CFD simulations for various operating conditions. The intention of this

section is to illustrate that the driving force for the flows discussed in this chapter comprises both wind and buoyancy generated components.

Vertical pressure profiles for three simulations are shown in Figure 5.37. The simulation conditions and results for these three flows are shown in Table 5.11.

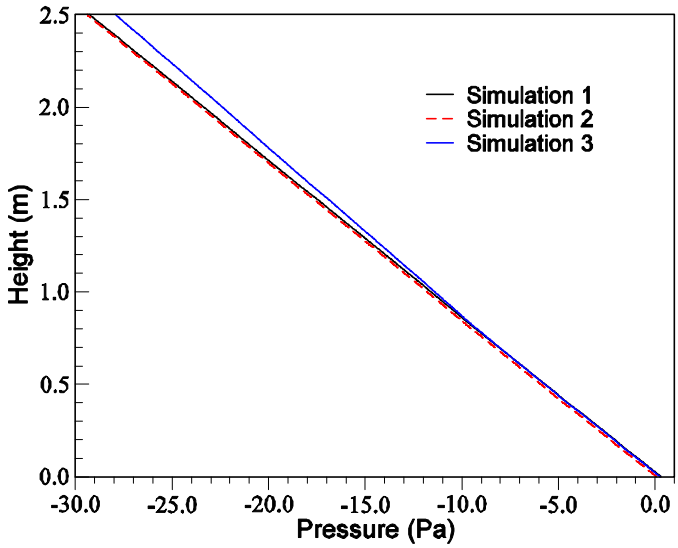

Figure 5.37 Vertical pressure profiles within the ventilated space

Table 5.11: Simulation conditions and the results of the simulation

Simulation	Fr	Heat source	h/H	g'/G'_H	mass flow rate
1	6	100 (W)	0.42	5.45	0.021 (kgs^{-1})
2	3	100 (W)	0.28	6.75	0.017 (kgs^{-1})
3	3	800 (W)	0.32	6.70	0.034 (kgs^{-1})

The internal pressure profiles (Figure 5.37) for simulation 1 (Fr = 6) and simulation 2 (Fr = 3) are almost identical, suggesting that the buoyancy component of the overall driving force is approximately equal for each. This is consistent with the simulation conditions in which a heat load of 100W is used in each. In simulation 3 (Fr = 3), the Froude number has been achieved using the same wind-driven pressure difference as in simulation 1 but with an increased heat load of 800W. The internal pressure profile for simulation 3 is significantly different above the level of the interface than for simulations 1 and 2. As expected a greater internal driving force is generated. This yields an

increase in mass flow rate through the box (c.f. simulations 1 and 2 in Table 5.11) and anticipated changes in h/H and g'/G'_H.

These results demonstrate that although the wind pressure boundary conditions imposed at the inlet and outlet openings are themselves unchanged, the flow through the openings is appropriately influenced (enhanced) by an increase in the internal heat gains. The similarities in the interface heights for simulations 2 and 3 (the same Fr) bear out the analytical predictions of Eq (2.16).

To check on the accuracy of the internal pressure profiles, comparisons were made between the internal (hydrostatic) vertical pressure difference predicted by the CFD simulations (Figure 5.37) and those predicted analytically by Hunt & Linden (2001), Eq (5.9),

$$p_2 = p_1 + \rho g\left(H - h - d_c\right) + \rho_o gh \qquad \text{Eq (5.9)}$$

where the symbols from left to right are internal pressure at level of lower openings, internal pressure at level of upper openings, density of upper (warm) layer, height of the space, height of interface and height between middle of upper openings and top of the space respectively.

The values used for h and ρ in the above equation were taken from the CFD results in order to provide a realistic comparison. The favourable agreement shown by this comparison (Table 5.12) adds confidence to the approach used for representing boundary conditions in the CFD model when the flow is driven by combined buoyancy and wind forces.

Table 5.12: comparison of internal vertical pressure differences

Simulation	$p_2 - p_1$ (pa)	
	Eq (5.9) of Hunt & Linden (2001)	CFD profile (Figure 5.37)
1	26.38	26.34
2	26.26	26.25
3	25.27	25.10

5.7 CFD investigations using CFX5.6

As discussed in section 4.8, CFX4.4 and CFX5.6 are two fundamentally different CFD codes. All simulations run in CFX5.6 are obtained by a transient evolution of the flow from the initial conditions provided by the user (or automatically generated by the solver). The solution of the steady state simulation does not depend on the initial conditions, nor on the timestep used to arrive at the steady state. Because CFX5 solver is a coupled, fully implicit solver, when a steady state solution is of interest, the timestep used can be as large as possible to minimise the number of iterations required to obtain the steady state flow. The 'timestep' used for a steady state solution is a pseudo-time, which can be treated as an under-relaxation factor. For a transient solution, a real timestep is needed to advance the whole flow system and within each real timestep a number of inner loop iterations are needed to ensure a converged solution is obtained at each real timestep. A steady state solution can also be achieved using a transient procedure, but the CPU computing time is dramatically increased (CFX5.6 2003).

In this section, techniques for modelling benchmark 1 using CFX5.6 are discussed. Both steady and transient state investigations are conducted in order to examine the capability of CFX5.6 to model natural ventilation flows driven by combined wind and buoyancy forces.

5.7.1 Boundary conditions

Boundary conditions used in CFX5 to model benchmark 1 cases are 'Opening', 'Wall', 'Symmetry Plane' and 'Fluid Sub-domains'.

- Opening boundary condition

An Opening boundary condition allows the fluid to cross the boundary surface in either direction, i.e. into the domain, out of the domain or simultaneously. For the Opening boundary in CFX5.6, users can set pressure and direction, which is to with the 'pressure boundary condition' used in CFX4 (section 5.2.3). The same method used for modelling loss coefficients at ventilation openings described in section 5.1.3.2 was applied in CFX5.6.

- Wall boundary conditions

Similarly as used in CFX4, no slip wall boundary was used in CFX5.6 simulations (the velocity of the fluid at the Wall boundary is set to zero). The heat source was modelled as Wall type boundary with a constant heat flux and all other Walls were assumed adiabatic. The RNG $k-\varepsilon$ model in CFX5.6 uses scalable wall function to avoid the fluid domain being over-refined. The scalable wall function ensures that the first cell used for CFD calculations dose not drop in the viscous sub-layer near walls.

- Symmetry plane boundary

These are applied in the same way as CFX4 (section 4.6.4).

- Fluid sub-domains

In CFX5 the porous medium was represented using a fluid sub-domain. This enables the user to define a flow domain with different properties (resistance) to those in the main domain. These resistances, which include a linear resistance coefficient (kg/m^3s^{-1}) and the quadratic resistance coefficient (kg/m^4), are used to achieve a pressure drop after the working fluid flows through the sub-domains, similar to flow through a porous medium boundary in CFX4.

5.7.2 Convergence control for steady state

For natural ventilation driven by buoyancy, a physical timestep control on the governing equations is required. This timestep is used to under-relax the governing equations. However, it was found to be difficult to control convergence using CFX5.6 for steady state modelling of the benchmark 1 cases. Various control techniques were applied in order to assist the convergence, but fully converged solutions were not attainable. Root Mean Square (RMS) residuals were used to monitor the convergence of the flow system. The target residuals should be in the range of 10^{-6} to 10^{-4}.

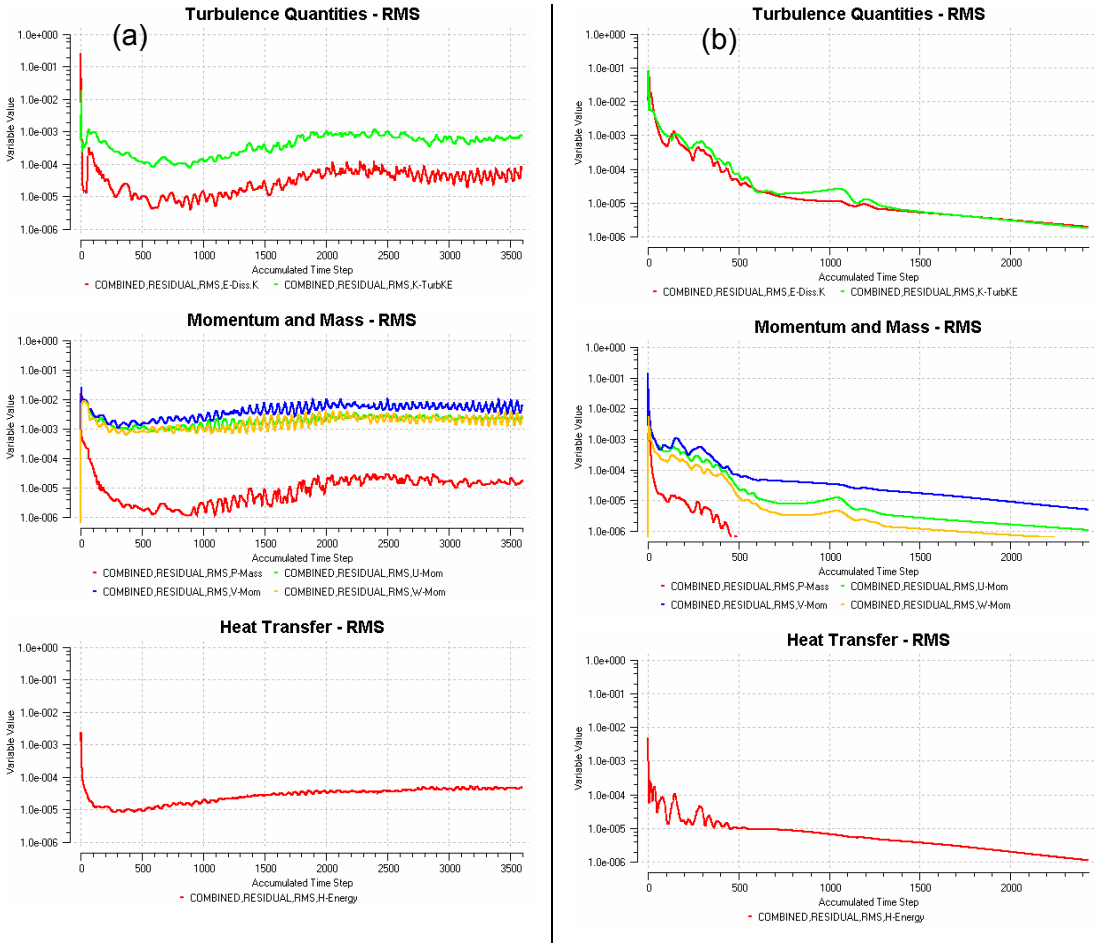

Figure 5.38 Typical convergence history of CFX5.6 for steady state simulations, (a) with buoyancy production terms in the transport equations of k and ε, (b) without.

A typical convergence history for CFX5.6 is shown in Figure 5.38. The RMS residuals show that the solution has not converged in Figure 5.38a, but has converged in Figure 5.38b. The same geometry and boundary conditions were used for the two simulations (Table 5.2, no wind effect). The only difference for them is that the buoyancy production terms in the transport equations of k and ε were invoked in the simulation of Figure 5.38a, but were ignored in the simulation of Figure 5.38b (Eqs (4.32 & 4.33)). The convergence is most likely to be influenced by the buoyancy terms in the transport equations of k and ε. The CFD results of the non-converged simulations showed unsteady behaviour of the thermal plumes and the interface height (see the animations referred to the following section).

5.7.3 Steady state simulation results

The evolution of the non-converged steady state solutions using CFX5.6 for benchmark 1 were generated and presented as animation files in which the details of the flow development could be observed based on pseudo time scales. Together with this thesis, a CD is provided and all the animation files are included (the files can also be found at (www.iesd.dmu.ac.uk/~yingchun/ThesisCD/). The names of animation files start with a letter 'A' followed by section numbers, and if there is more than one animation files in one section, Arabic numbers are used in sequence. For example, in this section there are two animation files which show the flow development of steady state calculations of benchmark 1.

A-573-1.gif: the flow development of benchmark 1 using un-structured mesh.

A-573-2.gif: the flow development of benchmark 1 using structured mesh.

Converged solutions for benchmark1 were achieved without using the buoyancy production terms in the transport equations of k and ε. The resulting temperature field for purely buoyancy driven flow is shown in Figure 5.39. The thickness of the stratification using a CFX5.6 calculation remained large compared with the analytical model and Figure 5.10a. This is thought to be caused by the absence of the buoyancy production terms in k and ε equations (Eqs (4.32 and 4.33)). After achieving the convergence, the buoyancy terms were invoked to test their influences on stratifications. It was found that these terms reduced the thickness of the interface, however, the RMS residuals increased rapidly and the convergence criteria could not be achieved after 50 to 100 iterations. Therefore, the difficulty of convergence for the steady state solution using CFX5.6 remained.

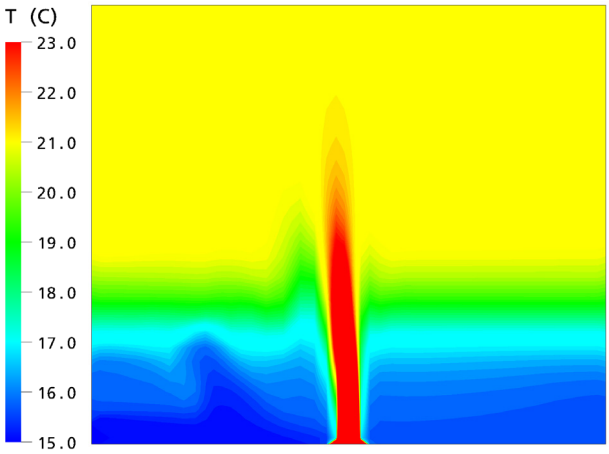

Figure 5.39 Temperature contour for a converged solution using CFX5.6 without buoyancy production terms in k and ε equations, structured mesh, $Fr = 0$.

5.7.4. Convergence control for transient state

Transient simulations require real time information to calculate the flow field at user-defined time intervals. In this simulation the buoyancy production terms in the k and ε equations (Eqs (4.32 & 4.33)) were used. It is possible that transient behaviour might be present when simulations which are run in steady state do not converge. If running a steady state simulation and reducing or increasing the physical timestep size, the period of oscillation of the residual plot changes in proportion to the physical timestep size, then the phenomenon is most likely to be a numerical effect (CFX5 2003); if the period stays the same, then it is probably a transient effect, so a transient simulation should be attempted. However, the residuals of the steady state simulations (section 5.7.2) were not very clear to examine whether the non-convergence of the flow system was caused by transient phenomena or numerical effects. In CFX5, a transient solution can always be attained regardless of whether the convergence is caused by numerical or transient effects. A transient calculation was conducted using CFX5.6 by setting a real timestep and 10 inner iterations on each timestep. The size of the timestep was varied (see below).

In order to achieve converged solutions for each time step, very short time intervals were needed initially, e.g. 0.1s, then 0.3s and 0.5s were used. When the convergence of each real time step could be reached within two or three

inner loop iterations, the size of the timestep was increased to accelerate the calculation. Figure 5.40 shows the convergence history of a transient simulation for $Fr = 0$ using a structured mesh.

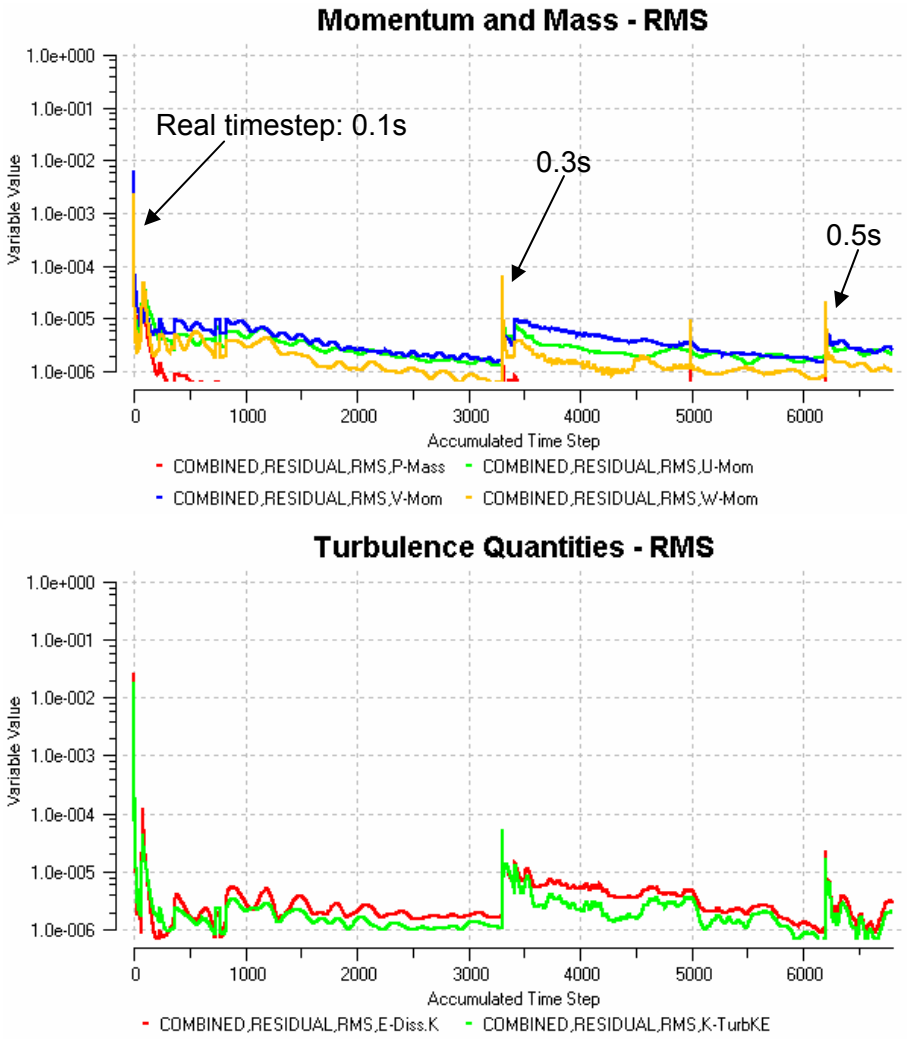

Figure 5.40 Transient simulation convergence history, structured mesh, $Fr = 0$

5.7.5 Transient state simulation results

The resulting temperature field within the domain at 1200 seconds is shown in Figure 5.41. This result shows a reduced stratification thickness compared with Figure 5.39 due to the use of the buoyancy production terms in the k and ε equations.

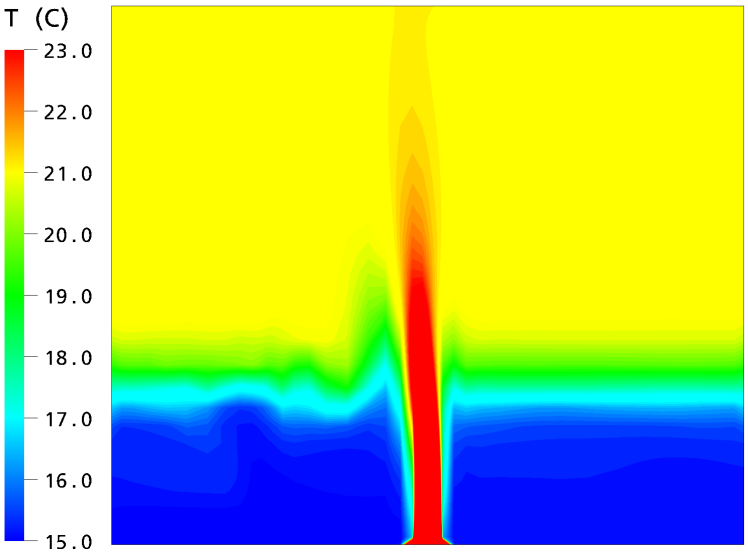

Figure 5.41 Temperature field of the domain by transient simulation after 1200s real time, using structured mesh, $Fr = 0$

To determine whether a steady state solution was reached or not by the transient simulations, the transient calculation was continued until the solution remained unchanged.

The flow development within the domain can be examined using the animation files produced from the transient simulations. From these files, the flow phenomena can be clearly observed.

A-575-1.mpg (transient flow of benchmark 1, $Fr = 0$): This animation shows the flow development within the ventilated space driven purely by buoyancy. The heat source generates an uprising thermal plume which entrains and warms the surrounding air. The warm air reaches the ceiling then spreads downwards. A sharp stratification is produced when the solution of the flow field is unchanged.

A-575-2.mpg (transient flow of benchmark 1, $Fr = 9$): Using the previous simulation result (Fr =0) as the initial condition, a pressure drop was imposed across the ventilation openings. The interface was then gradually increased and the temperature above the interface decreased, which can be examined when viewing the animation.

5.8 Summary

In this chapter, the development of benchmark 1, displacement natural ventilation flow driven by combined wind and buoyancy forces, has been addressed. Most of the steady state simulations were conducted using the RNG $k-\varepsilon$ turbulence model. The standard $k-\varepsilon$ model and the Low Reynolds number $k-\varepsilon$ were also used for a few cases in order to compare the effects of turbulence models. The predictions of RNG model are closer to the analytical models and salt bath experiments than the other two turbulence models used.

Both assisting wind and opposing wind effects were considered for the development of benchmark 1. In order to achieve the convergence of the flow system using CFX4.4, it has been found that the use of false timesteps was essential to under-relax the governing equations.

A series of CFD simulations have been conducted to investigate the dependency of the key natural ventilation design parameters (interfaces, temperature gradients, reduced gravities) for both assisting and opposing wind effects, size of ventilation openings and heat source strengths. Using the modelling techniques developed in sections 5.2 and 5.3, the CFD results offered good qualitative (Tables 5.8 and 5.10) and quantitative (e.g. sections 5.3 and 5.4) agreement compared with the analytical models and salt bath experiments of Hunt & Linden (2001, 2005). This showed the capability of CFD to modelling natural ventilation flows in a simple ventilated enclosures driven by buoyancy combined with wind forces.

The ventilation flow rates for opposing wind cases were not examined in this chapter. The quantitative comparisons of reduced gravities between CFD and analytical model showed good agreement and this is assumed to be a result of relatively accurate predictions of ventilation flow rates, which has been discussed in section 5.3.

In order to examine the volume flow rates through the ventilated space of benchmark 1, the experimental results of Hunt & Kaye (2001) were used to validate CFD predictions. Close agreements were achieved (Figures 5.34 & 5.35). It is concluded that the ventilation flow does not depend on the interface

position but the driving forces and the ventilation opening sizes, e.g. ventilation flow rates were well predicted by CFD even when the interface heights were over or under-predicted (Figures 5.16a & 5.17). The relatively accurate predictions of the temperature field of the domain (represented by the reduced gravity, i.e. Figures 5.16b & 5.18b) showed that a relatively accurate amount of heat was taken out of the space by the ventilation flow. Both experimental results and CFD predictions agreed well with the analytical solution of Morton et al (1956).

The time dependent flow development of benchmark 1 was investigated using CFX5.6, the resulting temperature fields showed similar performances between the two CFD codes. The animations produced by CFX5.6 showed the development of the natural ventilation flow dynamically and they were used to provide a good understanding of the processes of natural ventilation flows.

Chapter 6

CFD modelling of a single-storey building with an atrium

6. CFD modelling of a single-storey building with an atrium

The capability of CFD for modelling buoyancy-driven flows in a single space connected to a tall atrium is investigated in this chapter (benchmark 2). Useful knowledge has been obtained from the successful modelling strategies used in Chapter 5 for benchmark 1, e.g. the airflow features could be well predicted without modelling external fluid domains and a porous medium boundary could be used when the vertical thermal plume could not be maintained due to the impinging effect of the inflow momentum. In this chapter the loss coefficients at different locations are examined to ensure that an accurate effective ventilation opening size is used. The physical parameters of the fluid domain, such as total effective opening size, atrium height, atrium outlet opening size and atrium inlet opening size were varied in order to test the reliability of CFD predictions.

The definition of benchmark 2 is given in section 6.1, followed by the boundary conditions used. Loss coefficients at different locations (due to expansion or discharge) and initial simulations are discussed in sections 6.3 and 6.4. Simulation conditions and mesh dependency test are given in sections 6.5 and 6.6. Results of the CFD simulations for benchmark 2 are given in section 6.7 in which key design parameters, such as interface heights, temperature gradients and ventilation flow rates are investigated. The effects of geometrical parameters (i.e. floor to ceiling height, floor plan depth and atrium width) and air inlet strategies are also discussed in section 6.7. Finally, in section 6.8, transient flows of the system are conducted in order to examine the airflow features in both the single storey and the atrium at real time scales.

6.1 Definition of benchmark 2

Figure 6.1 shows the airflow system of benchmark 2: a single storey building connected to a tall atrium and with a top-down-chimney (TDC) bringing fresh air from high level. The nature of flow of this benchmark case is similar to benchmark 1. In order to meet the assumptions of the analytical models and experiments, radiation and conduction effects are not considered.

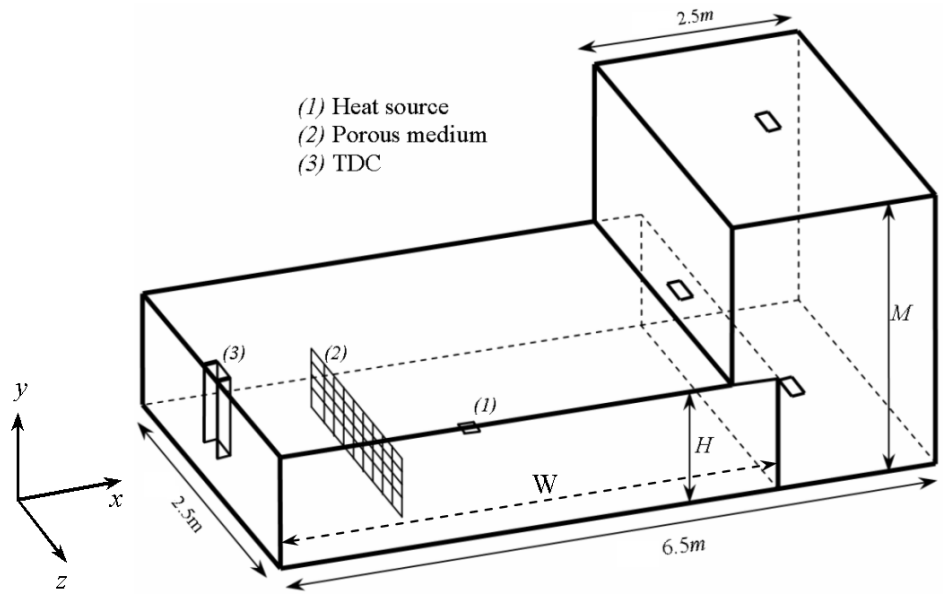

Figure 6.1 Geometrical description of benchmark 2

In the salt bath experiments (Holford & Hunt (2003)) a correction (y_{avs} =1.8cm) for virtual source origin was used due to the non-ideal brine plume. This dimension was added to the height of the storey directly since in CFD simulations, no correction was needed for a pure plume (without initial volume and momentum fluxes) generated by a small area heat source in CFD simulations (section 5.5.3). The ratio of the heat source area and the cross section area of the storey is 2.5×10^{-4} and this has been assumed to be small enough to conduct CFD simulations as a 'point' heat source (section 5.5). Further discussions of the heat source area are made Appendix C.

Initially the ratio of M/H was set to 2.35. It was varied by modifying the atrium height to investigate the influence of the stack effect provided by the atrium. The dimensions of the storey height and atrium height are 3.0m and 7.06m respectively for initial investigations.

Holford & Hunt (2003) assumed a two-layer stratification in the storey (section 2.2.5). The temperature difference between the upper and lower layers observed in the CFD simulations was greater than or equal to 2K. This corresponds to a Rayleigh number of the order of 1×10^{11}. It is therefore reasonable to consider the flow as fully turbulent although in some regions,

e.g. near walls but away from the ventilation openings, the airflow could be laminar or weakly turbulent.

Because the RNG k-epsilon model produced good results for benchmark 1 it was also used in benchmark 2. The central differencing scheme was used to discretize the mass conservation equation; the momentum equations were discretized using the QUICK scheme; for all other equations, the hybrid scheme was used. Pressure coupling is treated using the SIMPLEC algorithms and the Rhie-Chow interpolation technique is used to overcome the problem of decoupling due to co-located meshes.

6.2 Boundary conditions

The heat source was modelled as a no-slip wall boundary condition with a constant heat flux (the same as section 5.2.3). A symmetry boundary bisecting all the ventilation openings and the heat source was used to reduce computing time. All other solid boundaries of the domain, except the ventilation openings, were modelled as no-slip wall boundaries with zero heat flux.

A constant pressure of 0 Pa (relative pressure) was imposed across the TDC inlet and the atrium outlet (as well as the atrium bottom inlet for ventilated atrium case, Figure 2.17b). However, this type of boundary at the ventilation openings in CFD does not represent the true physical nature of the flow due to loss coefficients either by expansion or discharge as discussed in chapter 5. Modelling some of the exterior airflow and moving the pressure boundary condition to the domain boundary can overcome this but has the disadvantage of increasing the computational time and the difficulties of determining the loss coefficient at the opening (section 5.2.3). In this work, the loss coefficients along the airflow path at different locations (1 to 5 in Figure 2.17a and location 6 at Figure 2.17b) are discussed in section 6.3 in detail.

In order to maintain an upright plume a porous medium boundary was applied midway between the TDC and the heat source (Figure 6.1). This is the same means as used in the development of benchmark 1 to prevent the inflow from impinging on the plume directly. In benchmark 2 cases the inflow air is brought in from the TDC and the incoming momentum is parallel with (but opposite to)

the vertical momentum generated by the thermal plume. The impinging effect on the thermal plume is not as strong as the benchmark 1 cases. However, after the incoming air reaches the bottoms of the storey, it spreads into different directions and builds up horizontal momentum which still has the impinging effect on the thermal plume. A piece of porous medium boundary is needed to partially block this effect and maintain an upright plume. In practice, ventilation systems are usually designed to minimise draughts, so the indoor airflow pattern in natural ventilation system is commonly dominated by rising buoyant plumes.

6.3 Loss coefficients for CFD modelling

6.3.1 Definition of effective opening areas

The arrangement of openings of the benchmark 2 case (Figure 2.17) is different to that of the benchmark 1 cases (Figure 5.4). Loss coefficients at different locations along the flow paths need to be considered. As predefined in section 2.2.5 an individual effective opening area at different locations can be expressed by (c.f. Eq (2.26))

$$A_i^* = \sqrt{2} C_{di} a_i \qquad \text{Eq (6.1)}$$

where a_i is the individual opening area; i indicates the location of an individual effective opening along an airflow path, which may include the top-down-chimney (TDC) inlet A_1^*, the TDC A_2^*, the storey inlet A_3^* (TDC outlet), the storey outlet A_4^*, the atrium top outlet A_5^* and the atrium bottom inlet A_6^*.

The total effective opening areas can be obtained using Eq (2.28). The individual or total effective opening areas used in this research are summarised as followings:

The total effective opening area of the flow path inFigure 2.17 (a), A_t;

$$\frac{1}{A_t^2} = \frac{1}{A_{tot-5}^{*2}} = \frac{1}{2}\left(\frac{1}{C_{d1}^2 a_1^2} + \frac{1}{C_{d2}^2 a_2^2} + \frac{1}{C_{d3}^2 a_3^2} + \frac{1}{C_{d4}^2 a_4^2} + \frac{1}{C_{d5}^2 a_5^2} \right) \qquad \text{Eq (6.2)}$$

The effective opening area for the single storey, A_s;

$$\frac{1}{A_s^2} = \frac{1}{A_{tot-4}^{*2}} = \frac{1}{2}\left(\frac{1}{C_{d1}^2 a_1^2} + \frac{1}{C_{d2}^2 a_2^2} + \frac{1}{C_{d3}^2 a_3^2} + \frac{1}{C_{d4}^2 a_4^2}\right) \quad \text{Eq (6.3)}$$

The effective opening area for atrium upper opening, A_u;

$$\frac{1}{A_u^2} = \frac{1}{A_5^{*2}} = \frac{1}{2}\left(\frac{1}{C_{d5}^2 a_5^2}\right) \quad \text{Eq (6.4)}$$

The effective opening area for atrium bottom opening, A_b;

$$\frac{1}{A_b^2} = \frac{1}{A_6^{*2}} = \frac{1}{2}\left(\frac{1}{C_{d6}^2 a_6^2}\right) \quad \text{Eq (6.5)}$$

These effective opening areas are used for the analysis of the CFD results in section 6.5.

6.3.2 Loss coefficients at different locations

Without modelling the external fluid domain for benchmark 2 the loss coefficient at the TDC inlet C_{d1} is treated as described in chapter 5 (section 5.1.3.2), for example, by applying pressure boundary condition with zero relative pressure C_{d1} =1.0. The same method was used for the atrium top outlet a_5 (with C_{d5} =1.0) and the atrium bottom inlet a_6 (with C_{d6} =1.0). Therefore the effective opening areas of the atrium top outlet (A_u) and the atrium bottom inlet (A_b) are $\sqrt{2}a_5$ and $\sqrt{2}a_6$ respectively.

The loss coefficient of the TDC shaft (C_{d2}) is not due to the physical processes of expansion and discharge like sharp openings along the system but due to the pressure losses along the TDC caused by friction. As discussed in section 5.2.3 the thermal driving force of natural ventilation flows is normally very small, so the pressure losses due to frictions along the TDC may be significant and need to be quantified. Designers need to know if the driving force is sufficient enough to overcome all the losses along the flow paths. In order to quantify the magnitude of the pressure losses along a TDC, an aspect ratio l/d is defined (l is the length and d is the diameter of the TDC). For a cylindrical top-down-chimney drawing air of density ρ_o at a ventilation flow

rate Q, the frictional pressure loss ΔP_{TDC} has been defined by (Hunt & Holford (1998)) as

$$\Delta P_{TDC} = \rho_o Q^2 / 2C_{d2}^2 a_2^2 \qquad \text{Eq (6.6)}$$

where $$C_{d2} = 1/(4f(l/d)) \qquad \text{Eq (6.7)}$$

and f is a friction factor.

From Eqs (6.6 and 6.7) the frictional pressure losses along a TDC increases with ventilation flow rates, increases as the TDC area a_2 and the loss coefficient C_{d2} decrease; in contrast, the loss coefficient C_{d2} decreases as the friction factor f and the aspect ratio of l/d increase. The friction factor f is a function of the Reynolds number of the airflow in the TDC. Hunt and Holford (1998) suggested a value of f =0.005 for building ventilation applications.

For CFD simulations, the TDC is not cylindrical but has a rectangular cross section. The ratio of l/d was therefore replaced with the ratio of the TDC length l to its hydraulic diameter $\overline{d}$, which is defined by

$$\overline{d} = 4m \qquad \text{Eq (6.8)}$$

where m is the hydraulic mean depth, expressed by

$$m = a_2 / s \qquad \text{Eq (6.9)}$$

where s is the perimeter of the TDC.

Airflow leaving the TDC experiences a sudden expansion. The cross section of the TDC is much smaller than the cross section of the single storey the losses due to this expansion effects can be ignored. Therefore unity can be used for the loss coefficient of the TDC outlet C_{d3} (Nakayama & Boucher (1999), page 119)

The storey outlet is a free opening within the computational domain which experiences losses due to both contraction and expansion. A value of 0.63 for

the loss coefficient of the storey outlet C_{d4} was assumed here, to match that used in the analytical models and experiments by Holford & Hunt (2003).

6.4 Initial simulations

The conditions used for initial simulations are M/H = 2.35 with total effective opening area A_t = 0.072m^2 and buoyancy flux B = 0.0055m^{4}s^{-3}. As discussed in the definition of benchmark 2 (section 6.1) the storey height is 3.0m and the estimated Rayleigh number is in an order of 1.0×10^{11}. When this height is reduced and the same ratio of M/H is used the non-dimensional analysis of benchmark 2 cases should be consistent providing the airflow within the flow system is turbulent (Holford & Hunt (2003)). For example, if the key dimensions (H and M) of the CFD domain are 10 time greater than the experimental boxes the storey and atrium heights are 1.58m and 2.37m. This gives a Rayleigh number at the order of 1.0×10^{10}. The onset of turbulence is said to occur when the Rayleigh number is in a range of 10^6 to 10^9 (Jones & Whittle (1992)). It is therefore reasonable to assume that the flows investigated for the two storey heights (3.0m and 1.58m) are both turbulent. The non-dimensional results are expected to be the same. The non-dimensional analysis of the benchmark 2 cases enables the wide applications for the benchmark.

The resulting velocity fields for the two storey heights are shown in Figure 6.2. For both cases the rising plumes from the heat sources and the airflows from the storey outlet into the atrium can be observed clearly. Air is then driven out through the atrium top outlet. The thermal plumes here have similar performances to the plume discussed in section 5.3.1, e.g. entraining its surrounding air when it rises and forming an interface at some vertical location which separates a warm buoyant layer above a cool ambient layer.

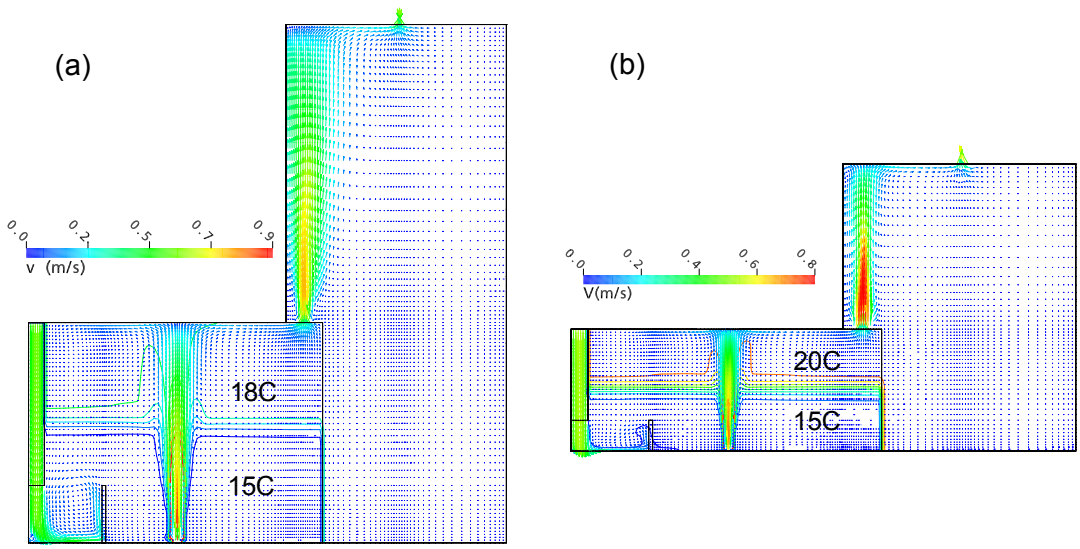

Figure 6.2 Typical speed vectors of the domain (a) 3.0m storey height and 200W heat source strength and (b) 1.58m storey height and 100W heat source strength. For both cases the dimensionless total effective opening area A_t / H^2 = 0.008m^2.

The incoming air is brought from the high level of the TDC and the incoming momentum is vertically downwards. When this air reaches the bottom of the TDC it spreads horizontally in different directions and its strength is decentralized. The decentralisation avoids the strong momentum impinging on the vertical plume. However, part of this momentum can still have a relatively strong effect horizontally on the thermal plume. A small piece of porous boundary (the vertical and narrow rectangular box above the floor shown in Figure 6.5) was used to reduce this effect for maintaining a vertically rising plume.

The temperature fields of the domain are shown in Figure 6.3. The vertical thermal plume, position of stratification, warm and cool layers can be clearly observed on the figure.

A fully mixed atrium with uniform temperature was predicted by CFD. However, a stagnant layer at the storey outlet level existed in the atrium when conducting the salt bath experiments (Figure 6.3c). This difference was initially thought to be due to the rapid numerical diffusion of heat in air compared with brine in water. A number of numerical variations were investigated, e.g. using higher order differencing schemes (Appendix B), and setting a very large Prandtl number in Eq (4.31) to reduce the diffusion. However, the air

temperature in the atrium calculated by CFD was still uniform rather than stratified like the salt bath experiments. Time dependent simulations were carried out using CFX4 to investigate the flow development in the atrium. Details of these transient investigations are discussed in section 6.8.

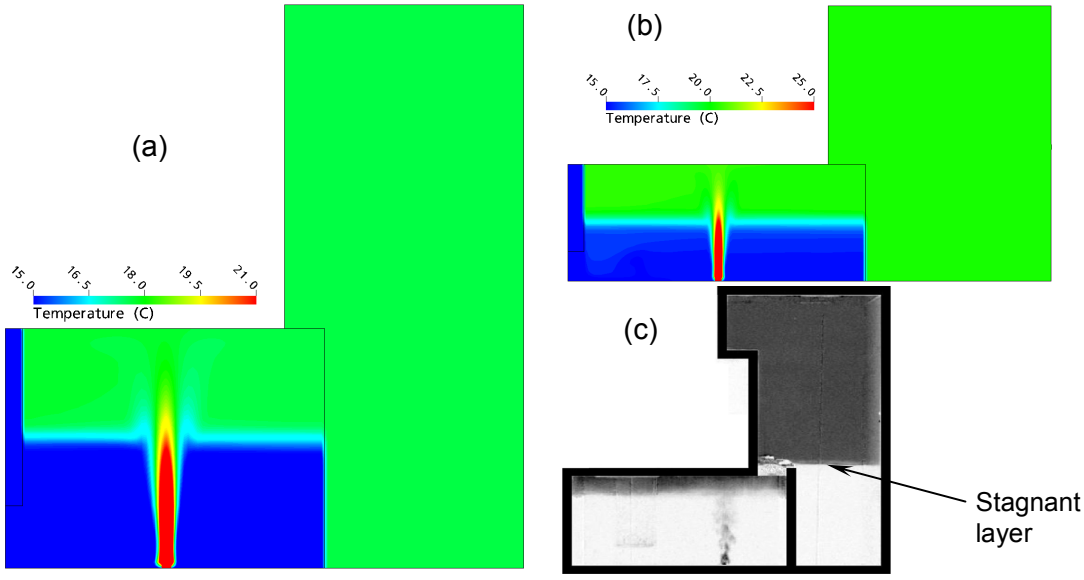

Figure 6.3 Typical temperature fields of the domain (a) 3.0m storey height 200W heat source strength, (b) 1.58m storey height and 100W heat source strength and (c) an illustration of the salt bath experiments (after Holford & Hunt (2003)).

The heat sources for the two initial cases are not the same but this should not affect the non-dimensional analysis because the interface height and non-dimensional reduced gravity are independent on the source strength (Eq 2.31). This point is verified using CFD in section 6.7.4.

The definition of interface position for benchmark 2 is the same as benchmark 1 (section 5.3.3) and the temperature gradients of the domain have similar properties as discussed in section 5.3.2.

Figure 6.4 shows the quantitative results of the two cases discussed above. The results are compared with the analytical solution of Holford & Hunt (2003). The qualitative results for the ratio of M/H = 5.0 is similar to the cases of M/H =2.35 for the two storey heights therefore they are not further discussed.

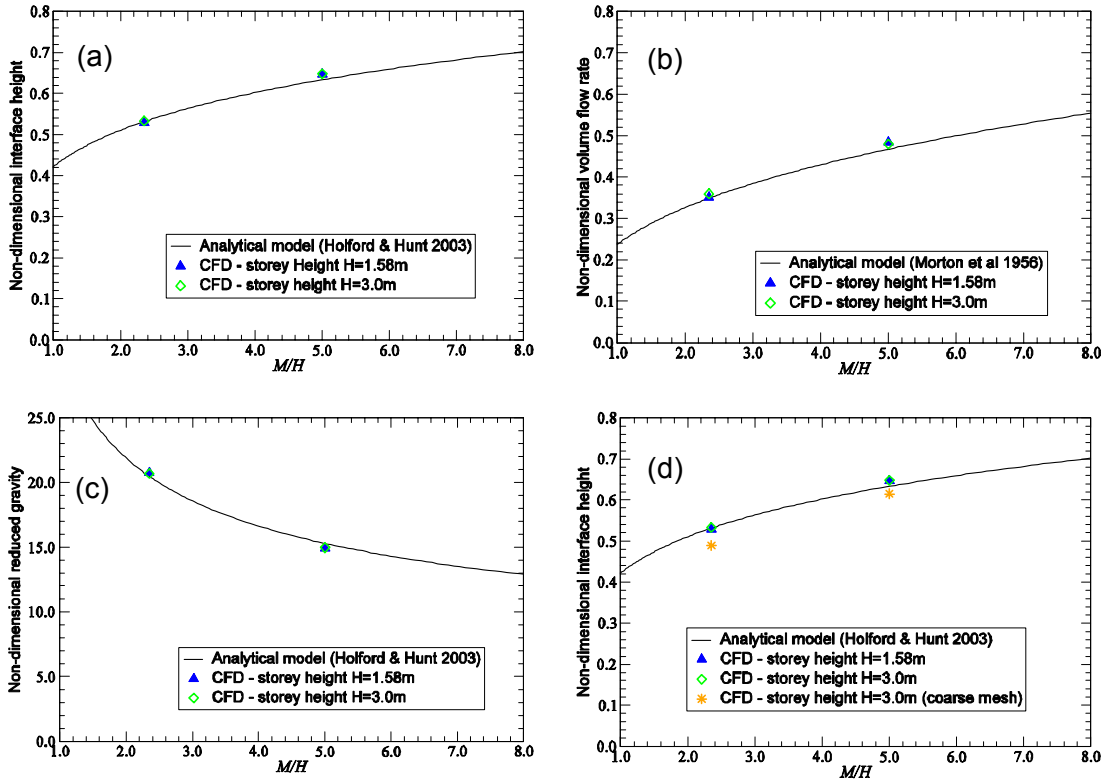

Figure 6.4 Comparisons between CFD and analytical predictions (a) interface heights, (b) volume flow rates and (c) reduced gravities for different storey heights; (d) interface heights (with a coarse mesh for H = 3.0m)

As shown in Figure 6.4 a, b & c, the key non-dimensional parameters predicted by the two storey heights are almost the same. This implies that the non-dimensional quantities of the flow system are not dependent on the physical dimensions when the airflow is turbulent. The number of cells in the computational mesh, for the two cases, is about 150k (with the storey height 1.58m) and 250k (with the storey height 3.0m). The cell number of cases with a 3.0m storey height was reduced to 145k and the prediction of interface height using this coarse mesh is shown in Figure 6.4d. Clearly, the interface heights were under-predicted by the coarse mesh. This comparison, using different mesh densities, shows that, in order to achieve the similar performance using CFD large dimension needs more cells to solve the flow system. This will potentially increase the CPU computing time. Considering both accuracy and the CPU computing time a storey height of 1.58m is used for the development of benchmark 2 cases.

6.5 Simulation conditions

Table 6.1 shows a summary of the analytical analysis of section 2.2.5. Some of these analytical predictions have been validated by salt bath experiments conducted by Holford & Hunt (2003).

Table 6.1 Summary of analytical analysis of Holford & Hunt (2003)

Conditions	results						
	$\frac{h_s}{H}$	$\frac{h_a}{H}$	$\frac{g'_s}{CG'_H}$	$\frac{g'_a}{CG'_H}$	Q_s	Q_{up}	Q_{low}
$\frac{A_t}{H^2}\uparrow;\ \frac{A_b}{H^2}=0$	↑	—	↓	↓	↑	↑	—
$\frac{M}{H}\uparrow;\ \frac{A_b}{H^2}=0$	↑	—	↓	↓	↑	↑	—
$\frac{A_u}{H^2}\uparrow;\ \frac{A_b}{H^2}=0$	↑	—	↓	↓	↑	↑	—
$\frac{A_b}{H^2}\uparrow$	↓	↑	↑	↓	↓	↑	↑

Note: The symbols used in table 6.1 denote '↑ increase', '↓ decrease' and '— not applied'.

To investigate the analytical models developed by Holford & Hunt (2003) CFD simulations for different parameters (first column of Table 6.1) were carried out. The simulation conditions are summarized in Tables 6.2 to 6.5 (see also Appendix D)

Table 6.2 Simulation conditions for varying total effective opening areas

Operating conditions for all cases	A_t (m^2)	$A_t / H^2 \times 10^{-2}$
Ambient temperature: 15 ºC Ratio of the atrium height and the room height M/H =2.35 Buoyancy flux B =2.75×10^{-3} (m^{4}s^{-3})	0.015	0.60
	0.020	0.80
	0.028	1.12
	0.040	1.60
	0.056	2.25
	0.076	3.05
	0.099	3.95
	0.119	4.75

Table 6.3 Simulation conditions for varying the stack height

Operating conditions for all cases	M (m)	M/H
Ambient temperature: 15 ºC Total dimensionless effective opening area A_t/H^2 =0.80×10^{-2} Buoyancy flux B =2.75×10^{-3} (m^{4}s^{-3})	2.37	1.5
	3.72	2.35
	6.32	4.0
	7.90	5.0
	11.06	7.0

Table 6.4 Simulation conditions for varying effective atrium top outlet area

Operating conditions for all cases	A_u (m^2)	A_u/H^2 ×10^{-2}
Ambient temperature: 15 ºC The storey dimensionless effective opening area A_s/H^2 =1.77×10^{-2} and M/H =2.35 Buoyancy flux B =2.75×10^{-3} (m^{4}s^{-3})	0.015	0.60
	0.030	1.20
	0.056	2.24
	0.067	2.69
	0.095	3.79

Table 6.5 Simulation conditions for varying effective atrium bottom area

Operating conditions for all cases	A_b (m^2)	A_b/H^2
Ambient temperature: 15 ºC The total dimensionless effective opening area A_t/H^2 =4.75×10^{-2} and M/H =2.35 Buoyancy flux B =2.75×10^{-3} (m^{4}s^{-3})	0.00	0.00
	0.10	0.04
	0.15	0.06
	0.275	0.11
	0.45	0.18

The convergence criteria for benchmark 2 were the same as those for benchmark 1: (i) the enthalpy residual to be less than 1% of the total heat entering the domain; and (ii) the absolute values of all variables at the monitoring point should not change by more than 0.1% for the last 100 iterations. It took about 4000 iterations for the cases listed in the above tables (6.2 ~ 6.5) with a mesh of approximately 1.65×10^5 cells to achieve the convergence criteria.

6.6 Mesh investigation

The effects of mesh resolution were tested using three different mesh densities. Structured meshes generated by CFX4 were used. Mesh1 is about 75k cells. Mesh2 and Mesh3 are about 165k and 320k cells. Figure 6.2 shows the surface mesh structure of Mesh2. For Mesh1 and Mesh3, cells were reduced/added uniformly over the whole domain.

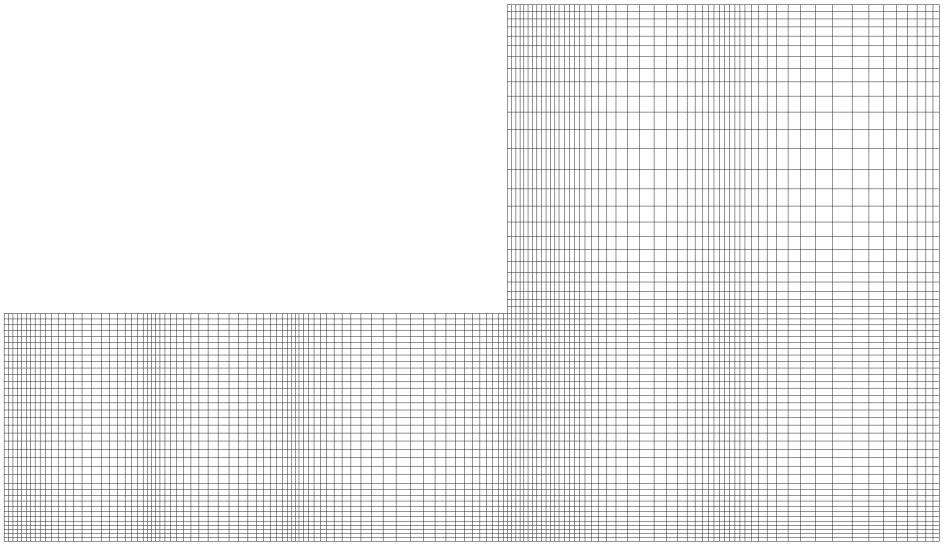

Figure 6.5 Typical mesh structure used for simulations of Benchmark 2

Simulations were carried out to test the mesh dependency for benchmark 2. The conditions selected here are from Table 6.2 in section 6.5 for A_t / H^2=0.0112.

The two computed mean velocities at $x = 2.025$m (in the middle of the thermal plume) and y =0.79 m (half storey height) for the three mesh densities are given in Figure 6.6. Clearly, results for Mesh1 are relatively different to that of Mesh2 and Mesh3 which suggests that the resolution of Mesh1 is not fine enough.

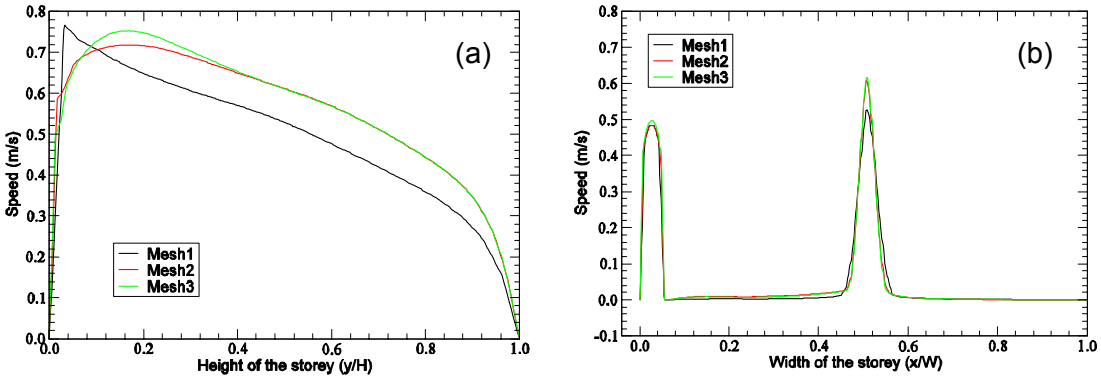

Figure 6.6 Mean velocities at different locations in the domain, (a) x =2.025m and (b) y =0.79 (refer to Figure 6.1)

Further investigation of the temperature field in the domain is given in Figure 6.4. The temperature field with Mesh1 indicates a lower interface height (18% lower than Mesh1 and Mesh3). The performance of Mesh2 and Mesh3 in predicting the interface height of the domain is similar (4% difference). However the interface predicted by Mesh3 was slightly higher than Mesh2. This is thought to be due to the higher maximum vertical speed of the thermal plume calculated by the fine mesh. The finest mesh (Mesh3) resolved the largest vertical speeds and a relatively accurate height of interface compared with the other two mesh densities at the same location (Figure 6.7).

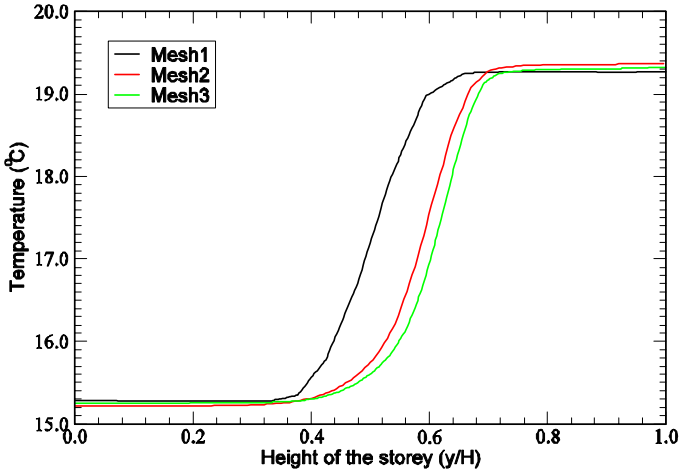

Figure 6.7 Temperature field of the domain on a line at $x/L = 0.5$ on the symmetry plane (refer to Figure 6.1).

In Figure 6.7, the differences in temperature of the upper and lower layers are very small for all three mesh densities. This may imply that the interface

positions are more sensitive to mesh densities while the reduced gravities of the flow field (which depend on the temperature) are not.

The mass flow rates through the storey for these mesh densities were only slightly different. There was less than 2% difference between Mesh1 (0.0116 kg/s) and Mesh2 (0.0114 kg/s) and less than 1% difference between Mesh2 and Mesh3 (0.0115 kg/s). Considering both accuracies and the CPU computing time Mesh2 was used for the development of benchmark 2.

6.7 Analysis of results for benchmark 2

6.7.1 Effect of total effective opening area

To investigate the dependency of interface positions, reduced gravities and volume flow rates of the single storey on the total effective opening area A_t (Eq (6.2)) of the system (Figure 6.1) a series of simulations were conducted (Table 6.2). The simulation results were compared with the analytical model and salt bath experiments and good agreement between the three techniques was achieved.

The predictions of non-dimensional interface heights and volume flow rates are shown in Figure 6.8.

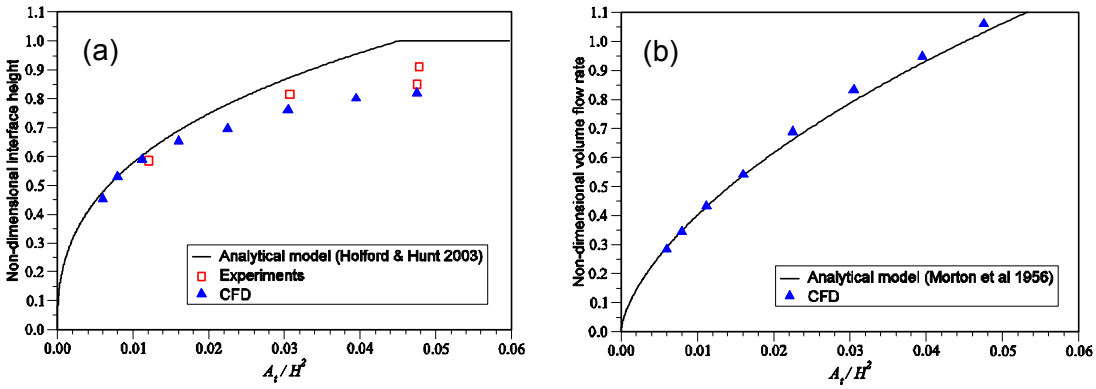

Figure 6.8 Variation of (a) non-dimensional interface heights and (b) non-dimensional volume flow rates with non-dimensional total effective areas

The non-dimensional interface height (h_s/H) predicted by the CFD model agreed well with those of experimental and analytical work for non-dimensional total effective areas of A_t/H^2 less than about 0.02 (equivalent to

$h_s / H \approx 0.7$, see Figure 6.8a). For larger values of A_t / H^2 the non-dimensional interface heights were under-predicted. In the CFD simulations, a layer of warm air remained beneath the ceiling for all values of A_t whereas the theory predicted 'complete ventilation' (e.g. h_s / H =1 for $A_t / H^2 \geq 0.0475$). Salt bath experiments showed the same trend as the CFD predictions (Figure 6.8a). This discrepancy is thought to be caused by the assumption of stationary fluid in the hydrostatic buoyant layer in the analytical model for all interface heights. In both the salt bath experiments and CFD simulations, as the stratification level rises and the interface approaches the ceiling, the buoyant layer becomes unsteady and the homogeneous layer breaks down (e.g. the experimental case of Figure 6.3c was the 'complete ventilation' case, however, a layer of denser brine was remained at the level near the ceiling).

Using Eq (2.2), the analytical equation of non-dimensional volume flow for benchmark 2, is given by the ratio of the volume flow in the plume at the interface height ($Q_h = CB^{1/3} h_s^{5/3}$) and at the ceiling H ($Q_H = CB^{1/3} H^{5/3}$)

$$Q_h / Q_H = \left(h_s / H\right)^{5/3} \qquad \text{Eq (6.10)}$$

and the non-dimensional volume flow rates for the CFD simulations were calculated by the volume flow rates through the ventilation system (Figure 6.1) predicted by CFD, over the volume flow rates of the analytical equation (Eq (2.2)) at the ceiling height, Q_s / Q_H. Good agreement was achieved for all non-dimensional total effective opening areas in the predictions of non-dimensional volume flow rates between Eq (6.10) and CFD (Figure 6.8b). This is because the quantity of the volume flow rate predicted by the CFD technique depends on the size of the ventilation openings and the strength of the heat source strength but is not influenced by the position of the interface. There were no experimental data for validating the volume flow rate through the ventilated spaces in the work of Holford & Hunt (2003) which is why the comparisons were only made between analytical equation and CFD predictions for this parameter (Figure 6.8b). Hunt & Kaye (2001) conducted salt bath experiments to validate the volume flow rate through a single space driven by buoyancy. This work was used to validate the ventilation flow rates for benchmark 1

cases (section 5.5). Again, this work will be used for the same purpose for benchmark 2 cases in section 6.7.8.

As in the analytical equation for non-dimensional volume flow rates, using Eq (2.3), non-dimensional reduced gravities were calculated by the ratio of the reduced gravity in the plume at the interface height h_s ($g'_h = (B^2 h_s^{-5})^{1/3} / C$) and at the ceiling ($CG'_H = B^{2/3} H^{-5/3}$) multiplied by entrainment constant C

$$g'_h / CG'_H = (h_s / H)^{-5/3} / C \qquad \text{Eq (6.11)}$$

and the non-dimensional reduced gravities were calculated by the reduced gravities predicted by CFD (Eq (5.5)) for the warm upper layer over the reduced gravity at the ceiling multiplied by entrainment constant, g'_s / CG'_H.

Figure 6.9 shows the comparisons between analytical model, salt bath experiments and CFD for the predictions of non-dimensional reduced gravities. Although non-dimensional interface heights were not well predicted when the values of A_t / H^2 were larger than 0.02 the non-dimensional reduced gravities agreed favourably. This is thought to be due to the relatively accurate predictions of the ventilation flow rates through the system (Figure 6.8b). A reliable prediction of the ventilation flow rate indicated that the correct amount of heat was driven out of the domain by the ventilation flow. The temperature contrast predicted by CFD would therefore reflect this accuracy in the prediction of the reduced gravities (Eq (5.5)).

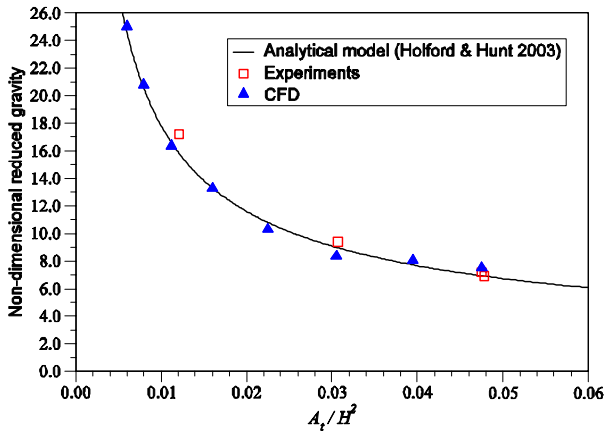

Figure 6.9 Variation of non-dimensional reduced gravities with non-dimensional total effective areas

6.7.2 Effect of atrium top opening area

Variation of interface positions and reduced gravities with atrium outlet opening areas were investigated using CFD. As discussed in section 2.2.5, the intention of using a tall atrium was to provide a large stack effect, and therefore enhance the ventilation flow. However, because the resistance of the atrium outlet is added on the ventilation opening system the tall atrium does not always enhance the ventilation flow through the storey. In Eq (2.28), A^*_{tot-5} can be expressed in the following form using Eqs (6.3 and 6.4)

$$1/A^{*}_{tot-5}{}^{2} = 1/A_t^2 = 1/A_s^2 + 1/A_u^2 \qquad \text{Eq (6.12)}$$

Rearranging Eq (2.28) by Eq (6.12) gives

$$\frac{A_u}{H^2} = \left\{ \left[\frac{C^3 (h_s/H)^5}{(M/H - h_s/H)} \times \left(\frac{A_s}{H^2} \right)^2 \right] / \left[\left(\frac{A_s}{H^2} \right)^2 - \frac{C(h_s/H)^5}{(M/H - h_s/H)} \right] \right\}^{1/2} \qquad \text{Eq (6.13)}$$

CFD predictions of non-dimensional interfaces, volume flow rates and reduced gravities were compared with the analytical predictions of Eqs (6.13, 6.10 and 6.11) and good agreement was achieved (Figures 6.10 and 6.11).

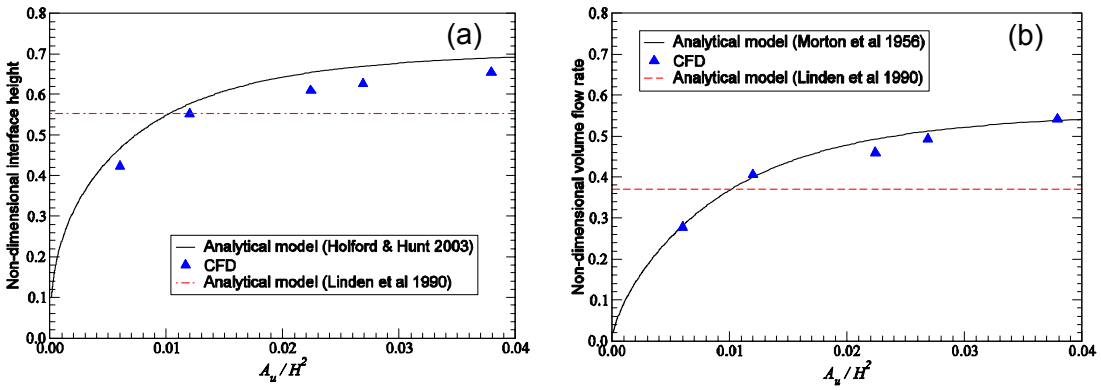

Figure 6.10 Variation of (a) non-dimensional interface heights and (b) volume flow rates with non-dimensional effective atrium outlet areas

CFD slightly under-predicted the non-dimensional interfaces in Figure 6.10a compared with the analytical prediction. This small discrepancy might be caused by the mesh density (recall section 6.6). The finest mesh used (Mesh3) does alter the interface position slightly (Figure 6.6) compared with the mesh size used here (about 165K). Therefore it is reasonable to conclude that this

small under-prediction might be compensated by refining the mesh. However, if the finest mesh size (about 320K) in figure 6.7 was used, the CUP computing time would be doubled and this does not improve the predictions of other key parameters, e.g. volume flow rates and reduced gravities. These parameters had already been well predicted (Figures 6.10b and 6.11) using the current mesh density (about 165K).

The red dashed lines in Figure 6.10 shows the non-dimensional interface height and volume flow rate predicted by the single storey system without the tall atrium. The fluid dynamics of the single storey was the same as that studied by Linden et al (1990) with an exception that a TDC was used here. Below these red dashed lines the tall atrium ($M/H=$2.35) employed in the system does not enhance the flow due to the resistance of the atrium outlet being added to the ventilation system (Figure 6.1). This indicates that the atrium outlet opening is too small and its resistance on the ventilation flow is larger than the enhancement provided by the tall atrium. The actual critical opening size of the atrium outlet can be obtained in Figure 6.10, which is $a_5=\sqrt{2}A_u/2$ =0.018m^2 ($A_u/H^2\approx$0.01, while H =1.58m). This is far too small for a real building practice. The potential resistance of the atrium outlet can be ignored because in real buildings the ventilation openings will not be unrealistic small.

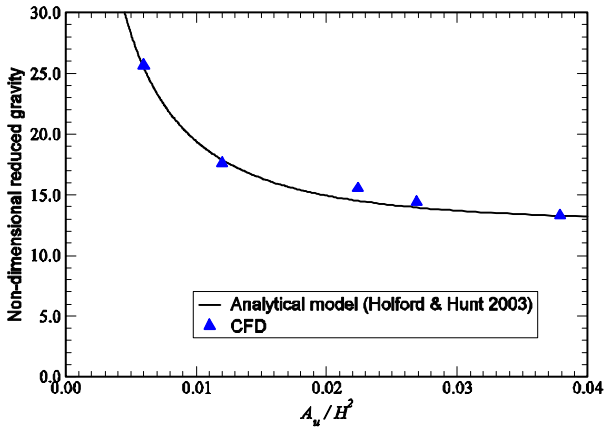

Figure 6.11 Variation of non-dimensional reduced gravities with non-dimensional effective atrium outlet areas

6.7.3 Effect of atrium height

An enhancement of ventilation flow rates in the single storey would be expected as the atrium height is increased when the total effective opening area A_t and the storey height are fixed. The dependency of the non-dimensional interface heights can be tested by rearranging Eq (2.28)

$$\frac{M}{H} = C^3 \left(\frac{h_s}{H}\right)^5 / \left(\frac{A_t}{H^2}\right)^2 + \frac{h_s}{H} \qquad \text{Eq (6.14)}$$

and the non-dimensional quantities of volume flow rates and reduced gravities predicted by CFD could be tested by the Eqs (6.10 and 6.11).

As expected, non-dimensional interface height and volume flow rate were increased when increasing the dimensionless atrium height (M/H). CFD predictions of these parameters agreed favourably with the analytical predictions of Eqs (6.14) and (6.10) in Figure 6.12.

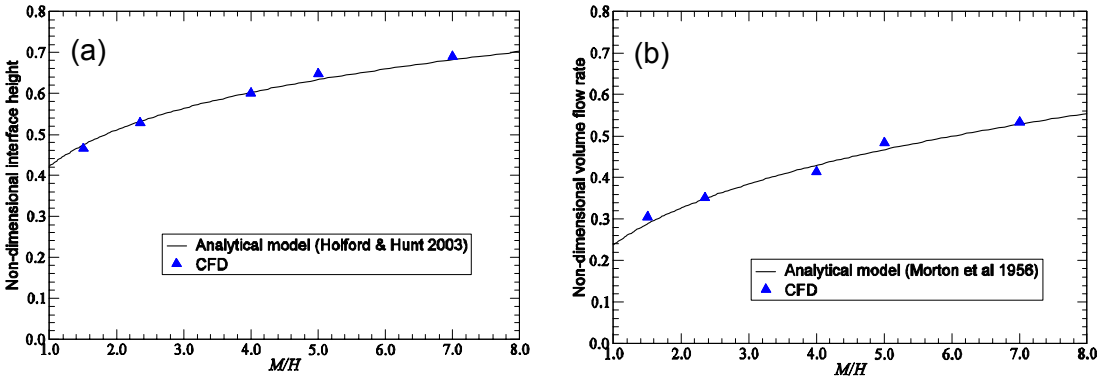

Figure 6.12 Variation of (a) non-dimensional interface heights and (b) volume flow rates with dimensionless atrium height

Ventilation flow rates predicted by CFD (Figure 6.12b) compared well with the analytical predictions therefore a relatively accurate temperature field of the warm upper layer would be expected and consequently an accurate prediction of the reduced gravities (Figure 6.13).

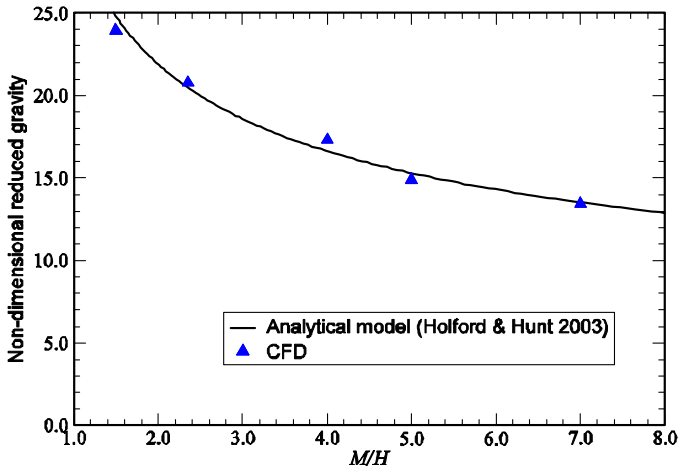

Figure 6.13 Variation of non-dimensional reduced gravities with M/H

Figure 6.14 shows a temperature field with a taller atrium ($M/H = 5$) than Figure 6.3b ($M/H = 2.35$, shown here as reference) where the same total effective opening area was used. In figure 6.14 a higher interface and a cooler upper layer were predicted compared with Figure 6.3b, which indicates that a taller atrium does enhance the ventilation flow for this combination of openings size (A_t = 0.02m^2).

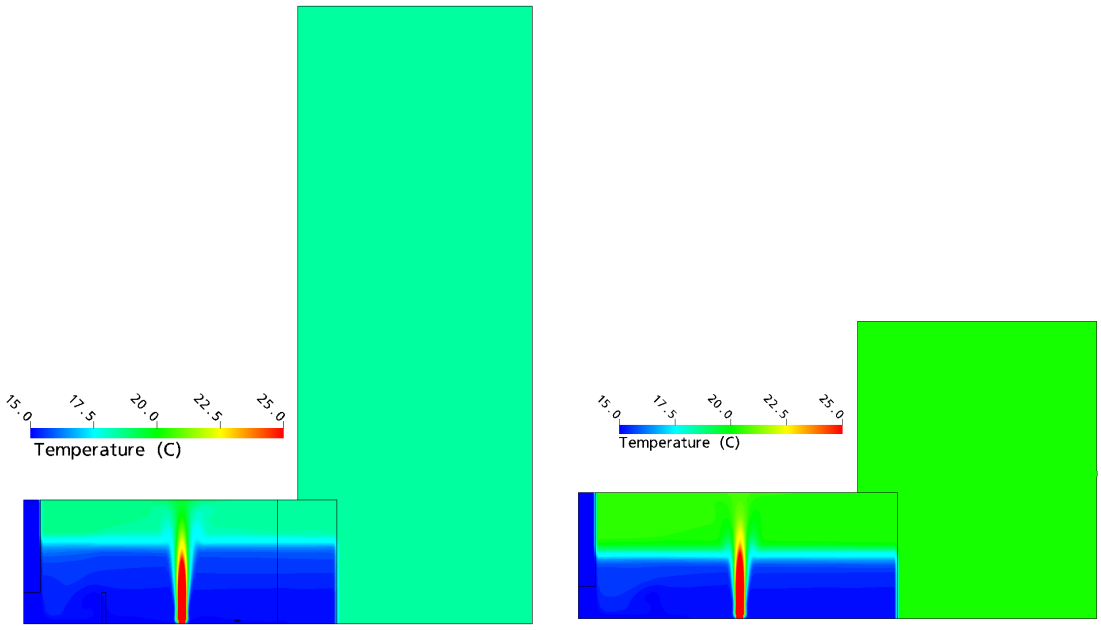

Figure 6.14 Temperature field of the domain with M/H =5 (left), figure on the right is Figure 6.3b, shown here as a reference)

As discussed in section 2.2.5 if there are heat sources in the atrium, for example solar radiation, the effect of solar energy can be treated as an

increase of the atrium height (Eq (2.29)). The simulation conditions in table 6.3 for varying atrium heights can be thought of as equivalent to varying source strengths in the atrium, e.g. M/H = (4.0, 5.0 and 7.0) are equivalent to M/H = 2.35 with B_{solar} = 3.36, 5.40 and 9.47 $\times 10^{-3}$ $m^4 s^{-3}$ (Eq (2.29)).

6.7.4 Effect of source strength

For buoyancy combined with wind cases, the dimensionless interface heights depend on the source strength (section 5.3.6). The natural driving force of benchmark 2 is purely buoyancy. The mathematical analysis of Holford & Hunt (2003) shows that the non-dimensional interface heights in the storey does not depend on the source strength (Eq (2.28)). To investigate the dependency of the source strength on the non-dimensional interface height, volume flow rate and reduced gravity, a CFD simulation with a relatively high heat input (500 W) was conducted. The selected case was from Table 6.2 with A_t = 0.028 m^2.

The resulting temperature field is shown in Figure 6.15a and compared with the previous simulation result with 100W heat input (Figure 15b).

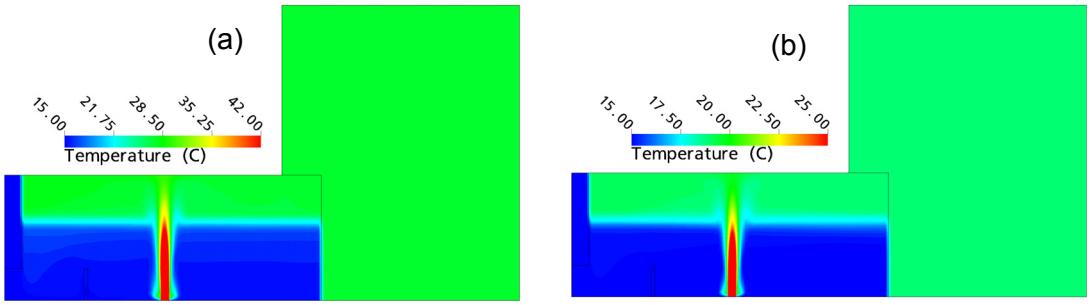

Figure 6.15 Temperature fields of the domain with (a) 500 W and (b) 100 W heat inputs, A_t = 0.028m^2.

The location of the interface height for the two cases is almost identical which indicates the independency of the interface on the source strength. Other non-dimensional quantities (volume flow rates and reduced gravities) are also the same as well. The differences between the two cases are the dimensional ventilation flow rate and the reduced gravity. As expected, the temperature of the upper layer for the case with 500W heat input was much higher than that with 100W heat input (Note that the temperature scales of Figure 6.15a and b

are different). The resulting ventilation flow rate for the high heat input was larger than that for the low heat input. Table 6.6 shows the quantitative comparisons of the two cases.

Table 6.6 Quantitative comparisons of different heat source strength

conditions		h_s (m)	h_s / H	g_s' (m/s^2)	g_s' / CG_H'	Q_s (m^3/s)	Q_s / Q_H
$E = 100$ W	theory	0.941	0.596	0.149	16.4	0.0183	0.427
	CFD	0.929	0.588	0.149	16.35	0.0186	0.4335
$E = 500$ W	theory	0.941	0.596	0.497	16.4	0.0313	0.427
	CFD	0.932	0.590	0.503	16.50	0.0323	0.440

The dimensional quantities (g_s' (m/s^2) and Q_s (m^3/s)) of these two cases show the expected differences (Table 6.6).

6.7.5 Effect of a ventilated atrium

With a ventilation opening at the base of the atrium, more than one airflow path is present (Figure 2.17b) and the airflow features are far more complicated than with an unventilated atrium (section 2.2.5). A series of CFD simulations were conducted in which all physical parameters were fixed, except the area of the low atrium opening. Both qualitative and quantitative results were compared with the analysis and salt bath experiments.

The resulting flow fields for the speed vector and temperature contour of a ventilated atrium are shown in Figure 6.16.

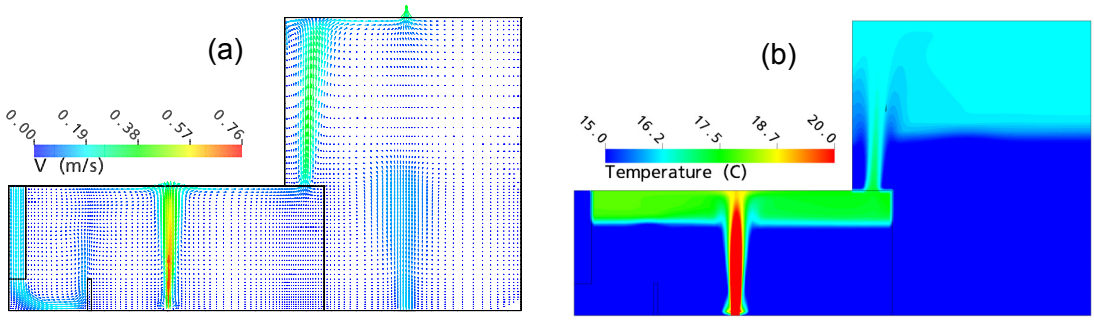

Figure 6.16 Velocity field (a) and temperature contour (b) on symmetry plane of a ventilated atrium case ($A_b / H^2 = 0.11$)

As shown in Figure 6.16a, there was an inflow of fresh air at the bottom of the atrium. The outflow from the storey to the atrium can be considered as a plume-like air jet. This air jet entrains surrounding fresh air and forms a stratification at some level in the atrium similar to the thermal plume in the storey (Figure 6.15b). This is different to the well-mixed atrium discussed in the unventilated atrium case (Figures 6.3a & b). The simulation results for the ventilated atrium were shown in Figure 6.17.

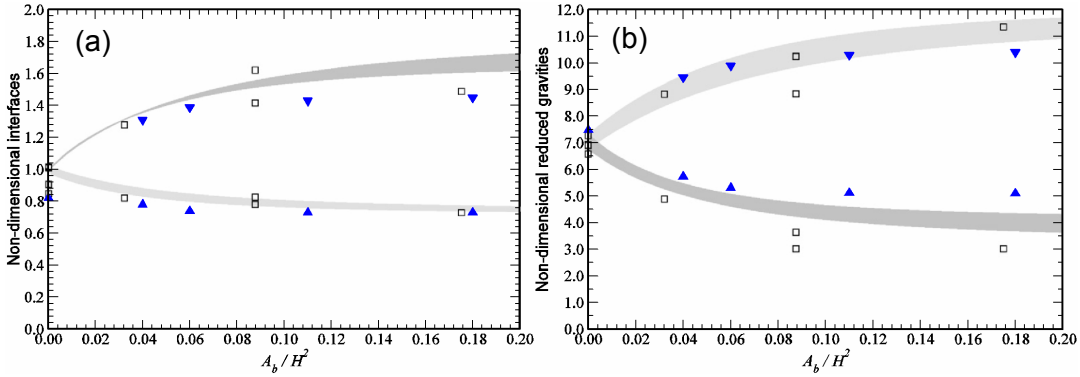

Figure 6.17 Variations of (a) non-dimensional interface heights and (b) reduced gravities in the storey (light shaded bands) and the atrium (dark shaded bands) with variations of A_b / H^2 (after Holford & Hunt (2003)). Squares were from salt bath experiments, triangle symbols were from CFD predictions.

As shown in Figure 6.17, due to the dependence of the loss coefficients on density contrast the effective opening areas of the storey and upper atrium opening do vary slightly which is why the resulting predictions of analytical model were a shaded band rather than solid lines. CFD predictions of non-dimensional interfaces of the storey agreed favourably with the analysis of Holford & Hunt (2003) when the ventilation openings of the atrium bottom were large. For small A_b / H^2 the height of the interface in the storey was under-predicted. The possible reasons for these under-predictions were discussed in section 6.5.3. Both CFD and salt bath experiments experience difficulties in predicting storey interface heights when these heights are near the ceiling. The warm buoyant air of the upper layer is not as stable and uniform as the cases non-dimensional interfaces below 0.7 (Ji et al (2004)).

The height of the interfaces in the atrium were under-predicted by CFD for large A_b while for small A_b CFD predictions agreed well with mathematical analysis. This is thought to be a result of the plume-like jet flow from the storey outlet. Its entrainment might not be as uniform as the thermal plumes due to its close proximity to the side wall of the atrium. For large A_b the entrainment may be over-predicted which results a low interface prediction.

The agreement between mathematical analysis, salt bath experiments and CFD on the predictions of non-dimensional reduced gravities was good, especially in the atrium, and the small disagreement for the comparison in the storey was possibly a result of the unstable buoyant layer when the interface approaches the ceiling.

6.7.6 Effect of other geometrical parameters

6.7.6.1 Floor-to-ceiling height

Increasing the floor-to-ceiling height will lead to changes of dimensionless total effective opening area (A_t / H^2) and the aspect ratio of the atrium height and the storey height (M / H). Both of them are decreased due to the increase of H. As expected from the summary of the mathematical analysis in Table 6.1, the non-dimensional quantities of the interface and volume flow rate will be decreased and the non-dimensional reduced gravity will be increased.

From Table 6.2, a case with A_t =0.02m^2 and M = 3.72m was selected to investigate the effects of a relatively large storey heights (2.3m and 3.0m were used for H) while M and A_t were kept fixed. The total dimensionless effective area and the aspect ratio of atrium and storey height are 0.00378, 0.00222 and 1.62, 1.24 respectively. The resulting temperature field is shown in Figure 6.18.

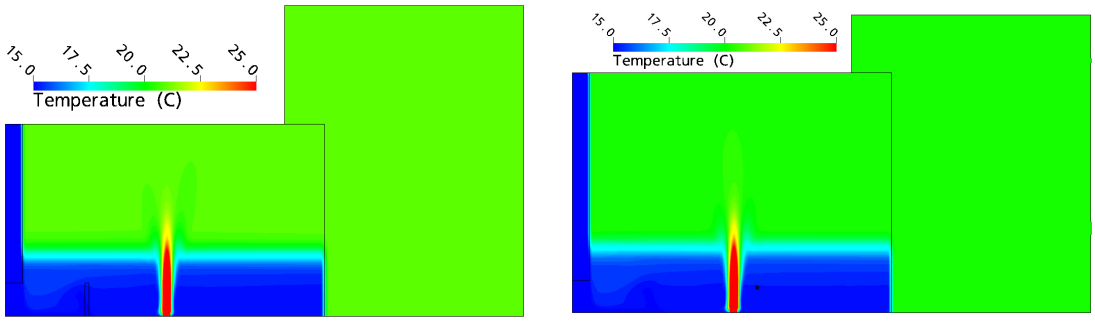

Figure 6.18 Temperature field of the domain for 2.3m, 3.0 m storey heights

The temperature field and interface height of Figure 6.18 are similar to these of Figure 6.3b in which $H = 1.58$m and all other parameters were kept the same. Comparisons for both dimensional and non-dimensional quantities of the three cases and analytical solutions are shown in Table 6.7.

Table 6.7 Quantitative comparisons of different storey heights

conditions		h_s (m)	h_s / H	g_s' (m/s^2)	g_s' / CG_H'	Q_s (m^3/s)	Q_s / Q_H
$H = 1.58$ m	theory	0.830	0.525	0.1865	20.5	0.0146	0.432
	CFD	0.837	0.530	0.1889	20.76	0.0147	0.434
$H = 2.30$ m	Theory	0.833	0.361	0.1867	43.98	0.0147	0.268
	CFD	0.841	0.366	0.1890	44.04	0.149	0.267
$H = 3.0$ m	theory	0.831	0.277	0.1868	59.5	0.0147	0.118
	CFD	0.840	0.280	0.1872	59.60	0.0148	0.1185

The dimensional quantities (h_s, g_s' and Q_s) of these two cases are almost identical (Table 6.7). This indicates that the same ventilation opening size (A_t =0.02m^2), source strength (100 W) and total height of the of the connected spaces ($M = 3.72$m) results in an identical thermal plume by which the location of the stratification is fixed physically in a confined region. The variations of the non-dimensional quantities were only due to the change of the single storey height. Figure 6.19 shows the temperature gradient for both dimensional and non-dimensional heights for these three cases. As expected from Table 6.6, the dimensional height of the interface was the same (Figure 6.19a) and the non-dimensional interface height (Figure 6.19b) was different.

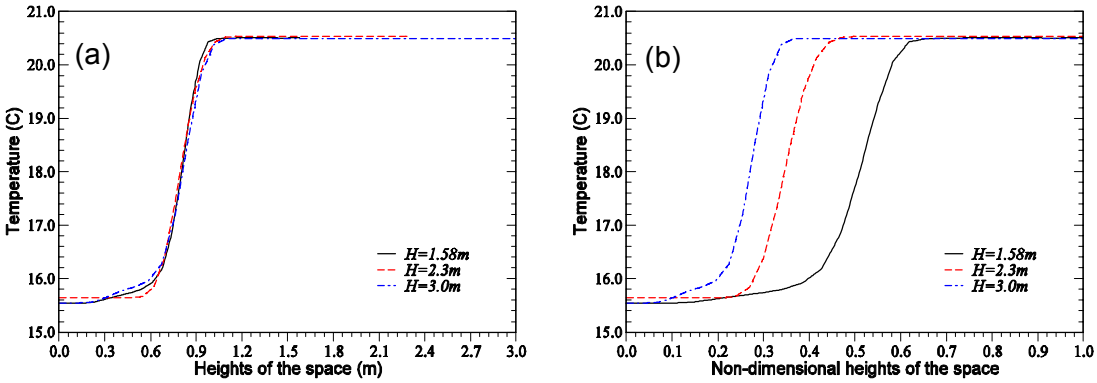

Figure 6.19 Temperature gradients with (a) dimensional heights and (b) non-dimensional heights of the space.

In building ventilation, the air change rate (ach^{-1}) of the space is normally used to estimate the efficiency of the ventilation strategy. It is defined as follows

$$ach^{-1} = \frac{Volume\ flow\ rate\ Q_s}{Total\ volume\ of\ the\ ventilated\ space} \times 3600\,. \qquad \text{Eq (6.15)}$$

Using this equation the air change rates calculated by CFD for these three cases are 3.35ach^{-1} (H = 1.58m), 2.45ach^{-1} (H = 2.3m) and 1.78ach^{-1} (H = 3.0m) respectively. The air change rate is reduced due to the large volume of the ventilated space.

6.7.6.2 Floor plan width and depth

From the mathematical analysis of Eq (2.28) the non-dimensional parameters (interface height, volume flow rate and reduced gravity) of the ventilation system are neither dependent on the floor plan width nor the floor plan depth. This was tested by a case (with A_t = 0.028 m^2) selected from Table 6.2. The floor plan width was increased from 2.5m to 5.0m and depth was increased from 4.0m to 8.0m. The resulting temperature fields of the domain for the increased floor plan width and depth are shown in Figure 6.20a & c, and compared with the original case (A_t = 0.028m^2) of Table 6.2 (Figure 6.20b). Except the floor plan width and depth the temperature fields and the locations of the interface for the two cases were exactly the same.

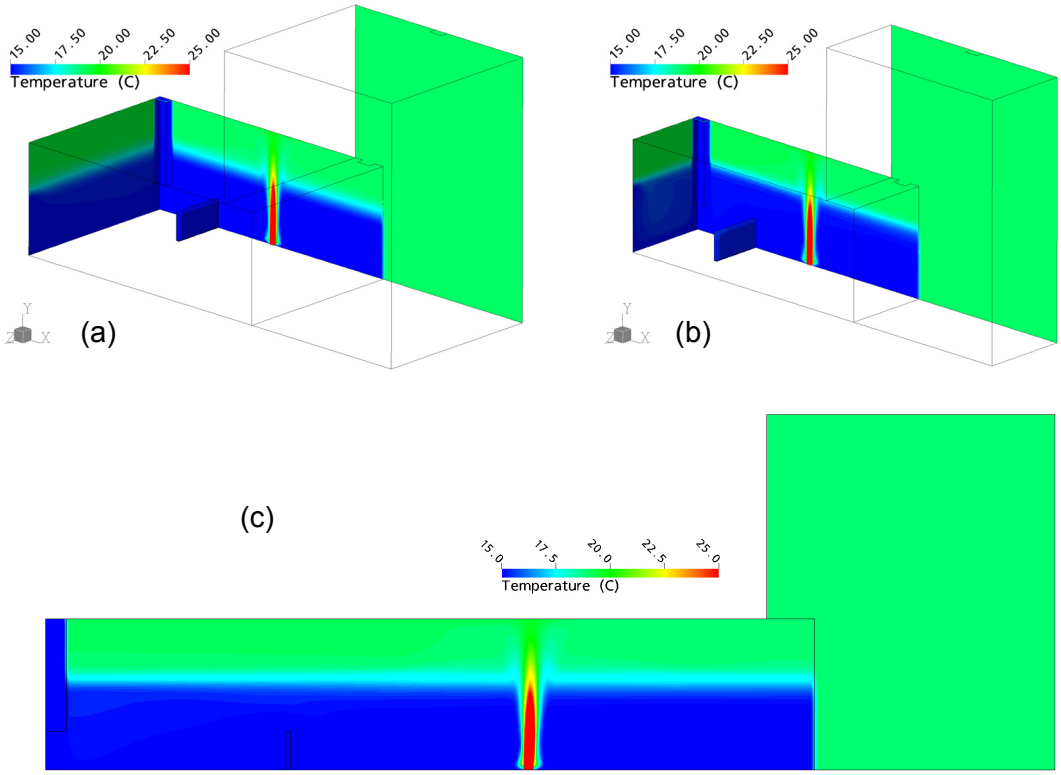

Figure 6.20 Temperature fields for a case from Table 6.2 ($A_t = 0.028$ m^2) (a) large floor plan width; (b) normal floor plan width and depth; (c) large floor plan depth.

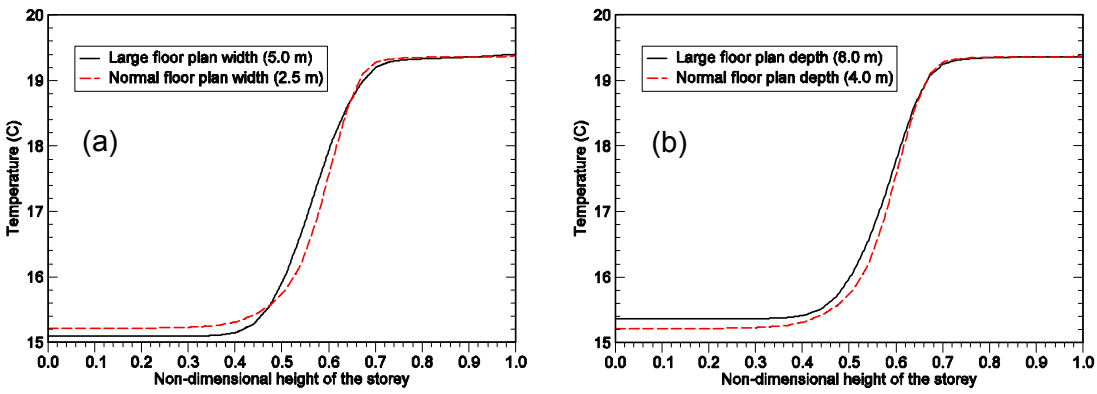

Figure 6.21 Variation of temperature gradients with non-dimensional heights of the storey for the comparison of increased floor plan width (a) and depth (b).

The quantitative temperature gradients on the line at $x = 3.25$m on the symmetry plane of the normal and increased floor plan width cases were shown in Figure 6.21a. For the increased floor plan depth cases the temperature gradient is on the line at $x = 7.25$m on the symmetry plane. The comparison with the normal floor plan depth is made in Figure 6.21b. Overall,

the agreement of the temperature gradients was good. The only difference for these three cases would be the air change rate because the total volume of the domain was changed due to the different floor plan width and depth.

6.7.6.3 Atrium width

In the original ventilation system of Figure 6.1 the atrium width was 2.5 m. To investigate the effect of the atrium space a narrow atrium (1.0 m) was used. The reference case was selected from Table 6.2 with A_t = 0.028m^2. The resulting temperature fields are shown in Figure 6.22.

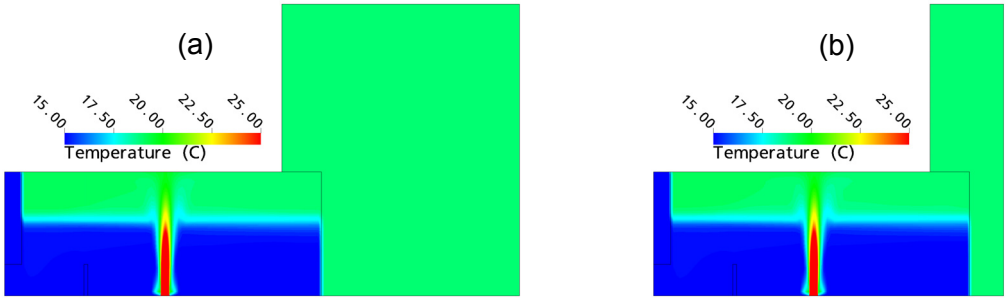

Figure 6.22 Temperature fields of different atrium spaces, (a) normal atrium space from Figure 6.1 and (b) a narrow atrium.

As expected, a narrow atrium with the same height did not alter the interface position of the storey and the resulting temperature contrast remained similar for both cases, too. However, when the atrium cross section area is too small, the hydraulic diameter of the atrium would be small (Eqs 6.8 and 6.9), and then the aspect ratio of atrium height and its hydraulic diameter would be large. The frictional losses should be therefore taken into account (Eq (6.7)). When the cross section of the atrium is large enough to ignore its frictional losses, the ventilation parameters of the storey would not be affected by the cross section of the tall atrium.

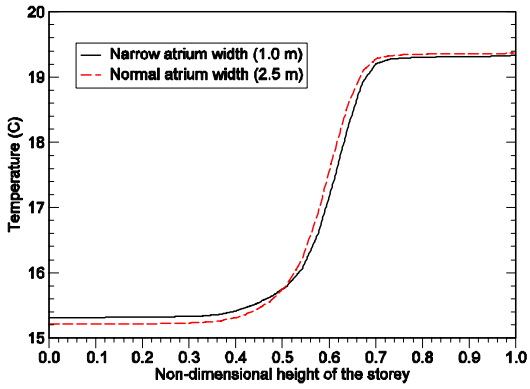

Figure 6.23 Variation of temperature gradient with non-dimensional heights of the storey

Figure 6.23 showed the quantitative temperature gradient of the two cases at the same location within the single storey, say, $x = 3.25$m, the agreement is good.

6.7.7 Air Inlet strategies

To test the effects of different air inlet strategies on ventilation flows for benchmark 2, three inlet types were used. The illustrations of these inlet strategies are shown in Figure 6.24

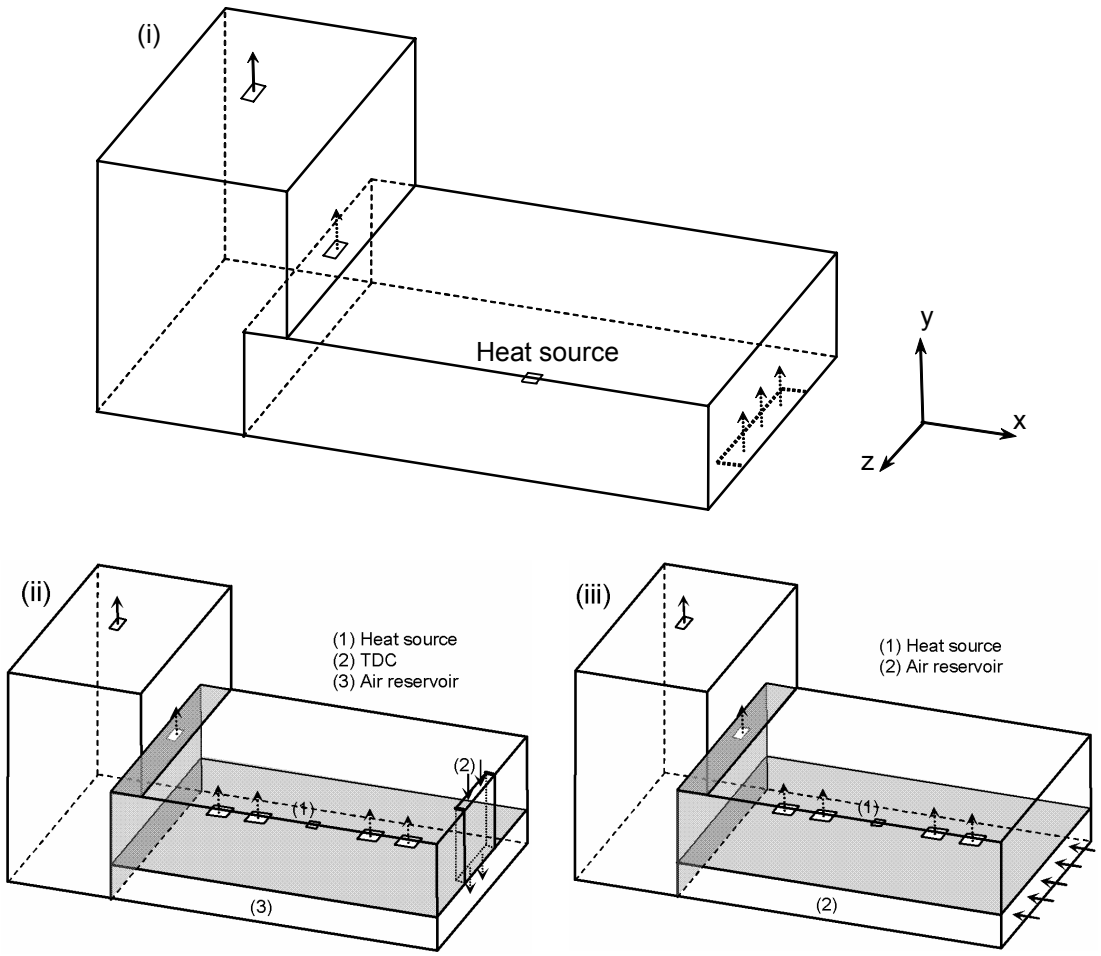

Figure 6.24 Air inlet strategies, (i) air flows in from the bottom of the single storey; (ii) air is brought in from TDC to an air reservoir plenum underneath the floor of the storey; (iii) air flows directly into the reservoir from a large side opening.

In figure 6.24(i) air enters the single storey from the bottom rather than via a TDC (Figure 6.1). The flow dynamics are the same as in the mathematical analysis of Holford & Hunt (2003) in which the TDC was excluded (but

included for salt bath experiments). The total effective opening area used A_t was calculated using Eq (6.2) but without the effects of the TDC and the TDC outlet, A_t = 0.025 m^2, and the dimensionless total effective opening area is $A_t / H^2 = 0.01$.

A TDC was used for figure 6.24(ii) to bring fresh air from high level. The incoming air flows into the air reservoir underneath the floor of the single storey via the TDC. Four openings are sized on the bottom of the single storey in order to supply fresh air into the storey. These openings are sized and arranged symmetrically in order to apply the symmetry plane boundary. The total area of these openings (0.15 m^2 each) is much larger than the storey outlet area or the atrium outlet area, consequently, the vertical air velocity from these openings is much smaller than that at the storey outlet or atrium outlet. In this way the effect of the vertical momentum from these openings on the stratification is reduced and a relatively smooth interface may then be expected. The total effective opening area for air inlet strategy (ii) is then calculated using Eq (6.2). However, more constraints are added due to the openings on the floor of the single storey. The loss coefficient for these openings is assumed to be the same as at the storey outlet, 0.63, say. The resulting A_t of figure 6.24(ii) is 0.0244 m^2 and $A_t / H^2 = 0.01$.

In the third case (Figure 6.24(iii)) fresh air is brought into the air reservoir through a side slot with area 0.5m^2. There is no TDC. The resulting total effective area of this air inlet strategy is A_t = 0.025m^2 and $A_t / H^2 = 0.01$.

CFD simulations were conducted for these three air inlet strategies and the resulting velocity and temperature fields are shown in Figures 6.25 to 6.27. As shown in these figures, the flow patterns are similar with those discussed in the previous sections of this chapter, e.g. the uprising thermal plumes, strong stratifications in the storey and the fully mixed atrium, etc.

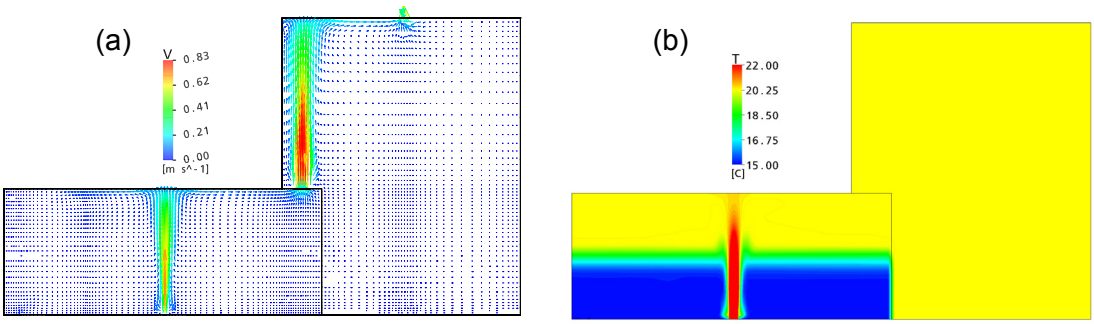

Figure 6.25 Air inlet strategy (i), (a) speed vectors, (b) domain temperature field.

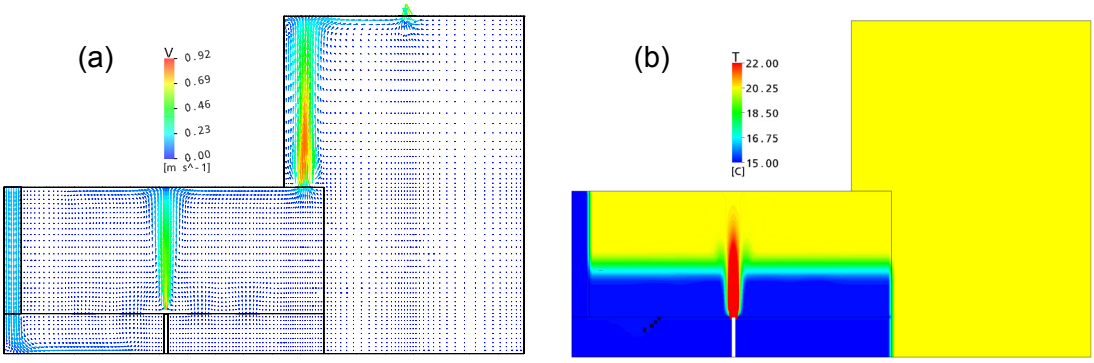

Figure 6.26 Air inlet strategy (ii), (a) speed vectors, (b) domain temperature field.

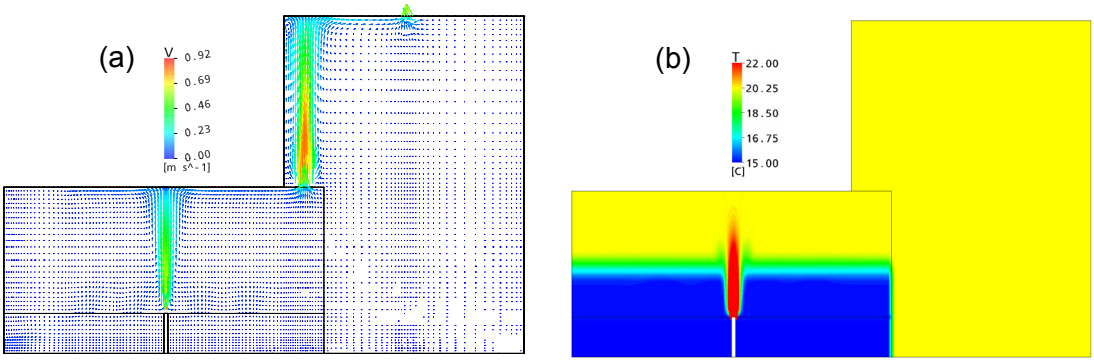

Figure 6.27 Air inlet strategy (iii), (a) speed vectors, (b) domain temperature field.

In figures 6.26 & 6.27 there is a vertical rectangular box is shown below the thermal plume. This is due to the generation of the geometry, a block was deleted there. The small hollow area (with cross section area about the same as the heat source area) should not have any effect on the flow into the storey.

The quantitative results for these air inlet strategies agreed favourably with the analytical models. In Figure 6.8a when A_t / H^2 = 0.01 the interface height h_s / H = 0.575. The interface heights predicted by these three air inlet strategies are 0.52, 0.56 and 0.57 respectively. The maximum difference is

then less than 10% between the predictions of the CFD and the analytical model.

6.7.8 Validation of volume flow rate

A method has been proposed in section 5.5 to validate the ventilation flow rate for benchmark 1 cases. In benchmark 2 cases the ventilation flow rate (unventilated atrium cases) through the storey is assumed to be equal to the ventilation flow rate through the storey. This is the same assumption used in Hunt & Linden (2001, 2005) and Hunt & Kaye (2001). Therefore the method used in benchmark 1 cases can also be used to validate the volume flow rate for benchmark 2 cases.

In the work of Hunt & Kaye (2001) a plume with non-ideal source was assumed to be equivalent to a pure point source plume, located at a virtual source with a distance (y_{avs}) below the actual source. The predictions of Eq (5.8) are non-dimensionalised by a length scale D (diameter of the source in Figure 6.28)

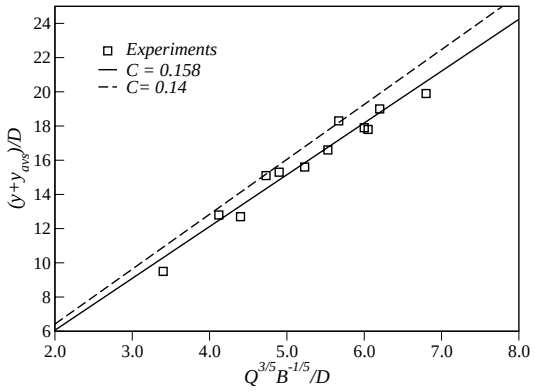

Figure 6.28 Non-dimensional volume flow rate predicted by Eq (5.8) and salt bath experiments corrected by virtual source origin, the constant $C =$ 0.158 was used in Hunt & Kaye (2001)

The ventilation flow rates predicted by the CFD model are non-dimensionlised and compared with the theoretical predictions and the experimental measurements (Figure 6.29). The cases used here are from Tables 6.2 to 6.4. For the ventilated atrium cases of table 6.5 there were only slight changes in the prediction of the interface heights (Figure 6.17). The CFD predictions in

Figure 6.28 would be highly localised and above the range of the experiments (e.g. $Q^{3/5}B^{-1/5}/D$ is larger than 8.0 and $(y+y_{avs})/D$ is larger than 22). Therefore the validation of volume flow rates for ventilated atrium cases was not conducted in this work.

As shown in Figure 6.29, CFD predictions of non-dimensional volume flow rates agreed favourably with theory and experiments. The constant C used in Hunt & Kaye (2001) is larger than the constant used in this chapter ($C = 0.14$) which indicates that a smaller entrainment constant of the thermal plume is used (c.f. section 5.5.3). The resulting theoretical predictions (continued line and dashed line in Figures 6.28 & 6.29) are slightly different. However, the experimental measurements and the predictions of the CFD model are not far from these theoretical lines. The close agreement between the three modelling techniques has shown that the proposed numerical methods used in this research are robust (Figure 6.29).

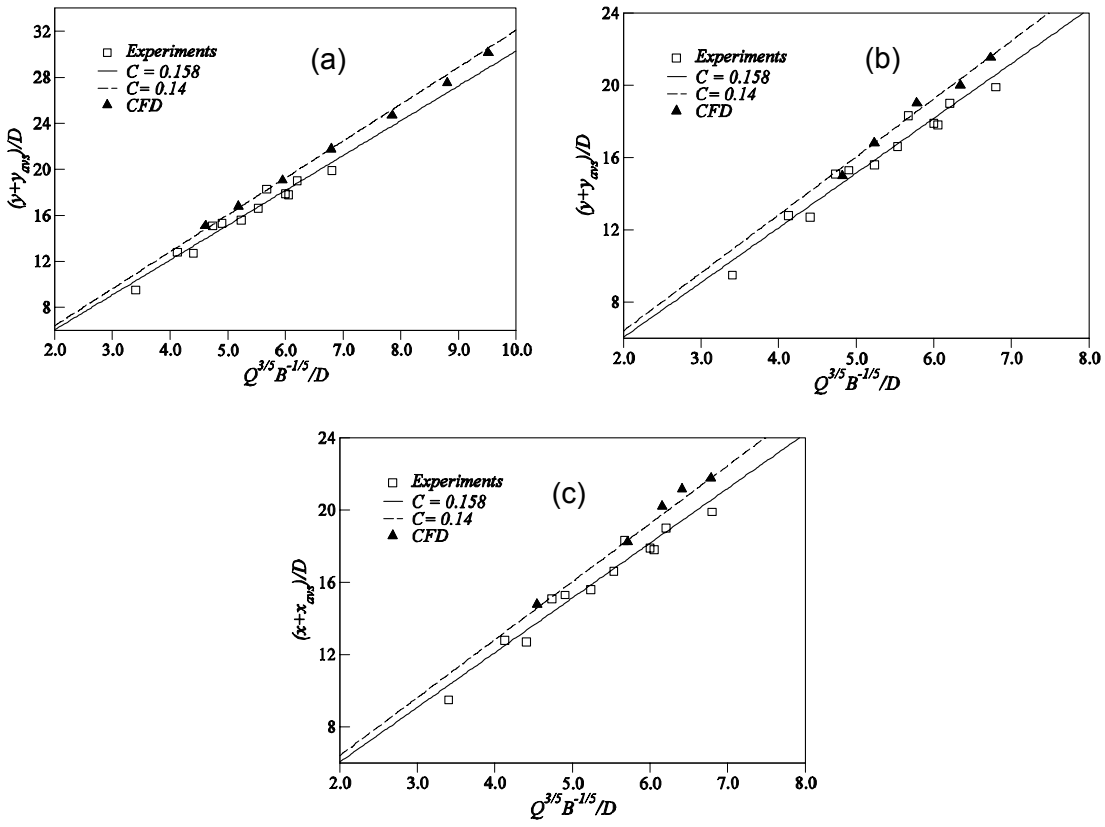

Figure 6.29 Non-dimensional volume flow rate through the storey predicted by theoretical equation, salt bath experiments and CFD for the cases of (a) Table 6.2, (b) Table 6.3 and (c) Table 6.4.

6.8 Transient investigations using CFX4

As discussed in section 6.5.2, there was a difference in the temperature prediction in the atrium between the CFD and salt bath experiments for non-ventilated atrium cases. Salt bath experiments predicted a stagnant layer in the atrium (Figure 6.3c) while CFD predicted a well mixed atrium (Figure 6.3a&b). To investigate the development of this flow, a time dependent simulation was conducted using CFX4. The purpose of running a transient flow was to examine whether a stagnant layer within the atrium ever exists in the CFD simulations or how it is mixed and over what time-scale.

6.8.1 Solution control

Fixed time stepping was used for the transient solution control in CFX4. The residual of enthalpy was used to test the convergence at each time step. Within the domain, the heat source gives 100W heat input. The maximum and minimum residual values of enthalpy were set to be 1.0W and 0.5W respectively. Forty inner loop iterations for each time step were set and the time steps were increased gradually when the convergence criteria were reached within 10 inner loop iterations. For each time step, all the variables were calculated in order to examine the flow features at that time interval.

All other controls for the CFD calculations, e.g. differencing scheme, turbulence model, false time stepping, etc, were the same as in the steady state calculations (sections 6.1 and 6.2).

6.8.2 Results of transient simulations

Table 6.8 shows the real time control information. In total, 13.7 hours of real time was used for the full development of the flow system (Figure 6.1).

Table 6.8 Time control information of transient simulation for benchmark 2

Real Timesteps used (s)	No. of Timesteps	Real time increment (s)	Cumulative time (s)	Total frames saved
0.2	5	1.0	1.0	5
1.0	38	38.0	39.0	43
2.0	50	100.0	139.0	93
3.0	5	15.0	154.0	98
5.0	20	100.0	254.0	118
10.0	20	200.0	454.0	138
20.0	20	400.0	854.0	158
30.0	80	2400.0	3254.0	238
60.0	30	1800.0	5054.0	268
120.0	30	3600.0	8654.0	298
240.0	20	4800.0	13454.0	318
300.0	120	36000.0	49454.0	438

An animation file was generated by putting the temperature solution fields (as frames) at each timestep together in sequence. In the standard file format these frames are played at a rate of 24 frames per seconds, therefore the display time of the animation file does not reflect the real time information in Table 6.8. For example, the real timestep first used was 0.2s, and 5 timesteps were calculated at this timestep. At each timestep a solution of the flow field was given. This gave 5 solutions (frames) for generating animation files. Whilst the final real timestep used in Table 6.8 was 300.0s, which means a frame could only be provided for every 300.0s of real time.

It was observed that a ‘stagnant layer’ in the atrium did form, however, the layer gradually descended with time. It took about 30 minutes of real time to form a ‘stagnant layer’ at the storey outlet level in the atrium, but 11.0 to 12.0 hours later, the atrium was fully mixed. Figure 6.30 shows the transient solutions at different real times.

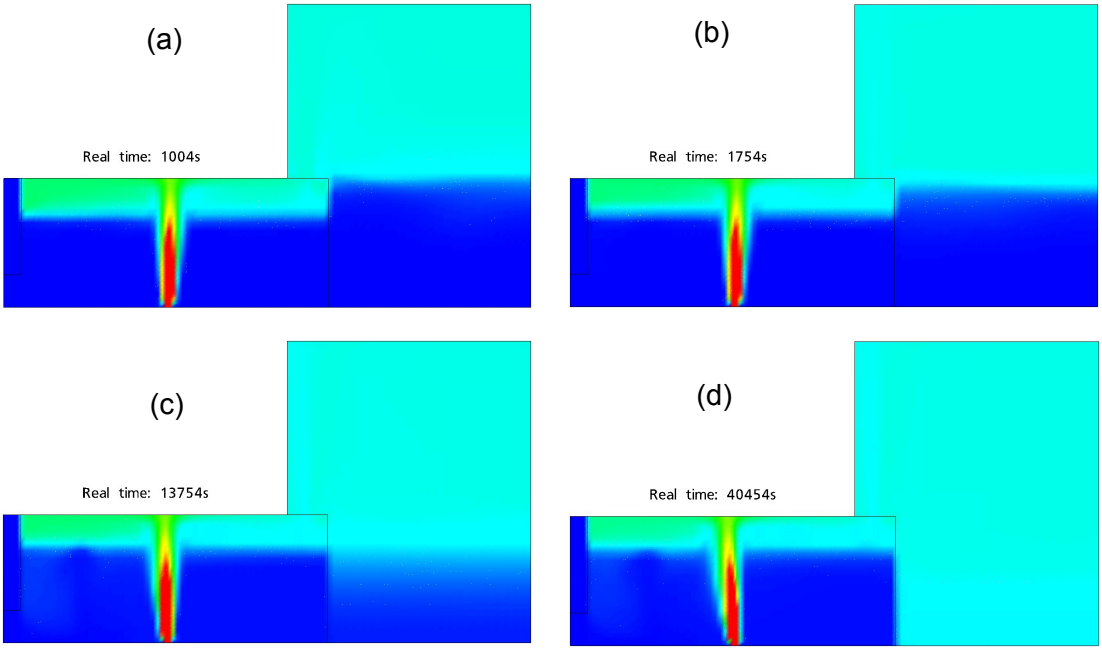

Figure 6.30 Transient temperature fields of the domain at different real times, (a) 1004s, (b) 1754s, (c) 13754s and (d) 40454s (A_t / H^2 =0.0225).

Animation file “A-662-1.mpg” was generated to show the whole process of the fluid flow for benchmark 2. The images of Figure 6.30 were the frames at the real times taken out from the animation.

This transient investigation for benchmark 2 provided a means of understanding how the atrium was fully mixed by CFD simulations. There are two reasons for CFD to predict a fully mixed atrium. One is the heat diffusion in air (the thermal diffusion term in Eq 4.31) and the other is the turbulence mixing (turbulence viscosity term in Eqs 4.30, 4.32 & 4.33) when turbulence model is used. One two-dimensional transient simulation to model the heat transfer from the ‘stagnant layer’ to the bottom of atrium without the effect of turbulence mixing was conducted. The simulation showed that the mixing time of the atrium was slower than simulations with turbulence model. However, after 60 hours later, the space was still fully mixed. It is therefore reasonable to assume that the salt bath experiments conducted by Holfort & Hunt (2003) might not have been running in an ‘infinite’ time scale. If the salt bath experiments were run longer time enough, a fully mixed atrium might have occurred.

6.9 Summary

CFD modelling of natural ventilation flows in a single storey connected to a tall atrium driven by buoyancy (benchmark 2) has been addressed in this chapter. Both quantitative and qualitative results produced by CFD calculations have been compared with the mathematical analysis and salt bath experiments of Holford & Hunt (2003).

The flow system of benchmark 2 is more complicated than benchmark 1 in which the airflow path was comprised of air inlet and outlet openings. The benchmark 2 cases have up to six openings at different locations and the modelling of loss coefficients at these openings was essential to give an accurate calculation of effective opening areas for the flow system. The methods used in section 6.3 proved robust for offering reliable CFD predictions on this type of natural ventilation flow. Except for the stagnant layer predicted by salt bath experiments in the atrium, CFD predictions of interfaces, temperature differences and ventilation flow rates of the system agreed favourably with both salt bath experiments and mathematical model.

Different geometrical parameters and air inlet strategies were investigated and the CFD predictions agreed well with the mathematical analysis using the proposed modelling techniques

The transient investigation of benchmark 2 showed that the ‘stagnant layer’ at the storey outlet level within the atrium does form during the development of the flow. However, it was not stable. This layer eventually descended to the bottom of the atrium after a long time period (in 12 hours) and a fully mixed atrium was predicted.

Chapter 7

Mathematical analysis of natural ventilation in a multi-storey building with an atrium

7. Mathematical analysis of natural ventilation in a multi-storey building with an atrium

The ventilation system studied in chapter 5 was for a single space, while the ventilation system of chapter 6 considered a single space connected to a tall atrium. For both cases the flow dynamics of the single space was of the main interest because these contained the heat sources driving the flow. Following the successful CFD modelling on these two natural ventilation systems, more complex building ventilation systems are considered in this chapter. The intention of this chapter is to develop new mathematical models of natural ventilation for multi-storey buildings connected to a tall atrium shared by all storeys.

A description of a two-storey building connected a tall atrium is given in section 7.1. The previous research of multi-storey buildings is discussed in section 7.2 and new theoretical models are developed in section 7.3 followed by a summary of this chapter.

7.1 Definition of ventilation system

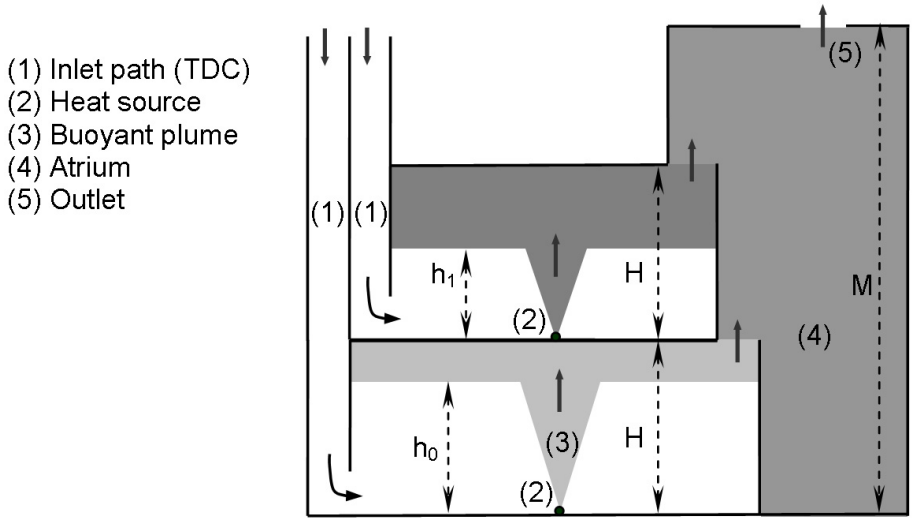

Figure 7.1 Geometrical description of a two-storey building connected to an atrium

Figure 7.1 shows an illustration of a two-storey building connected to a tall atrium. The atrium is not ventilated at its base therefore the system has two flow paths: from the lower and higher storeys into the stack, and then out of the system. The two flow paths share the common atrium, therefore the

ventilation flows of the two storeys must be considered simultaneously. A well mixed atrium with uniform temperature is assumed here following the development of benchmark 2. The enhancement effect of the tall atrium for the higher storey would be smaller than for the lower storey due to the vertical distance, therefore a cooler upper layer and higher interface are expected for the lower storey than that of the higher storey when the ventilation opening system for both storeys are the same. The loss coefficients at different ventilation openings can be defined in the same way as Eq (6.1) along each flow path. Extending this flow system to a n-storey building, the opening areas of the j^{th} storey are defined as a_{j1} to a_{j5} which are used to refer to the TDC inlet opening, the TDC, the TDC outlet opening, the j^{th} storey outlet opening and the atrium top opening respectively. Corresponding to the definition of the openings along the j^{th} storey the loss coefficients at these openings are C_{dj1} to C_{dj5} respectively. By these definitions, the effective opening areas of the j^{th} storey (A_{js}) and the atrium outlet opening (A_a) may be written in the following form

$$\frac{1}{A_{js}^2} = \frac{1}{2}\left(\frac{1}{C_{dj1}^2 a_{j1}^2} + \frac{1}{C_{dj2}^2 a_{j2}^2} + \frac{1}{C_{dj3}^2 a_{j3}^2} + \frac{1}{C_{dj4}^2 a_{j4}^2} \right) \qquad \text{Eq (7.1)}$$

and

$$\frac{1}{A_a^2} = \frac{1}{2}\left(\frac{1}{C_{dj5}^2 a_{j5}^2} \right) \qquad \text{Eq (7.2)}$$

The heat gains of each storey are modelled as a point heat source, as assumed by Linden et al (1990), Hunt & Linden (2001) and Holford & Hunt (2003). This simplification is rather ideal for real building applications. However, simple mathematical analysis under this assumption can provide useful information for building ventilations.

7.2 Previous research

By conservation of volume flow rates and heat fluxes for each storey, Hunt & Holford (1998) gave a relationship between ventilation flow rate and stratification along the flow path of a multi-storey building (a well mixed atrium is also assumed for the research).

$$Q_{js}^2\left(\frac{1}{A_{js}^2}\right)+Q_a^2\left(\frac{1}{A_a^2}\right)=\frac{\Delta T_j}{T_o}g\left(H_j-h_j\right)+\frac{\Delta T_a}{T_o}g\left(M-\sum_{k=0}^{j}H_k\right) \qquad \text{Eq (7.3)}$$

where $j=0$, …, n-1; Q_{js}, Q_a, ΔT_j, T_o, g, H_j, h_j, ΔT_a, and M are ventilation flow rate for the j^{th} storey, ventilation flow rate for the atrium, temperature difference between the upper layer and ambient for the j^{th} storey, ambient temperature, gravity acceleration, height of the j^{th} storey, temperature difference between the ambient and of the atrium and the atrium height, respectively.

The ventilation flow rate of the atrium and the temperature difference between the atrium and the ambient are defined by

$$Q_a=\sum_{j=0}^{n-1}Q_{js} \qquad \text{Eq (7.4)}$$

and $$\Delta T_a Q_a=\sum_{j=0}^{n-1}Q_{js}\Delta T_j \qquad \text{Eq (7.5)}$$

The theory of turbulent plumes of Morton (1956) was used to model the heat gains of Hunt & Holford (1998). The temperature difference between the upper layer and the ambient (ΔT_j) and the volume flow rate (Q_{js}) for the j^{th} storey are defined by the heat input E_j and the interface height h_j

$$\frac{\Delta T_j}{T_o}=\left(\frac{\beta E_j}{\rho c_p}\right)^{2/3}\left(\frac{1}{Cg^{1/3}}\right)h_j^{-5/3} \qquad \text{Eq (7.6)}$$

and $$Q_j=C\left(\frac{g\beta E_j}{\rho c_p}\right)^{1/3}h_j^{5/3} \qquad \text{Eq (7.7)}$$

It was suggested by Hunt & Holford (1998) that, a simultaneous root-finding algorithm may be used to solve above the equations (Eqs (7.4 to 7.8) numerically in order to determine interface heights for each storey (h_j). However, when the ventilation flow rates or the total effective opening areas are designed to be the same for each storey, simple analytical equations can be derived. The derivation of new mathematical models for these cases is given in section 7.3.

7.3 Simple mathematical models

Assuming the same heat gains for each storey ($E_j = E$), using Eqs (7.3 to 7.7) a simultaneous equation set can be written in the following form for determining the interface height of each storey (h_j)

$$C^3\left(\left(\frac{1}{A_{js}^2}\right)h_j^{10/3}+\left(\frac{1}{A_a^2}\right)\left(\sum_{j=0}^{n-1}h_j^{5/3}\right)^2\right)=h_j^{-5/3}\left(H_j-h_j\right)+\frac{n\left(M-\sum_{k=0}^{j}H_k\right)}{\sum_{j=0}^{n-1}h_j^{5/3}} \qquad \text{Eq (7.8)}$$

The above simultaneous equations show that when ventilation is driven solely by a single localized heat source E, the interface height, separating the buoyant upper layer and the lower layer at ambient temperature, is independent of heat input E, and depends only on the geometrical factors (the storey height H_j, the atrium height M and the effective areas of the storey A_{js} and the atrium A_a) and the plume entrainment constant.

7.3.1 Same ventilation rate for each storey

Consider a n-storey building with the same storey height ($H_j = H$) connected to a tall atrium where the ventilation strategy is designed to achieve the same ventilation flow rate for each storey. A simple equation for the non-dimensional interface height ξ ($= h_j / H_j$) for each storey can be obtained using Eq (7.8)

$$\frac{A_{jt}}{H^2}=\left(\frac{C^3\xi^5}{\left(M-jH\right)/H-\xi}\right)^{1/2} \qquad \text{Eq (7.9)}$$

where $$A_{jt}=\left(\frac{1}{A_{js}^2}+\frac{n^2}{A_a^2}\right)^{-1/2} \qquad \text{Eq (7.10)}$$

Eq (7.9) gives a general description of natural ventilation flow driven by a localised point heat source in one space or connected spaces. When only a single storey is connected to the common atrium ($j = 0$), Eq (7.9) becomes

$$\frac{A_{0t}}{H^2}=\left(\frac{C^3\xi^5}{M/H-\xi}\right)^{1/2} \qquad \text{Eq (7.11)}$$

This is consistent with the mathematical analysis of Holford & Hunt (2003) (c.f. Eq (2.28)). For a single space without an atrium, $M = H$, so Eq (7.11) is changed to be the analytical model of Linden et al (1990) (c.f. Eq (2.10)).

$$\frac{A_{0s}}{H^2} = \left(\frac{C^3 \xi^5}{1-\xi} \right)^{1/2} \qquad \text{Eq (7.12)}$$

For buildings with more than one storey, e.g. a three-storey building ($j = 2$), the analytical equations for the first and second floors are

$$\frac{A_{1t}}{H^2} = \left(\frac{c^3 \xi^5}{(M-H)/H - \xi} \right)^{1/2} \text{ and } \frac{A_{2t}}{H^2} = \left(\frac{c^3 \xi^5}{(M-2H)/H - \xi} \right)^{1/2} \qquad \text{Eq (7.13)}$$

The dependence of non-dimensional interface heights ξ on the non-dimensional total effective opening areas A_{jt}/H^2 for $M = 4H$ is shown in Figure 7.2.

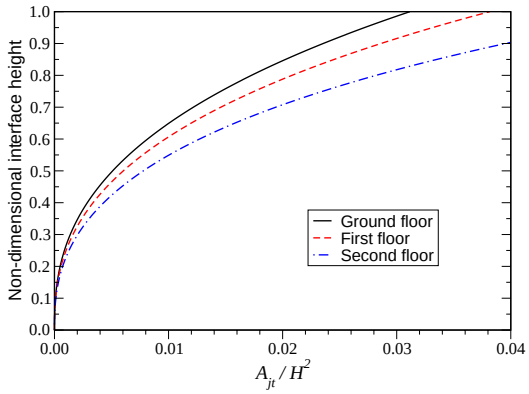

Figure 7.2 Variation of non-dimensional interface heights at each storey with non-dimensional total effective opening areas.

Increasing the total effective opening areas for a storey causes a rise in the interface height on that storey. Interface heights on each storey differ when the total effective opening area is the same for each storey due to the different stack effect acting. This implies that, in order to achieve the same ventilation flow rate for each storey (with the same interface height), the total effective opening areas of each storey should be different. The higher up the storey is, the less stack effect is provided by the atrium, and the larger the total effective opening area that is needed.

The buoyancy flux B can be converted from the heat gain of each storey E using Eq (2.18). Using H as the length scale and $(H^4/B)^{1/3}$ as the time scale, the non-dimensional quantities of reduced gravity and volume flow rate can be given by

$$g'_j / B^{2/3} H^{-5/3} = (h_j / H_j)^{-5/3} / C \qquad \text{Eq (7.14)}$$

$$\text{and } Q_{js} / CB^{1/3} H^{5/3} = (h_j / H_j)^{5/3} \qquad \text{Eq (7.15)}$$

The analytical predictions of these non-dimensional quantities are shown in Figure 7.3.

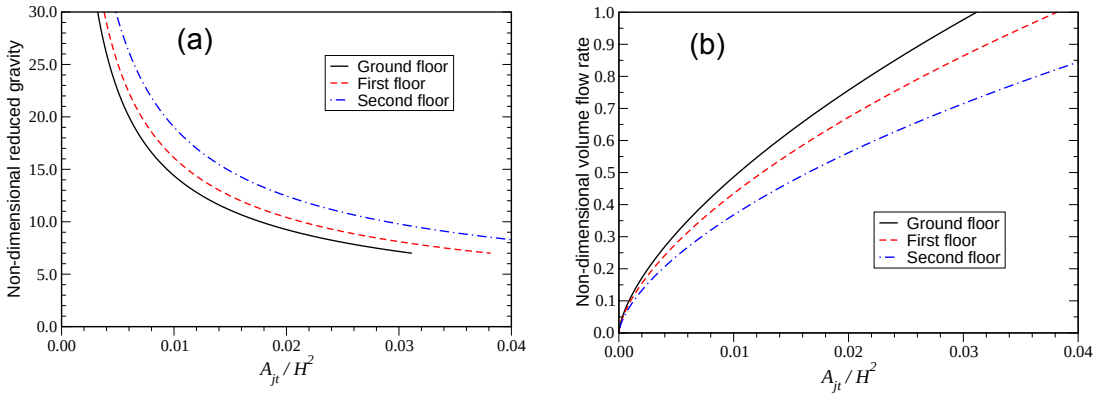

Figure 7.3 Variation of non-dimensional total effective opening areas at each storey with (a) non-dimensional reduced gravity and (b) non-dimensional flow rate.

As shown in the figure, when the reduced gravities of each storey are the same, a larger total effective opening area is expected on the higher storeys (Figure 7.3a). Similarly, when the ventilation flow rate of each storey is the same a smaller effective opening area is expected on the lower storeys (Figure 7.3b). In order to quantify the difference in the total effective opening areas for different storeys, the total effective opening area for ground floor (A_{0t}) is selected as a reference. Assuming the j^{th} storey has a total effective opening area of A_{jt} and the ventilation flow rates for each storey is the same (the interface height is also the same due to the same ventilation flow rates). Using Eq 7.10, the ratio of A_{0t} and A_{jt} can be given by

$$\frac{A_{jt}}{A_{0t}} = \left(\frac{M/H - \xi}{M/H - \xi - j} \right)^{1/2} \qquad \text{Eq (7.16)}$$

As an illustration, Figure 7.4 shows the variation of ratio of total effective opening areas of ground floor and first floor ($j = 1$) with ξ for different atrium heights.

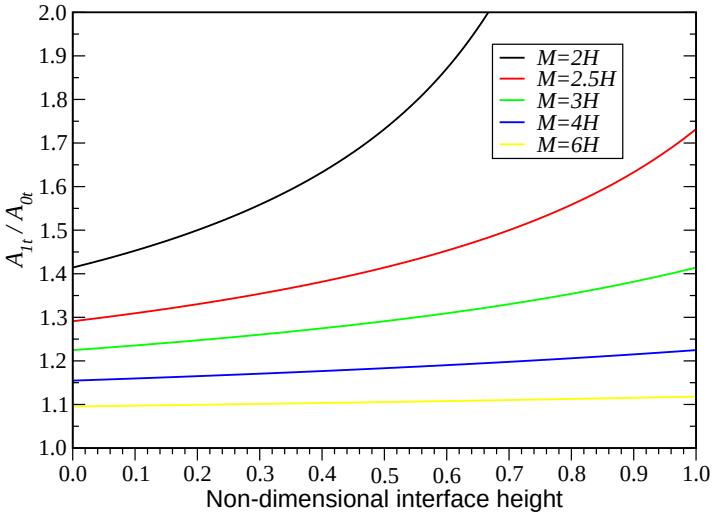

Figure 7.4 The ratio of total effective opening area at different non-dimensional interface heights for various atrium heights.

For a fixed atrium height, Figure 7.4 gives the ratio of the total effective opening areas in order to achieve the same interface height (and therefore ventilation flow rate) for each storey. When the atrium height is increased, the ratio of the total effective opening areas is reduced and becomes less sensitive to the non-dimensional interface heights.

7.3.2 Same ventilation opening size for each storey

When a building structure is arranged with the same total effective opening area for each storey, the ventilation flow rate of each storey is different due to the varying stack effect of the tall atrium on each storey. As a result the interface height of each storey will be different. Eq (7.8) can not be solved analytically like Eq (7.9), instead, simultaneous equation set has to be solved. In this work a root-finding algorithm is used to examine the interface for each storey. For example, for two-storey building connected to a tall atrium, the two simultaneous equations of the ground floor and the first floor can be defined using Eq (7.8), thus:

$$C^3\left(\left(\frac{1}{A_{0s}^2}\right)h_0^{10/3}+\left(\frac{1}{A_a^2}\right)\left(h_0^{5/3}+h_1^{5/3}\right)^2\right)=h_0^{-5/3}\left(H-h_0\right)+\frac{2(M-H)}{h_0^{5/3}+h_1^{5/3}} \qquad \text{Eq (7.17)}$$

$$C^3\left(\left(\frac{1}{A_{1s}^2}\right)h_1^{10/3}+\left(\frac{1}{A_a^2}\right)\left(h_0^{5/3}+h_1^{5/3}\right)^2\right)=h_1^{-5/3}\left(H-h_1\right)+\frac{2(M-2H)}{h_0^{5/3}+h_1^{5/3}} \qquad \text{Eq (7.18)}$$

Before solving Eqs (7.17 & 7.18) for the interface height of each storey, the effective opening areas A_{js} and A_a need to be calculated first based on the given total effective opening areas A_{jt} using Eq (7.10). For given values of M and H, there are only two variables (h_0 and h_1) remaining in the two simultaneous equations.

Freely available software (Goman & Demenkov (2004)) was used as the root-finding tool to solve above simultaneous equations.

A proposed building structure is given in Figure 7.5. The dimensions are used to calculate the geometrical parameters (A_{js}, A_a, M and H) which can be used in Eqs (7.17 and 7.18) to determine interface heights.

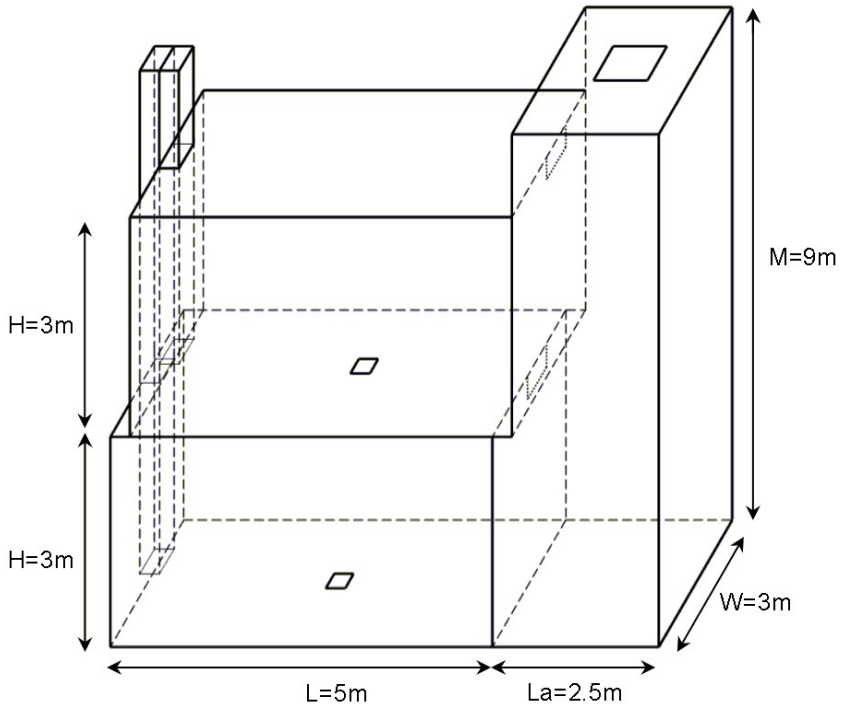

Figure 7.5 An example of a two-storey building structure

The resulting non-dimensional interface heights are given in Figure 7.6. Using Eqs (7.14 & 7.15) the non-dimensional volume flow rates and reduced gravities are given in Figure 7.7.

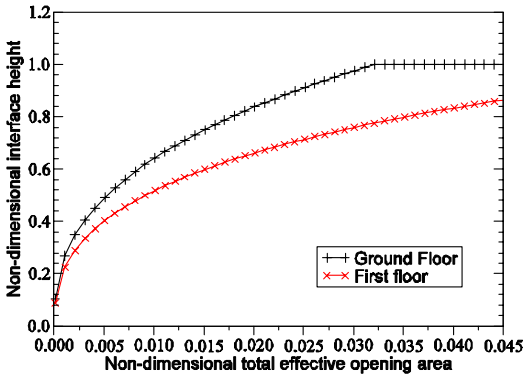

Figure 7.6 Variation of non-dimensional total effective opening areas with non-dimensional interface heights.

As shown in Figure 7.6, the same non-dimensional total effective opening area in the two storey leads to a difference of the non-dimensional interface heights for each storey. This difference increases as the total effective opening area increases. For the ground floor, complete ventilation ($\xi = 1$) happens when the total non-dimensional effective opening area is larger than 0.032. The ventilation flow rates increase as total effective opening areas increase (Figure 7.7a). As expected, the ventilation flow rate of the ground floor is larger than that of the first floor. For buildings with more than two storeys, the same principles can be applied. The higher the storey is, the lower the stack effect relative to the lower storey.

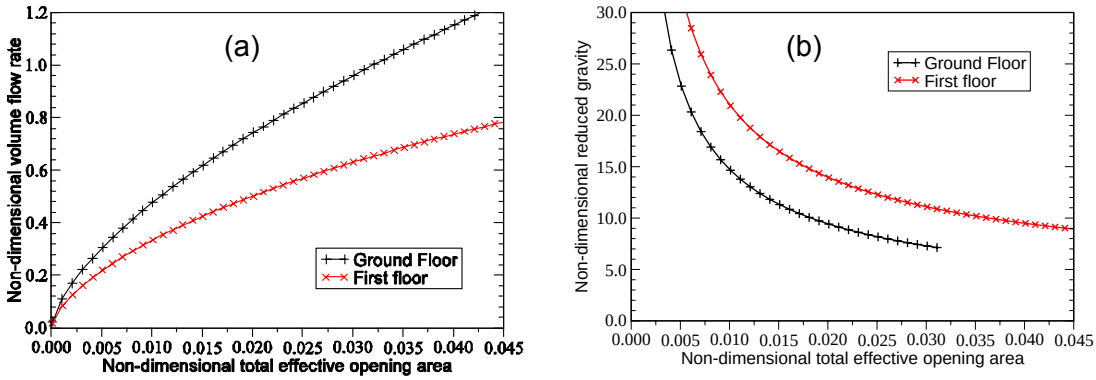

Figure 7.7 Variation of non-dimensional total effective opening areas with non-dimensional (a) volume flow rates and (b) reduced gravities.

The ventilation flow rate of the ground floor is larger than the first floor for the same total effective opening area (Figure 7.7a). A cooler upper layer is therefore expected for the ground floor compared with that of the first floor, which is shown in Figure 7.7b. After the interface reaches the ceiling

(complete ventilation), the physical parameter of the reduced gravity in the storey is not applied due to the absence of the warm upper layer.

The variation of interface heights, reduced gravities and ventilation flow with the atrium height has been studied by Holford & Hunt (2003) for a single storey building with a tall atrium. Similar outcomes would be expected for multi-storey buildings when the total effective opening area of each floor is fixed. For the two-storey building above, increasing the atrium height will cause the non-dimensional interface heights and volume flow rates to be increased (Figures 7.8 and 7.9) and the non-dimensional reduced gravities to be decreased (Figure 7.10).

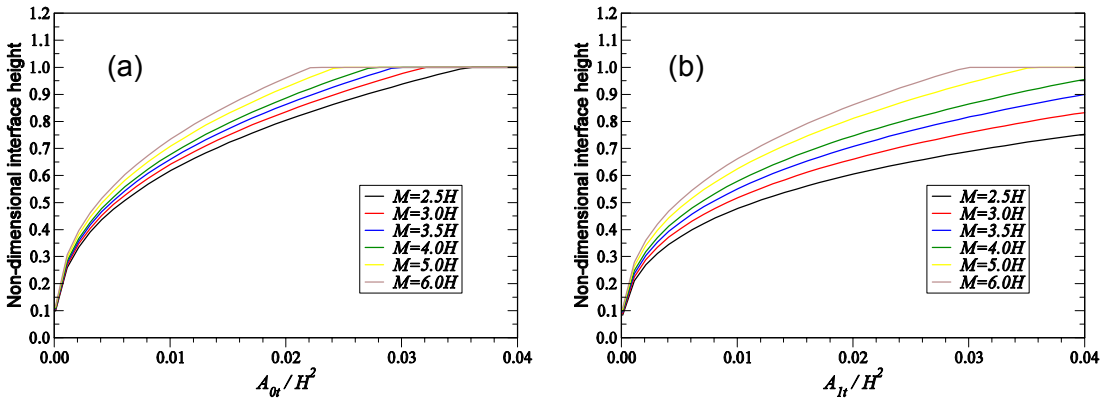

Figure 7.8 Variation of non-dimensional total effective opening areas with non-dimensional interface heights, (a) ground floor and (b) first floor.

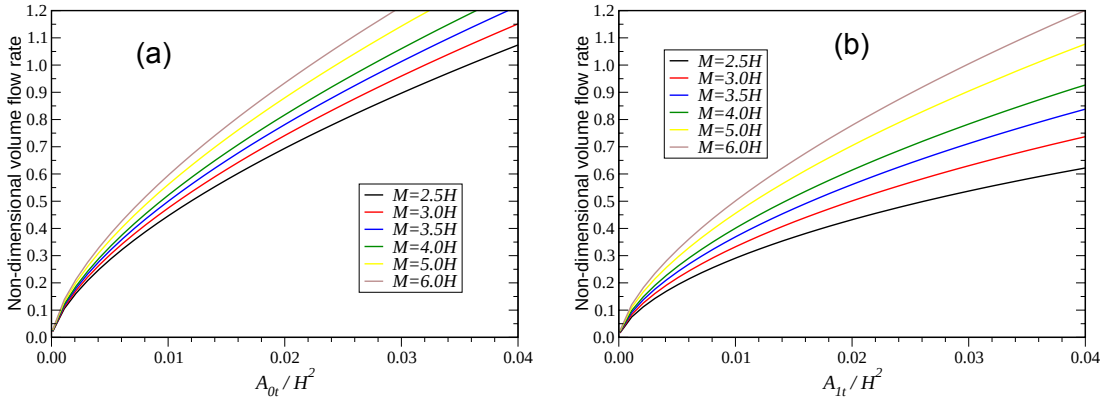

Figure 7.9 Variation of non-dimensional total effective opening areas with non-dimensional volume flow rates, (a) ground floor and (b) first floor.

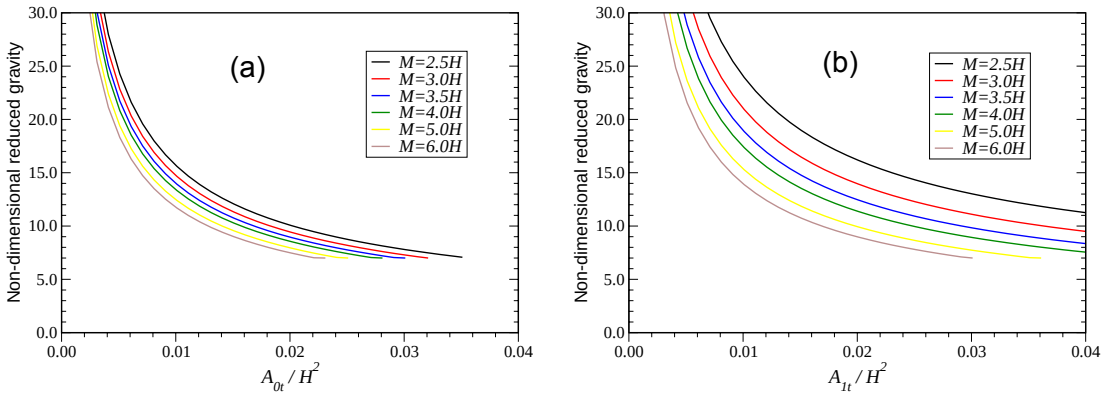

Figure 7.10 Variation of non-dimensional total effective opening areas with non-dimensional reduced gravities, (a) ground floor and (b) first floor.

7.4 Summary

Simple mathematical models for multi-storey buildings connected to a tall atrium have been derived in this chapter based on the research of Hunt & Holford (1998). Eq (7.8) gives a general description of natural ventilation flows driven by a localised point heat source in a single space or connected spaces, i.e. single storey or multi-storeys connected to an atrium.

For multi-storey spaces connected to a common atrium, two situations are considered. Firstly, when the same ventilation flow rate for each storey is the main objective, the flow dynamics of each storey can be described by simple analytical equations. These simple equations can be used to determine the interface heights, ventilation flow rates and temperature gradients of the domain. When the ventilation flow rate is not the same, the mathematical equations to describe the flow system of a multi-storey building become non-linear simultaneous equations. These simultaneous equations can be solved by a root-finding algorithm.

The models developed in this chapter successfully predict that ventilation flow rates and interface heights can be increased by increasing the height of the atrium when the effective opening size of the ventilation flow system is fixed, while the reduced gravities are reduced, accordingly.

Chapter 8

Guidelines for modelling natural ventilation and applications to real buildings

8 Guidelines for modelling natural ventilation and applications to real buildings

The main objectives of this research were to evaluate the ability of CFD to model natural ventilation flows driven by thermal buoyancy forces or buoyancy combined with wind forces and to investigate how best to model such flows using CFD. In this chapter, guidance on how best to model natural ventilation flows in a single space (benchmark 1) and connected spaces (benchmark 2) is given in section 8.1 and the applications to real buildings are addressed in section 8.2.

8.1 Guidance on how to model the benchmark cases

8.1.1 Benchmark 1 cases

- Turbulence models

For all the benchmark 1 cases in this research the RNG $k-\varepsilon$ model (section 4.4.4) was employed and was able to predict accurate results for natural ventilation flows in a single space driven by combined natural forces of wind and buoyancy. The eddy viscosity concept is used in this model. This makes the assumption that the fluid is isotropic throughout the computing domain. However, the nature of the flow inside the ventilated space did not always meet this assumption, e.g. the incoming air was unidirectional and recirculating regions existed in the upper corners of the space. However, these features did not influence the overall performance of this model in terms of the predictions of the key ventilation parameters (i.e. interface heights, ventilation flow rates and temperature gradient). Using this model the thermal plume generated by the small area source was able to dominate the flow and create thermal stratifications within the space as assumed in the analytical models.

The standard $k-\varepsilon$ model (section 4.4.4) may also be used to model this type of airflow. However, the interface height calculated by the standard $k-\varepsilon$ model was slightly lower than that predicted using the RNG $k-\varepsilon$ model and the predictions of the RNG $k-\varepsilon$ model were close to both the analytical

models and the salt bath experiments of Hunt & Linden (2001, 2005). The low Reynolds number $k-\varepsilon$ model was not able to predict a clear interface for the given mesh density used for the RNG model. In order to improve the accuracy of the low Reynolds number $k-\varepsilon$ model, a large number of cells was needed close to the wall boundaries. This increases the computing cost dramatically and was considered to be uneconomical.

- Mesh structure

Both structured and unstructured meshes were investigated for this benchmark. Structured meshes were used in the CFX4.4 solver while the unstructured mesh was used in the CFX5.6 solver (section 4.8).

For both mesh structures the grid distributions were non-uniform. Denser grids were arranged near the solid walls and the anticipated vertical thermal plume to account for the large expected gradients of computational variables. The mesh dependency test was conducted by increasing the mesh densities. Namely, refine the mesh until the stage at which increasing the resolution does not lead to a significant difference (or improvement) in the predictions of key parameters. A requirement for a suitable mesh density used in this work was to balance both CPU computing time and accuracy.

- Boundary conditions

Four types of boundaries were used for benchmark 1 cases. These are ‘wall boundary’, ‘pressure boundary’, ‘porous medium boundary’ and ‘symmetry plane boundary’.

A pressure boundary condition was employed across the ventilation openings. Whether the pressure boundary experiences an inflow or outflow depends on the absolute pressures inside and outside of the space. When the natural ventilation flow of the space was driven purely by buoyancy, the relative pressure of the pressure boundary was set to zero. When wind effects were taken into account, a relative pressure difference was set on the pressure boundary. The relative pressure was the total pressure drop induced by wind flowing over and around the ventilated space and this pressure was divided

between the inlet and outlet according to the pressure coefficients of 0.7 (windward) and -0.2 (leeward).

A porous medium boundary was used to avoid the incoming horizontal momentum from impinging on the thermal plume. This was essential to maintain a vertical plume to meet the analytical assumptions of Hunt & Linden (2001, 2005). Without this, the plume generated by the small area heat source was deflected to the floor even for no wind case. The volume porosities and resistance constants used for the porous medium boundary were obtained through 'trial and error'. For volume porosity, a value of 0.5 was used thought out of this thesis; for resistance constants, a range of 100 to 300 kg/m^{3}s was used. This proved to be feasible for benchmark 1 because it was not necessary to know how much the pressure dropped across the porous medium.

All the other surfaces (except the heat source) of the ventilated space were modelled as no-slip wall boundaries ($u_i = 0$) with zero heat flux. The heat source was modelled as a no-slip wall boundary with a steady heat flux. The standard wall function (section 4.6.1) was used for these wall boundaries. In the regions away from the ventilation openings and the heat source, the y^+ values were below the critical value (y^+=11.23) for applying the wall function which indicated that the first cell of these regions was placed in the viscous sub-layer. The small Yplus values were in fact not due to the fine mesh but the slow motion of air at these regions. Therefore the effects of these regions on the overall airflows (volume flow rate, interface height and reduced gravity) were very small. It was therefore not necessary to increase cell sizes in these regions.

- Loss coefficient at pressure boundaries

The constant pressure boundaries do not account for the losses of volume flow at ventilation openings due to the physical phenomena of expansion and discharge. This was modelled by physically reducing the opening sizes. In the CFD simulations a value of unity was used as the loss coefficients for both

high and low level openings (section 5.1.3.2). The opening areas used for CFD simulations were calculated using Eq (5.2).

- Ambient and reference temperatures

The ambient temperature of 15 ºC was used for the benchmark 1 cases. The standard fluid reference temperature in CFX4 was taken to be the expected average temperature of the domain. This temperature was used to calculate the air properties, such as density, thermal expansion coefficient, specific heat, thermal conductivity and laminar viscosity. The enthalpy reference temperature is a temperature at which the enthalpy is defined to be zero. In this study the enthalpy reference temperature was set to ambient temperature. The buoyancy reference temperature is used to calculate the relative strength of the buoyancy forces. It is a reference for calculating the density changes using the Boussinesq approximation (Eq (4.28)), therefore it is important to set it accurately. This reference temperature was set to ambient, which is the same as the temperature at inlet and outlet openings in order to avoid the possible artificial flows.

- Under-relaxation factors

Default under-relaxation factors were used in the CFX4 simulations. These were 1.0, 0.65 and 0.7 for mass conservation equation, momentum equations and k, ε equations respectively.

- False time steps

The under-relaxation factors (either default or modified) were not sufficient for obtaining convergence. In addition to the under-relaxation factors on the governing equations, false time steps (of the order of 0.01s) should also be used to further under-relax all three momentum equations.

- Solution procedure

The central differencing scheme was used to discretize the mass conservation equation and the hybrid differencing scheme was used for all other equations. Pressure correction was carried out using the SIMPLEC algorithm with the

Rhie and Chow (1983) interpolation algorithm to avoid pressure velocity decoupling due to the non-staggered grid system.

- Convergence criteria

The criteria were that the enthalpy residual shall be less than 1% of the total heat entering the domain and the absolute values of all variables at the monitoring point should not change by more than 0.1% for the last 100 iterations. The first criterion reflects the overall numerical behaviour of the whole fluid domain because the enthalpy residual is the sum of all the errors of the enthalpy equation over the whole computational domain. The second criterion reflects the stability of all absolute values at some user-defined monitoring point. The location of the point selected to monitor the absolute values of the computational domain should reflect the overall behaviour of the flow rather than some specific feature (e.g. the plume). Setting the monitoring point at the downstream position of the flow was therefore more beneficial than the core of the flow domain. In this research the monitoring point was set close to the outlet – an area which is affected by the overall solution of the domain as well as the important ventilation parameters, such as ventilation flow rate and temperature close to the ventilation outlet openings.

8.1.2 Benchmark 2 cases

Benchmark 2 cases were purely buoyancy driven natural ventilation flows. Similar modelling techniques as benchmark 1 cases were adopted: The RNG $k-\varepsilon$ model was used for all simulations; mesh structure, boundary conditions, ambient and reference temperatures, under-relaxation factors, false time steps and the convergence criteria were all the same as used in benchmark 1. For the solution techniques, QUICK scheme was used to discretize the momentum equations and hybrid scheme was used for k and ε equations. The major difference between these two benchmarks was the methods of modelling the loss coefficients at different ventilation openings.

Unlike benchmark 1, in benchmark 2 there were up to 5 locations which experience losses of ventilation flow. The loss coefficients at each opening along the flow path were determined by the applied boundary conditions or the

airflow physics. A pressure boundary condition was applied to the TDC inlet opening, atrium bottom inlet opening and the atrium outlet opening therefore the losses of ventilation flow at these openings were neglected (unity was used as the loss coefficient). The loss of ventilation flow due to the frictional effect of the TDC used in the system was calculated by Eq (6.7), while the loss coefficient of the TDC outlet was assumed to be unity due to the small cross section area of TDC compared with the cross area of the single storey (section 6.3.2). In this research the loss coefficient of the storey outlet was assumed to be 0.63, the same as assumed in the salt bath experiments. This may not be accurate when there is a large temperature difference between the single storey and the atrium (Hunt & Holford (2000) and Holford & Hunt (2001)). The temperature differences of benchmark 2 were normally very small because the temperature of the upper layer of the storey was similar to the air temperature of the atrium. It is essential to use the correct loss coefficients in order to calculate an accurate effective opening area for CFD simulations (Eqs 6.2 to 6.5), which ensures the good performance of CFD modelling.

8.2 Application to real buildings

Successful modelling of the simple benchmark cases using CFD offers confidence in the use of CFD for modelling real building. This section presents some generic guidance on the modelling of natural ventilation in real buildings followed by two examples.

8.2.1 General guidance

- Simplification of the geometry

In the real buildings there are solid obstructions inside the ventilated space, such as tables, chairs, cupboards, shelves etc. These obstructions will lead to a very complicated internal air flow pattern but they may not lead to a large difference with the ventilation flow rate. Therefore running a CFD simulation with simplified geometry (i.e. without modelling the internal obstructions) will give an approximation to the ventilation flow rate. If the building structure and boundary conditions are symmetrical the symmetry plane boundary can be used to simplify the simulation.

- Turbulence model

For airflow in buildings driven by natural forces the eddy viscosity turbulence models are suggested, of which the RNG $k-\varepsilon$ model with standard wall functions has been found to be the most accurate.

- Boundary conditions

The boundary conditions used in the benchmark cases can also be applied directly for modelling real naturally ventilated buildings. For example, a pressure boundary can be used at the ventilation openings of a real building. The ventilation flow losses across the openings need to be estimated or tested and these will be converted into loss coefficients due to expansion or discharge. For the CFD modelling, these openings may be reduced based on the loss coefficients in order to calculate an accurate ventilation flow rate.

In real building applications, the internal airflow is often far more complicated than the benchmark cases. For example, multiple source locations, obstructions within the domain, radiation effects, etc. As suggested in this research (chapters 5 & 6), the ventilation flow rate is determined by the ventilation opening areas and the driving source strengths (buoyancy or wind strength) it is not sensitive to the temperature distribution in the flow domain for CFD simulations.

For a naturally ventilated building the heat inputs are directly from occupants, electric appliances and radiators. These heat sources can be modelled as wall boundaries with constant heat fluxes.

- Mesh resolution

The mesh resolutions used for the benchmark cases are much denser than what might be used in real building simulations. In the benchmark cases fine meshes were used to solve the details of the plume development and the temperature distributions in order to compare with other modelling techniques. In real building structures the ventilation flow rate is the key parameter to predict and it is not very mesh sensitive (sections 5.2.7 & 6.6), therefore the mesh used for real building applications can be much coarser than the benchmark cases. However, tests need to be undertaken to ensure that the

predictions of ventilation flow rate are grid independent by refining the mesh, in areas such as over heat sources, ventilation openings.

- Convergence criteria and solution technique

The convergence criteria and solution techniques used in benchmark cases can also be used in real building applications. In order to achieve the convergence criteria (for example, the enthalpy residual is less than 1% of the total heat input of the domain) default under-relaxation factors and a small false time steps for the three momentum equations are needed. This is particularly important for buoyancy driven natural ventilation flows, because the driving forces are normally small and this leads to a weak coupling between energy equation and momentum equations, false time steps are needed to manage convergence using CFX4. The monitoring point to examine the absolute values of variables should be located at a downstream location, where the flow is unlikely to settle until the overall flow has converged.

The central differencing scheme can be used to discretize the continuity equation and either hybrid differencing or the QUICK scheme should be used for all other equations. The SIMPLEC algorithm should be used to deal with the pressure correction between continuity and momentum equations.

8.2.2 Application examples

Towards the end of this research the author was involved in several consultancy projects. The aim of these projects was to assess the ventilation performance of real naturally ventilated buildings using CFD modelling. In this section two real building examples are introduced. One is an Art Room and the other is a Dining hall, both are part of the proposed new Design Centre at a secondary school in the UK.

The strategy for the Design Centre is to use natural ventilation driven by the thermal stack effect. Fresh air enters the ventilated area through low level ventilation openings and is driven out of the space through vertical stacks leading to outlet openings at high level. The overall dimensions of the ventilated spaces were 10.5m $\times$ 6.35m $\times$ 5.45m (Art Room) and 26m $\times$ 8.8m $\times$ 15m (Dining Hall) respectively (Figure 8.1). The opening sizes for the Art

Room and the Dining Hall were set to 1.5% of the floor area being served. Therefore in the Art Room, openings of 0.86m^2 at the inlet and outlet positions were modelled while in the Dining Hall 5.0m^2 was used at the inlet and outlet.

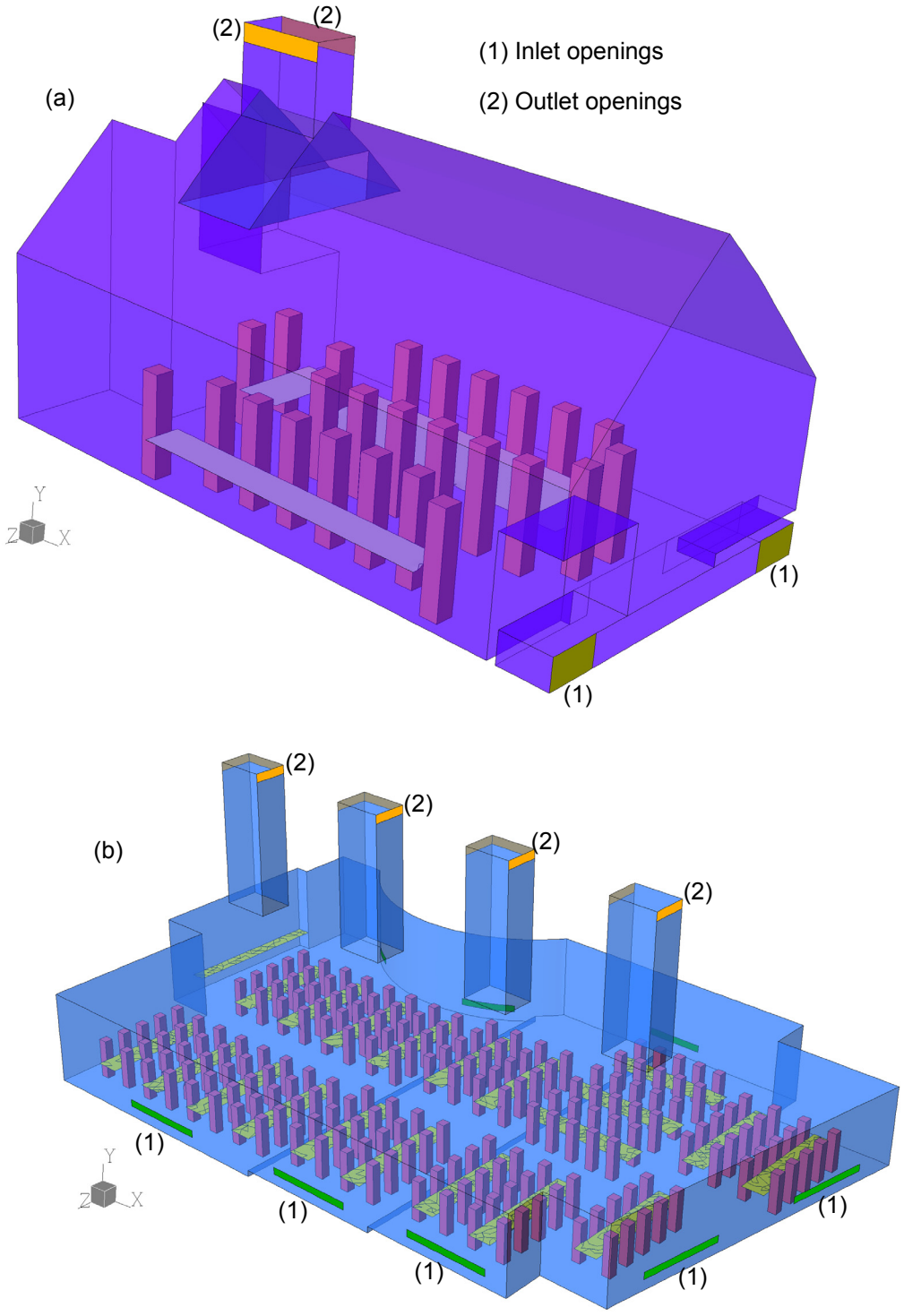

Figure 8.1 CFD models of the Art Room (a) and the Dining Hall (b).

Full occupancy was assumed in these two application examples. It was assumed that each occupant emits 100W, of which 60W was emitted as

convection and the remainder as radiation. Due to the light-weight nature of the ceiling in the Art Room, it was assumed that the radiant component of heat was re-emitted into the space at the ceiling level. Conversely, in the Dining Hall, it was assumed that the radiant gain was absorbed into the ceiling structure. There were 25 occupants in the Art Room and 200 occupants in the Dinning Hall.

In the Art Room, the total heat gains were 1500W from occupants and 1000W from the ceiling. While in the Dining Hall heat gains were 12000W from occupants and 2552W from lighting. These heat sources are modelled as uniformly distributed heat fluxes on their surfaces in the CFD modelling. This representation of heat source is the same as the benchmark cases although in the benchmark cases there was only one small area source was used.

The turbulence model used for these application examples were the RNG k-epsilon model with standard wall function. This model has been successfully used to model the benchmark cases studied in the thesis. The solution techniques are also the same as the benchmark cases.

The code used for these applications was CFX5.7 In this version there is no need to physically reduce the opening size in order to obtain an accurate ventilation flow rate of the flow system as suggested from the benchmark cases. The code introduces a loss coefficient which is related to the discharge coefficient. For example, discharge coefficients of 0.61 were assumed at all openings corresponding to a sharp-edged orifice. This discharge coefficient can be expressed as a loss coefficient f ($=1/C_d^2$ =1/0.61^2=2.69). Users can explicitly specify this loss coefficient which will be used to represent the losses.

The same convergence criteria used in the benchmark cases are also used for these application examples. When CFX5.6 was used to model benchmark 1 cases (section 6.7) it has been found that the buoyancy production terms in k and epsilon equations were the main reasons for the difficulties of achieving convergence. In these application examples simulations were conducted without these terms in order to achieve convergence criteria (the residuals for all variables were below 10^{-5}), and then these terms were invoked to continue. The residuals experienced a rapid increase after switched on these terms.

After 50 to 100 iterations, the residuals were stable, reducing gradually to reach the criteria. This is thought to be due to the coarser mesh used in these real building applications.

The minimum recommended fresh air ventilation flow rate in teaching accommodation is 8 litres/s for each of the usual number of occupants (Building Bulletin 87). The CFD simulations were carried out to test whether the proposed ventilation strategy was able to meet this criterion.

The CFD simulation results of the two application examples are shown in Figures 8.2 to 8.5. The temperature distribution in the Art Room shows that throughout the occupied space the temperature is about 3.5 degree higher than ambient (Figure 8.2). Warm air can be seen stratifying at high level which drives a natural ventilation flow out of the space at high level outlets as intended. The large floor-to-ceiling height is of benefit in providing a large stack effect. It can be seen from the velocity plot in Figure 8.3 that most of the fresh air flows into the core of the space along a narrow zone. This may lead to a risk of draughts. Distributed air inlets (more than one location) may be used to reduce risk. The predicted ventilation flow rate for the Art Room was 13.2 liters/s per person.

The Dining Hall performs well (Figures 8.4 & 8.5), primarily due to an even distribution of inlets around the perimeter of the space. The temperature in the breathing zone is about 3.5 degrees above ambient. Again, a clear stratification of warm air above the incoming cooler air is observed which drives the ventilation flow.

These application examples demonstrate the potential of CFD for informing the design of naturally ventilated buildings by enabling the accurate specification of opening sizes required for delivering sufficient fresh air flow rate, identifying potential problems such as draughts and predicting stratification height within the ventilated space.

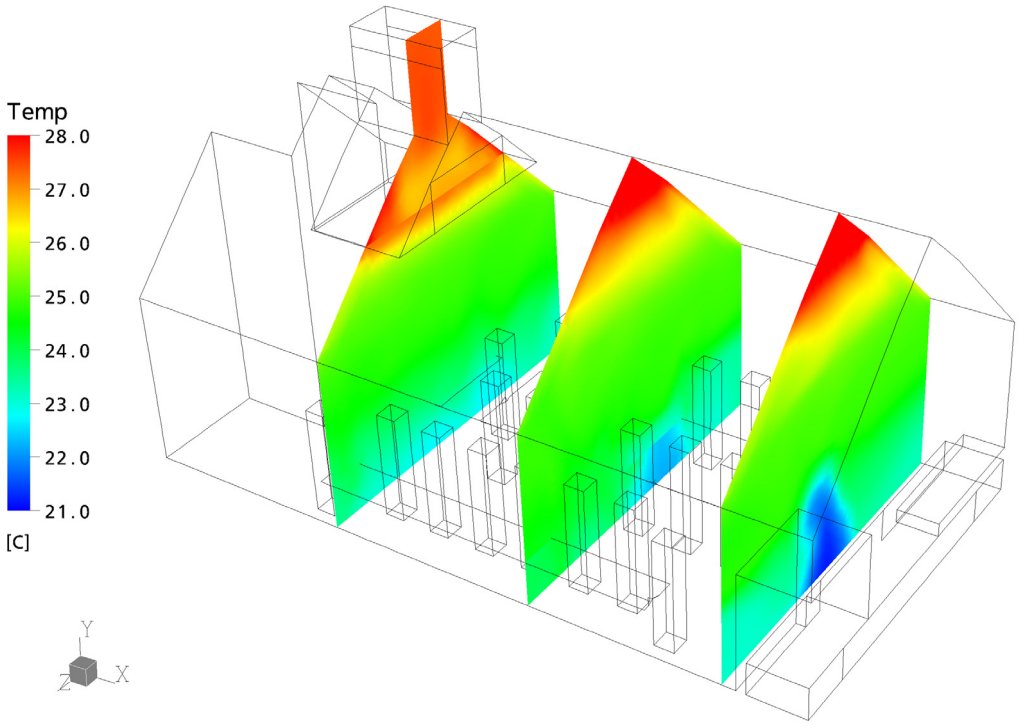

Figure 8.2 Predicted temperature distributions in the Art Room

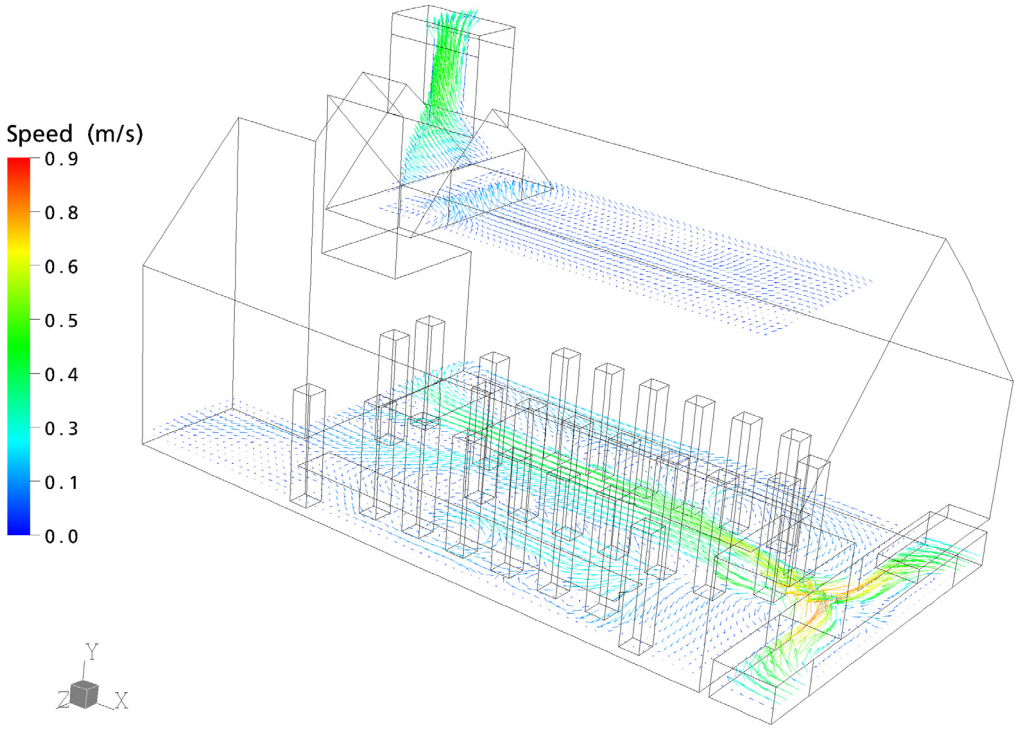

Figure 8.3 Predicted air flow distribution in the Art Room

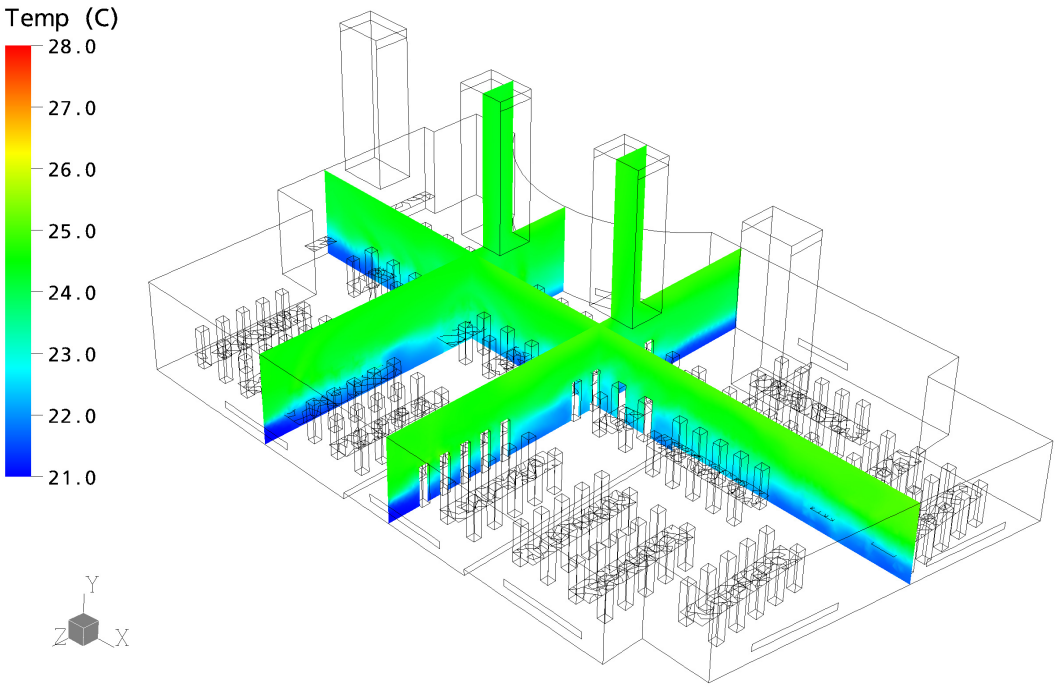

Figure 8.4 Predicted temperature distributions in the Dining Hall

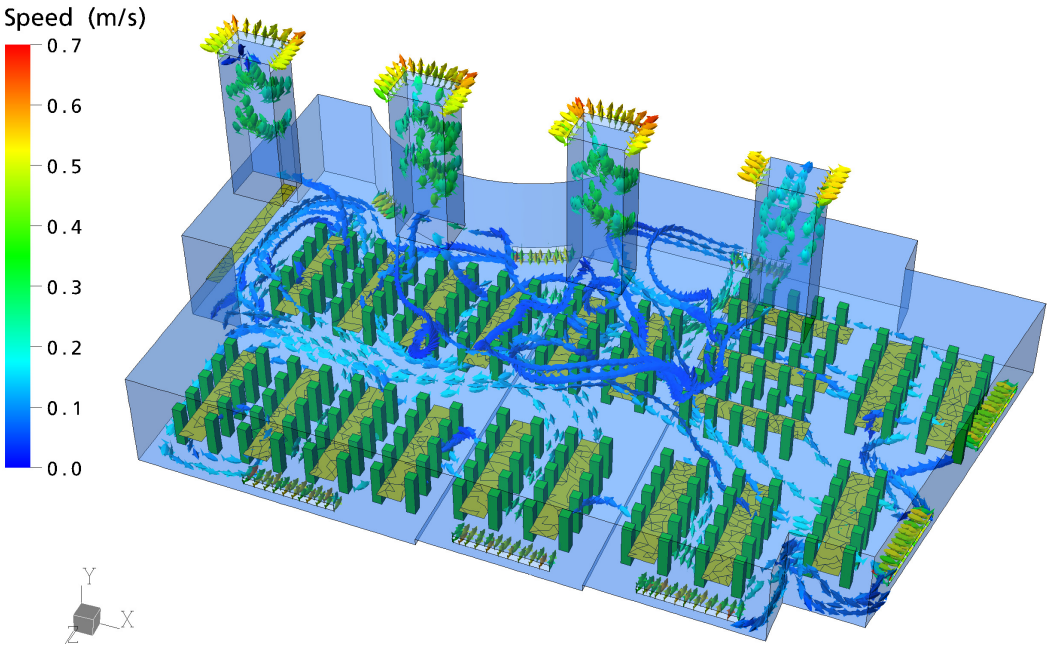

Figure 8.5 Predicted stream line in the Dining Hall

Chapter 9

Conclusions and future work

9 Conclusions and future work

9.1 Conclusions

The purpose of this study was to investigate the accuracy of CFD modelling of building ventilation flows driven by natural forces. Two benchmarks have been developed. The first benchmark considers natural ventilation flow in a single space with high and low level openings driven by buoyancy and wind forces. The second benchmark considers natural ventilation flow driven by buoyancy alone in a single space connected to a tall atrium. For both benchmarks the numerical representation of the thermal buoyancy source was important to ensure the airflow features of the ventilated space. As observed by CFD simulations the continuous release of heat from the heat source generates an uprising buoyant plume. This plume entrains the surrounding ambient air and transports the warm air upwards. Close to the ceiling of the ventilated space the warm air accumulates and spreads downwards, gradually an interface is formed separating the warm, upper layer above it from the cool, ambient layer below. After some time when the volume flow through the space equals the volume flow in the buoyant plume at the interface level a steady state is achieved. This flow regime has been supported by the salt bath experiments (Morton et al (1956), Linden et al (1990), Hunt & Linden (2001, 2005) and Holford & Hunt (2003)) and examined by the CFD simulations. This section summarizes the findings of these benchmark simulations and states the conclusions reached.

9.1.1 Benchmark 1

The CFD modelling of benchmark 1 has demonstrated the capabilities of CFD for modelling passive displacement ventilation flows driven by combined wind and buoyancy forces in a simple space. Both qualitative and quantitative results predicted by CFD using the RNG k-epsilon model have been compared with the predictions of corresponding analytical models and salt bath experiments and favourable agreement has been achieved. In this research the RNG k-epsilon model was found to perform better than other

eddy viscosity two equation models such as the standard k-epsilon model and the low-Reynolds number k-epsilon model.

The 'point' heat source assumed in the analytical models was represented by a small area source with a constant heat flux in the CFD model. In order to meet the analytical assumption this area source needs to be sufficiently small. However, the smaller the area heat source used in the CFD model, the greater the number of cells needed to solve the whole flow field; and hence the computing costs would be increased. A ratio of 2.5×10^{-4} between the area heat source and the floor area of the ventilated space used in this work have proved to meet the accuracy.

The influence of wind effects on thermal buoyancy are categorised by two conditions – buoyancy-driven ventilation flows assisted or opposed by wind. When an assisting wind is present, both interface height and ventilation flow rate are enhanced and the temperature of the upper layer is decreased. When buoyancy is opposed by wind effects the displacement ventilation flow can only be maintained for wind speeds up to some critical value. Both interface height and ventilation flow rate are decreased and the temperature difference between the warm, upper layer and cool, lower layer remains large. For larger opposing wind speeds the displacement flow breaks down. CFD modelling successfully re-produces these effects of wind on thermal buoyancy for the ventilated space studied in this research.

Maintaining a vertical thermal plume in the CFD modelling to meet the assumption of the analytical models is essential to ensure the good performances of CFD for modelling the benchmark cases. A porous medium boundary was used midway between the air inlets and the heat source in order to dissipate the horizontal momentum of the incoming airflow. The momentum of the vertical airflow generated by the heat source then dominates the flow pattern as assumed by the analytical models. The principle of using a porous medium in the CFD model was also used in the salt bath experiments in which a perforated plate was used. Without the porous medium boundary (or without the perforated plate) the thermal plume (or the brine plume) is driven sideways, and the flow pattern varies significantly from what was assumed in the analytical models.

Special care is needed when applying pressure boundaries onto ventilation openings directly to account for the losses in volume flow rate due to either frictional or pressure head losses. In the analytical models and salt bath experiments this has been taken into account by loss coefficients (due to expansion or discharge). Using CFD to model the true nature of the flow close to the ventilation openings would require the exterior of the ventilated space to be included in the model. However, computing costs are potentially increased in this case and there are uncertainties of determining the values of these coefficients to calculate the opening sizes because these coefficients may be case sensitive. The method adopted in this research was to apply the pressure boundary directly onto the ventilation inlet and outlet openings using unity as the loss coefficient and reducing the physical opening size to account for the losses. Close agreement with the experimental measurements and predictions of the analytical models indicates that this approach of modelling the boundary conditions is robust although the real flow nature (the physical processes of expansion and discharge) is not captured at the openings.

Time dependent simulations were used to examine the development of the flow within the ventilated space. This was done using CFX5.6. The thickness of the interface was found to be sensitive to the buoyancy production terms in the equations for the turbulent kinetic energy k and its dissipation rate ε. Without these buoyancy production terms The CFD simulations predicted a greater thickness of interface compared with the CFD simulations which included these terms. However, the use of these buoyancy production terms created convergence difficulties for steady state simulations.

For the high Froude numbers of the opposing wind cases investigated, some inflow was observed through the windward upper openings, particularly when the larger opening areas were used. This suggests the onset of transition from natural displacement ventilation to mixing ventilation as a result of which the two-layer stratification eventually breaks down.

CFD predictions of the ventilation flow rate through the space compare favourably with the plume theory and the salt bath experiments. The ventilation flow rate through the space depends on the ventilation opening sizes and the heat source strengths, and is neither sensitive to the

entrainment into the plume nor the interface position. This explains why the volume flow rates can be well predicted even when the interface heights are not. The reliable volume flow rate predictions using CFD also explain the good predictions of the temperature difference between the warm, upper layer and the cool, lower layer. An accurate prediction of ventilation flow rate may indicate that the correct amount of heat within the ventilated space has been removed and this ensures an accurate prediction of the temperature change within the space.

9.1.2 Benchmark 2

Benchmark 2 is more complex than benchmark 1 although the natural driving force for benchmark 2 is buoyancy alone. For benchmark 2 cases, one airflow path may involve ventilation losses at up to 5 locations. Representing ventilation losses due to discharge, expansion and friction is important to ensure the accuracy and reliability of the CFD results. Constant pressure boundaries (with 0 relative pressure) at the ventilation inlet and outlet openings with a loss coefficient of unity are used for all benchmark 2 cases. The close agreement of the predictions of interface heights, volume flow rates and reduced gravities indicates that this approach is robust.

Although the salt bath experiments of benchmark 2 did not use any device to assist in maintaining an uprising brine plume a small zone of porous medium boundary is still used for CFD simulations. The fresh air is brought into the ventilated space through a top-down-chimney; however, the incoming air momentum may still have a strong effect on the development of the thermal plume. This porous medium boundary with relatively small resistance constants (compared with benchmark 1) is still important for CFD simulations to maintain a vertical thermal plume to meet the assumption of the plume theory.

For all steady state simulations with an unventilated atrium, CFD was not able to predict the stagnant layer in the atrium which was observed in the salt bath experiments. Instead, a well mixed atrium with relatively uniform air temperature was predicted by CFD. A time dependent simulation indicates that the stagnant layer does exist in the atrium at the storey outlet opening

level during the evolution of the flow but was not maintained due to the heat diffusion in air and the turbulence mixing. The layer moves downwards very slowly and eventually reaches the bottom of the atrium. Consequently, a well mixed atrium is predicted. This explains why the steady state simulations can not predict the stagnant layer because the steady state simulations are running with an infinite time scale and the diffusion of heat in air exists and can not be ignored in the turbulence model.

Both salt bath experiments and CFD modelling show difficulty in the prediction of the interface height with large ventilation openings (large total effective opening areas). When the interface approaches the ceiling, the warm upper layer does not remain homogenous and stable. An unstable layer of warm air remains even though the analytical model predicts complete ventilation. Although the interface heights are not well predicted for large ventilation openings, CFD performs well in the prediction of the ventilation flow rates for all the ventilation opening sizes investigated. This again reflects the lower sensitivity of the ventilation flow rates on the interface position for CFD studies.

A tall atrium is commonly used to enhance the stack effect acting on the ventilated space. However, the atrium may actually limit flow due to the resistance of the atrium outlet openings. If the atrium outlet opening areas are below some critical value, the atrium may not enhance the flow. CFD simulations of varying the atrium outlet openings have illustrated this principle.

For the ventilated atrium cases, close agreement has been achieved between CFD, the analytical model and salt bath experiments. Because the atrium is self-ventilated the stagnant layer observed in the salt bath experiments for the unventilated atrium no longer exists.

A mesh dependency test (sections 6.6) showed that the interface position is more mesh sensitive than the ventilation flow rate and reduced gravity. a finer mesh was needed to resolve an accurate interface height.

CFD was also used to examine the effect of changing key aspects of the building design parameters. This was done by varying the stack height, floor-to-ceiling height, floor plan depth and the air inlet strategy. The modelling

techniques developed in this work were able to model these changes and the simulation results (both quantitative and qualitative) agreed favourably with the corresponding theories.

9.1.3 New analytical models

Simple analytical models for a multi-storey building connected to a tall atrium have been derived for the unventilated atrium case. The tall atrium is shared by all the storeys. The stack effects of the atrium on each storey are different. The largest driving force provided by the atrium occurs at the ground floor.

When each storey has the same heat gain and ventilation requirement, the total effective opening area for each storey will be different. The higher the storey, the larger the total effective opening area needs to be in order to achieve the same ventilation flow rate. A general analytical model has been derived for these conditions. The model is consistent with the previous analytical models (e.g. Linden et al (1990), Hunt & Linden (2001, 2005) and Holford & Hunt (2003)). Using the analytical model, predictions of interface heights, ventilation flow rates and reduced gravities of each storey have been made.

When the same ventilation openings are used for each storey, the ventilation flow rate of each storey will be different. This difference is reflected in the difference of interface heights of each storey. The model becomes more complex and can not be solved analytically. A root-finding algorithm was used to solve the simultaneous equations. The increase of the atrium height will lead to an increase of interface heights and ventilation flow rates in each storey, while the temperature of the upper layer of each storey will be decreased.

9.2 Future work

In practice, the nature of heat transfer within the ventilated space for both benchmark cases, may involve convection, conduction and radiation. However, only convection is considered in this work to meet the assumptions of the analytical models. When modelling a well insulated space, it is reasonable to ignore the heat transfer due to conduction through walls, however, radiation

could be significant. Further validation work using CFD in conjunction with radiation modelling is therefore suggested. Analytical modelling of a single space driven purely by buoyancy forces with the effects of both radiation and convection has been studied by Li (2000). The model may be useful to guide and evaluate the CFD modelling with both convection and radiation effects.

Both displacement and mixing modes of natural ventilation flow in a single space driven by buoyancy opposed by wind are addressed by Hunt & Linden (2005). The main interest of this research is the displacement mode natural. Further work is needed to evaluate the accuracy of CFD for modelling the mixing mode natural ventilation driven by buoyancy combined with wind effects.

In this research, time dependent CFD simulations were used to provide a visual examination of the development of the natural ventilation flow. There are no experimental results or analytical time-dependent models for either benchmark to evaluate the transient simulations of CFD. Transient draining flows in a ventilated space driven by buoyant fluid assisted by wind effects have been studied by Hunt & Linden (1999). New transient CFD simulations based on this research may offer more confidence in the use of CFD for modelling transient flows.

It is important to know the accuracy of CFD for modelling the frictional or pressure losses due to flows through ventilation openings. Experimental studies to investigate the discharge coefficients have been conducted by Hunt & Holford (2000) and Holford & Hunt (2001). It is reported by these authors that it may be inappropriate to treat the loss coefficients (due to discharge) as constants when the airflows across ventilation openings experience a density change. CFD modelling of the orifice flow with varying temperature difference will be valuable to give some guidance on how to select the loss coefficients at ventilation openings inside the computing domain.

This research focuses on natural ventilation airflows in a single ventilated space or connected spaces. The rising thermal plume generated by the localised ‘point’ heat source is the key to ensuring the overall flow performance. Validation of the thermal plume theory is not addressed

quantitatively. Some important parameters predicted by CFD, such as the plume width and the volume flow within the plume at different heights and the plume entrainments, may be verified using the plume theory of Morton et al (1956).

It is important to assess the capability of CFD for modelling the effects of surface temperature in building ventilations, such as cold windows during the winter, cold ceiling soffits following night-time cooling. Gladstone & Woods (2001) proposed analytical models for buoyancy driven flow in a space connected to a tall atrium with a cooled roof and a heated floor. It is valuable to know how important it is to include such boundary conditions in CFD simulations and how well CFD can model this phenomena.

Analytical models for a multi-storey building connected to an atrium were developed in chapter 7. It is important to test these models using the proposed guidance in this research. Following the successful modelling of a single storey building connected to a tall atrium, CFD modelling of multi-storey buildings would be valuable for offering advice on design parameters for this ventilation strategy.

Only one localised point heat source exists for the benchmark cases studied in this thesis. In a real ventilated space of a building, there may have more heat sources and the sources may have different shapes with various areas. Therefore, more sophisticated benchmarks need to be defined in order to widen the use of CFD for natural ventilation modelling.

The airflow in real naturally ventilated buildings is far more complex and is impractical to model using analytical techniques. Experiments on small scale structures are one method to understand the ventilation performance. However, this can be time consuming, and difficulty to modify. Therefore, it is often desirable to use CFD to model real buildings at the design stage to provide knowledge of building ventilation performance because it is relatively easy to investigate on variety of scenarios. However, building performance data are not available at the design stage to compare with CFD predictions. The accuracy and reliability of the CFD modelling need to be tested. One way to gain more confidence for using CFD on the prediction of real buildings is to

model the existing naturally ventilated buildings because the performance data of them are normally available.

9.3 Closing remarks

The research of this thesis has focused on the ventilation flows in simple geometry buildings driven by natural forces (either buoyancy alone, or buoyancy combined with wind). The contribution of this thesis is to offer guidance on how best to model these types of natural ventilation flows using CFD. The guidance will be beneficial for other CFD practitioners for modelling similar airflows in buildings. CFD offers an alternative to simple analytical models and small scale experimental studies, with acceptable accuracy and reliability at least for the benchmark cases discussed.

References and publications

References

Awbi, H.B. Ventilation of building, E & FN Spon, London. ISBN 0419 156909, 1991.

Alderton, J.H. & Wilkes, N.S. Some applications of new finite difference schemes for fluid flow problems. AERE-R 13234, 1988.

Baines, W.D., A technique for the direct measurement of volume flux of a plume, J. Fluid Mech. vol. 132, pp. 247-256, 1983.

Baines, W.D. & Turner, J.S. Turbulent buoyant convection from a source in a confined region, J. Fluid Mech., vol. 37, part 1, pp. 51-80, 1969.

Billington, N. The art of ventilation, Proc 3rd Air Infiltration and Ventilation Centre (AIVC) Conference 1982.

BRE: NatVent Case Study Summary – The Canning Crescent Centre, at http://projects.bre.co.uk/natvent/reports/monitoring/summary/gb2summ.pdf .

BSI (1991): Code of practice for Ventilation principles and designing for natural ventilation, British Standards Institution, BS 5925: 1991.

Building Bulletin 87: Department for Education and Skills, Guidelines for Environmental Design in Schools, 2nd edition, version 1, Crown, Copyright 2003.

Building Research Establishment BRE's Environmental Building Compact Disc. Available from the BRE, Garston, Watford, WD2 7JR, UK, 1997.

CFX4 "User Guide Version 4.4" CFX international, Harwell, UK, 2001.

CFX5 "User Menu Version 5.6" CFX international, Harwell, UK, 2003.

Chen, Q. Comparison of different k-epsilon models for indoor air flow computations. Numerical Heat Transfer, Part B, 28; pp. 353-369, 1995.

Chen, Q. Indoor Airflow, Air Quality and Energy Consumption of Buildings, Ph.D thesis, Technicsche University Delft, Delft 1988.

Chen, Q. & Chao, N.T. Comparing turbulence models for buoyant plume and displacement ventilation simulation, Indoor Built Environment, vol. 6, pp. 140-149, 1997.

Chen, Q. & Srebric, J. A procedure for verification, validation, and reporting of indoor environment CFD analyses, HVAC&R Research, vol. 8, no. 2, pp. 201-215, 2002.

Chen, Q. & Xu, W. A zero-equation turbulence model for indoor airflow simulation, Energy and Buildings, 28, pp. 137-144, 1998.

Chen, Z.D. & Li, Y. Buoyancy-driven natural displacement ventilation in a single-zone building with three-level openings, Building and Environment, vol. 37, pp. 295-303, 2002.

Chen, Z.D., Li, Y. & Mahoney, J. Experimental modelling of buoyancy-driven flows in buildings using a fine-bubble technique, Building and Environment vol. 36 pp. 447-45, 2001a

Chen, Z.D., Li, Y. & Mahoney, J. Natural ventilation in an enclosure induced by a heat source distributed uniformly over a vertical wall, Building and Environment, vol. 36, pp. 493-501, 2001b.

CIBSE (the Chartered Institution of Building Services Engineers) Natural ventilation in Non-Domestic Buildings, CIBSE Application Manual AM10, 1997.

CIBSE Building Services Journal, October 1993, pp. 20-25.

CIBSE, Energy efficiency in buildings CIBSE guide, London, 1998.

Cook, M.J. & Lomas K.J. Guidance on the Use of Computational Fluid Dynamics for Modelling Buoyancy Driven Flows. Proc. IBPSA BS'97 Conf., Prague, vol. 3, pp. 57-64. ISBN 80-01-01646-3, 1997.

Cook, M.J. & Lomas, K.J. Buoyancy-driven displacement ventilation flows: Evaluation of two eddy viscosity models for prediction, Building Services Engineering Research and Technology, vol. 19, No. 1, pp. 15-21, ISSN 0143-6244, 1998.

Cook, M.J. An evaluation of computational fluid dynamics for modelling buoyancy-driven displacement ventilation. PhD thesis, De Montfort University, 1998.

Cook M.J., Ji, Y. & Hunt GR. CFD modelling of natural ventilation: combined wind and buoyancy forces, International Journal of Ventilation, vol. 1, pp. 169-180, 2003.

Cook, N.J. The designers guide to wind loading of building structures Part 1: Static structures, Butterworths, London, 1992.

Cooper, P. & Linden, P.F. Natural ventilation of an enclosure containing two buoyancy sources, J. Fluid Mech. vol. 311, pp. 153-176, 1996.

Cooper, P., Mayo, G.A. & Sorensen, P. Natural ventilation of an enclosure with a distributed buoyancy source applied to one vertical wall, Proceedings of the 6th International Conference on Air Distribution in Rooms, Stockholm, Sweden, pp.14-17, 1998.

Dalziel, S.B. Rayleigh-Taylor instability: experiments with image analysis. Dyn. Atoms. Oceans, vol. 20, pp. 127-153.

Deardorff, J. W. A numerical study of three-dimensional channel flow at large Reynolds numbers, J. Fluid Mech., Vol. 41, pp. 453-480, 1970.

Edwards M., Linden P.F. & Walker R.R. Theory and practice – natural ventilation modelling, Proc. of CIBSE national conference, pp. 102-108, 1994.

Etheridge, D & Sandberg, M. Building Ventilation – Theory and Measurement. John Wiley and Sons Ltd, First Edition, 1996, ISBN 0-471-96087-X.

Gan, G. Prediction of turbulent buoyant flow using an RNG k-eps model, Numerical Heat Transfer, Part A, vol. 33, pp.169-189, 1998.

Garratt, J. R. The atmospheric boundary layer, Cambridge University Press, Cambridge, 1992.

Goman & Demenkow "www.iesd.dmu.ac.uk/~yingchun/MultiNewton.m"

Gosman, A.D. & Ideriah, F.J.K. TEACH-2E: A general computer program for two-dimensional, turbulent re-circulating flows. Mechanical Engineering Department, Imperial college, London. Report No FM-83-2, 1983.

Holford, J. M. & Hunt, G. R. When does an atrium enhance natural ventilation, Proceedings 21st AIVC Annual Conference, “Innovations in Ventilation Technology”, 26-29 September 2000.

Holford, J.M. & Hunt, G.R. The dependence of the discharge coefficient on density contrast - experimental measurements. Proc. 14th Australasian Fluid Mechanics Conf. 2001, Adelaide University, Adelaide, NSW, Australia, vol. 1, pp. 123-126. Editor B.B.Dally, ISBN 1 876346 34 5 2001.

Holford J. M & Hunt G. R. Fundamental atrium design for natural ventilation, Building and Environment, vol. 38, pp. 409-426, 2003.

Hunt, G. R. & Kaye, N. G. Virtual origin correction for lazy turbulent plumes, J. Fluid Mech., vol. 435, pp. 377-396, 2001.

Hunt, G.R. & Holford, J.M. Top-down natural ventilation of multi-story buildings, 19th Annual AIVC conference, Oslo, Norway, pp. 197-205, September 1998.

Hunt ,G.R. & Holford, J.M. The discharge coefficient - experimental measurement of a dependence on density contrast. Proc. 21st AIVC Conf., The Hague, Netherlands, vol. 12, pp. 2000.

Hunt, G.R. & Linden, P.F. The natural ventilation of an enclosure by the Combined effect of buoyancy and wind, Roomvent, pp. 239-246, 1996.

Hunt, G.R. & Linden, P.F. Passive cooling by natural ventilation: Salt Bath modeling of combined wind and buoyancy forces” Proc. 19th AIVC conference, Greece, vol. 1, pp. 176-183, 1997.

Hunt, G.R. & Linden, P.F. The fluid mechanics of natural ventilation - displacement ventilation by buoyancy-driven flows assisted by wind, Building and Environment, vol. 34, pp. 707- 720, 1999.

Hunt, G.R. & Linden, P.F. Steady-state flows in an enclosure ventilated by buoyancy forces assisted by wind, J. Fluid Mech. vol. 426, pp. 355-386, 2001.

Hunt, G.R. & Linden, P.F. Displacement and mixing ventilation driven by opposing wind and buoyancy, J. Fluid Mech. Vol 527, pp. 27-55, 2005.

Kato, S., Murakaimi, S. & Ooka, R. Numerical simulation of horizontal nonisothermal 3-D jet in room by DSM, Roomvent'92, vol. 1 pp. 93-108, 1992.

Kulmala, I Calculation of vertical buoyant plumes, Ventilation'97, session 7-3, pp. 393-399, 1997.

Lane-Serff G.F., Linden P.F., Parker D.J. & Smeed D. A. Laboratory modelling of natural ventilation via chimneys, Proc. PLEA 91 Architecture and Urban Space, pp. 505-510, 1991.

Launder, B.E., Reece, G.J. & Rodi, W. Progress in the development of a Reynolds Stress turbulence model, Journal of Fluid Mechanics, Vol. 68, pt. 3, pp. 537 – 566, 1975.

Launder, B.E. & Spalding, D.B. Mathematical Models of Turbulence, Academic Press, London, 1972.

Launder B.E. & Spalding D.B. The numerical computation of turbulent flows, Computer methods in applied mechanics and engineering, Vol. 3, pp. 269-289, 1974.

Laurence, D. Modelling flows around bluff bodies by Reynolds Averaged Transport Equations, J. Wind Eng. Ind. Aerodyn., vols. 46 and 47, pp. 53-68, 1993.

Leschziner, M. A. Modelling engineering flows with Reynolds stress turbulence closure, Journal of Wind Engineering and Industrial Aerodynamics, Vol. 35, pp. 21-47, Elsevier, Amsterdam, Netherlands, 1990.

Leoonard, B.P. A stable and accurate convective modelling procedure based on quadratic upstream interpolation. Compt. Mechods Appl. Mech. Eng., Vol. 19, pp. 59-98, 1979.

Linden, P.F., Lane-serff, G.G. & Smeed D.A. Emptying filling boxes: the fluid mechanics of natural ventilation, J. Fluid Mech. Vol. 212 pp. 309-335, 1990.

Li, Y. Buoyancy-driven natural ventilation in a thermally stratified one-zone building, Building and Environment, vol. 35, pp. 207-214, 2000.

Miller, J.D. Microbial contamination on indoor air, Proc Indoor Air Quality, Ventilation and Energy Conservation, 5th International Jacques Cartier Conference, Montreal, Canada 1992.

Morton, B.R., Taylor, G.I. & Turner, J.S. Turbulent gravitational convection from maintained and instantaneous sources, Proc. Roy. Soc. A 234. pp.1-23, 1956.

Morton, B.R., Forced plumes, J. Fluid Mech. vol. 5, pp. 151-163, 1959.

Murakami, S., Mochida, A. & Hibi, K. Three-dimensional numerical simulation of air flow around a cubic model by means of large eddy simulation, Journal of Wind Engineering and Industrial Aerodynamics, Vol. 25, pp. 291-305, 1987.

Murakami, S. Overview of turbulence models applied in CWE-1997, 2nd, EACWE, Italy, pp.3-23, 1997.

Nakayama, Y. & Boucher, R.F. Introduction to Fluid Mechanics, ISBN 0 340 67649 3, 1999.

Oke, T.R. Boundary Layer Climates. Methuen, 1987.

Park, H.J. & Holland, D. The effect of location of a convective heat source on displacement ventilation: CFD study, Building and Environment, vol. 36, pp. 883-889, 2001.

Patankar, S.V. & Spalding, D.B. Heat and Mass Transfer in Boundary Layers, Morgan-Grampian, London 1967.

Patankar, S.V. & Spalding, D.B. A calculation procedure for heat, mass and momentum transfer in three-dimensional parabolic flows. Int. J. Heat & Mass Transfer, Vol. 15, p. 1787, 1972.

Patankar, S.V. Numerical heat transfer and fluid flow. Hemisphere Publishing Corporation, Taylor & Francis Group. New York, 1980.

Rhie, C.M. & Chow, W.L. Numerical study of the turbulent flow past an airfoil with trailing edge separation, American Inst. Aeronautics and Astronautics J. 21 (11), pp. 1527-1532, 1983.

Schlichting, H. Boundary-layer theory, 7th ed., McGraw-Hill, New York, 1979.

Seppanen, O.A., Fisk, W.J. & Mendell, M.J. Association of ventilation rates and CO2 concentrations with health and other responses in commercial and institutional buildings, Indoor Air, vol. 9, pp. 226-252, 1999.

Shankar, V., Davidson, L. & Oisson, E. Numerical Investigation of Turbulent Plumes in both Ambient and Stratified Surroundings (Code: CALC-BFC), Indoor Air 1995, Vol. 5, pp. 136-146, 1995.

Spalding, D.B. A novel finite-difference formulation for differential expressions involving both first and second derivatives. Int. J. Number. Methods Eng., Vol. 4, p. 551, 1972.

Symons, J.G. & Peck, M. K. Natural convection heat transfer through inclined longitudinal slots, J. Heat Transfer, 106, 824-829, 1984.

Turner, J.S. Turbulent entrainment: the development of the entrainment assumption, and its application to geophysical flows, J. Fluid Mech., vol. 173, pp. 431-471, 1986.

Van Doormaal, J. P. & Raithby, G. D. Enhancement of the SIMPLE methods for predicting incompressible fluid flows. Numerical Heat transfer, vol. 7, pp. 147-63, 1984.

Versteeg, H.K. & Malalasekera, W. An introduction to computational fluid dynamics – The finite volume method, First published 1995. Copyright Longman Group Ltd 1995, ISBN 0-470-23515-2.

Xu, W. & Chen, Q. A two-layer turbulence model for simulating indoor airflow Part II. Applications, Energy and Buildings, 33, pp. 627-639, 2001.

Yakhot, V., Orszag, S.A., Thangham, S., Gatski, T.B. & Speziale, C.G. Development of turbulence models for shear flows by a double expansion technique, Phys. Fluids A, 4(7), pp. 1510-1520, 1992.

Yuan, X., Huber, A., Schaelin, A., Hachmann, P. & Moser, A. New wall functions for the numerical simulations of air flow pattern in rooms, Proc. Roomvent, Vol. 1, Aalborg 1992.

Publications

Cook, M.J. and Ji, Y. “CFD Modelling of Natural Ventilation”, CFX European User Conference, 2002, Strasbourg, France, 2002.

Cook, M.J. Ji, Y. & Hunt, G.R. “CFD modelling of natural ventilation: combined wind and buoyancy forces”, International Journal of Ventilation, Vol. 1, pp. 169-180, 2003

Ji, Y. Cook, M.J. & Hunt, G.R. “CFD modelling of Atrium-assisted Natural Ventilation”, The 9th International Conference on Air Distribution in Rooms, Portugal, September, 2004.

Ji, Y. “Numerical studies on natural ventilation flow in an enclosure with both buoyancy and wind effects”, the national conference of the Chartered Institute of Building Services Engineers, London, September, 2004

Ji, Y. Cook, M.J. & Hanby, V.I. "Modelling of displacement natural ventilation in an enclosure connected to a tall atrium", Building & Environment, to be submitted soon.

Ji, Y. Cook, M.J. "Atrium-assisted natural ventilation of multi-storey buildings" The international conference of Indoor Air, Beijing, China, September, 2005 (full paper submitted).

Cook, M.J. Ji, Y. “CFD Modelling of Natural Displacement Ventilation: Wind Opposing Buoyancy”, Building and Simulations conference, 2005 (full paper submitted)

Appendix A

Suffices and function symbols

Appendix A: Suffices and function symbols

- Suffices i, j : i = (1, 2, 3); j = (1, 2, 3)
- Velocities components: U_i (same as U_j) = (U_1, U_2, U_3) = (U, V, W)
- Coordinates: x_i = (x_1, x_2, x_3) = (x, y, z)
- Velocity component combinations:

$$U_i U_j = \begin{bmatrix} U_1U_1 & U_1U_2 & U_1U_3 \\ U_2U_1 & U_2U_2 & U_2U_3 \\ U_3U_1 & U_3U_2 & U_3U_3 \end{bmatrix} = \begin{bmatrix} UU & UV & UW \\ VU & VV & VW \\ WU & WV & WW \end{bmatrix}$$

- Body forces: B_i = (B_1, B_2, B_3) = (B_x, B_y, B_z)
- Function symbol: div

div is generally called the divergence of a vector, for example, '$div\ U_i$' is equal to: $\frac{\partial U}{\partial x} + \frac{\partial V}{\partial y} + \frac{\partial W}{\partial w}$, can also be expressed by ∇U_i

- Function symbol: $grad$

$grad$ is slightly different with div , only varying the directions of the coordinates, for example

$grad\, T$ = $\partial T / \partial x + \partial T / \partial y + \partial T / \partial z$

- Suffix notation: τ_{ij} or e_{ij}

The convection of this notation is that i or j =1 or 2 or 3 corresponds to the x, y, z directions, namely:

$$\tau_{ij} = \begin{bmatrix} \tau_{11} & \tau_{21} & \tau_{31} \\ \tau_{12} & \tau_{22} & \tau_{32} \\ \tau_{13} & \tau_{23} & \tau_{33} \end{bmatrix} = \begin{bmatrix} \tau_{xx} & \tau_{yx} & \tau_{zx} \\ \tau_{xy} & \tau_{yy} & \tau_{zy} \\ \tau_{xz} & \tau_{yz} & \tau_{zz} \end{bmatrix}$$

For example, $\tau_{12} = \tau_{xy} = \mu\left(\frac{\partial u_1}{\partial x_2} + \frac{\partial u_2}{\partial x_1}\right) = \mu\left(\frac{\partial u}{\partial y} + \frac{\partial v}{\partial x}\right)$, acts in the y direction on a surface whose normal is in the x direction.

Appendix B

Solving the governing equations

Appendix B: Solving the governing equations

The Finite Volume Method (FVM) is a widely used solution technique to discretise governing equations in commercial CFD codes. The most popular algorithm used in CFD is the SIMPLE (semi-implicit method for pressure-linked equations (Patankar & Spalding (1972)) for coupling pressure and velocity in continuity and momentum equations. A brief introduction for this algorithm is presented in this appendix, detailed descriptions can be found in (Awbi (1991), Versteeg & Malalasekera (1995), CFX4 solver manual (1997)).

If a general variable ϕ is introduced into the governing equations (Eqs (4.29 ~ 4.33) for steady state flow, the general conservative form of the governing equations of fluid flow may be written as

$$div(\rho\phi u_i) = div(\Gamma grad\phi) + S_\phi \qquad \text{Eq (B1)}$$

Integrating Eq (B1) over a control volume gives

$$\int_A n.(\rho\phi u_i)dA = \int_A n.(\Gamma\, grad\phi)dA + \int_{CV} S_\phi dV \qquad \text{Eq (B2)}$$

This equation represents the flux balance in a control volume. The left hand side gives the net convective flux and the right hand side contains the net diffusive flux and the generation or destruction of the property within the control volume.

In the case of one-dimension convection and diffusion, the source term is omitted, the flow field of properties u and ϕ are governed by

$$\frac{d}{dx}(\rho\phi u) = \frac{d}{dx}\left(\Gamma\frac{d\phi}{dx}\right) \qquad \text{Eq (B3)}$$

and the flow must also satisfy continuity equation therefore

$$\frac{d}{dx}(\rho u) = 0 \qquad \text{Eq (B4)}$$

In the integration process of numerical methods, a general node P is focused and the neighboring nodes are identified by W and E. The control volume surfaces are represented by w and e (Figure B1).

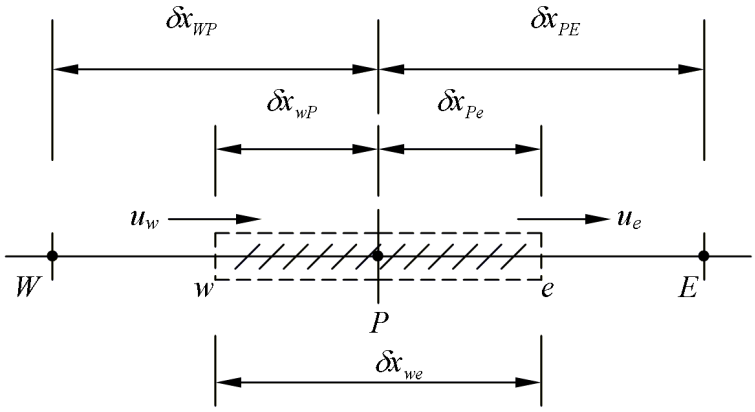

Figure B1 Grid points for one dimension flow field (after Versteeg & Malalasekera (1995)).

Integrating the transport equation (Eq (B3)) gives

$$(\rho u A\phi)_e - (\rho u A\phi)_w = \left(\Gamma A \frac{\partial \phi}{\partial x}\right)_e - \left(\Gamma A \frac{\partial \phi}{\partial x}\right)_w \qquad \text{Eq (B5)}$$

and the integration of Eq (B4) yields

$$(\rho u A\phi)_e - (\rho u A\phi)_w = 0 \qquad \text{Eq (B6)}$$

where subscripts e and w denote values at the east and west faces of the control volume respectively.

Using F to represent the convective mass flux per unit area and D to denote the diffusion conductance (flux) at cell faces for each direction (A_w and A_e), then F and D are expressed by:

$$F = \rho u \text{ and } D = \frac{\Gamma}{\delta x} \qquad \text{Eq (B7)}$$

The cell face values of the variables F and D can be written as

$$F_w = (\rho u)_w \text{ and } F_e = (\rho u)_e \qquad \text{Eq (B8)}$$

$$D_w = \frac{\Gamma_w}{\delta x_{WP}} \text{ and } D_e = \frac{\Gamma_e}{\delta x_{PE}} \qquad \text{Eq (B9)}$$

Assuming that the cross areas at the west and east of the control volume are the same, $A_w = A_e = A$, Eq (B5) can now be rewritten as

$$F_e\phi_e - F_w\phi_w = D_e(\phi_E - \phi_P) - D_w(\phi_P - \phi_W) \quad \text{Eq (B10)}$$

where ϕ_e and ϕ_w are determined by differencing schemes. The following schemes are commonly used by CFD codes.

The central differencing scheme

For a uniform grid the cell face values of property ϕ can be written as

$$\phi_e = \tfrac{1}{2}(\phi_P + \phi_E) \text{ and } \phi_w = \tfrac{1}{2}(\phi_W + \phi_P) \quad \text{Eq (B11)}$$

Substituting Eq (B11) into convection terms of Eq (B10) gives

$$\frac{F_e}{2}(\phi_P + \phi_E) - \frac{F_w}{2}(\phi_W + \phi_P) = D_e(\phi_E - \phi_P) - D_w(\phi_P - \phi_W) \quad \text{Eq (B12)}$$

Identifying the coefficients of ϕ_W and ϕ_E as a_W and a_E the discretised convection-diffusion equation becomes

$$a_P\phi_P = a_W\phi_W + a_E\phi_E \quad \text{Eq (B13)}$$

$$\text{where} \quad a_E = D_e - \frac{F_e}{2},\ a_W = D_w + \frac{F_w}{2} \quad \text{Eq (B14)}$$

$$\text{and} \quad a_P = a_W + a_E + (F_e - F_w) \quad \text{Eq (B15)}$$

Eq (B13) is a general equation form used for solving the one-dimensional convection-diffusion problem.

The upwind differencing scheme

A central differencing scheme does not provide a converged solution for high Reynolds number or high Peclet number flows because of the possibility that a_E or a_W may become negative with the consequence that an unrealistic solution may be obtained. The Peclet number, P_e, is the ratio of convection flux to diffusion flux and is defined by

$$P_e = F/D = \rho u \Delta x/\Gamma \quad \text{Eq (B16)}$$

In this scheme the value of ϕ at the control surfaces is taken as the value at the upstream node point, e.g.

$$\phi_e = \phi_P \text{ for } \phi_e > 0 \;\; ; \;\; \phi_e = \phi_E \text{ for } \phi_e < 0 \qquad \text{Eq (B17)}$$

Using the general equation forms (Eqs (B14 and B15)), the coefficients a_W and a_E are defined by

$$a_E = D_e + \max(0, -F_e) \text{ and } a_W = D_w + \max(F_w, 0) \qquad \text{Eq (B18)}$$

where, the notation of $\max(A,B)$ denotes the greater of A and B.

The hybrid differencing scheme

The hybrid scheme combines the central and upwind differencing schemes and can be applied more generally to solve equations with both convection and diffusion terms (Spalding (1972)). When $-2 \le P_e \le 2$, this scheme is identical with the central differencing scheme; when $|P_e| > 2$ the upwind differencing scheme is applied.

The coefficients a_E and a_W in this scheme are defined as

$$a_E = \max\left[-F_e, \left(D_e - \frac{F_e}{2}\right), 0\right] \text{ and } a_W = \max\left[F_w, \left(D_w + \frac{F_w}{2}\right), 0\right] \qquad \text{Eq (B19)}$$

Other advanced differencing schemes like the QUICK scheme (Leonard (1979)) and the CCCT scheme (Alderton & Wilkes (1988)) are not addressed here but can be found either in the solver manual of CFX (1997) or Versteeg and Malalasekera (1995).

Applying the hybrid-differencing scheme to three-dimensional, time dependent fluid flow with a source term, the integrated form is given by

$$\left(\rho_P \phi_P - \rho_P^o \phi_P^o\right)\frac{\Delta V}{\mathrm{A}t} + (\rho u A \phi)_e - (\rho u A \phi)_w + (\rho u A \phi)_n - (\rho u A \phi)_s + (\rho u A \phi)_r - (\rho u A \phi)_l$$

$$= \left(\Gamma A \frac{\partial \phi}{\partial x}\right)_e - \left(\Gamma A \frac{\partial \phi}{\partial x}\right)_w + \left(\Gamma A \frac{\partial \phi}{\partial x}\right)_e - \left(\Gamma A \frac{\partial \phi}{\partial x}\right)_w + \left(\Gamma A \frac{\partial \phi}{\partial x}\right)_e - \left(\Gamma A \frac{\partial \phi}{\partial x}\right)_w + S_\phi \Delta V \qquad \text{Eq (B20)}$$

where n (north) and s (south) are the neighbouring points of P in the y direction, l (left) and r (right) are the neighbouring points of P in the z direction, $\Delta V = \Delta x \Delta y \Delta z$ is the control volume (Figure B2).

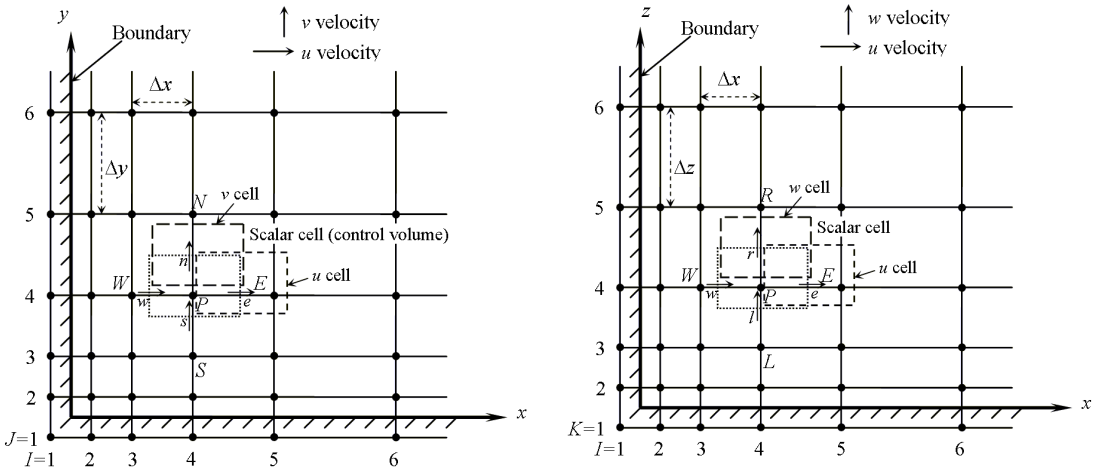

Figure B2 Grid and control volume for a three-dimensional field (after Awbi 1991).

The source term S_ϕ can be written as a linear expression:

$$S_\phi = b\phi_P + C \qquad \text{Eq (B21)}$$

The symbols with a superscript (º) represent the node values at time t and all the symbols without superscripts in Eq (B20) (as well as the following Eqs (B22, B23 & B25)) are treated as new values at time $t+\Delta t$. Similarly integrating the continuity equation over the control volume yields:

$$\left(\rho_P - \rho_P^o\right)\left(\Delta\rho / \Delta t\right) + \left(\rho uA\right)_e - \left(\rho uA\right)_w + \left(\rho uA\right)_n - \left(\rho uA\right)_s + \left(\rho uA\right)_r - \left(\rho uA\right)_l = 0 \qquad \text{Eq (B22)}$$

where $\left(\rho uA\right)_i = F_i$ is the mass flow rates over the control surfaces (i = e, w, n, s, r and l).

The general three-dimensional discretization equation can be obtained from Eqs (B20 & B22):

$$\left(\sum_i a_i + a_P^o - b\right)\phi_P = \sum_i a_i\phi_i + c\,, \qquad \text{Eq (B23)}$$

where $\sum_i a_i\phi_i = a_P\phi_P = a_W\phi_W + a_E\phi_E + a_N\phi_N + a_S\phi_S + a_R\phi_R + a_L\phi_L + c$ Eq (B24)

and $a_P^o = \rho_P^o\Delta V / \Delta t$, $b = S_P\Delta V$, $c = S_U\Delta V + a_P^o\phi_P^o$ Eq (B25)

S_P and S_U are coefficients in the source terms b and c respectively. All the positive terms in the source expressions are taken as S_U and all the negative

terms are divided by ϕ and taken to be S_P. In solving the momentum equations, the pressure terms are not included in S_U but added to the right-hand side of the discretization equation.

The coefficients a_i for i = N, S, L and R are similar to Eq (B19)

$$a_N = D_n + \max(0, -F_n) \text{ and } a_S = D_s + \max(F_s, 0) \quad \text{Eq (B26)}$$

$$a_R = D_r + \max(0, -F_r) \text{ and } a_L = D_l + \max(F_l, 0) \quad \text{Eq (B27)}$$

The algorithm of SIMPLE (Patankar & Spalding (1972)) excludes the pressure term from the coefficient of the source term S_U, the discretization equations for the three velocity components u_e, v_n and w_r at the velocity points e, n and r are

$$a_e u_e = \sum_i a_i u_i + c + (P_P - P_E)\Delta A_e \quad \text{Eq (B28a)}$$

$$a_n v_n = \sum_i a_i v_i + c + (P_P - P_N)\Delta A_n \quad \text{Eq (B28b)}$$

$$a_r w_r = \sum_i a_i w_i + c + (P_P - P_R)\Delta A_r \quad \text{Eq (B28c)}$$

where $\Delta A_e = \Delta y \Delta z = \Delta A_w$, $\Delta A_n = \Delta x \Delta z = \Delta A_s$, $\Delta A_r = \Delta x \Delta y = \Delta A_l$.

The velocities in Eqs (B28a, b & c) can not satisfy the continuity equation unless the pressures at the grid points are correct. At the start of calculation, only guessed values of pressure (and velocity) are available and continuity may not be satisfied. Therefore some means of correcting the pressures is needed to achieve numerical solutions. This is the aim of the SIMPLE procedure, the pressure and velocity components are then written as

$$p = p^* + p', \; u = u^* + u', \; v = v^* + v' \text{ and } w = w^* + w' \quad \text{Eq (B29)}$$

where the asterisk represents a guessed value and the prime is the correction necessary to satisfy continuity. The equations for the guessed velocities are

$$a_e u_e^* = \sum_i a_i u_i^* + c + (P_P^* - P_E^*)\Delta A_e \quad \text{Eq (B30a)}$$

$$a_n v_n^* = \sum_i a_i v_i^* + c + \left(P_P^* - P_N^*\right)\Delta A_n \qquad \text{Eq (B30b)}$$

$$a_r w_r^* = \sum_i a_i w_i^* + c + \left(P_P^* - P_{R*}\right)\Delta A_r \qquad \text{Eq (B30c)}$$

Subtracting Eq (B30a) from Eq (B28a) gives

$$a_e u_e' = \sum_i a_i u_i' + c + \left(P_P' - P_E'\right)\Delta A_e \qquad \text{Eq (B31)}$$

Omitting $\sum_i a_i u_i'$ for computing convenience, then

$$u_e' = \left(\Delta A_e / a_e\right)\left(P_P' - P_E'\right) \qquad \text{Eq (B32)}$$

Eq (B32) is the velocity correction formula and can be written for all the three components as:

$$u_e = u_e^* + \left(\Delta A_e / a_e\right)\left(P_P' - P_E'\right) \qquad \text{Eq (B33a)}$$

$$u_n = u_n^* + \left(\Delta A_n / a_n\right)\left(P_P' - P_N'\right) \qquad \text{Eq (B33b)}$$

$$u_r = u_r^* + \left(\Delta A_r / a_r\right)\left(P_P' - P_{RN}'\right) \qquad \text{Eq (B33c)}$$

A revised SIMPLE algorithm, called the SIMPLER algorithm (Patankar 1980) includes the $\sum_i a_i u_i'$ term in Eq (B31) instead of omitting it in the SIMPLE algorithm. The pressure field is obtained from an initially guessed velocity field and velocity corrections are obtained from the pressures in SIMPLER algorithm while the pressure field is guessed in SIMPLE. All other aspects of the two algorithms are the same. The SIMPLER algorithm normally gives faster convergence but in the meal while it involves more computational effort per iteration because the pressure equations are solved twice.

Another modification of the SIMPLE algorithm is the SIMPLEC method (C denotes consistent approximation, Doormaal & Raithy (1984)). In this method, the velocity correction term $\sum_i a_i u_i'$ is transferred to the left-hand side of Eq (B31):

$$u'_e = \frac{\Delta A_e}{a_e - \sum_i a_i}\left(P'_P - P'_E\right) \qquad \text{Eq (B34)}$$

All the other equations in SIMPLEC are identical to those given in SIMPLE with a_e replaced by $a_e - \sum_i a_i$. Doormaal & Raithby (1984) reported that the SIMPLEC was slightly less computing intensive compared with SIMPLE.

Spalding (1980) refined the SIMPLE procedure by including all the diffusion terms in the coefficients of the discretization equation for momentum and all the convection terms in the linearized source term. This so-called SIMPLEST algorithm is particularly suited to flows with large convection terms.

To solve the discretized equations for all the dependent variables (ϕ) a line-by-line (LBL) iterative procedure can be used. Initial values of ϕ of the flow field are guessed and these are improved by solving the equations along each grid line. The procedure is repeated for each grid line until the whole flow field is swept.

For an iterative solution the general discretization Eq (B23) may be written as a recurrence formula:

$$\phi_j = A_j\phi_{j+1} + B_j\phi_{j-1} + C_j \qquad \text{Eq (B35)}$$

where $\phi_P = \phi_j$, $\phi_N = \phi_{j+1}$ and $\phi_S = \phi_{j-1}$. The coefficients A_j, B_j and C_j take the following forms:

$$A_j = a_n \Big/ \left(\sum_i a_i + a_P^o - b\right),\ B_j = a_s \Big/ \left(\sum_i a_i + a_P^o - b\right) \quad \text{and}$$
$$C_j = \left(a_E\phi_E + a_W\phi_W + a_L\phi_L + a_R\phi_R + c\right) \Big/ \left(\sum_i a_i + a_P^o - b\right) \qquad \text{Eq (B36)}$$

The recurrence Eq (B35) can be solved easily using the tri-diagonal matrix algorithm (TDMA) starting from top to bottom of each grid line in succession until the whole field is swept from east to west (Gosman & Ideriah 1983).

Appendix C

Thermal plume shapes

Appendix C: Thermal plume shapes

The plume shape generated by an area heat source was different to that generated by a real point heat source assumed in the analytical models (section 2.2.4). These differences are shown in Figure C1.

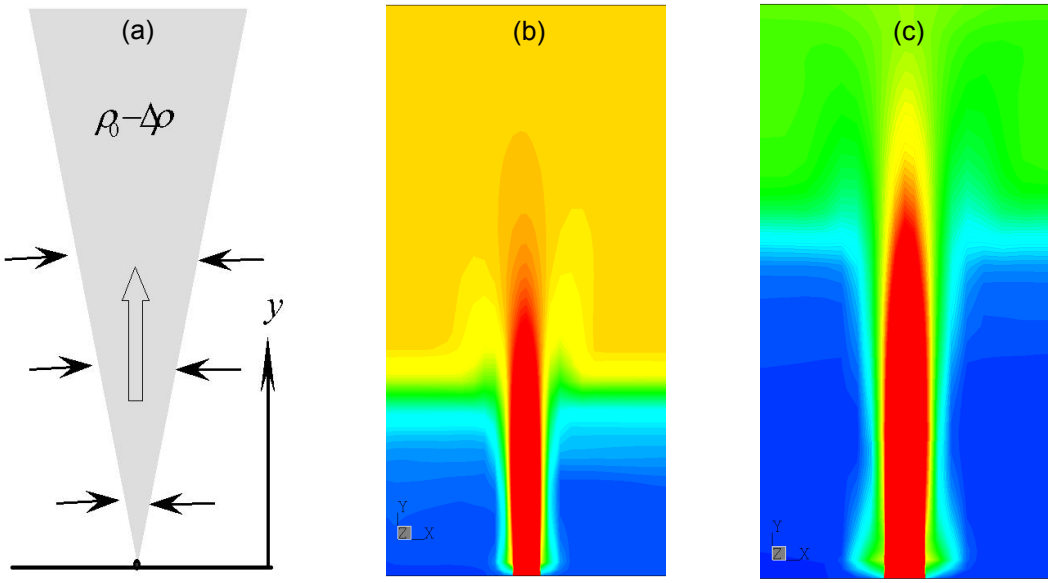

Figure C1 Plume shapes, (a) assumed by analytical models, (b) generated by an area heat source for benchmark 1 and (c) generated by an area heat source for benchmark 2.

The 'point' heat source in Figure C1a continually releases heat and the adjacent air is warmed, and then the warm air flows upwards due to the temperature difference. The surrounding air is entrained by the uprising warm air stream consequently a thermal plume is built up. In the CFD simulations the heat is released from the area heat source. However, the base of the thermal plume is larger than that of a point heat source plume (FiguresC1b, c). This difference in the plume shape was acceptable because the main focus of this research was to predict the key parameters of the flow using CFD rather than the plume performance.

To investigate the effect of different sizes of an area heat source, an even smaller area source was used in benchmark2. The simulation case is selected from table 6.2 with A_t =0.028m^2. The new area ratio between the heat source and the cross area of the single storey for this case is 1.0×10^{-5} (25 times

smaller than that used for the previous cases). The resulting plume shape is shown in Figure C2a and compared with the previous case shown in Figure C2b.

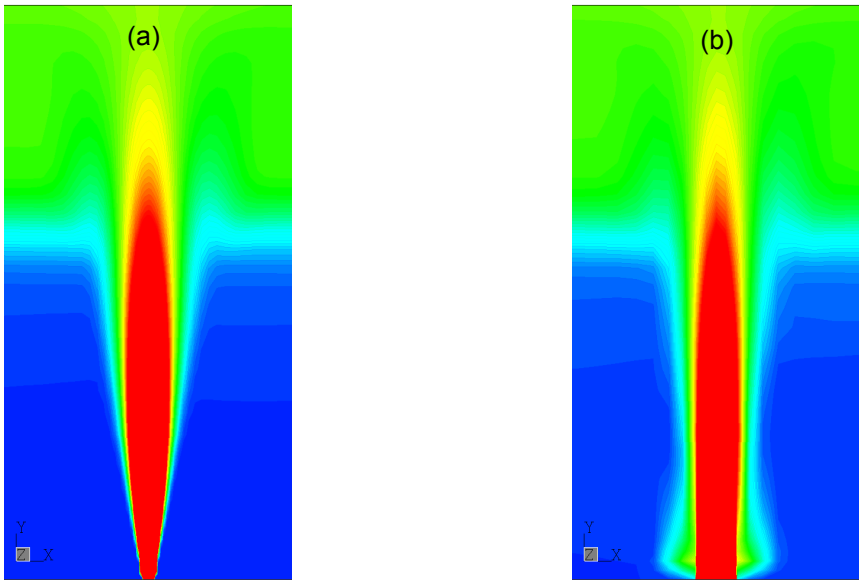

Figure C2 Plume shape comparisons with different area ratios of heat source area and cross section area of the single storey, (a) 1.0×10^{-5} and (b) 2.5×10^{-4}.

Comparison of the plume shapes shows a significant difference due to the size of the heat source area. The smaller heat source area generated a thermal plume whose shape is closer to what assumed by analytical models (e.g. Linden et al (1990), Hunt & Linden (2001, 2005) and Holford & Hunt (2003)).

To maintain a high quality mesh when defining a small heat source a large amount of cells may be needed. For the case showing in Figure C2a, a mesh with 372560 cells was used. The region occupied by the thermal plume and the floor of the storey were considerably refined. The computing time of this mesh will be doubled compared with the mesh size used in this research (about 160k cells).

As discussed in section 6.4 for benchmark 2 the mesh had more influence on the prediction of interface heights than on the reduced gravities and ventilation flow rates. The different mesh structures in the region occupied by the thermal plume are shown in Figure C3.

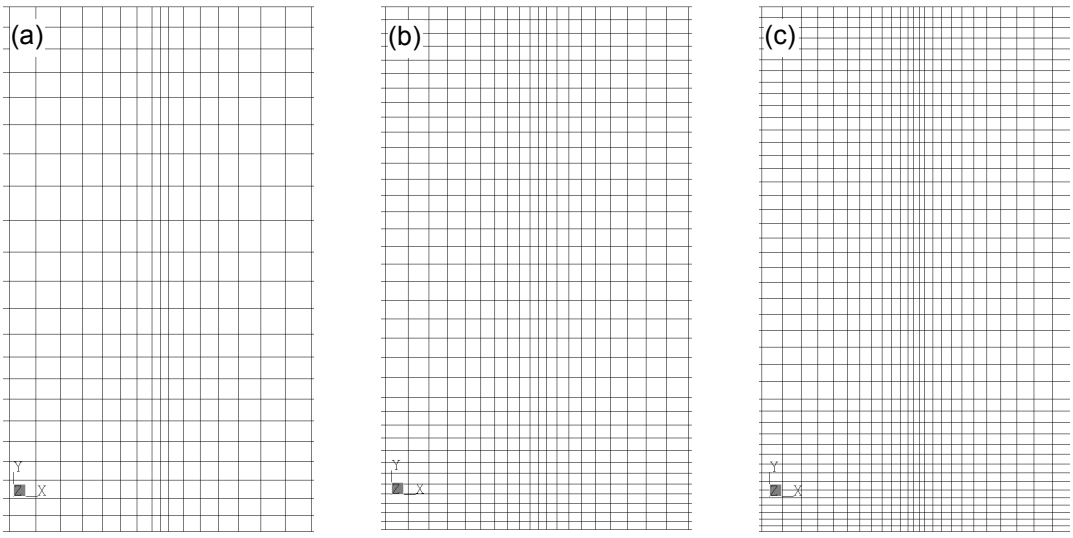

FigureC3 The mesh structures close to the region of the thermal plume for different mesh densities (a) 75K cells, (b) 165K cells and (c) 320K cells.

The predicted interface heights of these mesh structures are shown in Figure C4. The same temperature scale was used for these figures. Clearly shown in the figure, the coarse mesh with 75K cells under-predicted the interface position although the temperature between the upper and lower layers are very similar for these different mesh densities, while the interface position predicted by the 165K cells and 320K cells mesh densities are similar.

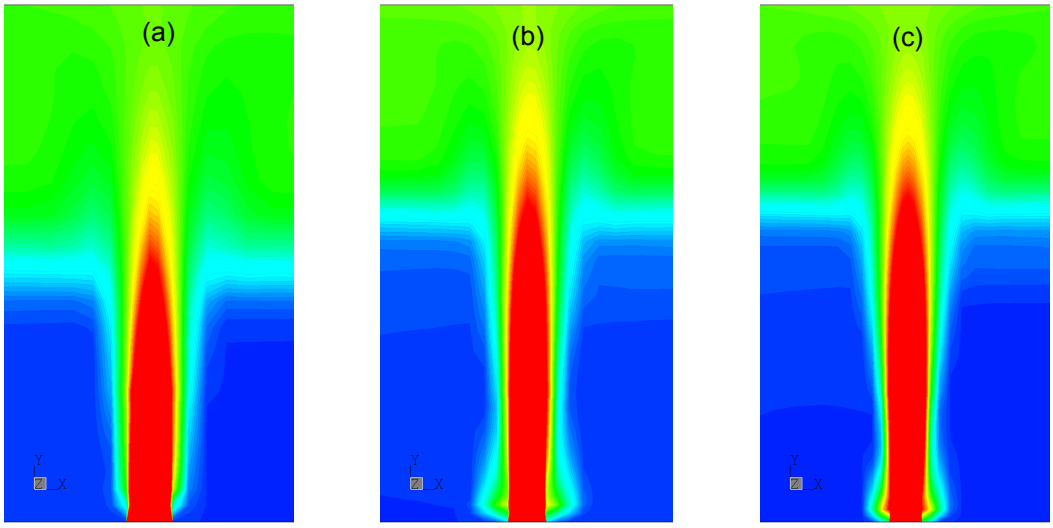

Figure C4 The interface position predicted by CFD using different mesh densities (a) 75K cells, (b) 165K cells and (c) 320K cells.

As discussed in section 8.2.2, a thermal plume shape closer to the analytical assumption was predicted using an area source of $0.01 \times 0.01 m^2$ (25 times

smaller than the area source used in Figure C4). The mesh structure for this case and the resulting CFD prediction of stratification and plume shape are shown in Figure C5 (Figure C4b is shown on the right for comparison).

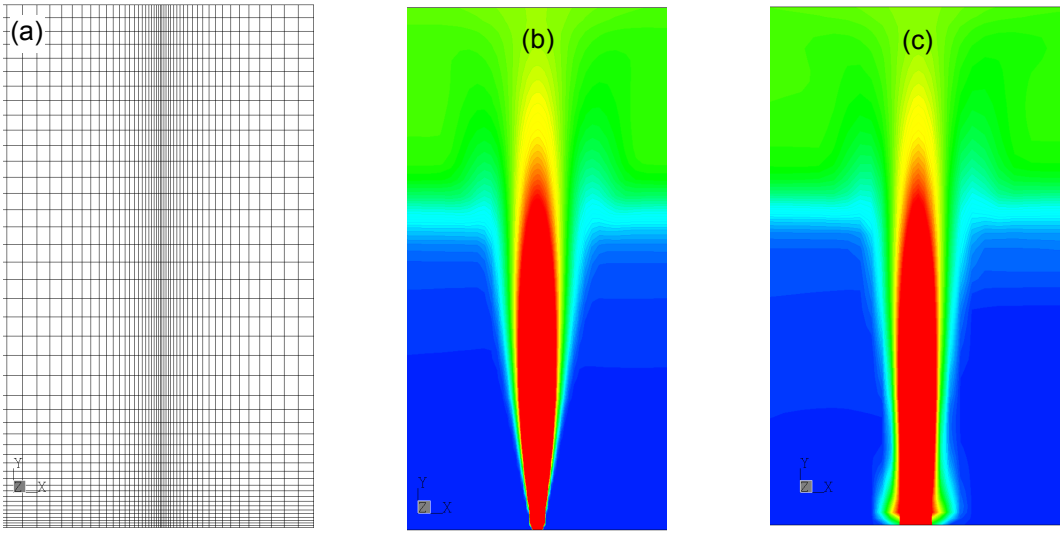

Figure C5 (a) The mesh structure used for a better prediction of the thermal plume shape, (b) resulting plume shape (c) Figure C4c.

The mesh used in Figure C5a, b has 380K cells, however, the overall predictions of interface height, temperature field and ventilation flow rates were similar to those obtained using the original source area ($0.05\times0.05m^2$) and the mesh (160k cells). Therefore, the original geometry using an area heat source ($0.05\times0.05m^2$) with medium mesh density (165K) was considered sufficient for predicting the airflow features of these benchmark cases.

Appendix D

Simulation Details

Table D1: Numerical parameters, solution techniques together and running conditions of Benchmark 1 cases.

Technique/Parameter	Details
Geometry	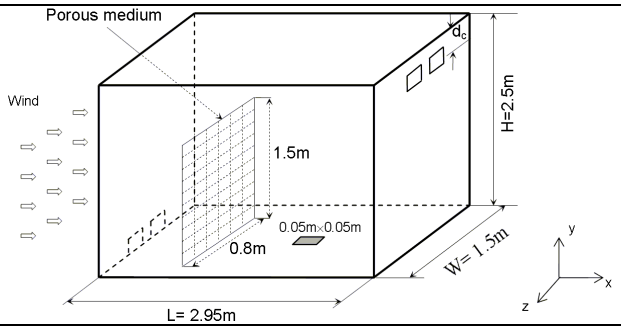
Solution procedure	Central differencing scheme was used for mass conservation equation; hybrid differencing was used for all other equations. Pressure correction was carried out using the SIMPLEC algorithm with the Rhie and Chow interpolation algorithm to overcome the pressure-velocity decoupling due to the non-staggered grid.
Under-relaxation factors	Mass equation: 1.0, momentum equations: 0.65, k, ε equations: 0.7
False time-Steps	This was only applied in the momentum equations with a value of 0.25s
Reference temperatures	Standard fluid ref. temperature: the estimated domain temperature; Buoyancy ref. temperature: ambient, 15ºC, Enthalpy ref. temperature: ambient, 15ºC
Turbulence model	RNG $k-\varepsilon$ model
Boundary conditions	Pressure boundary (applied onto ventilation openings directly with unity as loss coefficients); Wall boundary; Symmetry Plane Boundary; Porous Boundary

1. Varying assisting wind speed

Conditions	E =100 W ; B = 2.75×10^{-3} m^{4}s^{-3} (Eq 2.18); A^*/H^2 =3.4×10^{-3}						
U_w (m/s)	0.0	0.47	0.93	1.39	1.5	1.85	
Δ (Pa)	0.0	0.12	0.47	1.06	1.31	1.88	
Fr	0.0	3.0	6.0	9.0	10.0	12.0	

2. Varying A^*/H^2 with assisting wind

Conditions	E =100 W , U_w =0.65m/s, Δ =0.23 Pa, Fr =4.2, B = 2.75×10^{-3} m^{4}s^{-3}						
A^* (m^2)	0.025	0.0375	0.050	0.0625	0.075	0.0875	
$A^*/H^2 \times 10^{-2}$	0.4	0.6	0.8	1.0	1.2	1.4	

3. Varying source strength E with assisting wind

Conditions	Δ =0.23 Pa, U_w =0.65m/s, A^*/H^2 =3.4×10^{-3}							
E (W)	5	20	50	75	100	150	500	2000
B ×10^{-3} m^{4}s^{-3}	0.1375	0.55	1.375	2.0625	2.75	4.125	13.50	55.0
Fr	11.4	7.18	5.29	4.62	4.20	3.67	2.45	1.55

4. Varying opposing wind speed

Conditions	E =100 W , B = 2.75×10^{-3} m^{4}s^{-3}, A^*/H^2 =2.05×10^{-2} and 1.23×10^{-2}				
U_w (m/s)	0.0	0.31	0.47	0.62	0.78
Δ (Pa)	0.00	0.053	0.120	0.213	0.334
Fr	0.0	2.0	3.0	4.0	5.0

5. Varying A^*/H^2 with opposing wind

Conditions	E =100 W , U_w =0.545m/s, Δ =0.1634 Pa, Fr = 3.5, B = 2.75×10^{-3} m^{4}s^{-3}				
A^* (m^2)	0.020	0.045	0.080	0.097	0.125
A^*/H^2 (×10^{-2})	0.32	0.72	1.28	1.55	2.00

6. Varying source strength E with opposing wind

Conditions	U_w =0.545m/s, Δ =0.1634 Pa, A^*/H^2 =1.23×10^{-2}				
E (W)	50	75	100	150	200
B ×10^{-3} m^{4}s^{-3}	1.375	2.06	2.75	4.125	5.5
Fr	4.45	3.89	3.5	3.01	2.8

Table D2: Numerical parameters, solution techniques together and running conditions of Benchmark 2 cases.

Technique/Parameter	Details
Geometry	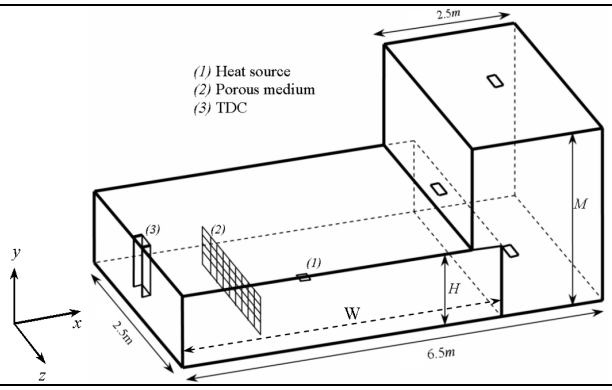
Solution procedure	Central differencing scheme was used for mass conservation equation; QUICK differencing was used for the three momentum equations and hybrid differencing was used for all other equations. Pressure correction was carried out using the SIMPLEC algorithm with the Rhie and Chow interpolation algorithm to overcome the pressure-velocity decoupling due to the non-staggered grid.
Under-relaxation factors	Mass equation: 1.0, momentum equations: 0.65, k , ε equations: 0.7
False time-Steps	This was only applied in the momentum equations with a value of 0.25s
Reference temperatures	Standard fluid ref. temperature: the estimated domain temperature; Buoyancy ref. temperature: ambient, 15°C Enthalpy ref. temperature: ambient, 15°C
Turbulence model	RNG $k-\varepsilon$ model
Boundary conditions	Pressure boundary (applied onto ventilation openings which connect exterior directly with unity as discharge/expansion coefficients); Wall boundary; Symmetry Plane Boundary; Porous Boundary

a. Varying total effective opening area								
Conditions	M/H =2.35, Buoyancy flux B =2.75×10^{-3} (m^{4}s^{-3})							
A_t (m^2)	0.015	0.020	0.028	0.040	0.056	0.076	0.099	0.119
$A_t/H^2\times10^{-2}$	0.60	0.80	1.12	1.60	2.25	3.05	3.95	4.75

b. Varying the stack height					
Conditions	A_t/H^2 =0.80×10^{-2} , Buoyancy flux B =2.75×10^{-3} (m^{4}s^{-3})				
M (m)	2.37	3.72	6.32	7.90	11.06
M/H	1.5	2.35	4.0	5.0	7.0

c. Varying effective atrium top outlet area					
Conditions	The storey dimensionless effective opening area A_s/H^2 =1.77×10^{-2} and M/H =2.35, Buoyancy flux B =2.75×10^{-3} (m^{4}s^{-3})				
A_u (m^2)	0.015	0.030	0.056	0.067	0.095
$A_u/H^2\times10^{-2}$	0.60	1.20	2.24	2.69	3.79

d. Varying effective atrium bottom inlet area					
Conditions	The total dimensionless effective opening area A_t/H^2 =4.75×10^{-2} and M/H =2.35, Buoyancy flux B =2.75×10^{-3} (m^{4}s^{-3})				
A_b (m^2)	0.00	0.10	0.15	0.275	0.45
A_b/H^2	0.00	0.04	0.06	0.11	0.18